Modelling plasma reactors

for sustainable CO_2 conversion and N_2 fixation

Senne Van Alphen

Proefschrift voorgelegd tot het behalen van de graad van Doctor in de Wetenschappen: Chemie

Promotors : prof. dr. Annemie Bogaerts and prof dr. Rony Snyders

University of Antwerp

Faculteit wetenschappen

Departement Chemie

UMONS University of Mons

Faculté des Sciences

Département de Chimie

Table of contents

SUMMARY

200 years ago, humanity started the industrial revolution by discovering one of the Earth's greatest sources of concentrated energy: fossil fuels. Thanks to fossil fuels, our civilization saw unprecedented technological advancements, facilitating work through engines and greatly improving our daily life through the production of plastics, pharmaceuticals and fertilizers.

However, after 200 years of burning fossil fuels, it has become alarmingly clear that these advancements came at a great cost, as greenhouse gas emissions, associated to burning fossil fuels, threaten to cause irreversible climate changes through global warming. Given the major environmental concerns associated with fossil fuels, a short-term transition from a carbon-based energy economy to a sustainable one based on green electricity, is essential. A key step concerning this transition exists in developing electricity-driven alternatives for chemical processes that rely on fossil fuels as a raw material. A technology that is gaining increasing interest to achieve this, is plasma technology.

Using plasmas to induce chemical reactions by selectively heating electrons in a gas has already delivered promising results for gas conversion applications like CO_2 conversion and N_2 fixation, but plasma reactors still require optimization to be considered industrially competitive to existing fossil fuel-based processes and emerging other electricity-based technologies. In this thesis I develop computational models to describe plasma reactors and identify key mechanisms in the plasma chemistry of plasma-based CO_2 conversion and N_2 fixation. By using modeling, I aim to answer questions that can't be solved by experiments alone and use the combined insights to optimize the plasma process.

After a general introduction in chapter 1, and a description of the developed models in chapter 2, I first use the models in chapter 3 to describe a new rotating gliding arc (GA) reactor operating in two arc modes, which, as revealed by my model, are characterized by distinct plasma chemistry pathways. By combining experiments from a fellow colleague and my modelling, we reach record values for N_2 fixation into NO_x in a GA reactor operating at atmospheric pressure, obtaining NO_x concentrations up to 3.4%, at an energy cost of 2.4 MJ mol^{-1}.

Subsequently in chapter 4, my colleague and I even further improve the reactor's performance by a combined computational and experimental study of an effusion nozzle added to the rotating GA reactor, reaching the best results to date for N_2 fixation into NO_x at atmospheric pressure, i.e., NO_x concentrations up to 5.9%, at an energy cost down to 2.1 MJ/mol. My simulations reveal that the

effusion nozzle acts as very efficient heat sink, causing a fast drop in gas temperature when the gas molecules leave the plasma, hence limiting the recombination of NO back into N_2 and O_2.

In chapter 5, I investigate the possible improvement of N_2 admixtures in plasma-based CO_2 and CH_4 conversion, as significant amounts of N_2 are often found in industrial CO_2 waste streams, and gas separations are financially costly. Through combining my models with the experiment from a fellow PhD student, we reveal that moderate amounts of N_2 (i.e. around 20%) increase both the electron density and the gas temperature to yield an overall energy cost reduction of 21%.

Finally, in chapter 6 I model quenching nozzles for plasma-based CO_2 conversion in a microwave reactor, to explain the enhancements in CO_2 conversion that were demonstrated in experiments. Through computational modelling I reveal that the nozzle introduces more convective cooling by mixing the gas, as well as more conductive cooling through the water-cooled walls of the nozzle. I show that gas quenching and the suppression of recombination reactions have more impact at low flow rates, where recombination is the most limiting factor in the conversion process.

Overall, I use computational models to reveal the underlying mechanisms in three different plasma reactors for three different gas conversion applications, i.e. N_2 fixation, combined CO_2-CH_4 conversion and CO_2 splitting to pinpoint the reason for the good results that were obtained in experiments. In chapter 7, I offer an overall conclusion to the previous chapters and present a future outlook for plasma-based N_2 fixation and CO_2 conversion.

SAMENVATTING

Zo'n 200 jaar geleden begon de industriële revolutie, de grootse technologische vooruitgang in de geschiedenis van de mensheid, toen één van de grootste energievoorraden op onze planeet ontdekt werd, nl. fossiele brandstoffen. De ontdekking van fossiele brandstoffen bracht zo een ongeziene vooruitgang voor onze samenleving en levenskwaliteit met de ontwikkeling van verbrandingsmotoren en de productie van kunststoffen, geneesmiddelen en meststoffen.

Echter, na twee eeuwen van fossiele brandstofconsumptie, is het duidelijk geworden dat er aan deze grote vooruitgang een duur prijskaartje hing: De broeikasgassen die vrijkomen bij het verbranden van fossiele brandstoffen en daardoor de afgelopen 200 jaar in toenemende concentraties aanwezig zijn in onze atmosfeer, veroorzaken wereldwijde klimaatsveranderingen door het broeikaseffect. Door de desastreuze gevolgen van de klimaatsveranderingen voor mens en dier, is men het wereldwijd eens dat we zo snel mogelijk moeten overstappen van fossiele brandstoffen naar duurzame energiebronnen die gebaseerd zijn op groene elektriciteit van bv. zonnepanelen en windmolens. Een belangrijke stap in deze overstap ligt in de ontwikkeling van elektriciteit-gebaseerde alternatieven voor chemische processen die op dit moment fossiele brandstoffen niet alleen gebruiken als energiebron maar ook als grondstof voor chemische reacties. Een technologie die op dit vlak grote vooruitgangen aan het boeken is, is plasmatechnologie.

Het gebruik van plasma's om chemische reacties uit te voeren door het selectief opwarmen van elektronen in een gas, heeft reeds beloftevolle resultaten opgeleverd voor belangrijke toepassingen zoals CO_2-conversie en N_2-fixatie. Echter, plasmareactoren moeten nog steeds grondig geoptimaliseerd worden om uiteindelijk op industrieel vlak te kunnen concurreren met zowel de huidige fossiele brandstofafhankelijke processen, alsook andere opkomende elektriciteit-gebaseerde technologieën. In deze thesis ontwikkel ik computermodellen om plasmareactoren te simuleren en zo belangrijke mechanismen in de plasmachemie van plasma-gebaseerde N_2-fixatie en CO_2-conversie te identificeren. Op deze manier probeer ik tot antwoorden te komen op onderzoeksvragen die met experimenten alleen niet volledig kunnen worden opgelost en probeer ik deze nieuwe inzichten te gebruiken om de plasmaprocessen verder te optimaliseren.

Na een algemene inleiding in hoofdstuk 1 en een beschrijving van de ontwikkelde computermodellen in hoofdstuk 2, gebruik ik de modellen in hoofdstuk 3 om een nieuw roterende gliding arc (GA) reactor te simuleren. Deze reactor werkt in twee verschillende arcmodes die, zoals aangetoond door de modellen, elks gekarakteriseerd worden door unieke chemische processen in het plasma. Via een combinatie van mijn modellen en experimenten in deze reactor van een collega uit de groep, bekomen we

recordwaarden voor N_2-fixatie tot NO_x in GA reactoren bij atmosferische druk, nl. NO_x concentraties van 5,5% bij een energiekost van 2,4 MJ mol^{-1}.

In hoofdstuk 4 verbeteren we de prestaties van deze reactor nog meer, via een gecombineerde computationele en experimentele studie van een mondstuk dat op de uitlaat van de roterende GA geplaatst kan worden, die we de "effusion nozzle" noemen. Met de effusion nozzle aan de reactor gemonteerd, bereiken we de tot op heden beste resultaten voor N_2-fixatie tot NO_x in een plasmareactor bij atmosferische druk, nl. een NO_x concentratie van 5,9% bij een energiekost van 2,1 MJ/mol. Mijn simulaties tonen aan dat de effusion nozzle warmte absorbeert uit de gasstroom, wat de gastemperatuur vlak na het plasma genoeg doet dalen om de terugreacties van NO tot N_2 en O_2 te onderdrukken.

In Hoofdstuk 5 onderzoek ik het effect van de aanwezigheid van N_2 op plasma-gebaseerde CO_2 -en CH_4-conversie, aangezien industriële CO_2-afvalstromen vaak een significante hoeveelheid N_2 bevatten, en het duur is om deze N_2 via scheidingsmethoden volledig te verwijderen. Via een combinatie van computermodellen en experimenten van een collega PhD student, tonen we aan dat een kleine hoeveelheid N_2 (nl. rond 20%) zowel de elektronendensiteit en de gastemperatuur verhoogt, wat de algemene energiekost van het conversieproces met 21% verlaagt.

In Hoofdstuk 6, modelleer ik het effect van koelende mondstukken op plasma-gebaseerde CO_2-conversies in microgolfplasma's, aangezien het aansluiten van deze mondstukken op de uitlaat van microgolfreactoren experimenteel enorme verbeteringen in CO_2-conversie heeft opgeleverd. Door middel van mijn computermodellen toon ik aan dat de mondstukken zowel meer convectiekoeling als conductiekoeling na het plasma veroorzaken, ten gevolge van respectievelijk verhoogde gasmixing in de uitlaat en warmtegeleiding via de waterkoeling van de mondstukken. Ik toon hierbij aan dat de verhoogde gaskoeling en het onderdrukken van recombinatiereacties meer impact heeft bij lage gastdebieten, waar recombinatie de meest limiterende factor is voor de CO_2-conversie.

Samengevat gebruik ik computermodellen om de onderliggende chemische mechanismen te onderzoeken in drie verschillende plasmareactoren voor drie verschillende plasmaprocessen, nl. N_2-fixatie, gecombineerde CO_2-CH_4-conversie en pure CO_2-conversie, om de exacte reden aan te duiden voor de goede experimentele resultaten. In hoofdstuk 7 geef ik een algemene conclusie van de bekomen resultaten en blik ik vooruit op toekomstig onderzoek voor plasma-gebaseerde N_2-fixatie en CO_2-conversie.

1 INTRODUCTION

1.1 THE COMBUSTION ERA

More than 1 million years ago, humanity discovered what is described in Greek mythology as a gift from the gods: fire. This can be marked as the very first combustion process, allowing humans to convert solar energy, that was captured over the years into organic compounds, into work and heat. Through combustion, humans no longer needed to rely solely on energy from their own metabolism, but it allowed them to harvest energy from the environment. Human energy consumption through combustion increased over the years, gradually at first, until the rate of consumption increased exponentially once industrialization occurred and the steam engine was invented. Among many other things, the steam engine allowed man to reach deep into the Earth's surface and uncover the greatest concentrated energy storage deposits of our planet, i.e. coal, gas and oil. These fossil fuels were created by decomposing and compressing organic matter below the Earth's surface over hundred millions of years, resulting in exceptionally energy dense energy sources. One barrel of oil (i.e. ca. 160 L) holds 6.1 Gigajoule of energy, which is the equivalent of 7,733 hours of man labor that can be accessed instantly through combustion.[1] It is no surprise that accessing this amount of energy allowed man to drastically speed up any work and technological advancements, enabling the industrial revolution 200 years ago.[2]

However, the major advancements brought by the discovery of fossil fuels were not only the result of using fossil fuels as an energy source in power engines. Their molecular structure being composed of long hydrocarbon chains also made these fuels the perfect starting material for the synthesis of a wide variety of chemicals. As a result, fossil fuels also enabled the birth of the petrochemical industry, in which fossil fuels are used as a starting material for the creation of versatile and valued materials for modern life, such as plastics, synthetic rubber, solvents, pharmaceuticals, explosives and adhesives. The mass production of all these products greatly improved almost all areas of modern life, including housing, mobility, communication, health, and also food. Indeed, Fritz Haber and Carl Bosch developed and industrialized one of the most important chemical processes based on fossil fuels, i.e. the production of synthetic fertilizer through the Haber-Bosch process. By removing the limitations related to being fully dependent on natural fertilizers, the discovery of fossil fuels and the invention of the Haber-Bosch process created a massive increase in production of food, resulting in the enormous increase of the human population during industrialization. This way the chemical industries have become crucial to our economy. The petrochemical industry sector in Europe, for example, creates many jobs (i.e. around 3.6 million jobs, while supporting around 19 million jobs across all value supply chains) and contributes for 3.5% to the gross domestic product (GDP) i.e. 565 billion in sales each year.[3]

It is impressive how far fossil fuels have advanced us in just three human life times from industrialization until now. Unfortunately, these enormous technological advancements and quality of life improvements came with a great cost. Burning fossil fuels, as well as converting them to plastics or fertilizers, emits greenhouse gasses (GHG's) like CO_2, CH_4 or N_2O into the atmosphere. Due to our excessive consumption of fossil fuels throughout the past centuries, these emissions have grown harmful to our Planet's ecosystem, threatening to cause irreversible climate changes through global warming. Intense drought, storms, heat waves, melting glaciers and rising sea levels because of global warming are threatening all creatures on Earth.[4] Today the common understanding has been reached that we should aim to move away from fossil fuels towards more sustainable alternatives. This is not an easy task, as throughout the years we have designed and built our infrastructures for transport, electricity and farming to suit oil, coal and gas. Especially in the chemical industry, processes rely on fossil fuels to produce the millions tons of plastic and fertilizer that are required to sustain our current lifestyle. However, just like the chemical industry brought many innovating technologies in the fossil fuel era, this sector might also hold the key for a post-fossil fuel era relying on renewable chemical processes.

1.2 THE DAWN OF THE GREEN ELECTRICITY ERA

To reduce GHG emissions, recent developments in renewable energy technology seem promising for replacing fossil fuels by green electricity on a global scale. This is nowadays coined the "electrification" of the process industry. Especially photovoltaic panels for capturing solar energy and wind turbines for converting wind energy into electricity are experiencing a rapid growth in development and application. For the heat and transport industry the electrification has already started and is expected to expand quickly in the upcoming years, as these industries do not require a fundamental change in the industrial process setup, but rather a replacement of a piece of equipment, e.g. replacing an engine, boiler or furnace running on conventional fuel with a piece of electric equipment.[5] This is already visible in our daily life, as solar panels, electric heating systems and electric cars are slowly coming into our home to replace our fossil fuel-based appliances. For the chemical industry, however, electrification is more complicated, as the industry does not only consume fossil fuels as an energy source, but about half of the chemical sector's fossil fuel input is used as reagent that undergoes chemical transformation into end products like plastic and fertilizer.[3,6] Developing electricity-driven alternatives for these chemical processes thus requires reinventing these conventional chemical processes in a fundamental way, which is very challenging considering the fact that these processes reached their most optimized form over the past century. Overcoming these hurdles, however, is of great importance, given the fact that the

chemical sector is the largest industrial energy consumer and the third largest industry subsector in terms of direct GHG emissions.

As stated in a recent paper by Van Geem et al:[6] "it is no longer a question if electrification of the chemical industry will happen, but when it will be the dominating technology". Van Geem et al. continues to explain the challenges attributed to the defossilization and electrification of the chemical industry using the analogy of a tree, the so-called “chemistree”. This chemistree, shown in Figure 1.1(a), represents the current structure of the chemical industry.[6] The base of this tree is formed by a relatively small group (ca. 20) of basic but essential products that are produced on a big scale of several million tons per year worldwide. These key chemicals are produced in enormous amounts as they serve as a common starting material for the intermediate products (higher up in the chemistree in figure 1.1(a) that branch out in the many applications of chemicals (dyes, pharmaceuticals, polymers, and coatings), with their many thousands of end products (the treetop of the chemistree). However, as shown in figure 1.1(a), the chemistree is rooted in fossil raw materials, representing the chemical industry’s heavy dependency on fossil fuels as raw materials. It is there, at the roots of the tree in figure 1.1(a), where the chemical processes with the largest emissions are found, making it an environmental burden for the whole chemistree. The critical hurdle of developing a cost-efficient low-carbon chemistree thus consists of redirecting the roots away from fossil-fuels towards renewable raw materials that are abundant, such as water, waste, biomass, air, biogas and CO_2. This is achieved in the "e-chemistree", presented in figure 1.1(b). In this figure the chemistree remains unchanged from the base up to its many branches, meaning end products are still produced using conventional chemical processes that emit relatively little GHG’s, but its polluting roots are replaced by these abundant, renewable raw materials and green electricity. A key element in this e-chemistree, and thus the key elements of an electrified chemical industry, is the linkage between these new roots and the conventional base of the tree in figure 1.1(b), the so-called e-fuels and e-chemicals. These e-chemicals, such as ammonia, nitrogen oxide, carbon monoxide, hydrogen, ethylene, and methanol, serve as the new renewable building blocks for the production of the base chemicals through conventional conversion processes (e.g. the industrially well-developed Fischer–Tropsch synthesis process for the production of fuels from CO/H_2 mixtures), but are produced themselves from abundant renewable resources such as CO_2, N_2, O_2, H_2O. The production process of these e-chemicals should use specifically green electricity to provide the required energy to drive the chemical reactions (e.g. the electrolysis of water to form H_2).

However, herein lies the greatest challenge of the electrification of the chemical industry, i.e. developing cost-efficient low-carbon technologies to produce these e-chemicals from green electricity.[6] One of these challenges is related to the intermittent energy supply of renewable electricity. As one has no control over the sun or the wind, solar panels and wind turbines produce a very irregular energy supply.

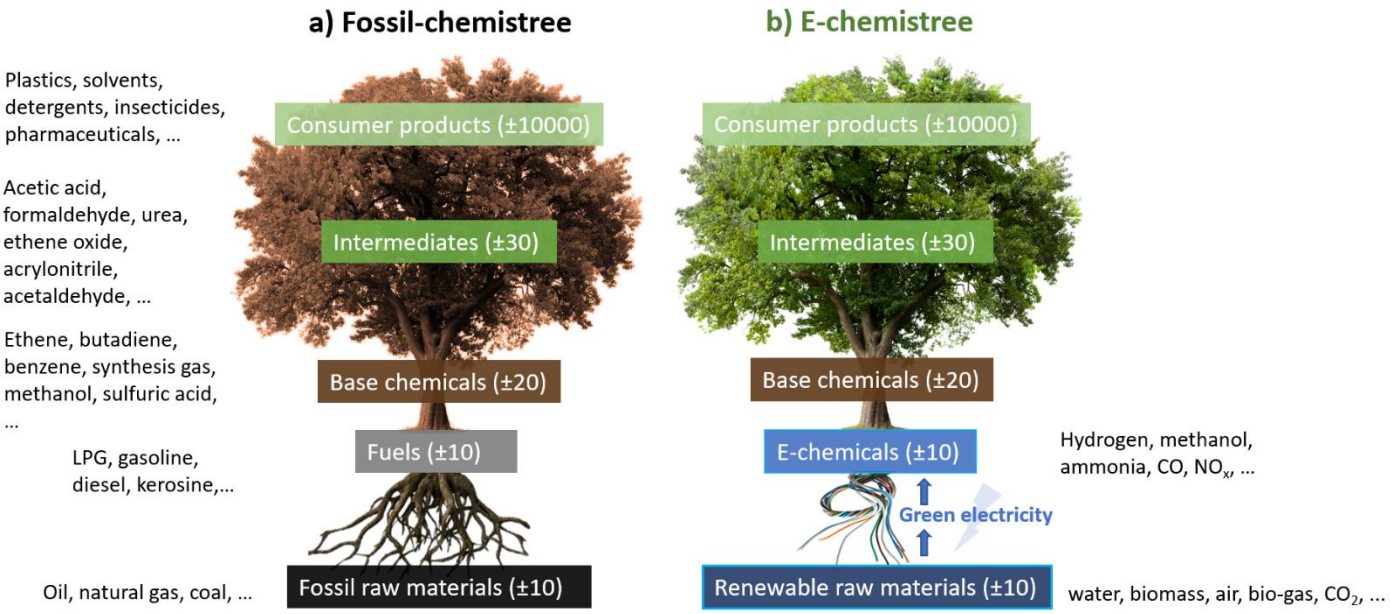

Figure 1.1: Schematic representation of a) the current fossil fuel-based chemical industry and b) a renewable chemical industry based on green electricity, using the analogy of a tree as proposed by Van Geem et al. [6]

The e-chemistry landscape is thus in need of a so-called "turnkey" process that can easily be switched on/off and is inherently flexible to follow the irregular supply of renewable electricity. Emerging technologies like photo- and electro-catalysis have already made great progress in this field, but another technology has recently gained a lot of interest to address this problem, namely plasma technology. Plasma, as will be discussed in more detail in the following sections, has some major advantages: (i) it is a turn-key process that can simply be switched on/off, allowing flexible storage of fluctuating energy; (ii) plasma chemistry is not limited to occur on the surface of an electrode (like in electro- and photo-catalysis) and can take place virtually in the entire discharge volume; (iii) it is a relatively low cost technology in comparison with photo- and electro-catalytic routes requiring more sophisticated and costly devices and materials.[7–9]

1.3 PLASMA TECHNOLOGY, THE FUTURE OF THE E-CHEMISTRY LANDSCAPE

1.3.1 Plasmas defying the rules of equilibrium chemistry

Plasmas, often referred to as the fourth state of matter, are partially ionized gasses. Plasmas thus distinguish themselves from normal gasses by containing significant amounts of charged species like ions and electrons. The latter make a plasma very interesting from a chemical perspective, as free electrons, when heated, cause ionization, dissociation or excitation upon impact with molecules, creating excited species, ions and radicals that quickly react further, creating new molecules. In so-called non-thermal plasmas, energy is predominantly transferred to electrons, typically reaching electron energies of a few eV (i.e. several 10 000 K), while the bulk gas remains virtually at room temperature,

up to a maximum of a few 1000 K.[10] Such a non-equilibrium between electrons and gas molecules can be achieved in its most simple way by two parallel plates with a potential difference between them. A few naturally present free electrons will be accelerated by the electric field between the plates, inducing collisions with the gas atoms/molecules that will sometimes lead to ionization of these species. These ionization reactions produce more ions and electrons, resulting in a partially ionized gas that we call a plasma. The cascade formation of charged species by ionization will ultimately create a conductive discharge channel between the plates. Within this discharge, collisions of gas molecules and high energy electrons will create energy-rich, reactive excited species and radicals, which easily react into new molecules. This chemically active plasma that ends up between the plates is achieved by nothing more than applying electrical energy to a gas, which explains why plasmas are potentially interesting in combination with renewable electricity for creating sustainable e-chemicals and e-fuels.

Due to the thermal non-equilibrium between electrons and gas molecules, non-thermal plasmas do not follow the rules of equilibrium chemistry. In thermal equilibrium, energy is shared equally between all degrees of freedom (translations, rotations, vibrations and electronic excitations) and they can all be described by a same single temperature. However, in non-thermal plasmas, collisions with high energy electrons can selectively excite one degree of freedom, leading to translational, rotational, vibrational, and electronic excitation of the molecule. If large amounts of energy are put into the degrees of freedom overlapping with the reaction coordinate of a reaction (e.g. vibrational excitation of a diatomic molecule and the dissociation of that molecule), the rate of that reaction is significantly increased, resulting in increased reactivity of molecules that would conventionally be considered too stable to react at low gas temperatures.[10] Herein lies the attractive applications of plasma technology to form e-chemicals from abundant renewable resources, such as CO_2, N_2 and O_2, as these compounds are known to be very stable due the strong double or triple bonds in these molecules. The thermal non-equilibrium facilitates the dissociation of these molecules, creating a very reactive mixture of radicals, ions and excited species that in turn form new products like ammonia, nitrogen oxide, carbon monoxide, hydrogen, ethylene, and methanol.[8,10]

The significance of the thermal non-equilibrium and the resulting increase in reactivity is strongly tied to the operating conditions of the plasma. As the gas temperature and pressure increase, more relaxation collisions occur between gas molecules, relaxing the overpopulation in any degree of freedom back to thermal levels, e.g. converting the energy from the excited vibrational mode to the translational mode, i.e. gas heating, through vibrational-translational (VT) relaxation collisions, which removes the increased reactivity resulting from the vibrational overpopulation. That's why non-thermal plasmas are categorized depending on the degree of thermal equilibrium that is present. In conventional non-thermal plasmas, the temperature of the electrons (Te) is the highest, followed by the vibrationally

excited molecules that were excited by the electrons (Tv), while the lowest temperature is shared by the translational degree of freedom (Tt, or simply the gas temperature, Tg), the ions (Ti) and the rotational degrees of freedom of the molecules (Tr); hence the temperature order is: Te ≫ Tv > Tr ≈ Ti ≈ Tg.[10] These plasmas try to take advantage of the enhanced chemistry due to vibrational excitation that is otherwise inaccessible to thermal processes. If a plasma is created at higher gas temperatures and pressures, i.e. pressure close to atmospheric pressures and gas temperatures significantly higher than room temperature (i.e up to 3000–5000 K), the plasma is called a quasi-thermal or warm plasma. These plasmas operate at the boundary of the transition between non-thermal and thermal plasma, having only the electron temperature significantly excited: Te ≫ Tv ≈ Tr ≈ Ti ≈ Tg, due to the increased presence of relaxation reactions.[10] These type of plasmas are able to take advantage of the (limited) non-equilibrium condition, while at the same time increase the rate of chemical reactions due to the higher pressure and gas temperatures. Finally, when no degree of non-equilibrium is present due to the increased temperature and pressure, the plasma is fully thermal: Te ≈ Tv ≈ Tr ≈ Ti ≈ Tg.[10] These very hot plasmas are sustained by thermal ionization of molecules, and mostly have applications in welding and cutting tools and fusion plasmas due to their very high temperatures.

1.3.2 Plasma reactors

Different types of plasmas are being investigated for sustainable gas conversion applications and the production of e-chemicals. The three most common plasma types are dielectric barrier discharges (DBDs), microwave (MW) plasmas and gliding arc (GA) plasmas. Each of these reactor types have a specific reactor design and operating conditions as well as a distinct way of generating a plasma. As a result, these reactors have different properties and features along with different advantages and disadvantages, which are discussed in the following sections.

1.3.2.1 The Dielectric barrier discharge reactor

Similar to the description in section 1.3.1 that illustrates the formation of a discharge between two parallel plates, a dielectric barrier discharge (DBD) reactor is created by applying an electric field between two electrodes. However, as the name implies, one (or both) electrodes in a DBD reactor is covered by a dielectric barrier. When a discharge channel is formed between the electrodes, this dielectric surface in between the electrodes gets locally charged at the place of impact. This local charge opposes the overall affecting electric field, locally reducing it to zero, which extinguishes the discharge within nanoseconds. Keeping these so-called micro-discharges short allows the electric field to heat the electrons while allowing minimal time to heat the gas, creating a thermal non-equilibrium between the electrons and gas molecules. The discharge is then reignited by reversing the applied potential which removes the opposing charge on the dielectric until a new discharge is formed and the cycle is repeated. DBD reactors thus use alternating current (AC) to constantly create short-lived, filamentary micro-

discharges over the whole surface of the electrodes.[11] These electrodes can be parallel plates (top configurations in figure 1.2) but a cylindrical configuration consisting of two concentric electrodes (bottom configurations in figure 1.2) is more common for gas conversion applications because it minimizes the amount of gas bypassing the plasma region. As a DBD has a simple design, which is convenient for upscaling, and operates at atmospheric pressure and (near) room temperature, it has great potential for industrial applications. This has already been demonstrated back in 1857 when DBD reactors saw its first industrial application for the production of ozone for water treatment.[12] In these reactors, several hundred of cylindrical discharge tubes are placed in parallel to create a high gas throughput.

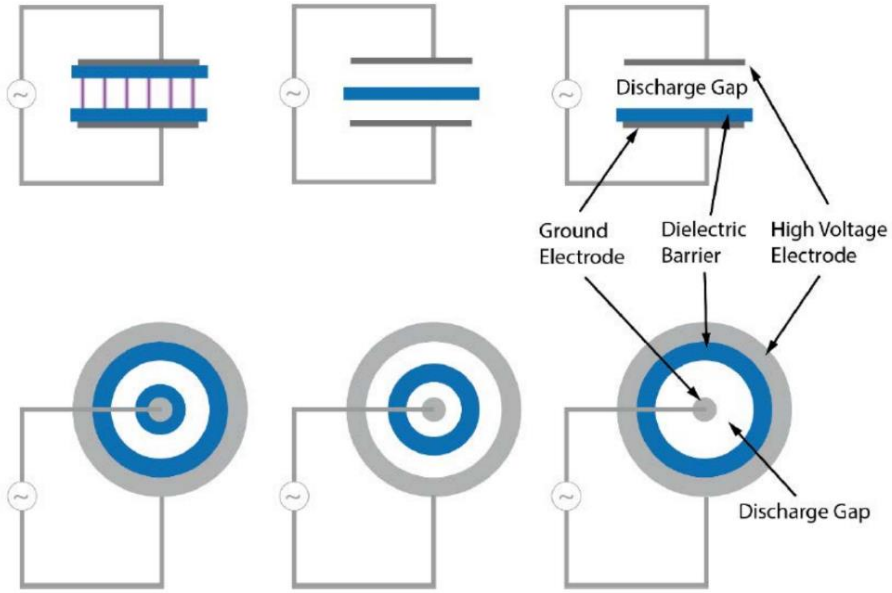

Figure 1.2: Schematic representation of basic planar (top) and cylindrical (bottom) dielectric barrier discharges, adopted from Snoeckx et al. [9]

As DBD's apply strong electric fields at atmospheric conditions, they yield a high reduced electric field, which is defined as the electric field divided by the gas number density (E/n). In DBD's the reduced electric field reaches 100 Td and higher (1 Td = 10^{21} V m^2), generating plasmas with high electron energies in the order of several eV.[7–10] While this yields a reasonable performance in terms of converting gasses like N_2 and CO_2 into value-added chemicals, the reactors don't achieve high energy efficiencies, as will be discussed in more detail in section 1.4 . More promising is the combination of DBD reactors with catalysis to better control the selective production of certain value-added compounds.[7] The simple design and ambient temperatures of the reactors allow them to be used in a packed-bed configuration, where the reactor zone between the electrodes is packed with beads (of a few mm diameter), typically coated by catalyst materials.

1.3.2.2 The Microwave reactor

Among different microwave plasma (MW) reactors (atmospheric plasma torches, resonant cavities, etc.), surface wave discharge reactors don't use electrodes to generate a plasma but make use of electromagnetic radiation, usually in the 300 MHz to 300 GHz range. The radiation is emitted through a waveguide, as shown in figure 1.3, applying microwaves to a gas flow inside a quartz tube, which is transparent to MW radiation. The electromagnetic radiation accelerates the electrons in the gas to initiate ionization reactions and generate a plasma in the quartz tube within the cavity of the waveguide. A MW reactor can operate the plasma in two different regimes depending on the operating pressure. Below ca. 300 mbar a CO_2 plasma operates in the diffuse regime, and fills up a significant part of the quartz tube, as shown in figure 1.3. Above ca. 300 mbar a CO_2 plasma operates in a contracted regime, being condensed in the center of the tube.[13] In both regimes the plasma is characterized by a rather low reduced electric field (80-180 Td for diffuse plasmas and 10-60 Td for contracted plasmas). These values are optimal for efficient vibrational excitation of gas molecules, creating a vibrational non-equilibrium.[7–10] Especially at low pressures, where these vibrationally excited species don't relax back to thermal levels, the vibrational overpopulation delivers a significant increase in performance. That's why the best performances of plasma-based gas conversion in microwave plasmas have been reported for MW plasmas at 100–200 mbar, as will be shown in more detail in section 1.4. In MW plasmas the gas temperature can easily rise to above 3000 K.[13–15] For this reason, catalyst materials cannot be easily implemented inside a MW plasma, but they can be placed after the plasma reactor (so-called "post-plasma catalysis"), although not many studies have reported on MW plasma catalysis yet.

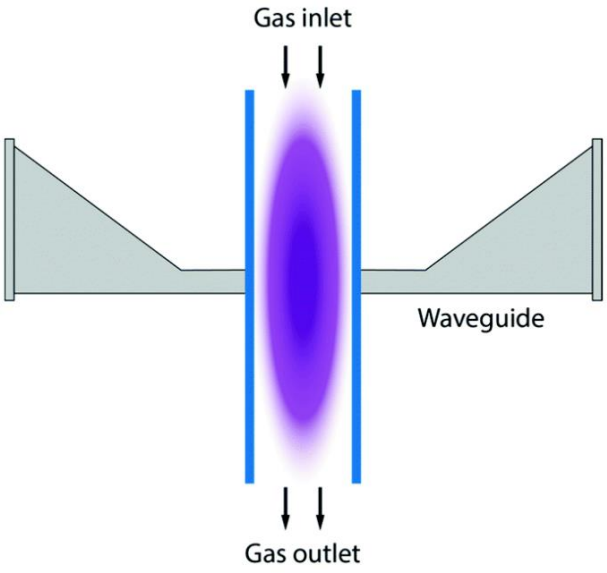

Figure 1.3: Schematic representation of a MW reactor in the diffuse regime, as adopted from Snoeckx et al. [9]

1.3.2.3 The gliding arc reactor

Just like the DBD, a gliding arc (GA) reactor is built by applying an electric potential difference between two electrodes. This reactor, however, does not involve a dielectric material that distributes the discharge into micro-discharges, but is characterized by the diverging shape of the electrodes, as shown in figure 1.4(a). Through the process described in section 1.3.1, a discharge arc self-initiates at the narrowest gap between the electrodes, which is where the gas inlet of the reactor is located. Being dragged along by the gas flow, the arc then travels or "glides" upwards over the diverging electrodes. When the distance between the electrodes becomes too large for the arc to be sustained, it extinguishes and a new arc is initiated at the narrowest gap, repeating the cycle. Like the MW reactor, GA plasmas are characterized by a low reduced electric field (below 100 Td), making vibrational excitation an important excitation mechanism.[7–10] However, as GA reactors operate at atmospheric pressure, a lot of relaxation collisions occur, relaxing the vibrational non-equilibrium quickly back to thermal levels, making a GA a so-called warm plasma.

This classical flat two-dimensional (2D) design of the GA has already been investigated for several gas conversion applications, but typically suffers from a couple of problems. The 2D electrode geometry leads to non-uniform gas treatment, as a significant amount of gas does not flow through the arc, or even flows around it as it glides upwards. Furthermore, the reactor deteriorates fast due to strong electrode degradation, as a result of the high current density of the discharge. For this reason, novel GA designs have been developed, aiming to improve the electrode lifetime, ionization efficiency and gas conversion. These new envisaged reactor designs abandon the classical 2D configuration and opt for a three-dimensional (3D) cylindrical geometry that introduces the gas stream through tangentially oriented gas inlets.[16] This initiates a vortex swirl flow along the walls of the reactor, capturing the arc in a so-called ‘tornado flow’ and dragging it along the reactor walls in a rotating movement, as illustrated in figure 1.4(b). This 3D movement of the arc increases the fraction of the gas treated by the plasma while also partially isolating the plasma from the reactor walls, hence increasing electrode (reactor) lifetime. Like in the MW plasma, catalysts cannot easily be implemented inside the plasma reactor due to the high temperature, but placing a catalyst bed after a GA plasma reactor has provided spectacular results in terms of enhanced conversion and energy efficiency.[17]

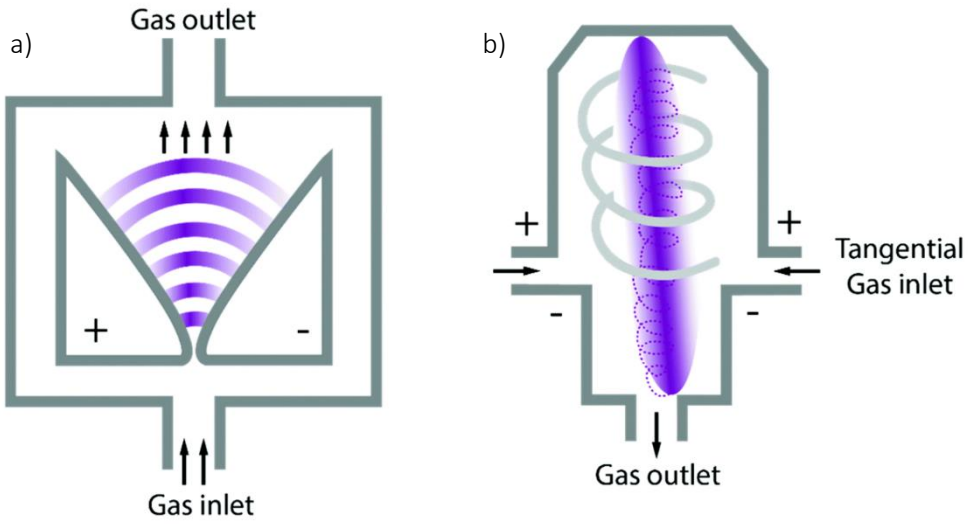

Figure 1.4: Schematic representation of a) a classical 2D GA reactor and b) a novel 3D GA reactor incorporating a vortex flow through tangential gas inlets, as adopted from Snoeckx et al. [9]

1.4 PLASMA-BASED GAS CONVERSION

Given the promising feature of plasma technology to induce chemical reactions using electricity, plasma technology presents itself as a possible missing link between renewable electricity sources and the production of sustainable chemicals. As a result, the above-mentioned plasma reactors are gaining increased interest for sustainable gas conversion applications. Two major field of applications, which are also the focus of this thesis, are plasma-based CO_2 conversion and plasma-based N_2 fixation. Plasma-based CO_2 conversion aims to convert CO_2 emissions into value-added chemicals and fuels, while N_2 fixation aims to convert N_2 from the air into precursors for mineral fertilizers. These two topics are discussed further in the following sections.

1.4.1 CO_2 conversion

1.4.1.1 CO_2, a problematic molecule

CO_2 is the most prevalent GHG, representing 79% of all GHG emissions. In 2020 the global average atmospheric carbon dioxide was measured to be 412.5 ppm, setting a new all-time record high amount despite the economic slowdown due to the COVID-19 pandemic.[4] Before the industrial revolution started in the mid-1700s, the global average amount of carbon dioxide was about 280 ppm. Since then the average temperature has shifted by about 1°C, as a result of the greenhouse effect trapping heat inside the atmosphere. Warmed by sunlight, Earth's land and ocean surfaces continuously radiate thermal infrared energy. Greenhouse gasses like CO_2 absorb that heat, and emit it again gradually over time, partially back again to the Earth's surface.[18] This entrapment of heat inside the Earth's atmosphere is called the "greenhouse effect", and is in its origin a natural process of vital importance: without it, the

Earth's average temperature would be -18 °C instead of the current 15°C. However, the enormous anthropogenic emission of GHG's has tipped this natural effect out of balance, trapping additional heat and globally raising the atmosphere's temperature.[18]

In their recent flagship report, the International Energy Association (IEA) has calculated that, in order to have a 50% chance of restricting global warming to 2°C, CO_2 emissions must be reduced by 17 Gt in 2030 and by 39 Gt in 2050 against projected emissions.[19] In this report, the importance of Carbon Capture and Utilization (CCU) is underlined, i.e. capturing CO_2 that would otherwise be emitted into the atmosphere, and converting it into value-added chemicals and renewable fuels. The upcycling of CO_2 waste streams enables the transition from a linear to a circular carbon economy, closing the so-called "carbon loop". This conversion fits perfectly within the concept of 'cradle-to-cradle', i.e. recycling waste products into new sustainable feedstock. [9,20]

One way to convert CO_2 into value-added products is by dissociating the molecule into CO and O_2:

$$CO_{2(g)} \rightarrow CO_{(g)} + \frac{1}{2} O_{2\ (g)} \qquad \Delta H^\circ = +283\ \mathrm{kJ/mol}$$

The produced CO can be combined with H_2 from another source to form a mixture that is known as syngas. Syngas is a crucial intermediate in the production of methanol and synthetic hydrocarbon fuels through the Fischer-Tropsch process, which is a great way to create a key base chemical through upcycling CO_2 emissions. However, as indicated by the high reaction enthalpy of the dissociation step, the CO_2 splitting process requires a lot of energy, as CO_2 is thermodynamically a very stable molecule due to its strong chemical C-O bond (783 kJ mol^{-1}). This is the reason why it is the end product of so many combustion processes and why it remains in our atmosphere without reacting away spontaneously. This is illustrated in figure 1.5, showing the CO_2 conversion and energy efficiency of the thermal CO_2 dissociation process at different temperatures.[9] As shown by the figure, no significant conversion occurs at moderate temperatures below 2000 K. Only around 3000 K, the splitting process occurs the most efficiently, as only then sufficient energy is provided through gas heating to break the stable CO_2 molecule in an efficient way, reaching CO_2 conversions around 50% . To dissociate nearly all CO_2 molecules, without the aid of a catalyst, a gas temperature up to 4000 K is required.

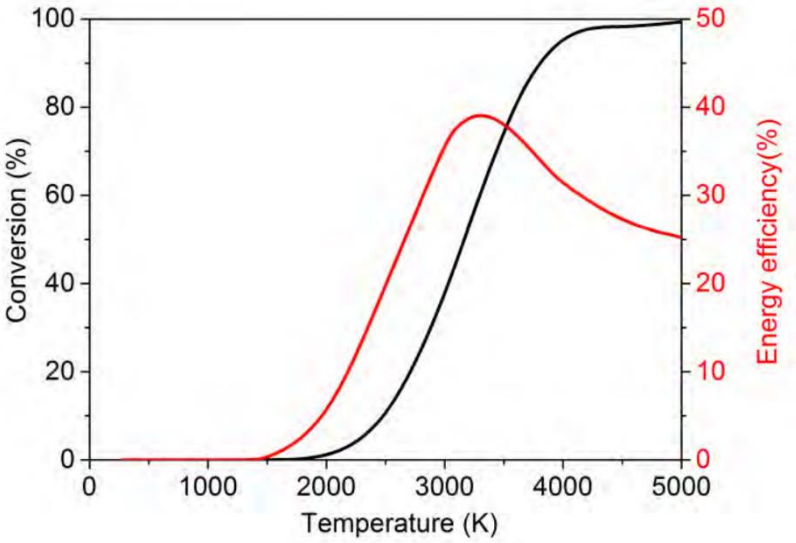

Figure 1.5: Calculated theoretical thermal conversion (left axis) and corresponding energy efficiency (right axis) as a function of temperature for the pure splitting of CO_2 into CO and O_2, adopted from Snoeckx et al. [9]

In the pursuit of making the CO_2 splitting process more energy-efficient, a second way of converting CO_2 was developed, i.e. by involving a co-reactant in the splitting process. Pairing CO_2 splitting with the conversion of a more reactive molecule allows the overall process to become thermodynamically more favorable and less energy consuming. Furthermore, a co-reactant containing H-atoms would allow the direct plasma-based production of syngas (CO/H_2), as well as the formation of oxygenates and higher hydrocarbons, which are much more valuable end products. This is achieved by combining the conversion of both CO_2 and CH_4 in the dry reforming of methane (DRM):

$$CO_{2(g)} + CH_{4(g)} \rightarrow 2CO_{(g)} + 2H_{2(g)} \qquad \Delta H^\circ = +247\ \text{kJ/mol}$$

Compared to the pure CO_2 splitting reaction, the addition of CH_4 lowers the overall enthalpy of the reaction by 36 kJ/mol, making the dry reforming reaction less thermodynamically unfavorable. Furthermore, as CH_4 is also a common GHG with a global warming potential that is even 28 times higher than that of CO_2, DRM has the potential to valorize two common GHG's at once.

Similar to figure 1.5, figure 1.6 shows the conversion and energy efficiency of the thermal conversion process, but now for the DRM reaction. In comparison with figure 1.5 , figure 1.6 clearly shows that adding CH_4 greatly optimizes the temperature dependency of the reaction towards lower temperatures. Whereas pure CO_2 splitting does not allow conversion below 2000 K, almost all the gas has already converged at 1000 K in the DRM process, reaching maximum conversion slightly above 1000 K. The peak in energy efficiency also shifted by ca. 2000 K (i.e. from ca. 3000 K to ca. 1000 K) by adding CH_4 to the mixture.

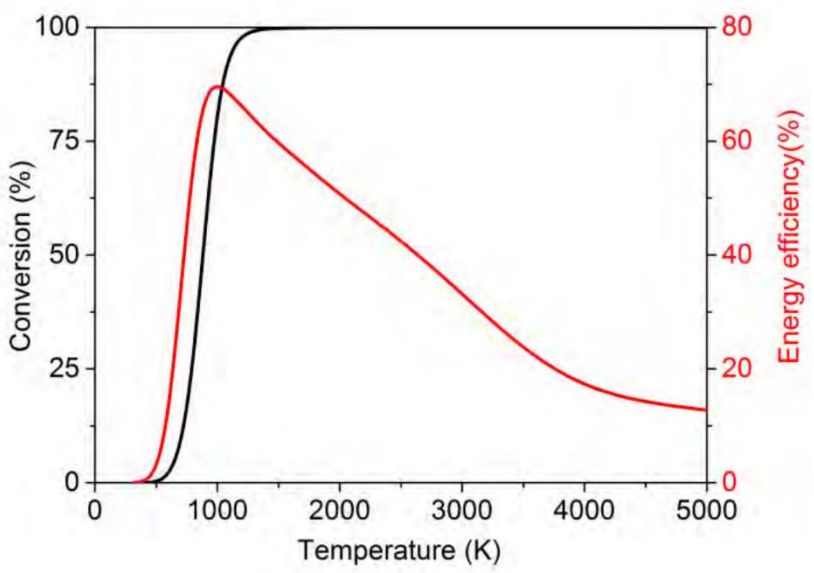

Figure 1.6: Calculated theoretical thermal conversion (left axis) and corresponding energy efficiency (right axis) as a function of temperature for the dry reforming of methane, adopted from Snoeckx et al. [9]

1.4.1.2 Plasma-based CO_2 conversion

Both ways of CO_2 conversion (pure CO_2 splitting or through DRM) have gained increasing interest when considering plasma-based processes. Research on plasma-based CO_2 splitting into CO and O_2 already started back in the 1980s in the former Soviet Union. The recent environmental concerns regarding CO_2 emissions renewed interest for this research topic, inspiring many researchers all around the world to try optimizing the process in various types of plasma reactors. The results of these efforts are summarized in figure 1.7, serving as an overview of the state-of-the-art for plasma-based CO_2 conversion. This figure, adopted from a review paper published by Snoeckx and Bogaerts[9], plots the reported energy efficiency and achieved CO_2 conversion in the literature for the various plasma reactor types discussed in section 1.3.2, and compares their performance to a 60 % efficiency target. This target is determined by comparison with technologies competing for renewable chemical production, being electrochemical water splitting, which reaches commercial energy efficiencies of 65–75%, and solar thermochemical conversion, for which a solar-to-fuel conversion efficiency of 20% is considered industrially competitive.[9] The latter value can only be compared to the solar-to-fuel efficiency of the plasma-based process, which would yield a competitive solar-to-fuel efficiency of 15–20%, if an energy efficiency of 60–80 % is reached for plasma-based CO_2 conversion, assuming a solar panel efficiency of 25%. As a result, a 60 % efficiency is deemed a reasonable target to be competitive to both emerging technologies.

As shown in figure 1.7, the highest energy efficiencies are achieved in GA and MW reactors, some even reaching the energy efficiency target of 60%. Extremely high energy efficiencies up to 90% with a conversion of 10% were reported back in the 1980s for MW plasmas operating at very specific

conditions, i.e., supersonic gas flow and pressures around 100–200 Torr.[21] These results, however, have not yet been reproduced since then. The highest recently reported energy efficiencies are around 40–50% with conversions around 10-20%,[14,22,23] while higher conversion of 50–80% can also be achieved at the cost of a lower energy efficiency, i.e. around 10%.[14] All of these results were obtained at reduced pressure, typically up to a few 100 mbar, where there is a clear thermal non-equilibrium. Close to 1 atm, MW plasmas are quasi-thermal and yield conversion around 10% at energy efficiencies around 30%.[24,25] GA plasmas, on the other hand, always operate at atmospheric pressure and provide similar results, achieving energy efficiencies around 30–40%, with some exceptions up to 60%, with the conversion typically being around of 10%.[26–28]

DBD reactors, on the other hand, typically yield CO_2 conversions up to 30 %, with energy efficiencies up to 5–10 %,[9,29] which is low compared to both the 60% efficiency target, as well as compared to the other plasma types shown in the figure. However, the performance of the reactor type can be improved by introducing a packed bed inside the DBD reactor. Van Laer et al.[30] and Mei et al.[31] have showed that some packing materials, like ZrO_2, TiO_2 and $BaTiO_3$, can enhance the electric field in the reactor due to polarization of the packing beads, or introduce a (photo)catalytic effect, which, in some cases, is able to make up for the lost plasma volume that results from introducing the packing inside the reactor.

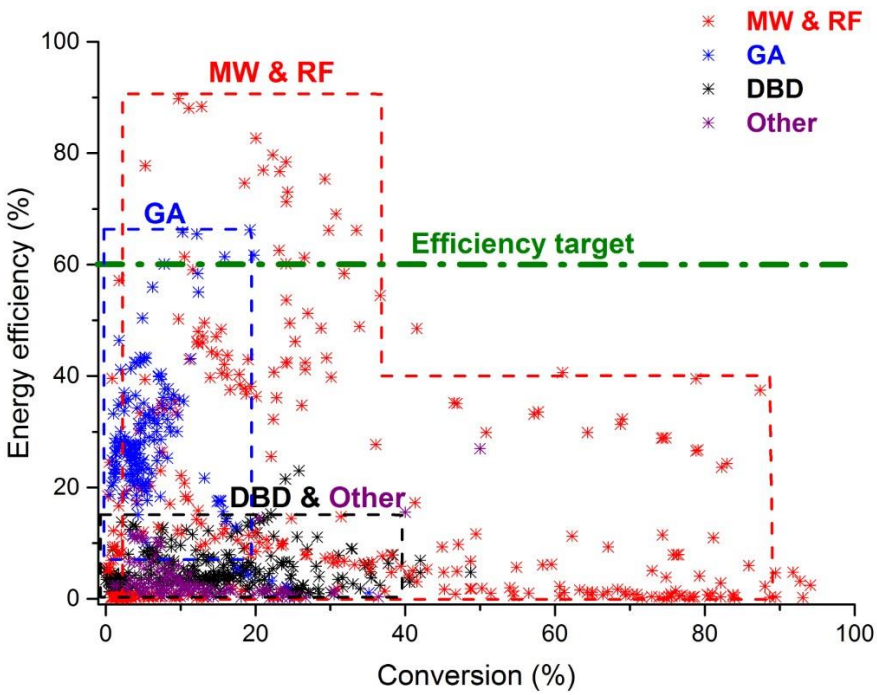

Figure 1.7: Comparison of all the data collected from literature for CO_2 splitting in the different plasma types, showing the energy efficiency as a function of the conversion, adopted from Snoeckx et al. [9]. The 60 % efficiency target is also indicated.

The reason for the more efficient CO_2 splitting in MW and GA plasmas, compared to DBD reactors is attributed to the dominant dissociation pathways in the different reactors, which are shown schematically in figure 1.8 . As mentioned in section 1.3.2, DBD's generally apply a high reduced electric field (i.e. above 100 Td), yielding high energies above 1 eV, at which 70-80% of the electron energy goes into electronic excitation of CO_2.[32] If enough energy (7 eV) is provided to a CO_2 molecule, it is excited into a dissociative (i.e. repulsive) electronic state, which will lead to its dissociation into CO and O, as illustrated in figure 1.8. However, while this pathway ensures that little energy is lost to gas heating (due to the thermal non-equilibrium in a DBD reactor), the amount of energy spent is significantly higher than the theoretical value necessary for C-O bond breaking (5.5 eV), making the dominant CO_2 splitting process in DBD reactors not very energy-efficient. GA and MW reactors, however, adopt a more energy-efficient CO_2 dissociation pathway. These reactors are characterized by lower reduced electric fields (i.e. below 100 Td) yielding electron energies around 1 eV, at which 90% of the energy goes into vibrational excitation.[9,10] This excitation process involves many small excitation steps, so-called ladder-climbing, gradually populating higher vibrational levels, which eventually lead to dissociation of the CO_2 molecule, as illustrated in figure 1.8. In this way, it is possible to dissociate CO_2 using only the minimum amount of 5.5 eV for breaking the C-O bond, without overshooting this value, resulting in a more energy-efficient process for these reactor types.

The dissociation pathway through vibrational ladder climbing is exploited the most at reduced pressures, where VT-relaxation collisions, that depopulate the vibrational ladder by converting vibrational energy to gas heating, occur less frequently.[10] That's why the best results in terms of both conversion and energy efficiency for CO_2 plasmas are found at reduced pressure.[14,25,33] At atmospheric pressure the vibrational overpopulation is completely lost, as VT-relaxation increases the gas temperature, which in turn increases the rate of VT-relaxation collisions, resulting in a self-accelerating effect until the vibrational ladder is depopulated to thermal levels.[34] As a result, at atmospheric pressure the conversion is largely thermal for MW and GA reactors.

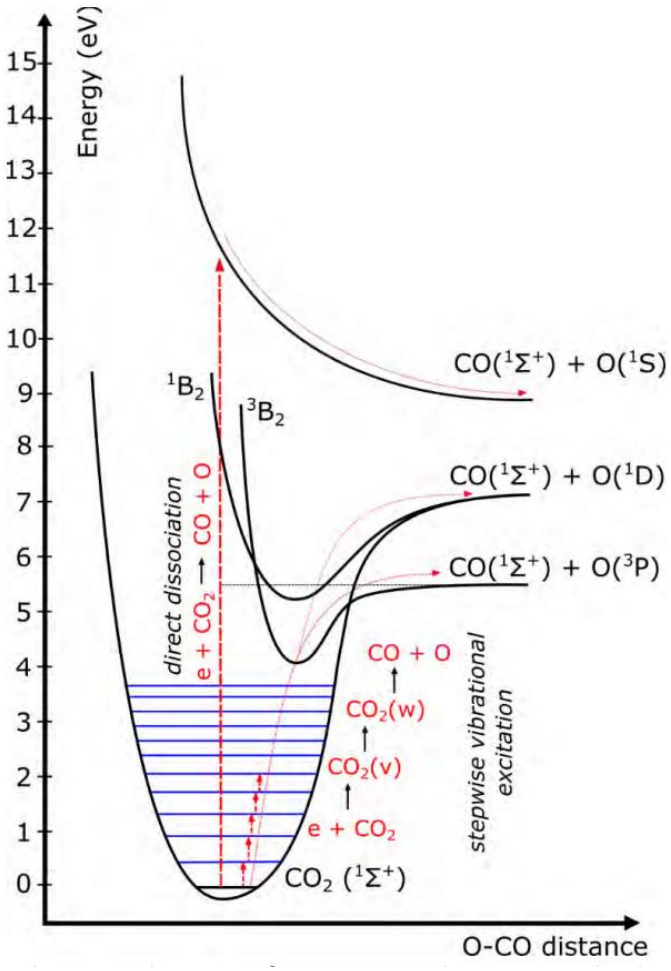

Figure 1.8: Schematic diagram of some CO_2 electronic and vibrational levels , adopted from Snoeckx et al., [9] illustrating that much more energy is needed for direct electronic excitation–dissociation than for stepwise vibrational excitation, i.e. the so-called ladder climbing process.

1.4.1.3 Plasma-based CO_2 and CH_4 conversion

As mentioned previously, pairing CO_2 splitting with a H-containing co-reactant makes the overall process less thermodynamically unfavorable. As a result, in addition to pure CO_2 splitting, a lot of research is dedicated to plasma-based DRM. Unlike pure CO_2 splitting, plasma-based DRM yields a wide variety of products. The main product is syngas (CO/H_2), but the direct production of oxygenates or higher hydrocarbons is also possible. Similar to figure 1.7, figure 1.9 shows an overview of the state-of-the-art for plasma-based DRM in literature, in terms of energy cost and conversion. The energy cost is plotted here instead of the energy efficiency (like in figure 1.7), because the true energy efficiency can only be determined if all formed products are taken into account in the theoretical reaction enthalpy, and literature typically only reports the yield toward CO and H_2 (and sometimes light hydrocarbons). As a result, the 60% efficiency target also only applies to syngas production, and corresponds to an energy cost of 4.27 eV/molecule.[9] This target would be drastically lowered if higher value hydrocarbons such as methanol could be formed directly in the plasma-based process, because the energy-intensive step

of further processing syngas into the desired products can then be circumvented, saving a lot of energy in the formation process as a whole.

Similar to pure CO_2 splitting, DBD reactors achieve a rather limited conversion for DRM (mostly around 20%) and generally lack the energy-efficiency to meet the 60% (or 4.27 eV/molecule) target, as a result of the energy-intensive electron impact dissociation mechanism. However, the compatibility with catalyst is especially valuable for DRM, given the possibility to increase the selectivity towards more valuable hydrocarbons. Indeed, the combination of plasma with catalyst yields the same products as without catalysts, but with some potential to tune the distribution of the different products due to the presence of both gas phase reactions as well as plasma-assisted surface reactions. This way, Scapinello et al. reported enhanced selectivity toward the formation of carboxylic acids in a DBD used for DRM when using copper or nickel electrodes instead of stainless steel, which was attributed to hydrogenation of chemisorbed CO_2 on the metals.[35].

GA reactors, on the other hand, are able to reach the 4.27 eV/molecule energy efficiency target. Wu et al.,[36] reported the lowest energy cost in literature for GA reactors (to our knowledge), reaching 1 eV/molecule for a conversion of 35 and 36 % for CO_2 and CH_4, respectively. The highest conversions are obtained by the "arc plasma reactor" of Dinh et al.,[37] reaching conversions up to 49 and 74 % for CO_2 and CH_4, respectively, with an energy cost of 4.6 eV/molecule. Similar to pure CO_2 splitting, GA reactors thank their low energy cost to their CO_2 and CH_4 dissociation pathways not overshooting the dissociation energy of the C-O and C-H bonds, unlike DBD reactors. It is expected that this also remains true for MW reactors. However, few experiments have been reported for DRM with a MW plasma, which is a bit surprising in view of the good results obtained for pure CO_2 splitting.

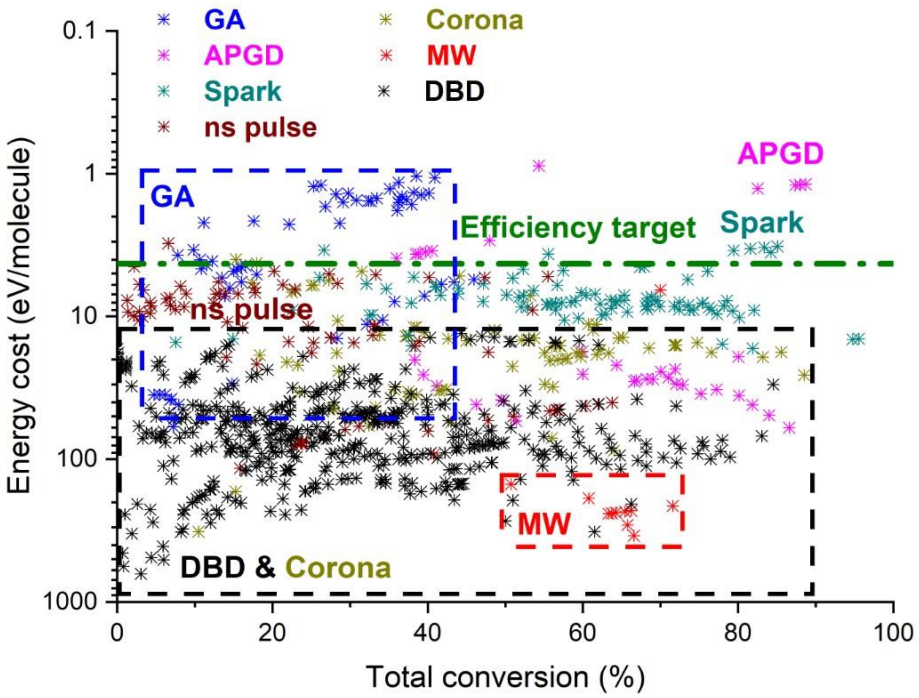

Figure 1.9: Comparison of all the data collected from literature for DRM in the different plasma types, showing the energy cost as a function of the conversion, adopted from Snoeckx et al. [9] The thermal equilibrium limit and the 60 % efficiency target for the production of syngas are also indicated.

1.4.2 N_2 fixation

1.4.2.1 The Haber-Bosch process, a blessing and a curse

The development of the petrochemical industry revolutionized many parts of our everyday life by the mass production of chemicals like plastics, pharmaceuticals, adhesives, … etc. However, the most important chemical process that came forth from the industrial revolution might be the Haber-Bosch process. In 1909, German chemist Fritz Haber successfully fixed atmospheric nitrogen in a laboratory, by forming NH_3 from N_2 and H_2. As NH_3 is the main precursor for forming nitrogen-rich fertilizers like NH_4NO_3, this discovery paved the way for the mass production of synthetic fertilizer.[38] Humans could now tap into the most abundant nitrogen source on Earth, i.e. the atmosphere being 78% nitrogen gas (N_2), which, up to that point, remained inaccessible due to the extremely stable N-N triple bond of N_2. Thanks to the iron-based catalyst developed by Carl Bosch in 1909, the Haber-Bosch process could break the strong N-N bond of N_2 under high pressures (250 to 350 bar) and moderately high temperatures (450 to 550 °C), producing NH_3 from N_2 and H_2 in large scale ammonia plants, thereby industrializing the fertilizer production. Due to its enormous impact on humanity's ability to grow food, the Haber-Bosch process is often called the "detonator of the population explosion", enabling the global population to increase from 1.6 billion in 1900 to 7.95 billion in 2022. Nowadays, the Haber-Bosch process provides

135 million tons of fixed N_2 each year, indirectly feeding 40 % of the world population through fertilizer production.[38]

While the Haber-Bosch process might be the single most important industrial chemical process, it is also the most energy-intensive one. The Haber-Bosch process uses fossil fuels, i.e. natural gas, for the production of H_2 through steam reforming, which makes this process one of the greatest energy consumers (1-2% of the world's annual energy supply, and 3-5% of the worldwide natural gas consumption), and greenhouse gas emitters (400 Mt of CO_2 per year, accounting for 1.2 % of the annual anthropogenic CO_2 emission).[39] For this reason, the carbon footprint of this process can't keep up with our current environmental standards, and changes have to be made towards a more sustainable fertilizer production. This is a significant challenge as the current Haber–Bosch process evolved in the context of fossil fuels being the main energy source, and has thus been optimized the past 100 years to its thermodynamic limit to suit this energy source. Any sustainable alternative for producing fertilizer, thus reinventing the fertilizer production in a fundamental way, has to compete with a 100 year optimized process.

1.4.2.2 Plasma-based N_2 fixation

Recently, plasma-based N_2 fixation has presented itself as a promising sustainable alternative to the Haber-Bosch process. While some plasma processes aim to produce NH_3, just like the Haber-Bosch process,[40–44] a very promising alternative plasma-based route aims for the formation of NO_x (i.e. NO and NO_2) out of N_2 and O_2, cutting the fossil fuel-consuming H_2 formation step out of the N_2 fixation process. In subsequent steps NO is fully oxidized into NO_2 and dissolved in water to form HNO_3, yielding an important fertilizer precursor in a very sustainable way, i.e. through an electrified process using the main constituents of air as its only resource.

In addition, plasma-produced HNO_3 can not only be used as precursor for synthetic fertilizer but also has the ability to enrich natural fertilizers, like manure. Approximately 50% of the nutrients in manure are lost as emissions in the form of volatile NH_3, created when bacteria degrade the waste, and in the form of nitrous oxide (N_2O), a major GHG.[45] Such losses dramatically decrease the N-fertilizer value of organic waste and contribute to perturbation of the global nitrogen cycle.[38] In current agricultural practices, these lost nutrients are replaced by synthetic fertilizers from the Haber-Bosch process. However, the volatile NH_3 in manure can be converted into involatile ammonium nitrate (NH_4NO_3) by treating the manure with plasma-produced HNO_3. The resulting NH_4NO_3 compound and the changes in pH of this composition enhance the nitrogen value of the organic fertilizer and prevent GHG emissions to the atmosphere, eliminating pollution and creating an economic benefit for farmers.[45]

The idea of using plasma to fix N_2 has actually been around before the Haber-Bosch process existed. The Norwegian duo Birkeland and Eyde were the first to develop an industrial thermal plasma reactor for N_2 fixation,[46,47] and achieved an NO production of 1-2 % with an energy cost of 2.41 MJ/mol. Since then several plasma types have been explored for NO_x synthesis; as described in depth in a recent overview and techno-economic analysis by Rouwenhorst et al.[48] Patil, et al., studied NO_x production in a packed bed DBD reactor with γ-Al_2O_3 catalyst, and reported a 0.5% NO_x concentration with an energy cost of 18 MJ/mol.[49] Similar to CO_2 conversion, DBD reactors have shown to be less energy-efficient than other reactor types. Krop and Pollo reported an NO production of 4.7% at an energy cost of 3.5 MJ/mol, in their electric arc plasma reactor with water injection [50]. Namihira et al. employed a pulsed arc discharge, and obtained 6.5% NO production and 4 MJ/mol energy cost [51]. The highest NO production with the lowest energy consumption were reported for MW plasmas at reduced pressure (50 torr) back in the 1980's. Mutel et al. reported a NO production of 6 % with a very low energy cost of 0.84 MJ/mol[52]. Azizov, et al. even achieved a lower energy cost by using a MW discharge with a magnetic field (so-called electron cyclotron resonance) and reported an NO production of 14 % with an energy cost of 0.28 MJ/mol[53]. However, these record values for MW discharges did not account for extra energy costs attributed to pumping for maintaining the low pressure regime and cooling the reactor with liquid nitrogen. Similar to the 1980's results for CO_2 splitting, these record values could never be reproduced. More recently, Kelly and Bogaerts showed very promising results for a MW reactor working at atmospheric pressure, achieving a NO_x concentration of 3.8% at an energy cost of 2.0 MJ/mol.[15] A record-low energy consumption of 0.42 MJ/mol was recently achieved by Vervloessem et al. for a pulsed plasma jet, even at atmospheric pressure, although for low NO_x concentration of 0.02 % [54]. In recent years, GA plasmas in several designs revealed promising results for NO production. A pulsed milli-scale classical GA reactor design, studied by Patil et al. and Wang et al., showed a NO_x production of 1-2 % with energy costs between 2.8-4.8 MJ/mol [55,56]. The promising results of classical 2D GA reactors led to the development of novel 3D GA designs, aiming to improve the gas conversion and the electrode lifetime. One of these designs, the gliding arc plasmatron (GAP), studied by Vervloessem et al., achieved a NO_x formation of 1.5% at an energy cost of 3.6 MJ/mol [57] Another example is the rotating GA, for which the results will be presented in chapter 3 of this thesis.

1.5 THE CHALLENGES OF PLASMA-BASED GAS CONVERSION AND AIM OF THIS THESIS

The above reported results in literature illustrate the potential of plasma technology to play a key role in the electrification of the chemical industry. For plasma-based CO_2 splitting and DRM, some MW and GA reactors have shown to reach the 60% efficiency target defined by Snoeckx and Bogaerts[9] to

compete with classical as well as other emerging technologies. Also for N_2 fixation, these two types of plasma reactors appear to be most promising, as these reactors adopt an energy-efficient dissociation channel of N_2, similar to CO_2, either through thermal dissociation (at atmospheric pressure) or through vibrational ladder climbing (at reduced pressures). However, while plasma technology can compete with other emerging technologies in terms of performance, further optimization of plasma reactors is definitely needed to make the process comparable to our current industrial processes. These conventional fossil fuel-based processes have been highly optimized in the past century, reaching conversions and energy efficiencies in large scale plants that plasma reactors cannot yet achieve on lab scale, which will affect the separation costs. Furthermore, the plasma process also needs to be optimized for a higher selectivity towards value-added compounds. Due to their high reactivity, the plasma process must be steered towards higher value target compounds using e.g. plasma catalysis, but clearly more fundamental research is still needed to obtain the necessary insights in the underlying mechanisms of plasma catalysis, needed to design catalysts tailored to the plasma environment

For pure CO_2 splitting into CO, Van Rooij et al.[58] recently performed an economic analysis of a MW reactor, envisioning the integration of renewable electricity and plasma technology in the chemical industry. In this analysis they not only considered the plasma reactor itself, but also the compressors, gas coolers and purification systems that are required to run a full scale green electricity-driven CO production plant. They estimated the capital expenditures (CAPEX) of an industrial scale MW reactor plant, which is assumed to be recovered within ten years, as well as the operating expenditures (OPEX), based on the current industrial electricity price rate. Through this calculation they estimated the manufacturing cost price of CO through the plasma process as 1200 US$/ton CO, which is not yet competitive with the current bulk CO price, which was estimated around 228 US$/ton. However, it has to be noted that all assumptions in the calculation of the base case CO price were chosen conservatively, e.g. electricity costs represent nearly 50% of the total price but are expected to go down significantly compared to fossil fuel costs as renewable electricity becomes more prevalent. Furthermore, Van Rooij et al. showed through a sensitivity analysis of the same plasma process that the achieved CO_2 conversion is the dominant cost factor.[58] Indeed, conversion propagates through separation costs, which was shown to contribute a lot to the OPEX, as well as capital costs (the same equipment produces less end product). Improving the conversion of the plasma-based process, and thereby reducing the amount of separation needed, is an important improvement to reduce the cost of the plasma-based process, and it is currently more effective to lower the OPEX related to energy consumption through e.g. improving the energy efficiency.

Similar to this CO_2 case study, Rouwenhorst et al.[48] estimated the CAPEX and OPEX of the plasma-based NO_x formation process (based on the GA reactor results that are presented in this thesis in chapter 3). However, unlike the CO_2 case study, the plasma process in this study is not compared to the current fossil-fuel based process, i.e. the highly optimized Haber-Bosch process, but to the main electricity-based competing technology for HNO_3 production, i.e. the electrolysis-based Haber-Bosch process combined with the Ostwald process. In this process the H_2 required for the Haber-Bosch process is not produced via fossil fuels but through the electrolysis of water using alkaline electrolizers.[59] The produced NH_3 is then oxidized in the presence of a rhodium–platinum gauze to form NO_x through the Ostwald process, which is the current conventional process of converting NH_3 into NO_x, ensuring a fair comparison with plasma-based NO_x formation delivering the same reaction products. Due to the costly rare earth metals in the electrolysis-based Haber–Bosch process combined with the Ostwald process, the plasma-based NO_x synthesis process benefits from a lower CAPEX over the electrolysis-based process. However, the current energy cost of ≥2.4 MJ (mol N)$^{-1}$ makes the OPEX of the plasma-based process too high to be competitive with the electrolysis-based Haber–Bosch process combined with the Ostwald process, which consumes about 0.6 MJ (mol N)$^{-1}$.[60] The plasma-based NO_x synthesis will become economically competitive if the energy consumption can be decreased to 0.7 MJ mol^{-1}.

These case studies show that significant further performance improvements of plasma reactors are still required, also beyond optimizing experimental conditions. Indeed, for plasma reactors to be competitive with conventional processes and other renewable emerging technologies, they need fundamental design and process optimizations, more than just optimizing the power and flow rate of a reactor. In this optimization process, it is important to fully understand the underlying mechanisms within plasma reactors, so that we are able to identify and enhance the reactor's strengths and improve upon its weaknesses. In addition, it is important that we can describe how any design or process optimizations change these mechanisms, to check if the optimization achieves the desired effect. An important tool in achieving this knowledge are computational models. Computational models allow one to simulate the performance of a reactor, delivering valuable insight on the underlying mechanisms that occur inside the plasma. Indeed, many plasma parameters or plasma species are difficult or impossible to measure or detect experimentally without disturbing the plasma, especially if the reactor captures the plasma inside walls of stainless steel, like e.g. many GA reactors do. Computational models can then be used to fill in the gaps left by the experiment to end up with a complete understanding of the process and provide indications for further optimization. These kind of optimizations often originate from a limitation that we have encountered in a previous design or that we know to exist from a publication. By modelling the chemical mechanisms that are involved in this limitation, we gain the knowledge to identify which parameters/conditions are crucial in chemical pathways leading to this limitation.

Knowing which parameter/conditions are required to be manipulated, a reactor design, aimed to specifically manipulate this parameter, is theorized and eventually tested. Models that are validated over a wide range of parameters can then even be used to predict possible design improvements and optimal operating conditions, before actually building a prototype, saving a lot of time and money in the optimization process.

In this thesis, we aim to develop computational models to describe several plasma reactors for both plasma-based CO_2 conversion and N_2 fixation to gain deeper insight in the underlying plasma chemistry inside these reactors. Furthermore, we aim to use these models as a tool to improve their design or operating conditions, and maximize their performance, improving upon the current literature and bringing plasma-based gas conversion a step closer to being a promising candidate for the electrification of the chemical industry on an industrial scale.

2 MODELLING PLASMA REACTORS

2.1 CFD

Since plasma reactors rely on the motion, heating and chemical transformation within gases, an important tool in the computational description of plasma reactors are Computational Fluid Dynamics (CFD) simulations, i.e. the description of fluid systems through numerical simulations. CFD is applied to a wide range of research and engineering problems in many fields of study, including aerodynamic and aerospace simulations, weather simulation, engine and combustion analysis, etc. In plasma research, CFD is used to describe the macroscopic fluid properties (gas velocity, pressure, gas temperature, …) of the gas flow through the plasma reactor. While these models are able to integrate the influence of chemistry to some extent (see section 2.1.3), the main focus remains on physical properties, rather than the chemical properties. This is in great contrast to (0D) chemical kinetics models, discussed in section 2.2, which heavily focus on the chemistry within the plasma reactor. CFD allows us to deliver a three-dimensional (3D) description of the fluid properties inside the reactor, making them very insightful, but computationally heavy.

2.1.1 Describing the gas flow

For describing the behavior of a gas flow in a plasma reactor, the most important governing equations in CFD are the Navier-Stokes equations, describing the motion of a fluid:

$$\rho_g \frac{\partial \vec{u}}{\partial t} + \rho_g(\vec{u} \cdot \nabla)\vec{u} = \nabla \cdot \left[-p\vec{I} + \mu(\nabla\vec{u} + \nabla(\vec{u})^T) - \frac{2}{3}\mu(\nabla \cdot \vec{u})\vec{I}\right] + \vec{F} \tag{2.1}$$

$$\rho_g \frac{\partial \vec{u}}{\partial t} + \nabla \cdot \left(\rho_g \vec{u}\right) = 0 \tag{2.2}$$

Where ρ_g stands for the gas density, $\vec{u}$ is the gas flow velocity vector, superscript T stands for transposition, p is the gas pressure, μ is the dynamic viscosity, $\vec{I}$ the unity tensor and $\vec{F}$ the body force vector.

These equations yield the gas flow velocity $\vec{u}$ (u,v,w) and the pressure p inside the reactor by introducing the following boundary conditions in the reactor geometry:

At the Inlet:

$$\vec{u} = \vec{u}_0 \tag{2.3}$$

In which $\vec{u}_0$ is the flow velocity defined by the input flow rate.

At the reactor walls:

$$\vec{u} = 0 \tag{2.4}$$

Where the velocity is zero as a result of the "no slip" condition at the walls.

At the outlet:

$$\left[-p\vec{I} + \mu(\nabla\vec{u} + \nabla(\vec{u})^T) - \frac{2}{3}\mu(\nabla \cdot \vec{u})\vec{I}\right]\vec{n} = p_0\vec{n}_{outlet} \tag{2.5}$$

In which p_0 is the pressure at the outlet, and $\vec{n}_{outlet}$ the unity vector normal to the outlet boundary.

The Navier-Stokes equations in equation (2.1) and (2.2) are defined for laminar flow, which occurs when a fluid flows in structured parallel layers. In this flow regime, the dampening effect of the fluid's viscosity is strong enough to subdue any chaotic fluid movement resulting from colliding into walls or obstacles. However, when the gas flow increases, at some point the fluid's inertia near walls or obstacles overcomes the damping effect of the viscosity, introducing swirling motions in the fluid, called eddies. These vertices disrupt the laminar flow layers, resulting in turbulent flow. The degree of turbulence is predicted by the Reynolds number (Re), which is defined as the ratio of the inertial forces and the viscous forces acting upon the fluid. When inertial forces dominate (in general: Re>2000), the flow is turbulent, and when viscous forces dominate (in general: Re<2000), the turbulent motion of the fluids is dampened by the fluid's viscosity and the flow is laminar.

Describing turbulent flow using the classical Navier-Stokes equations in their full form is computationally very intensive. For this reason, we simulate turbulent gas flow using a Reynolds-averaged-Navier-Stokes (RANS) turbulent model, which significantly reduces the computation time by averaging all fluctuating turbulent quantities over time. More specifically, we use the Menter's Shear Stress Transport (SST) model,[61] which uses the k-ω model[62] to specifically calculate the turbulent boundary layers near the walls, and combines it with the k-ε model[63] in the free stream, where the k-ω model fails.[61] The Navier-Stokes equations (Equation 2.1 and 2.2) then involve the turbulent dynamic viscosity (μ_T) and the turbulent kinetic energy (k_T) of the fluid:

$$\rho_g\frac{\partial\vec{u}}{\partial t} + \rho(\vec{u}\cdot\nabla)\vec{u} = \nabla\cdot\left[-p\vec{I} + (\mu+\mu_T)(\nabla\vec{u} + \nabla(\vec{u})^T) - \tfrac{2}{3}(\mu+\mu_T)(\nabla\cdot\vec{u})\vec{I} - \tfrac{2}{3}\rho_g k_T\vec{I}\right] + \vec{F} \tag{2.6}$$

$$\rho\frac{\partial\vec{u}}{\partial t} + \nabla\cdot\left(\rho_g\vec{u}\right) = 0 \tag{2.7}$$

An in depth description of this turbulent gas flow model and the equations for calculating k and μ_T are given in the appendix of this chapter (section 8.1)

2.1.2 Calculating the heat balance

As mentioned in section 1.3.1 (on page 14), warm plasmas heat up the gas to temperatures of a few 1000 K, making the simulation of the heat transfer inside the model an important part of the model. Transport of heat, generated by the plasma, can occur through the gas flow (convection) or can occur spontaneously over a temperature gradient (conduction). These two terms are simulated inside the reactor though solving the heat balance equation:

$$\rho_g C_p \frac{\partial T_g}{\partial t} + \rho_g C_p \vec{u} \cdot \nabla T_g + \nabla \cdot \vec{q} = Q_{heat} \tag{2.8}$$

Where ρ_g stands for the gas density, C_p for the isobaric heat capacity, T_g is the gas temperature, $\vec{u}$ the gas velocity (as calculated in section 2.1.1), Q_{heat} the heat source term representing the heating from the plasma, and $\vec{q}$ the conductive heat flux vector, which is calculated by:

$$\vec{q} = -(k_g + k_{g,T})\nabla T_g \tag{2.9}$$

Where k_g is the thermal conductivity of the gas and $k_{g,T}$ is the turbulent thermal conductivity of the gas, which equals zero in case of laminar flow. In case of turbulent flow $k_{g,T}$ is calculated by:

$$k_{g,T} = \frac{C_p \mu_T}{Pr_T} \tag{2.10}$$

In which μ_T is the turbulent dynamic viscosity and Pr_T the turbulent Prandtl number calculated as the ratio of the momentum eddy diffusivity and heat transfer eddy diffusivity, as defined by the Kays-Crawford model:[64]

$$Pr_T = \left(\frac{1}{2Pr_{T\infty}} + \frac{0.3}{\sqrt{Pr_{T\infty}}} \frac{C_p \mu_T}{k_g} - \left(0.3 \frac{C_p \mu_T}{k_g} \right)^2 \left(1 - e^{-\frac{k_g}{(0.3 C_p \mu_T \sqrt{Pr_{T\infty}})}} \right) \right) \tag{2.11}$$

Where $Pr_{T\infty}$ is the value of Pr_T in the "free stream" far away from the walls (~0.85).[64]

Note that equation 2.8 does not include the radiative heat transfer of the gas. At 3000 K (which is a typical gas temperature for a CO_2 arc at atmospheric pressure)[26] a perfect black body at 3000 radiates 3.04×10^6 W/m^2 to a 293.15 K environment (5.67×10^{-8} J/s m^2 K^4 * (3000-293.15 K)^4). Considering the typical dimension of the arc in a GA reactor (radius of ca. 1 mm, length of ca. 3 cm)[26] this results in a power loss of 574 W, which is a significant amount, considering the input plasma power of a GA reactor is ca. 500 W.[26] However, the emissivity coefficient (ε) of a gas is significantly lower than that of a black

body (for which ε = 1), due to their low density (especially at high temperatures), resulting in an emissivity coefficient between 10^{-3} and 10^{-2} for e.g. CO_2 at 3000 K.[65] The resulting power loss thus becomes insignificant at this small scale, compared to the plasma power of ca. 500 W.

Solving the heat balance equation (equation 2.8) yields the gas temperature T_g by introducing the following boundary conditions in the reactor geometry:

At the Inlet:

$$-\vec{n}_{inlet} \cdot \vec{q} = \rho\vec{u} \int_{T_{inlet}}^{T} C_p dT_g \cdot \vec{n}_{inlet} \tag{2.12}$$

In which T_{inlet} is the gas temperature of the inlet stream, usually 293.15 K, and $\vec{n}_{inlet}$ the unity vector normal to the inlet boundary

At the reactor walls:

If the walls are considered thermally insulated (i.e. when assuming an adiabatic system) the boundary condition states:

$$-\vec{n}_{wall} \cdot \vec{q} = 0 \tag{2.13}$$

In which $\vec{n}_{wall}$ is the unity vector normal to the wall boundary.

If heat is lost through the reactor walls to the environment at a heat loss rate q_{loss}, the boundary condition states:

$$-\vec{n}_{wall} \cdot \vec{q} = q_{loss} \tag{2.14}$$

$$q_{loss} = h(T_{ext} - T_g) \tag{2.15}$$

In which T_{ext} is the gas temperature of the environment, usually 293.15 K and h the heat transfer coefficient of the reactor wall material assuming external natural convection (20 W/(m²K) for stainless steel).

At the outlet:

$$-\vec{n}_{outlet} \cdot \vec{q} = 0 \tag{2.16}$$

In which $\vec{n}_{outlet}$ is the unity vector normal to the wall boundary

In the plasma:

Within the chemically active zone of the plasma, gas heating occurs as a result of exothermic chemical reactions and the relaxation reactions of excited species, which is represented in equation 2.8 by the heat source term Q_{heat}. The most straightforward, but approximative, way to determine this term is

using experimental data as input. This input consist of two different parameters, i.e. (i) the amount of power transferred to gas heating (P_{heat}, in W) and (ii) the plasma volume (V_{plasma}, in m³), such that the ratio of the two yields the power density (Q_{heat}, in W/m³):

$$Q_{heat} = \frac{P_{heat}}{V_{plasma}} \tag{2.17}$$

For P_{heat} in quasi-thermal plasmas at atmospheric pressure it is reasonable to assume that all the power absorbed by the electrons that did not go into chemical reactions is nearly fully transferred to gas heating,[10,13,66] which allows the plasma power transferred to heating to be calculated using the experimental plasma power P_{plasma} (which is usually calculated by measuring the voltage-current characteristics of the plasma setup using an oscilloscope) and the experimental energy efficiency EE (which is calculated from the concentrations of the plasma products at the outlet):

$$\mathrm{P}_{heat} = P_{plasma}(100\% - EE) \tag{2.18}$$

For V_{plasma}, experimental work on determining plasma shapes and volumes has been widely performed by CCD plasma emission imaging[24,67,68] or through high-speed cameras[69,70] for various plasma reactors, making this data either already available in literature or obtainable through a well-known experimental imaging procedure.

Alternatively, using a more computationally expensive but less approximative approach, Q_{heat} can be calculated self-consistently by accounting for the plasma chemistry reactions in the model, like in a plasma fluid model which is discussed in depth in next section. Additionally, specifically for GA plasmas, Q_{heat} and V_{plasma} can also be calculated self-consistently using a thermal plasma arc model, which is described and applied later in chapter 3.

2.1.3 Bringing chemistry into CFD in a plasma fluid model

While CFD primarily focuses on the physical properties, rather than the chemical properties of the plasma, these physical properties are often inevitably influenced by the plasma chemistry, e.g. exothermal reactions and relaxation of excited species influencing the gas temperature, or chemical transformations changing the gas mixture composition. These changes are taken into account in a plasma fluid model, which delivers a full description of a plasma reactor. In addition to the Navier-Stokes equations (equation 2.1 and 2.2) and the thermal balance equation (equation 2.8), this model simulates the transport of plasma species by calculating the diffusion, the convection and production/loss of plasma species due to chemical reactions in the following species balance equation:

$$\frac{\partial n}{\partial t} + \nabla(D\nabla n) + (\overrightarrow{u_g}.\nabla)n = R \tag{2.19}$$

In which n is the species density, D is the diffusion coefficient, $\overrightarrow{u_g}$ the gas flow velocity vector and R the sum of all production and loss rates due to chemical reactions. For the ions, an extra ion mobility (μ_i) term is added to the above equation, to account for their migration due to the ambipolar electric field $(\overrightarrow{E_{amb}})$:

$$\frac{\partial n_i}{\partial t} + \nabla\left(D_i \nabla n_i + \mu_i n_i \overrightarrow{E_{amb}}\right) + (\overrightarrow{u_g}.\nabla) n_i = R \tag{2.20}$$

For the electrons, the migration is calculated in the same way, using the electron mobility (μ_e):

$$\frac{\partial n_e}{\partial t} + \nabla\left(D_e \nabla n_e - \mu_e n_e \overrightarrow{E_{amb}}\right) + (\overrightarrow{u_g}.\nabla) n_e = R \tag{2.21}$$

The average electron energy $\bar{\varepsilon}_e$ is calculated through:

$$\frac{\partial n_e \bar{\varepsilon}_e}{\partial t} + \nabla.\left(-\mu_{\varepsilon,e} n_e \overrightarrow{E_{amb}} - D_{\varepsilon,e} \nabla(n_e \bar{\varepsilon}_e)\right) + \left(\overrightarrow{u_g}.\nabla\right) n_e \bar{\varepsilon}_e = q_e \vec{E}.\overrightarrow{G_e} + n_e \Delta\bar{\varepsilon}_e + Q_{bg} \tag{2.22}$$

Where n_e is the electron density, q_e the elementary charge, $\vec{E}$ the externally applied electric field, $\Delta\bar{\varepsilon}_e$ the energy exchanged in inelastic collisions with molecules, and Q_{bg} the background heat source serving as a stabilization term for the simulation. The terms $\mu_{\varepsilon,e}$ and $D_{\varepsilon,e}$ stand for the electron energy mobility and diffusion coefficient, respectively:

$$\mu_{\varepsilon,e} = \frac{5}{3}\mu_e \tag{2.23}$$

$$D_{\varepsilon,e} = \frac{2}{3}\mu_{\varepsilon,e}\bar{\varepsilon}_e \tag{2.24}$$

With μ_e the electron mobility. The factor 5/3 and 2/3 result from the electron energy distribution function (EEDF) being assumed Maxwellian. The electron flux $\overrightarrow{G_e}$ is derived from:

$$G_e = -D_e \nabla n_e - \mu_e n_e \overrightarrow{E_{amb}} \tag{2.25}$$

With D_e the electron diffusion coefficient. The ambipolar electric field $\overrightarrow{E_{amb}}$ is solved as follows:

$$\overrightarrow{E_{amb}} = \frac{\nabla n_i(-D_e + D_i)}{n_i(\mu_i + \mu_e)} \tag{2.26}$$

The influence of the chemistry on the thermal balance equation due to exothermic and endothermic reactions is represented by the heat source term Q_{heat} in equation 2.8 above, which includes the enthalpy differences from the chemical reactions:

$$Q_{heat} = \sum_j r_j \Delta H_j \tag{2.27}$$

In which j is the number of reactions, r_j is the reaction rate of reaction j, and ΔH_j is the enthalpy difference of reaction j, which, just like the reaction rate, is included in the chemistry set for each reaction j.

As accounting for the chemistry in a CFD model introduces many new equations, plasma fluid models can become very computationally intensive. To avoid prohibitively long calculation times, one can assume a quasi-neutral plasma, in which the negatively charged species (anions and electrons) and positive charged species (cations) are equal at all times. This is achieved by calculating the density of one ion (n_i) by balancing the electron density (n_e) with the densities of the other positive and negative ions ($n_{i+}$and n_{i-}, respectively) :

$$n_i = \pm (n_{i+} - n_{i-} - n_e) \tag{2.28}$$

In which the sign depends if n_i is positive (adds – sign) or negative (adds + sign).

This approach has a drawback that it cannot resolve the formation of Debye sheaths at the cathode and anode of the reactor. The latter description would however require a finite element mesh in the order of micrometers to be solved correctly, while the sheaths do not have significant influence on the final solution for the arc column. In this approach the charge conservation equation is solved using following Laplace equation:

$$\nabla\left[\sigma_{pl}(-\nabla\varphi)\right] = 0 \tag{2.29}$$

Where σ_{pl} stands for the plasma conductivity and φ stands for the electric potential.

$$\sigma_{pl} = |q_e|(\mu_e n_e + \mu_i n_i) \tag{2.30}$$

A second approximation that is commonly made in plasma fluid models to reduce calculation times is grouping the vibrational levels of molecules into lumped vibrational levels.[71] This approach avoids the need to describe every single vibrationally excited species separately through equation 2.19. The lumping is achieved by summing the number density of all vibrational levels into the lumped level number density n_g:

$$n_g = \sum_{i=0}^{j} n_i \tag{2.31}$$

In which n_i is the number density of the i[th] vibrational level (n_0 is considered the ground state number density) and j the number of vibrational levels in the lumped group.

The conservation equation in the non-thermal plasma model is then solved for the lumped level density n_g:

$$\frac{\partial n_g}{\partial t} + \nabla\left(D\nabla n_g\right) + (\overrightarrow{u_g}.\nabla)n_g = R_g \tag{2.32}$$

In which D is the diffusion coefficient, $\overrightarrow{u_g}$ the gas flow velocity vector and R_g the sum of all production and loss rates R_i of each individual vibrational level due to chemical reactions:

$$R_g = \sum_{i=0}^{j} R_i \tag{2.33}$$

After the calculation of n_g, the number density of each individual vibrational level within the group is described assuming a Maxwellian vibrational distribution function using the energy of the vibrational levels E_i and the vibrational temperature T_{vib}:

$$n_i = \frac{n_g exp\left(-\frac{E_i}{k_b.T_{vib}}\right)}{\sum_{i=0}^{j} exp\left(-\frac{E_i}{k_b.T_{vib}}\right)} \tag{2.34}$$

In which k_b is the Boltzmann constant.

The mean vibrational energy $\overline{E_{vib}}$ of a lumped level is then calculated through the following energy balance equation:

$$\frac{\partial n_g\overline{E_{vib}}}{\partial t} + \nabla.\left(\mathrm{D}\nabla\left(n_g\overline{E_{vib}}\right)\right) + \left(\overrightarrow{u_g}.\nabla\right)n_g\overline{E_{vib}} = R_{E_{vib}} \tag{2.35}$$

Where $R_{E_{vib}}$ is the sum of all vibrational energy production and loss rates due to chemical reactions in which vibrational energy is exchanged. These reactions are electron impact vibrational excitation, vibrational-translational (VT) relaxation and vibrational-vibrational (VV) relaxation.

The vibrational temperature (T_{vib}) is then calculated using the following relation between T_{vib} and $\overline{E_{vib}}$:

$$\overline{E_{vib}} = \frac{\sum_{i=0}^{j} E_i exp\left(-\frac{E_i}{k_b.T_{vib}}\right)}{\sum_{i=0}^{j} exp\left(-\frac{E_i}{k_b.T_{vib}}\right)} \tag{2.36}$$

Even with the quasi-neutral and vibrational level-lumping approach, solving this non-thermal plasma model in 3D would require an excessively long computation time. Therefore, fluid models are most often only calculated in a 2D axisymmetric geometry. Of course, this is only possible if the flow does not involve 3D movement, like a swirl. Moreover, as a full plasma chemistry set can contain thousands of reactions, a plasma fluid model is only solved with a limited chemical reaction set, which includes only the reactions that have the most impact on the physical properties of the model. 2D plasma fluid models have been evaluated and applied by Trenchev et al. for CO_2 conversion in GA plasmas with very satisfying results.[72–74]

2.2 0D MODELLING

While CFD modelling offers a very valuable tool for describing and optimizing the physical aspects of a plasma reactor, some chemical mechanisms are too complex to be described in a multi-dimensional plasma fluid model within reasonable calculation times. For instance, self consistently calculating a non-Maxwellian electron energy distribution function, describing energy exchanges between all vibrational levels of a molecule or simulating every single reaction pathway of a complex reaction mixture are not feasible with CFD models. Plasma chemistry is very complex when fully described, due to the enormous number of reactive species all interacting with each other. Yet, this kind of full description is needed to gain a deeper insight into how desired products are formed in the plasma and how the reaction pathways of these products can be optimized.

2.2.1 The species balance equation

Providing an in-depth description of the chemical aspects of the plasma is therefore done through 0D chemical kinetics modelling, rather than CFD. A 0D model does not account for spatial variations of the plasma but only calculates the time evolution of the density of all plasma species by solving the following continuity equation for the various species, taking into account the production and loss terms by the chemical reactions:

$$\frac{dn_i}{dt} = \sum_j \left[\left(a_{ij}^R - a_{ij}^L\right) k_j \prod_l n_l^L \right] \tag{2.37}$$

In which n_i is the density of species i and a_{ij}^R and a_{ij}^L are the stoichiometric coefficients of species i on the right-hand and left-hand side of the reaction j, respectively, n_l is the density of the reacting species l, and k_j is the reaction rate coefficient of reaction j, which has the general form:

$$a_A A + a_B B \xrightarrow{k_j} a_c C + a_D D + \Delta H \tag{2.38}$$

In which A, B, C and D are the species, and a_A, a_B, a_c and a_D their stoichiometric coefficients. ΔH represents the reaction enthalpy.

If the chemical reactions occur fast enough (i.e. high values of k_j) such that the impact of the chemistry on the species densities is much more significant than the impact of spatial variations like diffusion, turbulent gas mixing, etc., the 0D approximation (i.e. considering no spatial variations) holds better.

A well-known zero-dimensional kinetics solver, specifically for plasma chemistry is ZDPlasKin.[75] This program allows to input the rate coefficients of heavy particle reactions (i.e. not involving electrons) as a function of the gas or electron temperature, as adopted from literature, whereas the rate coefficients for the electron impact reactions are calculated with a Boltzmann solver, BOLSIG+[76], built in ZDPlasKin. This Boltzmann routine solves the Boltzmann equation for the electrons using a two-term approximation, yielding the electron energy distribution function (EEDF). From the EEDF the mean electron energy and the different electron impact rate coefficients are obtained through following equation:

$$k_j = \int_0^{+\infty} \sigma_j(\varepsilon)\, f_e(\varepsilon) \sqrt{\frac{2\varepsilon}{m_e}}\, d\varepsilon \tag{2.39}$$

In which ε represents the electron energy, $\sigma_j(\varepsilon)$ the cross section of the jth electron collision reaction, $f_e(\varepsilon)$ the EEDF and m_e the electron mass. The reaction cross sections $\sigma_j(\varepsilon)$ of the different elastic and inelastic collisions are adopted from literature[77,78] and they include a complete set of cross sections interconnecting all vibrational energy levels through single- and multi-quantum transitions, as well as super-elastic collisions.[79]

2.2.2 Converting 0D to quasi-1D models

0D models don't consider spatial variations, i.e. the species densities are assumed to be constant in the entire simulation volume, therefore a very extensive or complex plasma chemistry set can be described in the model without suffering from long calculation times. This means that any influence from 3D transport of mass (convection, diffusion, migration) or energy (convection, conduction), is either

omitted or estimated using experiments or another (multi-dimensional) model. However, the time dependence of the model can be converted to an axial variation of the plasma quantities by following a volume element moving through e.g. a cylindrical plasma tube, by means of the gas flow rate, as shown schematically in figure 2.1, hence resulting in a quasi-1D model. The considered simulation volume, which is always considered radially homogeneous in a 0D model, thus moves at a linear velocity v:

$$v = \frac{Q_m}{\rho_g A} \tag{2.40}$$

Where Q_m is the mass flow rate, $A = \pi R^2$ is the tube cross section area and $\rho_g = \sum n_i M_i$ is the gas mass density. n_i is the number density of species i and M_i is the mass of species i, while R is the tube radius.

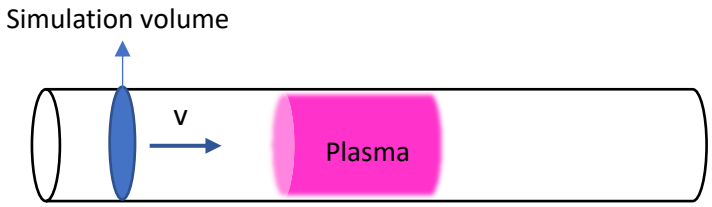

Figure 2.1: Schematic overview of a quasi-1D model, converting the time dependence of a 0D model to an axial variation using the gas flow velocity v.

0D or quasi-1D models have already been successfully applied in various plasma reactors for different gas conversion applications to map out all chemical pathways and identify the key ones.[56,57,80–85]

2.3 Combining 3D and quasi-1D model

Reading section 2.1 and 2.2, it might have become apparent that 3D CFD models and quasi-1D models (or 0D models) are very complementary. CFD models describe physical properties in 3D but lack an in-depth description of the chemistry (within acceptable calculation times), while quasi-1D models can describe complex chemistry sets but require input regarding 3D physical transport properties. A significant part of this thesis is dedicated to make a connection between these two complementary models and develop a new modelling method that combines the strengths of the two models, while mitigating their weaknesses: the complicated plasma chemistry is calculated through 0D (or quasi-1D) modelling, using input for physical parameters generated by 3D CFD models. While previous work at PLASMANT focused mainly on either 2D CFD modeling or on 0D chemical kinetics modelling, I tried to combine both approaches, as they are very compatible and complementary (0D modelling requires

input for physical parameters and CFD modelling requires chemical input). This approach will be further discussed in this section.

2.3.1 Streamlines and streamtubes

Important to this modelling approach is the representation of the flow trajectory through streamlines and streamtubes. In CFD streamlines are defined as lines that are tangential to the gas flow velocity vector. In a steady flow, they visualize the pathway of an infinitesimal small fluid element within the fluid flow. Several streamlines together make up a streamtube, i.e. a tubular region of fluid surrounded by the streamlines, as schematically shown in figure 2.2. An important feature of streamlines is that they never cross. Indeed, a crossing point between streamlines would mean that there are two different flow velocity directions in one point, while physically the flow cannot go in more than one direction at the same time (except at points where the velocity magnitude is zero). Since streamlines don't intersect, the same streamlines flow along a streamtube at all points along its length and the streamtube is impermeable to streamlines outside of the streamtube. In other words, this means that for steady flow, the mass flow over a streamtube is conserved. For two cross-sections of a streamtube, with cross-sectional areas A_1 and A_2 (as shown in figure 2.2), flow velocities v_1 and v_2 and mass flow rates $\dot{m}_1$ and $\dot{m}_2$ respectively, we have:

$$\dot{m}_1 = v_1 \rho_1 A_1 = v_2 \rho_2 A_2 = \dot{m}_2 \tag{2.41}$$

With ρ_1 and ρ_2 the densities at cross-section A_1 and A_2 respectively.

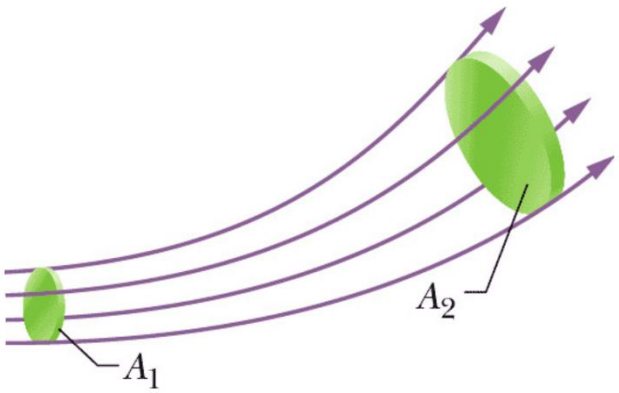

Figure 2.2: Schematic representation of a streamtube being composed of several flow lines adopted from the Galileo Physics webpage.[86]

This means that if we calculate the gas flow velocity through CFD as described by section 2.1, we can consider a quasi-1D simulation to model the chemistry of a fluid element, flowing over a streamtube in the 3D flow. This is done by integrating the streamline that defines the streamtube over time, yielding the trajectory of the fluid element (q) in the reactor.

$$q = \int_0^{t_{outlet}} v\, dt \tag{2.42}$$

$$v = \sqrt{{v_x}^2 + {v_y}^2 + {v_z}^2} \tag{2.43}$$

Here, v_x , v_z, and v_y are the gas flow velocities in x, y and z direction, and t_{outlet} is the time needed for the gas to flow to the outlet. The quasi-1D simulation then represents the chemistry along this trajectory through the reactor. Important physical parameters calculated by the 3D CFD model (like temperature and power density), which are experienced by the fluid element along this trajectory, can then be used as an input for the quasi-1D simulation. If this approach is repeated many times, essentially dividing the fluid flow in many streamtubes, the mass flow through each streamtube, i.e. in each quasi-1D simulation, is then calculated through equation 2.41, revealing the contribution of each quasi-1D simulation to the total mass flow. This approach allows us to describe the chemistry along 3D flow trajectories, without the need to fully describe the chemistry in a plasma fluid model, saving a lot of calculation time.

2.3.2 Approximations made by combining 3D and quasi 1D-modelling

In this section the approximations and assumptions of the previously discussed modelling approach and their validity are discussed. In this discussion the modelling approach is applied to a simple 2D axisymmetric CFD model considering an axial flow profile. This allows us to clearly display the approach in practice and evaluate the approximations of the approach by comparing our results with a fully-coupled plasma CFD model incorporating the chemistry. This also allows us to estimate the error made in the approach.

The 2D axisymmetric reactor model for this evaluation is illustrated by figure 2.3, representing a typical MW plasma reactor for CO_2 conversion at atmospheric pressure. The axisymmetric model geometry consists of a 3 cm radius tube in which gas enters the tube's inlet at 20 L/min (at 1 atm and 293.15 K), which is a typical flow rate for a MW reactor. The plasma in the tube is represented by a 5 cm long heat source of 500 W with a radius of 1 mm, as shown in the power density profile in figure 2.3.

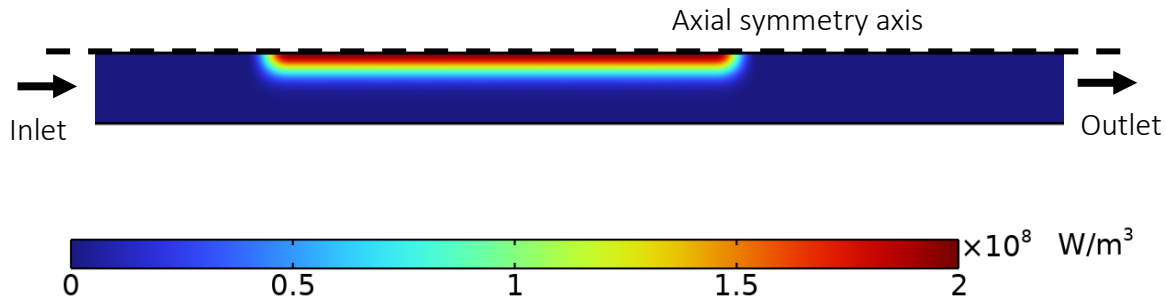

Figure 2.3: Schematic presentation of the 2D axisymmetric model including the power density profile of the heat source that represents the plasma in the simulation.

Solving the Navier-Stokes equations for laminar flow (equation 2.1 and 2.2) and the heat balance equation (equation 2.8) for these boundary conditions yields the calculated gas temperature profile in figure 2.4(a) (in 3D by revolution of the 2D axially symmetric model around the axial symmetry axis). With the chosen plasma power of 500 W, the figure predicts gas temperatures up to 3500 K, which are typical for quasi-thermal atmospheric pressure CO_2 plasmas. These high gas temperatures diminish the turbulence in the gas flow, as the gas density decreases by an order of magnitude and the viscosity increases by an order of magnitude by heating to 3500 K, while the gas flow velocity only increases by a factor 4. Given that Re ~ velocity, ~ density, ~1/viscosity, the overall effect of the increasing temperature is that it lowers the gas flow turbulence, making the regime more laminar, consolidating our choice for a laminar flow model.

The gas density (ρ_g), heat capacity (C_p), heat conductivity (k_g) and viscosity (μ_{tot}) for solving the Navier-Stokes equations and heat balance equation were determined by assuming that the CO_2 is perfectly mixed to its thermal equilibrium composition. For instance, at 3000 K the gas mixture does not consist of pure CO_2 anymore, but a mixture of CO_2, CO, O_2, C, and O in its thermal equilibrium concentrations.[87] This is considered to be a reasonable assumption for quasi-thermal plasmas, as shown by comparison of figure 2.4(a) with figure 2.4(b) in which the gas temperature is calculated by solving equation 2.19 and 2.27, in addition to the Navier-Stokes equations and the heat balance equation, yielding a fully coupled plasma-fluid model with the same 500 W power input. This model thus implements the equations in section 2.1.3 to account for the changes in gas density, viscosity, heat capacity and heat conductivity due to the production and destruction of species in chemical reactions, as well as the influence of the exothermic/endothermic reactions on the heat balance.

A comparison between the two pictures shows that both models yield very similar temperature profiles. Some difference can be seen in the afterglow of the plasma, which is predicted to be slightly wider in the model assuming the equilibrium concentration of all plasma species. This demonstrates that the gas

flow velocity and gas temperature in the plasma can be calculated quite accurately without involving complicated chemical kinetics.

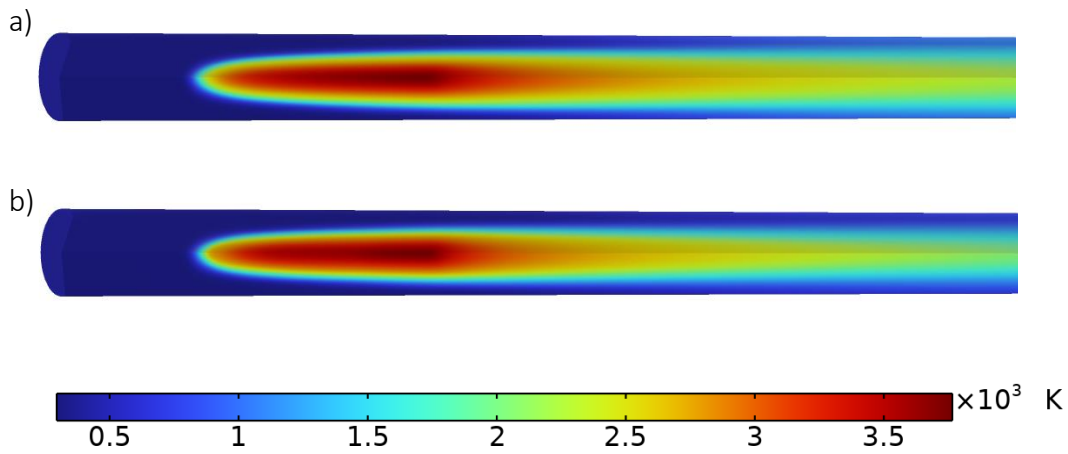

Figure 2.4: Gas temperature profiles calculated by the 2D axisymmetric reactor model, for a) a model assuming the gas mixture is perfectly mixed to the thermal equilibrium concentrations of the plasma species and b) a fully coupled plasma fluid model assuming the same power input.

To use the results in figure 2.4(a) as input for a quasi-1D chemical kinetics model along the pathway of the gas, the gas flow velocity along 5 streamlines is integrated using equation 2.42, yielding 5 different flow pathways, which are illustrated in 2D in figure 2.5. The temperature profiles along these trajectories are then used as input for 5 quasi-1D chemical kinetic simulations, calculating the species balance along these trajectories using equation 2.37.

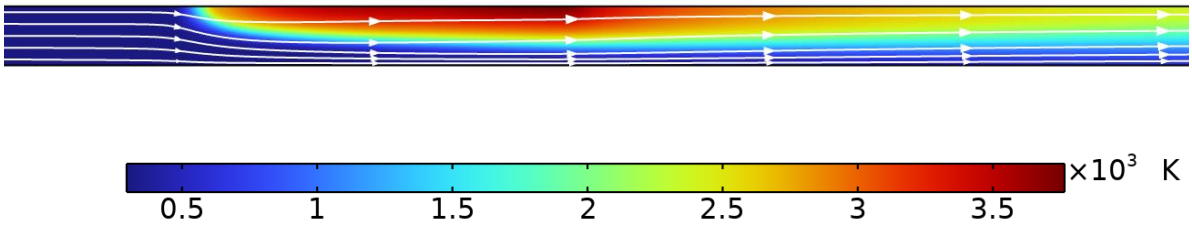

Figure 2.5: Calculated gas temperature profile inside the 2D asymmetrical reactor model, including a schematic representation of the 5 flow pathways that are used as input for the quasi-1D chemical kinetics simulation.

A consequence of describing the species balance in the quasi-1D model only in one direction, i.e. along the flow lines of the reactor, is that 3D transport of species is not accounted for in the model. While this approach does account for convective transport of chemical species, as convective transport occurs by definition along the direction of the flow velocity and thus along the streamlines, this does not take into account the transport due to diffusion, which occurs in all directions. Thus a significant approximation of the modelling approach is that species transport in any other direction than the direction of the flow velocity is omitted. However as demonstrated in figure 2.6, showing both (a) the diffusive and (b)

convective CO flux magnitude in a MW reactor (taken as example),calculated by the fully-coupled plasma fluid model, the diffusive heat flux within the MW reactor is two orders of magnitude smaller than the convective heat flux.

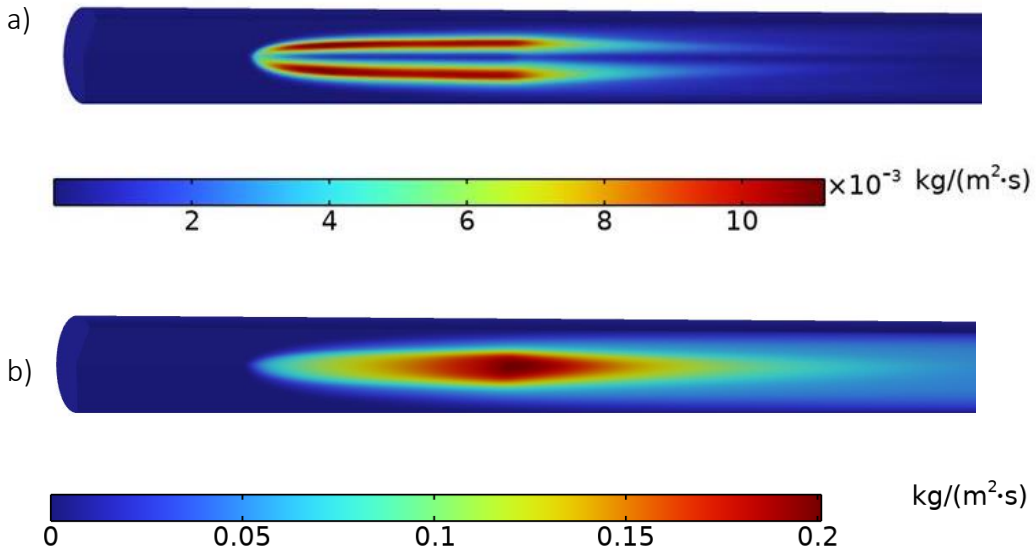

Figure 2.6: Magnitude of the a) diffusive and (b) convective CO flux as calculated by the fully-coupled plasma fluid model.

This is also represented in figure 2.7 showing the magnitude of the three source terms for CO in the species balance equation (equation 2.19), i.e. the diffusive term ($\nabla(D\nabla n)$) shown in figure 2.7(a), the convective term ($(\overrightarrow{u_g}.\nabla)n$, shown in figure 2.7(b) and the reactive term (R), shown in figure 2.7(c). In this comparison, it is also shown that the diffusive source term is the least impactful term in the species balance, being an order of magnitude lower than the convective and reactive term. In these reactors, the transport of species is thus predominantly determined by convection, making the approximation of omitting the species diffusion only moderately impactful on our results.

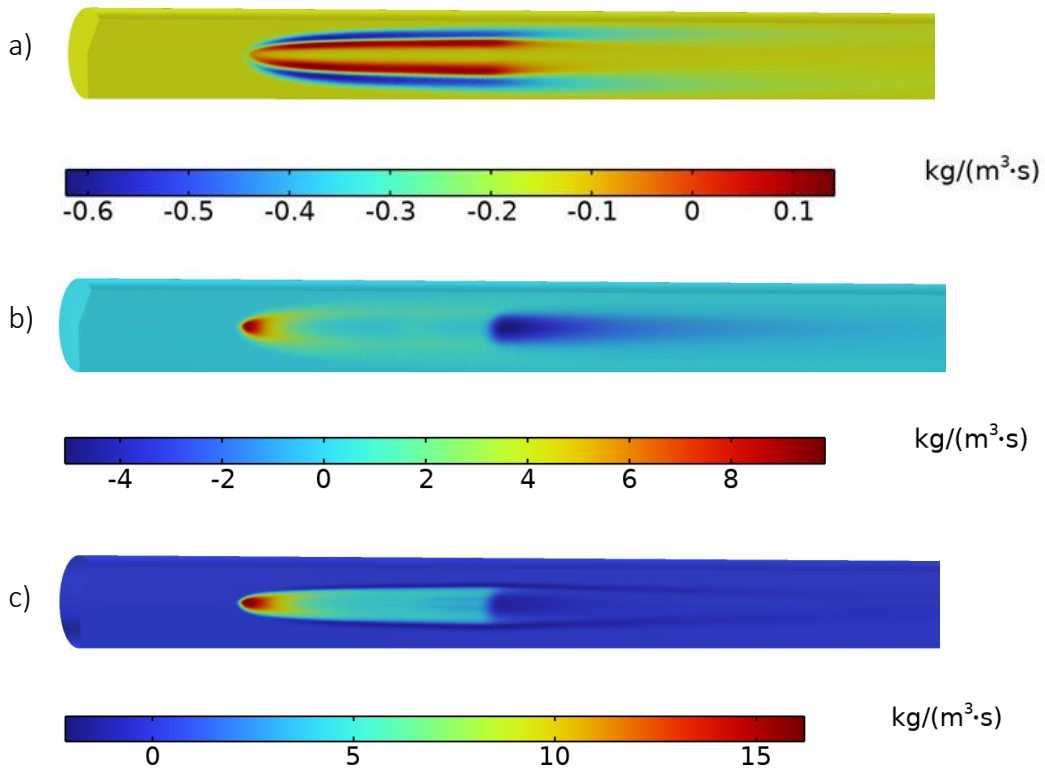

Figure 2.7: (a) Diffusive, (b) convective and (c) reactive source terms of the species balance equation in the fully-coupled plasma fluid model.

Finally, by calculating the mass flow along each pathway in figure 2.5, using equation 2.41, we can evaluate the contribution of each flow path to the total flow. The overall CO_2 conversion is then calculated by the weighted average of the calculated CO_2 conversion of each single quasi-1D simulation, in which the weight is determined by the contribution of the flow path to the overall mass flow. For the example case with the 5 flow pathways of figure 2.5, this yields an overall CO_2 conversion of 3.8 %. The fully-coupled plasma fluid simulation predicts a CO_2 conversion of 5.9 %, which is a significant difference. Indeed, describing the flow using only 5 streamlines does not yield a very refined representation of the temperature gradients in the reactor. As shown by figure 2.5, only one streamline flows through the hot center of the plasma, which means that the plasma volume V is currently represented by only one streamtube and one singular temperature. To increase the resolution and accuracy of the approach, the plasma volume should be represented by multiple streamtubes with volumes dV, such that the temperature in each volume dV approximates the radial temperature gradient of the plasma. This is achieved by increasing the number of streamlines (and thus streamtubes with volume dV) that are considered in the chemistry simulation. Figure 2.8 presents the calculated CO_2 conversion when solving the quasi-1D simulations along 5, 10 and 20 streamlines, while comparing it to the CO_2 conversion calculated by the fully-coupled plasma fluid model. As shown by the figure, increasing the number of streamlines improves the agreement with the plasma fluid model, as this decreases the considered

volume of each streamtube, eventually nearing the length scale of the radial temperature gradient. To reach a length scale of 1 to 0.1 mm for dB, which is the length scale of the reactor meshing, 10 to 100 streamtubes are required along the reactor radius in a cm scale reactor. In a 3D situation, this would translate to $10^2 \cdot \pi$ to $100^2 \cdot \pi$ streamlines. Considering the calculation time of integrating these streamlines, 10 000 streamlines is deemed an acceptable number to execute the approach and still yield a satisfying resolution.

Considering the approximation and validation of the approach in this section, we will apply the approach to real plasma reactor in the upcoming chapters.

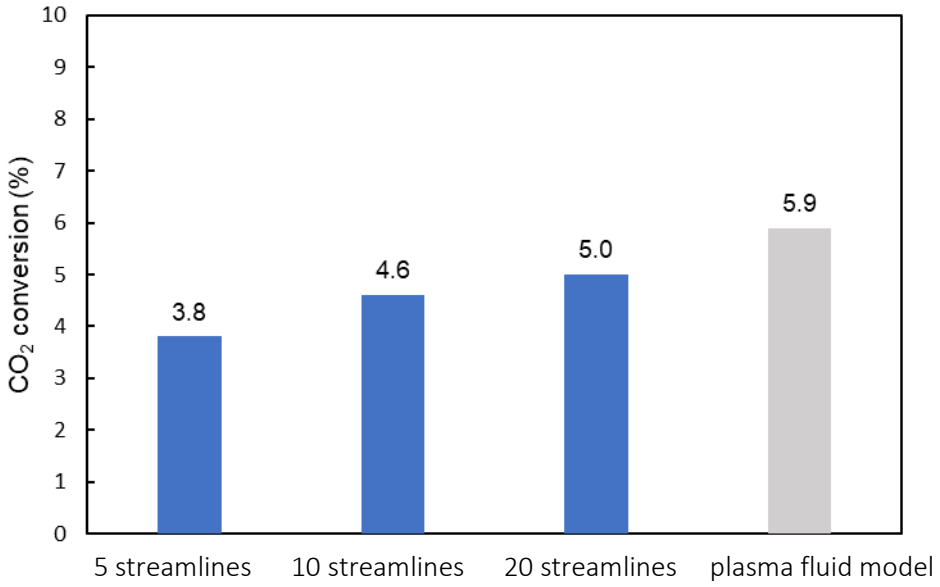

Figure 2.8: Calculated CO_2 conversion for solving the quasi-1D model along 5, 10 and 20 streamlines of the 2D axisymmetric model, as well as the CO_2 conversion calculated by the fully-coupled plasma fluid model.

3 NO_X PRODUCTION IN A ROTATING GLIDING ARC PLASMA: POTENTIAL AVENUE FOR SUSTAINABLE NITROGEN FIXATION

The results presented in this chapter were published in:

"NO_x production in a rotating gliding arc plasma: potential avenue for sustainable nitrogen fixation" Van Alphen S., Jardali F., Creel J., Ahmadi Eshtehardi H., Axelsson M., Ingels R., Snyders R., Bogaerts A., Green Chem 23, 1748 (2021)

DOI: 10.1039/D0GC03521A

"Sustainable gas conversion by gliding arc plasmas: a new modelling approach for reactor design improvement" Van Alphen S., Jardali F., Creel J., Trenchev G., Snyders R., Bogaerts A., Sustainable Energy & Fuels 5, 1786 (2021)

DOI: 10.1039/D0SE01782E

3.1 INTRODUCTION

As described in-depth in chapter 1, research in plasma reactor designs is developing rapidly as plasma technology is gaining increasing interest for sustainable gas conversion applications, like the conversion of greenhouse gases into value-added chemicals and renewable fuels, and fixation of N_2 from air into precursors of fertilizers.

GA plasma reactors have especially piqued interest of industry, as they operate at atmospheric pressure and are well suited for industrial applications and upscaling, given their simplicity and reliability.[10] Furthermore, GA are characterized by a low reduced electric field (below 100 Td), and thus may deliver energy-efficient conversion through vibrational excitation.[88] Especially innovative 3D cylindrical GA reactor designs that abandon the classical 2D configuration of the GA are gaining increasing interest for plasma-based gas conversion applications. This new generation of GA reactors introduce the gas stream through tangentially oriented gas inlets, initiating a vortex flow inside the reactor, capturing the arc in a so-called 'tornado flow'. The main goal of these reactor designs is to tackle one of the most significant shortcomings of GA reactors, i.e. a significant amount of gas does not flow through the arc, or even flows around it.

A great number of experiments, as well as some numerical simulations, have been conducted to evaluate these kind of new 3D GA designs for sustainable chemistry applications, like N_2 fixation, CO_2 conversion and dry reforming of CH_4, demonstrating promising results compared to other plasma reactor types.[16,26,80,89–91]

One of these novel designs is the rotating gliding arc (RGA) reactor, characterized by an arc that rotates through the whole reactor volume to treat as much of the incoming gas as possible. In this chapter, we investigate the performance of this new reactor for plasma-based N_2 fixation into NO_x for two different arc regimes of the RGA reactor, i.e. a rotating arc regime and a steady arc regime. In collaboration with F. Jardali in our group, we demonstrate the performance of the reactor through experiments (performed by F. Jardali) and identify the underlying mechanism of the plasma chemistry through a new comprehensive modelling approach, that I developed, which reveals the fluid dynamics, the arc behavior and the plasma chemistry by solving a unique combination of four complementary models. These insights will allow us to improve the reactor design and further enhance its performance in the following chapters and improve upon the best performance for plasma-based NO_x formation in GA reactors up to this study, which is a NO_x concentration up to 2% at an energy cost of 2.8 MJ mol^{-1}.[55,56]

3.2 MODEL DESCRIPTION

3.2.1 Reactor geometry and modelling strategy

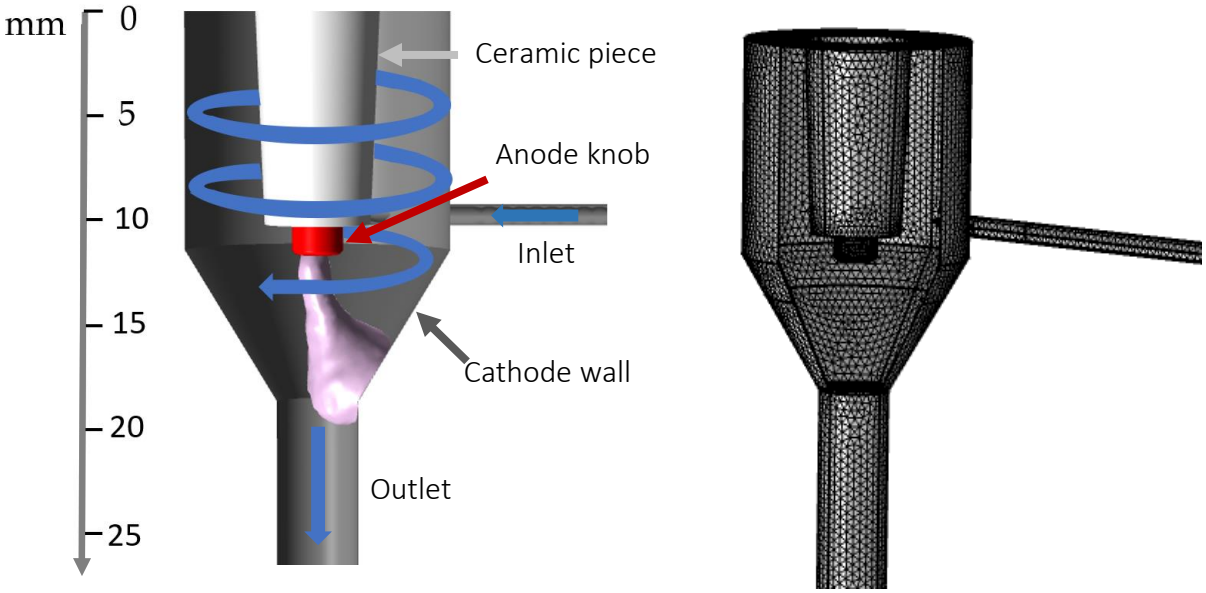

Figure 3.1: The RGA reactor geometry and its finite element mesh in the model.

A schematic representation of the RGA reactor is shown in figure 3.1, along with the finite element mesh of the reactor geometry in the 3D model. The reactor body is a cylinder with radius of 6.5 mm and height of 11.2 mm, connected to a cone that narrows the reactor tube down to 2 mm in radius at the outlet. The gas enters the reactor tangentially through an inlet tube with radius of 0.5 mm and length of 25 mm, at a typical flow rate of 2 L min^{-1}. The anode pin in the center of the reactor is enclosed by a piece of ceramic (100 mm in length, 3 mm in radius) so only a cylindrical knob with 1.3 mm radius and 1.4 mm

length is exposed. The arc is formed between this anode knob (i.e., high-voltage electrode, with typical applied voltage around 2-3 kV), and the cathode reactor wall.

The modelling strategy we developed considers all aspects needed to reveal the underlying mechanisms in the RGA design, by combining four complementary models: a 3D turbulent gas flow model, a 3D thermal plasma model, a 2D non-thermal plasma model, and a quasi-1D plasma chemistry model. Hybrid models, which combine different modelling approaches for different species or processes, to take benefit of their strengths and avoid their limitations, do exist in plasma research for many years, but to our knowledge, such a hybrid modelling approach that we propose here does not yet exist in literature. These models are solved sequentially in which each model builds further on the results of the previous calculations. We describe here the computational details of each model in the sequence they are solved.

3.2.2 Gas flow behavior

The gas flow velocity in the RGA is calculated by solving the Navier-Stokes equation for turbulent flow in the 3D reactor geometry shown in figure 3.1, using the (RANS) SST model, as described in section 2.1.1 (on page 34):

$$\rho_g \frac{\partial \vec{u}}{\partial t} + \rho(\vec{u} \cdot \nabla)\vec{u} = \nabla \cdot \left[-p\vec{I} + (\mu + \mu_T)(\nabla\vec{u} + \nabla(\vec{u})^T) - \frac{2}{3}(\mu + \mu_T)(\nabla \cdot \vec{u})\vec{I} - \frac{2}{3}\rho_g k_T \vec{I}\right] + \vec{F} \quad (3.1)$$

$$\rho \frac{\partial \vec{u}}{\partial t} + \nabla \cdot \left(\rho_g \vec{u}\right) = 0 \quad (3.2)$$

Where ρ_g stands for the gas density, $\vec{u}$ is the gas flow velocity vector, superscript T stands for transposition, p is the gas pressure, μ is the dynamic viscosity and μ_T the turbulent viscosity of the fluid, k_T is the turbulent kinetic energy, $\vec{I}$ is the unity tensor and $\vec{F}$ is the body force vector.

The physical properties for the N_2/O_2 mixture are shown in the appendix (section 8.2).

As described in section 2.1.2 (on page 35), the heat transfer is simulated by solving the thermal balance equation:

$$\rho_g C_p \frac{\partial T_g}{\partial t} + \rho_g C_p \vec{u} \cdot \nabla T_g + \nabla \cdot \vec{q} = Q_{heat} \quad (3.3)$$

Where ρ_g stands for the gas density, C_p for the isobaric heat capacity, T_g is the gas temperature, $\vec{u}$ the gas velocity, Q_{heat} the heat source term representing the heating from the plasma, and $\vec{q}$ the conductive heat flux vector, which is calculated by:

$$\vec{q} = -(k_g + k_{g,T})\nabla T_g \quad (3.4)$$

Where k_g is the thermal conductivity of the gas and $k_{g,T}$ is the turbulent thermal conductivity of the gas.

To calculate the heat source term (Q_{heat}) in equation,3.3 we solve a 3D thermal plasma model and a 2D non-thermal plasma model.

3.2.3 3D thermal plasma arc model

To simulate the plasma arc behavior in 3D, we simulate the plasma reactor as part of the electric circuit shown in figure 3.2. The anode is connected to a ballast resistor, which in turn is connected to a voltage source supplying 3kV, while the cathode is grounded. The current is limited by a ballast resistor (Rb, typically 200 Ω), and a capacitor (Cb, typically 10 pF) forms an RC filtering circuit. The gas breakdown between cathode and anode is then simulated by solving a current conservation equation based on Ohm's law:

$$\nabla \cdot \vec{J} = 0 \tag{3.5}$$

$$\vec{J} = \sigma \vec{E} \tag{3.6}$$

$$\vec{E} = -\nabla V \tag{3.7}$$

In which $\vec{J}$ is the current density and $\vec{E}$ is the electric field, V the electric potential and σ the electric conductivity of the gas.

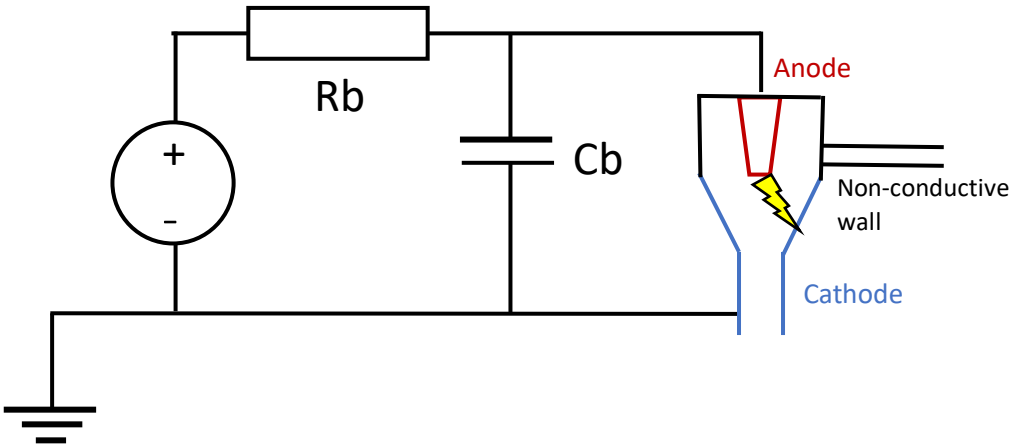

Figure 3.2: Schematic representation of the electrical circuit of the RGA reactor in the thermal plasma arc model

The thermal heat source of the arc ($Q_{thermal}$) is then calculated from the Ohmic heating resulting from the electric current:

$$Q_{thermal} = \vec{E} \cdot \vec{J} \tag{3.8}$$

3.2.4 2D non-thermal plasma model

While $Q_{thermal}$ (in W/m³) reasonably describes the shape and 3D movement of the arc in a GA reactor operating at atmospheric pressure, it overestimates the absolute value. Indeed, the model assumes that the plasma is in thermal equilibrium, meaning that the gas temperature and electron temperature are equal at any point in the discharge, yielding high gas temperatures up to 10 000 K. As discussed in section 1.3.2 (on page 18), GA plasmas are known to be only quasi-thermal by maintaining a thermal non-equilibrium between electrons and gas molecules. As a result, the gas temperature calculated by the thermal model is too high and needs to be corrected. This correction is provided by a more comprehensive non-thermal plasma model that explicitly describes the behavior of the various plasma species, i.e., the electrons, various ions, radicals, excited species and molecules. To avoid prohibitively long calculation times, however, we assume a quasi-neutral plasma, in which the electron and total ion densities are equal at all times. This is achieved by calculating the density of one ion ($n_{NO_2^-}$) upon balancing the electron density (n_e) with the densities of the other ions ($n_{N_2^+}, n_{O_2^+}, n_{NO^+}$) :

$$n_{NO_2^-} = \left(n_{N_2^+} + n_{O_2^+} + n_{NO^+} - n_e\right) \tag{3.9}$$

As described in detail in section 2.1.3 (on page 37), the model solves the following equation for the various neutral species, balancing the diffusion and convection of each plasma species with its production and loss rates due to chemical reactions:

$$\frac{\partial n}{\partial t} + \nabla(D\nabla n) + (\overrightarrow{u_g}.\nabla)n = R \tag{3.10}$$

In which n is the species density, D is the diffusion coefficient, $\overrightarrow{u_g}$ the gas flow velocity vector and R the sum of all production and loss rates due to chemical reactions.

For the ions, an extra ion mobility (μ_i) term is added to the above equation, to account for their migration due to the ambipolar electric field ($\overrightarrow{E_{amb}}$):

$$\frac{\partial n_i}{\partial t} + \nabla\left(D_i\nabla n_i + \mu_i n_i \overrightarrow{E_{amb}}\right) + (\overrightarrow{u_g}.\nabla)n_i = R \tag{3.11}$$

For the electrons, the migration is calculated in the same way, using the electron mobility (μ_e):

$$\frac{\partial n_e}{\partial t} + \nabla\left(D_e\nabla n_e - \mu_e n_e \overrightarrow{E_{amb}}\right) + (\overrightarrow{u_g}.\nabla)n_e = R \tag{3.12}$$

Solving this non-thermal plasma model in 3D, including the transport and reactions of all species in an N_2/O_2 plasma, would require an excessively long computation time. Therefore, the model is calculated for a 2D axisymmetric geometry with a limited chemical reaction set, as described in section 3.2.6 below. This approach was already evaluated by Trenchev et al. for CO_2 conversion in other types of plasma reactors with very satisfying results.[72–74] As this model correctly incorporates the heat terms of all plasma processes and reactions occurring in an N_2/O_2 plasma, the results from this 2D model can be used to correct the gas temperature of the 3D thermal model. We assume that the temperature calculated in a 2D axisymmetric non-thermal plasma model can be used as a reference to assess the temperature in an arc moving in three dimensions. This assumption is based on the fact that the magnitude of the main heat source, i.e. the exothermic plasma reactions, remains the same in an axial symmetric reactor geometry.

3.2.5 Quasi-1D plasma chemistry simulations

To reveal the chemical pathways of NO_x formation and to calculate the NO_x yield in this GA plasma reactor, we solve a quasi-1D chemical kinetics model along the streamlines of the flow as described in detail in section 2.3 (on page 43). In this model we solve the following continuity equation along the streamlines for the various species, taking into account the production and loss terms by the chemical reactions:

$$\frac{dn_i}{dt} = \sum_j \left[(a_{ij}^R - a_{ij}^L) k_j \prod_l n_l^L \right] \tag{3.13}$$

In which n_i is the density of species i and a_{ij}^R and a_{ij}^L are the stoichiometric coefficients of species i on the right-hand and left-hand side of the reaction j, respectively. n_l is the density of the reacting species l. k_j is the reaction rate coefficient of reaction j.

To cover the whole gas velocity space, 10,000 flow lines (equally spaced over the surface of the inlet boundary) are integrated from the inlet to the outlet :

$$q = \int_0^{t_{outlet}} v \, dt \tag{3.14}$$

$$v = \sqrt{{v_x}^2 + {v_y}^2 + {v_z}^2} \tag{3.15}$$

Here, v_x , v_z, and v_y are the gas flow velocities in x, y and z direction, and t_{outlet} is the time needed for the gas to flow to the outlet.

In principle, these 10,000 trajectories could serve as input for 10,000 different quasi-1D calculations, each calculating the NO_x concentration for a fraction of the gas. However, many of these flow lines experience similar conditions, so we group flow lines that experience a similar maximum temperature in the plasma and we compute the average values. By applying this averaging method, we narrow the 10,000 flow trajectories down to ten average trajectories, each describing the specific plasma conditions (i.e., gas temperature and power density) that the gas experiences as it follows that trajectory. These gas temperature and power density profiles are used in the quasi-1D chemical kinetics simulation, calculating the underlying chemistry and the NO_x concentration that is achieved in each group. Finally, the overall NO_x concentration is calculated from a weighted average of the ten simulations, in which the weight is determined by the mass flow in each group.

3.2.6 Plasma chemistry included in the models

The full chemistry set used in the quasi-1D chemical kinetics model was recently developed and validated for another type of GA plasma (GA plasmatron) by Vervloessem et al.[91] The reactions and corresponding rate coefficients, and the references where these data were adopted from, are listed in the appendix (section 8.3). The chemistry set includes 82 different species, which are presented in table 3.1 The reduced chemistry set of the 2D non-thermal plasma model contains 21 species, which are highlighted in blue bold face in table 3.1. In addition, in this reduced set the vibrational levels of N_2 and O_2 are considered as one lumped level, as explained in chapter 2 (section 2.1.3, page 39). The total set incorporates 1,214 electron impact reactions, 481 ionic reactions and 432 neutral reactions, as well as 2,478 vibration-vibration exchanges and vibration-translation relaxations between molecular and atomic nitrogen and oxygen, as detailed in the appendix (section 8.3). The reduced chemistry set includes 664 electron impact reactions, 25 ionic reactions and 124 neutral reactions, as well as 2,478 vibration-vibration exchanges and vibration-translation relaxations between molecular and atomic nitrogen and oxygen; these reactions are also highlighted in blue bold face in the appendix (section 8.3).

Table 3.1. Different plasma species included in the model. The symbol "V" followed by a number stands for the vibrational level of that species. Species included in the reduced chemistry set of the 2D model are presented in blue bold face.

Neutral species	Radicals	Charged species	Excited species
N_2, O_2, O_3,	**N**, N(2D), N(2P),	**e^-** N^+, **N_2^+**, N_3^+, N_4^+,	**$N_2(V1-V24)$, $O_2(V1-V15)$,**
NO, **NO_2**, N_2O,	**O**, O(1D), O(1S)	O^-, O_2^-, O_3^-, O_4^-,	**$N_2(A^3\Sigma_u^+)$**, **$N_2(B^3\Pi_g)$**, **$N_2(C^3\Pi_u)$**, **$N_2(a'^1\Sigma_u^-)$**, **$O_2(a^1\Delta)$**, **$O_2(b^1\Sigma^+)$**, **$O_2(A^3\Sigma^+, C^3\Delta, c^1\Sigma^-)$***
NO_3, N_2O_3,		O^+, **O_2^+**, O_4^+,	
N_2O_4, N_2O_5		**NO^+**, NO_2^+, N_2O^+, NO^-, **NO_2^-**, N_2O^-, NO_3^-, $O_2^+N_2$	

* $O_2(A^3\Sigma^+, C^3\Delta, c^1\Sigma^-)$ is a combination of three states with a threshold energy of 4.5 eV.

* While the 2D non-thermal model considers one lumped level, the number density of each individual vibrational level within the group is still described assuming a Maxwellian vibrational distribution, as described in equation 2.34 in section 2.1.3. As a result, the vibration-vibration exchanges and vibration-translation relaxations for the individual levels are also described in the reduced set.

3.3 RESULTS AND DISCUSSION

3.3.1 The rotating and steady arc regime

Our RGA reactor can operate in two distinct modes depending on the applied power: (i) a rotating arc with variable length, the so-called rotating mode, (ii) but also a more or less steady arc with stable length, the so-called steady mode. In the rotating mode the arc forms in the shortest gap between cathode and anode and elongates as it starts gliding along the reactor body dragged by the swirling gas flow. The elongation of the arc is represented by the nearly linear increase in the discharge voltage, as shown in figure 3.3, presenting the current–voltage characteristics of the rotating mode. During the elongation, the discharge current decreases due to the electrical resistance increasing as the length of the arc increases. Eventually the supplied power is not sufficient to sustain further arc extension (i.e., up to about 110 W) and the arc will extinguish (represented by a sudden drop of the discharge voltage in figure 3.3(a)), and reignition will take place in the shortest gap between both electrodes. In the steady mode, however, the supplied power is above 180 W, which is high enough for the arc to elongate and reach the furthest point of contact on the reactor outlet. In this regime the arc remains relatively stable in the center of the reactor with a constant arc length, which is also reflected by the current–voltage

characteristics in figure 3.3(b), showing constant values over time. In the following sections, we will investigate both arc modes in a combined experimental and computational study, starting with the rotating arc mode.

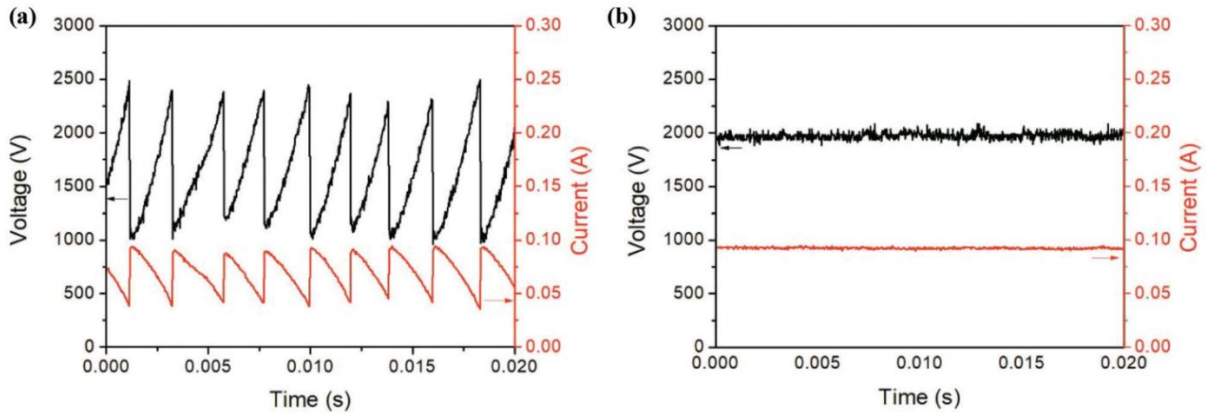

Figure 3.3: Current–voltage characteristics of the plasma arc in Mode I (a) and Mode II (b), for a 50% N_2/50% O_2 gas composition. The average plasma power for Modes I and II are 108 and 200 W, respectively.

3.3.2 Experimental results of the rotating arc mode

Figure 3.4 displays the NO_x concentrations and corresponding energy cost as a function of the N_2/O_2 feed ratio, obtained in the experiments (performed by F. Jardali in our group), and compared with the calculation results at a plasma power of 108 W and flow rate of 2 L min^{-1}. Details about the experimental setup and procedure, are presented in the appendix (section 8.3). As explained in section 3.2.5, the NO_x concentration is calculated for each group of streamlines by a quasi-1D chemical kinetics simulation (using the plasma conditions experienced by each group). Subsequently, the overall NO_x concentration is calculated as a weighted average over the ten groups. Note that the measured and calculated energy costs are both plotted using the same axes, and the values are given both in MJ mol^{-1} and kWh kN^{-1}, for easy comparison with literature, where energy cost is sometimes given in either unit. We evaluate the total NO_x concentration and not the separate NO and NO_2 concentrations, as these two compounds are easily converted into each other. Even in the tubing to the detector device, NO can oxidize to NO_2, changing the ratio of the output gas. The figure shows that the 40% N_2/60% O_2 mixture, where both N_2 and O_2 are present in high amounts to form NO_x, provides the highest NO_x concentration of 3.4% and the lowest energy cost of 2.4 MJ mol^{-1}. This result is significantly better than the 2% NO_x concentration at an energy cost of 2.8 MJ mol^{-1} that was the best result for GA reactors reported in literature before this research.[55,56] Both our modelling and experimental results indicate that the produced amounts of N_2O are very low (below 0.01 %), which is beneficial given its danger as greenhouse gas. The modelling results are in reasonable agreement with the experiments.

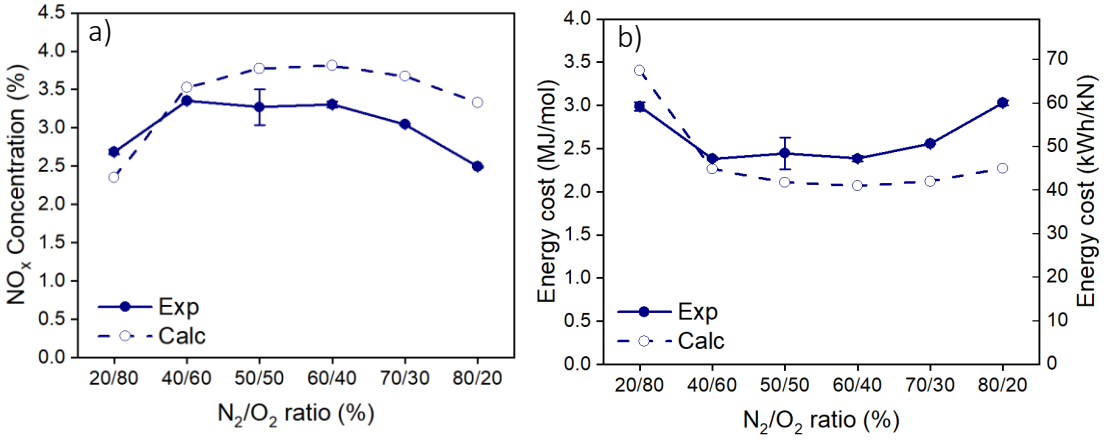

Figure 3.4: Experimental and calculated NO_x concentrations and corresponding energy cost as a function of the N_2/O_2 feed ratio in the rotating arc mode of the RGA. The error bars in the experimental data are obtained from the standard deviation of the measurements, and they are sometimes too small to be visible.

3.3.3 Describing the rotating arc mode through modelling

3.3.3.1 3D gas flow pattern and arc behavior

As shown in figure 3.5, which presents the calculated gas streamlines in the reactor and a schematic representation of the arc, the RGA reactor is characterized by a rotational gas flow pattern. This vortex flow is created specifically to initiate the rotational movement of the arc, as it is dragged along the rotating gas stream (hence the name of the reactor). As shown by the figure, this flow pattern is created by the high velocity stream of ~60 m/s in the tangential gas inlet. As the gas is released from the inlet tube and enters the reactor body, it follows the vortex flow pattern along the reactor walls, with a typical velocity up to ~30 m/s. As the gas spirals along the reactor walls towards the outlet, it loses its momentum and flows towards the center of the vortex, eventually slowing down to a typical velocity of 10 m/s when it leaves the reactor.

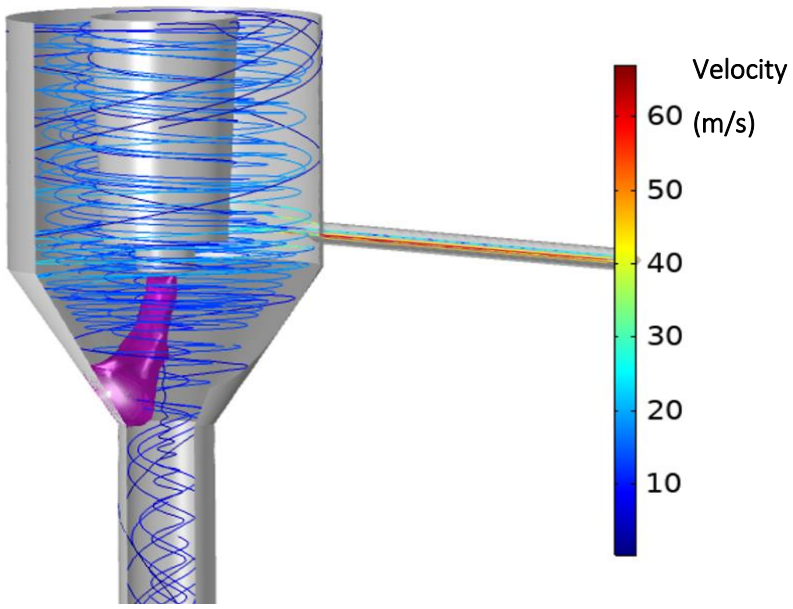

Figure 3.5: Calculated gas velocity streamlines and arc formation in the RGA reactor.

The high velocity stream near the walls and flow velocity in the center of the vortex is further illustrated by figure 3.6, presenting the flow velocity magnitude in a horizontal and vertical cross section of the reactor. The figure displays the significant difference in gas flow velocity between the peripheral stream along the reactor walls (i.e. ~20-30 m/s) and in the slower flow near the center of the reactor (i.e. 2 m/s).

As the arc ignites in the shortest gap between the anode pin and the cathode wall, it follows the rotational movement of the gas. Figure 3.5 only presents a snapshot of the arc (at 1.6 ms), but when looking at the temporal behavior, one end of the arc remains attached to the anode pin while the other glides over the reactor walls (cathode), as it is dragged around by the gas flow.

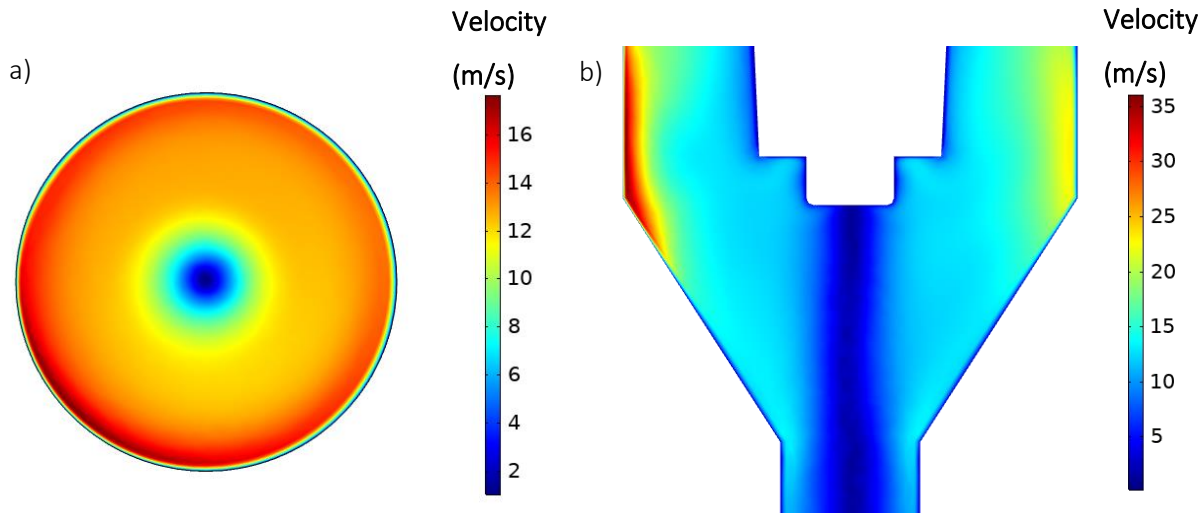

Figure 3.6: Gas velocity magnitude in the (a) horizontal cross section (1 mm under the anode) and (b) vertical cross section (reactor center) of the RGA reactor.

This rotation is illustrated by the sequence of calculated power density profiles in figure 3.7, as obtained from the 3D thermal arc model. These profiles demonstrate where the power is applied to the gas and thus where the plasma is formed. In these profiles, most of the power is applied near the anode pin and cathode wall (red power density hotspots), which is where most electrons and reactive plasma species will thus be created. The sequence of power profiles also clearly shows the rotation period of the arc, as ~1.75 ms.

As the arc rotates, it quickly heats the gas. This rise in gas temperature is calculated by the 3D thermal plasma model based on Joule heating, to which the correction of the 2D non-thermal plasma model adds the effect of the exothermic plasma chemistry. The reactions contributing most to this effect are the conversion of NO into NO_2 and the relaxation of vibrationally excited molecules. The gas heating is illustrated by the sequence of calculated temperature profiles in figure 3.8, as obtained from the 3D thermal arc model (again corrected by means of the 2D non-thermal arc model). Like the rotation of the power density, we observe the rotation of a very hot plasma zone, reaching temperatures up to 3500 K. These peak temperatures are found in the same locations as the power density hotspots, because gas heating is here the most pronounced, but the high temperatures are also spread out to some extent, due to thermal conductivity. The rotation of this very hot plasma zone initiates significant temperature swings: at a fixed position in the reactor, the temperature can change from 3500 K to room temperature every 1.75 ms.

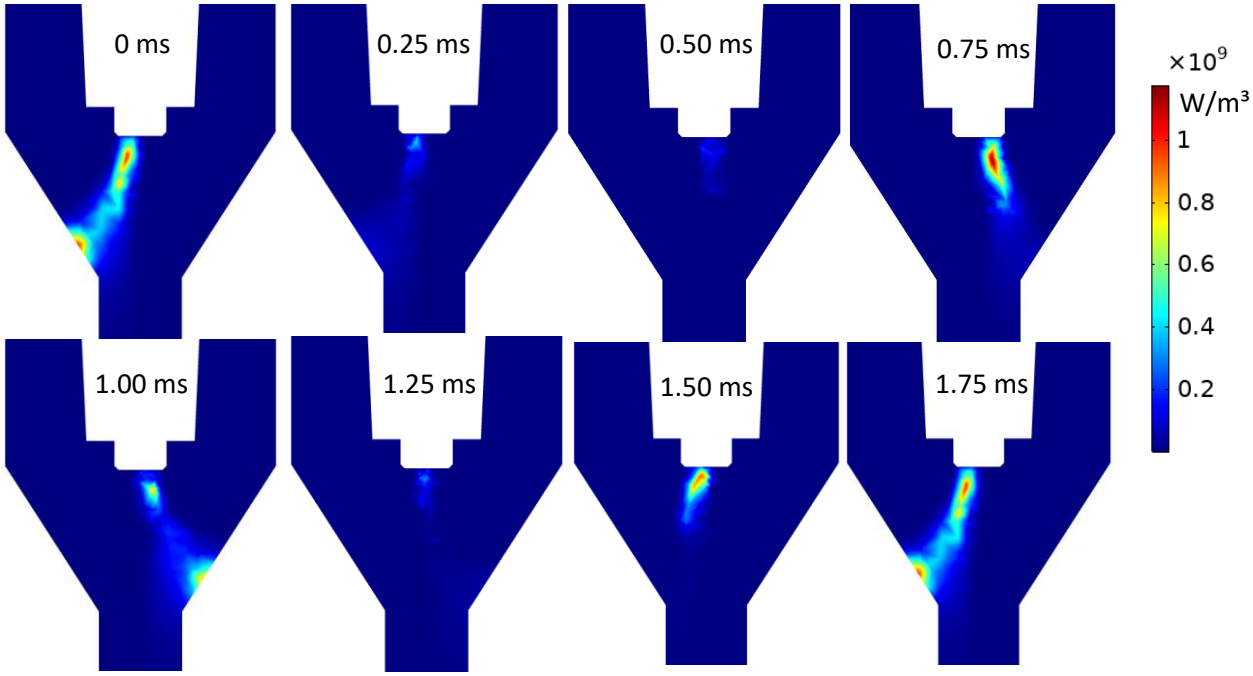

Figure 3.7: Calculated power density profiles at different time instants during the rotation of the plasma arc.

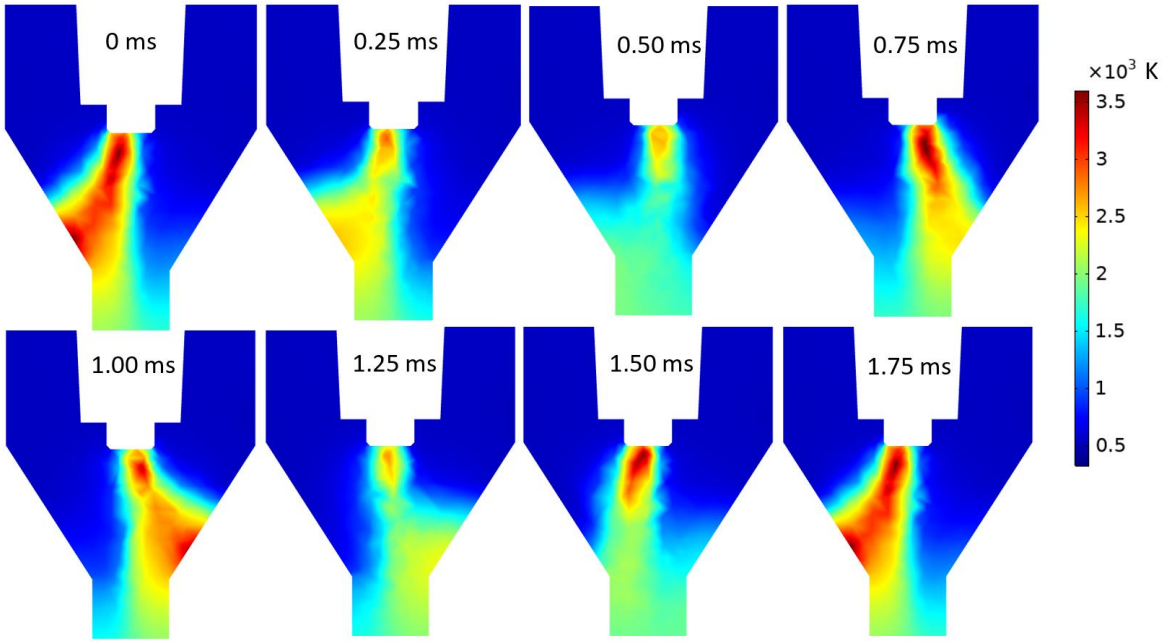

Figure 3.8: Calculated plasma gas temperature profiles at different time instants during the rotation of the plasma arc.

As gas is treated by the rotating plasma arc, it feels a certain temperature and power density. This temperature and power density will be significantly higher if it flows close to the anode pin or the cathode wall, since most of the power is applied near the anode pin and cathode wall, as shown by figure 3.7 . To visualize what percentage of the gas is treated by these hot plasma zones, a distribution can be made for the amount of gas that experiences a certain gas temperature as it flows through the reactor.

This distribution is illustrated in figure 3.9, showing the gas temperature ranges inside the plasma on the x-axis and the calculated fraction of gas that is found within each range of gas temperatures on the y-axis. The temperature intervals of the distribution are chosen to be smaller in the range between 2000 K and 3200 K, as in this temperature range the gas conversion is most sensitive to the temperature (as will be shown in next section). This distribution shows that 15% of the gas flows through the reactor where the temperature is below 2000 K, and is thus not treated by the arc when flowing towards the outlet. Note, however, that this fraction is significantly less than in other GA designs, such as a classical (2D) GA or the GA Plasmatron, where 85% of the gas flows through the reactor without actually passing the plasma.[88,91] These numbers demonstrate that the aim the RGA design to increase the fraction of gas treated by the plasma through a rotating arc was successful. The largest fraction of the gas (± 60%) experiences temperatures between 2600 K and 3000 K, which are found in the hot center of the arc. A small portion of the gas (5%) experience temperatures above 3000 K, which are located near the electrodes of the reactor.

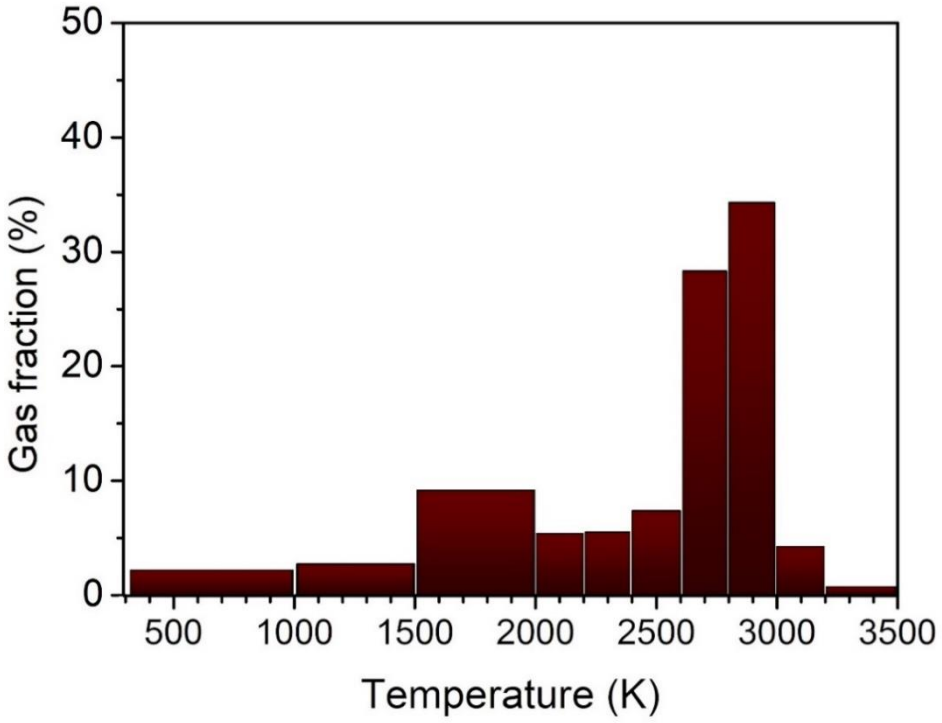

Figure 3.9: Distribution of gas molecules according to the temperature they experience when flowing through the reactor.

The difference in temperature experienced by the gas molecules, as shown in figure 3.9, will have its implications for the NO_x formation in each part of the reactor, which will be discussed in the next section.

3.3.3.2 NO_x formation in the RGA reactor

As the gas flows through the reactor, the N_2 and O_2 gas molecules will gradually be converted into NO_x (i.e., NO and NO_2). To calculate the NO_x formation in the RGA, we simulate the plasma chemistry along

the gas streamlines by means of a quasi-1D chemical kinetics model, as described in section 3.2.5, using the calculated gas temperature and power density from the 3D model as input.

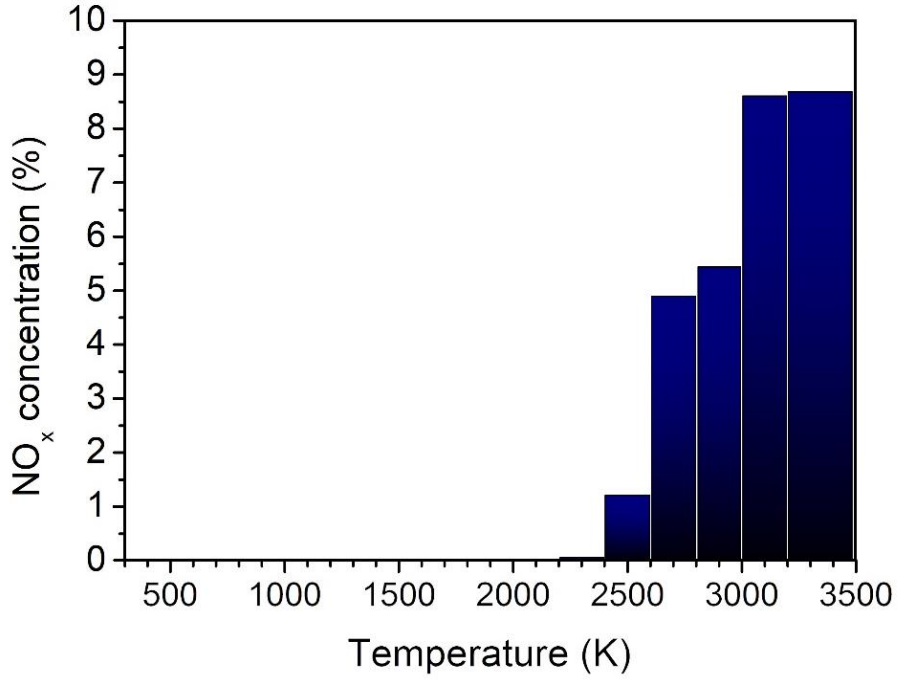

Figure 3.10: Calculated molar NO_x concentration obtained for each group of gas molecules, experiencing a different temperature, for a gas mixture of 50% N_2 and 50% O_2.

The NO_x formation is calculated for each temperature interval in the temperature distribution of figure 3.9 and is plotted in figure 3.10. The overall molar NO_x concentration equals 4.29 %, and is calculated by the weighted average over these ten groups, in which the weight is determined by the distribution of the gas presented in figure 3.9. The figure displays the trend that a higher temperature leads to a higher NO_x concentration, as the higher temperature significantly increases the rate of the plasma reactions to produce more reactive species and thus enhances the plasma-based NO_x formation. The increase in NO_x concentration seems to be the most significant between 2400 K and 3000 K. Below 2400 K, the plasma kinetics are too slow to produce significant amounts of NO_x at the given residence times. Above 3000 K, the higher temperature still increases the NO_x formation, but the increase is less significant, as at these temperatures both the NO_x formation and destruction reactions are accelerated to a point where equilibrium is reached, approaching an upper limit in the NO_x formation.

The fact that the highest NO_x production is achieved above 2600 K, i.e. in the hot center of the arc or in the power density hotspots near the electrodes, is important information to consider in reactor design improvement. For our reactor design, this is found beneficial, as figure 3.9 indicated that more than 65% of the gas experiences temperatures between 2600 K and 3500 K. This fraction is thus responsible

for most of the NO_x production (i.e. 98% of the NO_x produced in the reactor), indicating that, in these conditions, our model could be narrowed down to simulating only this fraction of the gas.

3.3.3.3 Underlying chemistry for NO_x production, and the role of vibrational excitation

The quasi-1D model also reveals the underlying plasma chemistry of NO_x production, providing deeper insight into why certain plasma conditions lead to a higher or lower NO_x concentration, which is very valuable information for further reactor development. Wang et al.[88] and Vervloessem et al.[91] reported that the plasma chemistry in GA reactors is defined by the vibrational excitation of N_2 and O_2 molecules by the high energy electrons in the plasma. Indeed, the electron temperature in GA plasmas is typically around 1 eV (11 605 K), at which vibrational excitation is the most favored excitation pathway.[88,91]

Figure 3.11 displays the electron temperature calculated by the quasi-1D model along a streamline close to the center of the RGA reactor, as schematically shown in the upper right corner of the figure. As shown by the two distinct electron temperature peaks in the figure, this streamline experiences two rotations of the arc along its trajectory. It is clear that the electron temperature within the arc indeed lies around 1 eV, and therefore a significant fraction of the electron energy is transferred to vibrational excitation of the gas. This is especially important for N_2, since vibrational excitation of N_2 facilitates the splitting of the strong triple bond of the molecule (≈ 10 eV) and promotes NO_x production through the Zeldovich mechanism:

$O + N_2(V) \rightarrow N + NO$

$N + O_2(V) \rightarrow O + NO$

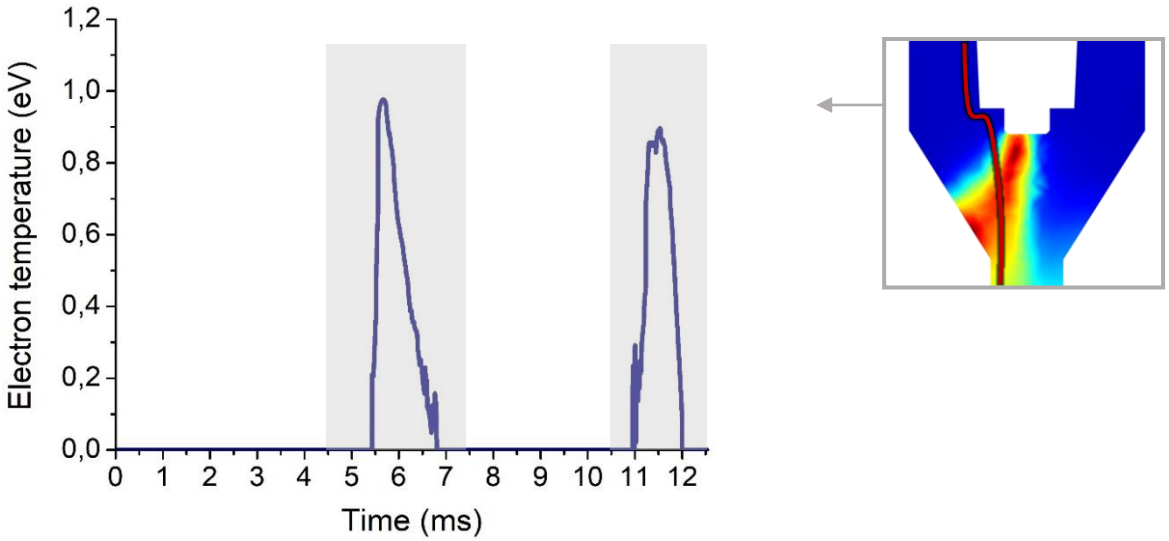

Figure 3.11: Time evolution of the calculated electron temperature along a streamline close to the center of the RGA. The grey zones indicate when the gas passes through the rotating arc.

However, at high gas temperature around 3000 K, which is a typical value for a GA at atmospheric pressure[90–92] (cf. also figure 3.8 and 3.9 above), the lifetime of these vibrationally excited molecules ($N_2(V)$ and $O_2(V)$) is limited, because a high gas temperature greatly increases the rate of vibrational-translational (VT) relaxation collisions, in which the vibrational energy from excited molecules is lost to gas heating. Thus, a thermal equilibrium between the translational and vibrational temperature is eventually achieved.

In the RGA, however, the gas cools down very fast after leaving the arc (cf. figure 3.8), i.e., after every arc rotation, inhibiting the VT relaxation and allowing for vibrationally excited molecules to exist for a significantly longer time. Figure 3.12 depicts the time evolution of the gas and vibrational temperature along the same streamline as figure 3.11, experiencing two arc rotations. The fast cooling in between the arc rotations develops a clear non-equilibrium between both temperatures. The characteristic timescale of VT relaxation is plotted in figure 3.13, showing that the fast cooling drastically slows down the vibrational relaxation. Indeed, while VT relaxation operates on a sub-ms timescale in the arc (see figure 3.13), it only occurs on a seconds timescale outside the hot plasma zone, so the lifetime of the vibrationally excited molecules is on the order of seconds, once they are created in the arc.

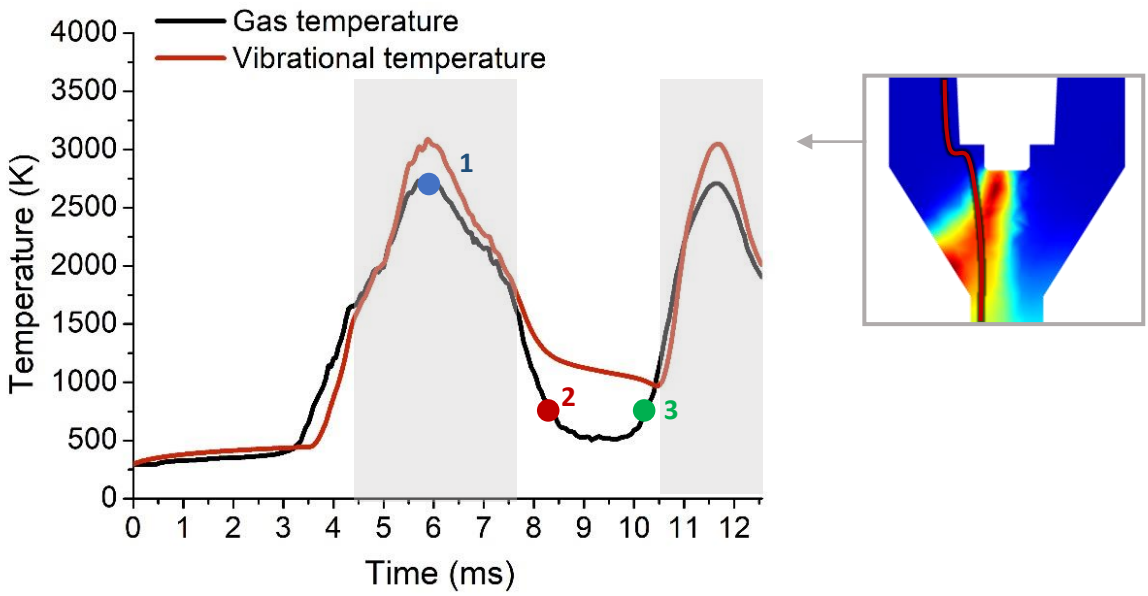

Figure 3.12: Time evolution of the calculated gas and vibrational temperature along a streamline close to the center of the arc. The grey zones indicate when the gas passes through the rotating arc. The colored numbers (1, 2, 3) indicate the time points at which the VDFs are plotted in figure 3.14 below.

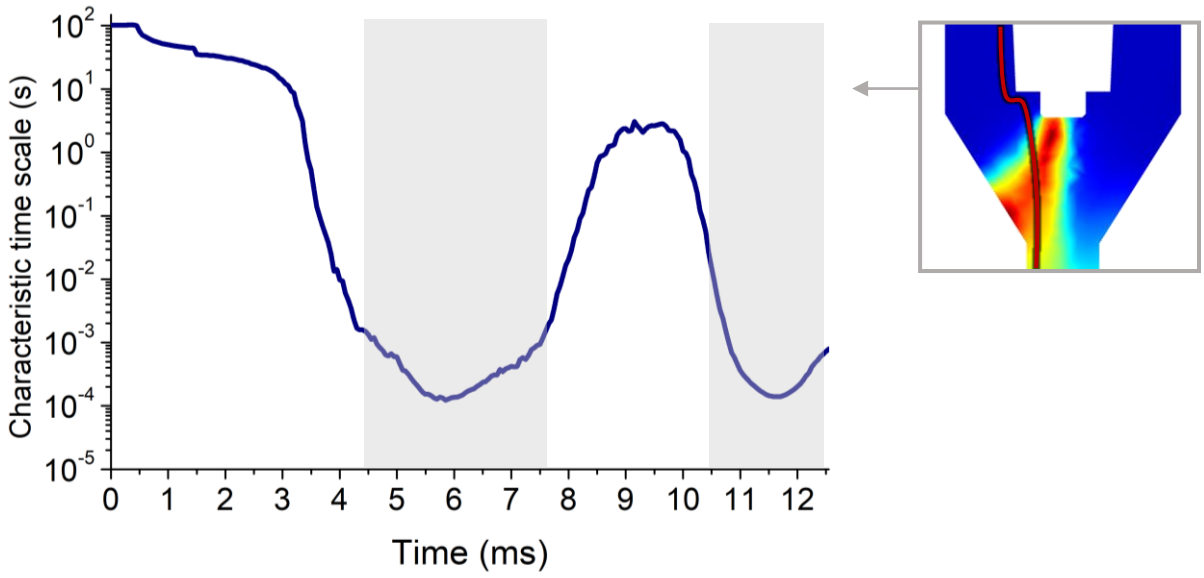

Figure 3.13: Time evolution of the characteristic timescale of VT relaxation along a streamline close to the center of the arc. The grey zones indicate when the gas passes through the rotating arc.

The extended lifetime of the vibrationally excited molecules after leaving the arc, and the presence of vibrational-translational (VT) equilibrium inside the arc are also noticeable from the calculated vibrational distribution function (VDF) of N_2, plotted in figure 3.14. While the vibrational temperature only accounts for the excitation of the first vibrational level of the N_2 stretching mode, the VDF indicates how the energy is distributed among all vibrational levels of N_2 by presenting the relative population of each vibrational level. Figure 3.14 illustrates the VDFs of N_2 at three different time points of the temperature profile in figure 3.12, displaying the evolution of the VDF during the fast cooling. As a reference, the Boltzmann distribution functions at the corresponding calculated gas temperatures are also plotted with dashed lines in the same color, to indicate the degree of vibrational-translational (VT) (non)equilibrium. The VDFs all exhibit a Boltzmann distribution, but only inside the arc (point 1), the VDF coincides more or less with the Boltzmann distribution defined by the gas temperature, showing that the gas is in VT equilibrium due to the high temperature in the arc. Once the cooling starts and VT-relaxation processes are inhibited, the vibrational levels of N_2 stay highly populated. They still exhibit a Boltzmann distribution, but with a clear overpopulation compared to the Boltzmann distribution at the corresponding gas temperature (points 2 and 3). Even 2 ms after the arc rotation (cf. time point 3 in figure 3.12, lying 2 ms after the end of the pulse), these higher vibrational levels are still strongly

overpopulated.

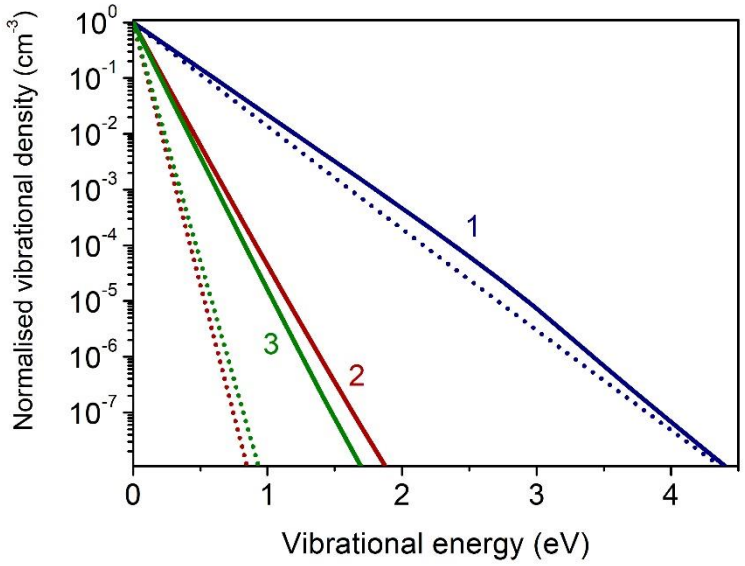

Figure 3.14: VDFs at three different points in time indicated in the temperature profile in figure 3.12. The full lines represent the calculated VDFs, while the dotted lines represent the Boltzmann distributions at the corresponding gas temperature.

Thus, as the vibrational levels are highly populated even when no plasma is present, vibrational splitting of N_2 and the vibrationally-promoted Zeldovich reactions still occur outside of the arc. This uninterrupted NO_x production is illustrated in figure 3.15, showing the calculated NO_x production rate as a function of time, along the same gas streamline flowing close to the center of the reactor as shown in the previous figures. The NO_x formation clearly rises within the arc, but even in between two arc rotations, the NO_x formation is still significant, also because the lower temperature inhibits back-reactions that destroy NO_x. Although the NO_x production in between two arc rotations certainly is beneficial for the performance of the RGA, figure 3.15 indicates that the great majority of the NO_x production still occurs inside the arc, due to the high electron density and the formation of many reactive plasma species.

The model thus suggests that higher NO_x production would be achieved if the residence time in the arc during each rotation would be longer. Possible design modifications that would either slow down the rotational movement of the arc or locally increase the residence time of the gas in the hot plasma zone are thus important targets for design improvements of this RGA reactor.

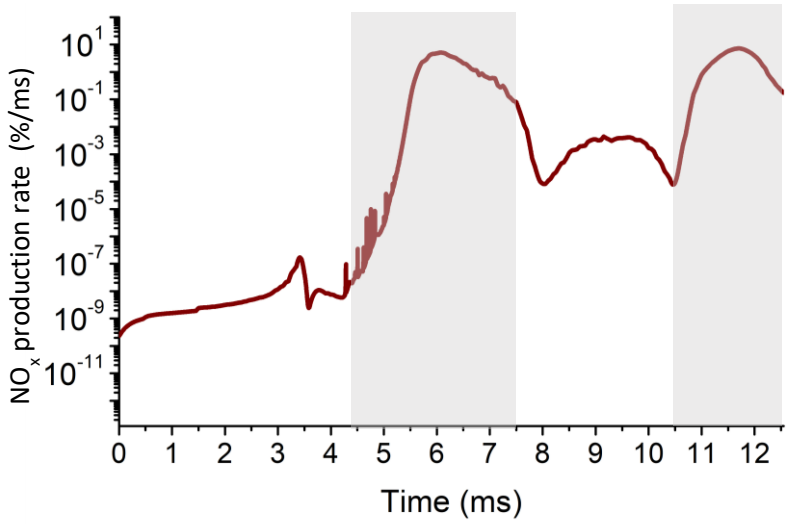

Figure 3.15: Time evolution of the molar NO_x production along a streamline close to the center of the arc. The grey zones indicate when the gas passes through the rotating arc.

3.3.4 Experimental results of the steady arc mode

Contrary to the rotating arc regime, the power in the steady arc regime is high enough for the arc to elongate and reach the furthest point of contact on the reactor outlet. As illustrated in figure 3.16, which shows a schematic representation of the steady arc regime, the rotating gas flow (described in detail in section 3.3.1, and shown schematically by the black streamline in figure 3.16) does not drag the arc in a rotating movement like in the rotating arc regime. In the steady arc regime, the arc is long enough to remain stabilized in the center of the tornado flow where it is shielded from the reactor walls by the rotating gas flow. Indeed figure 3.6(a) showed that the gas flow velocity is lower in the center of the reactor, such that the arc remains immobile in this location (blue zone), surrounded by fast moving gas (orange and red zone).

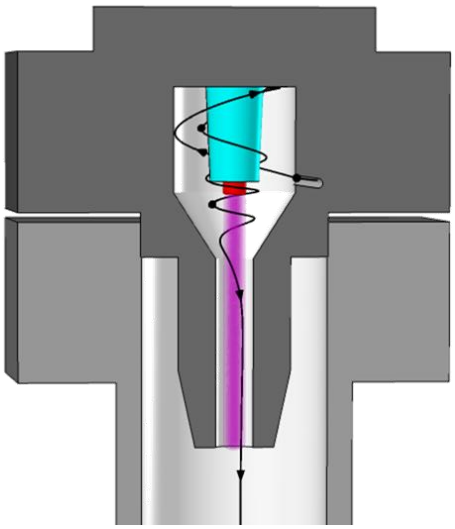

Figure 3.16: Schematic representation of the RGA reactor operating in the steady regime. The arc is depicted in purple, while the rotating gas flow is illustrated by the black streamline.

Figure 3.17 displays a) the NO_x concentrations and b) the corresponding energy cost, for the plasma arc operating in the steady mode, as a function of the N_2/O_2 feed ratio, obtained in the experiments (by F. Jardali), and compared with the calculation results. The NO_x concentration is again calculated for each group of streamlines by a quasi-1D chemical kinetics simulation (using the plasma conditions experienced by each group). Subsequently, the overall NO_x concentration is calculated by weighted average over the ten groups. Note that the measured and calculated energy costs are both plotted using the same axes, and the values are again given both in MJ mol^{-1} and kWh kN^{-1}, for easy comparison with literature, where energy cost is sometimes given in either unit. In section 3.3.2, we revealed that our RGA reactor (in the rotating mode regime) outperforms the best results for N_2 fixation in atmospheric pressure plasma reactors reported in literature up to this research, achieving a NO_x concentration of 3.35 % at an energy cost of 2.4 MJ/mol. Comparing those results to the performance of the steady regime in figure 3.17, we find a further increase in the NO_x concentration, reaching up to 5.5% for a 50% N_2/50% O_2 gas mixture, i.e., 1.7 times more than the maximum concentration achieved in the rotating regime. Such a high NO_x concentration has never been obtained in any plasma reactor operating at atmospheric pressure. Again, good agreement is obtained with the modelling results.

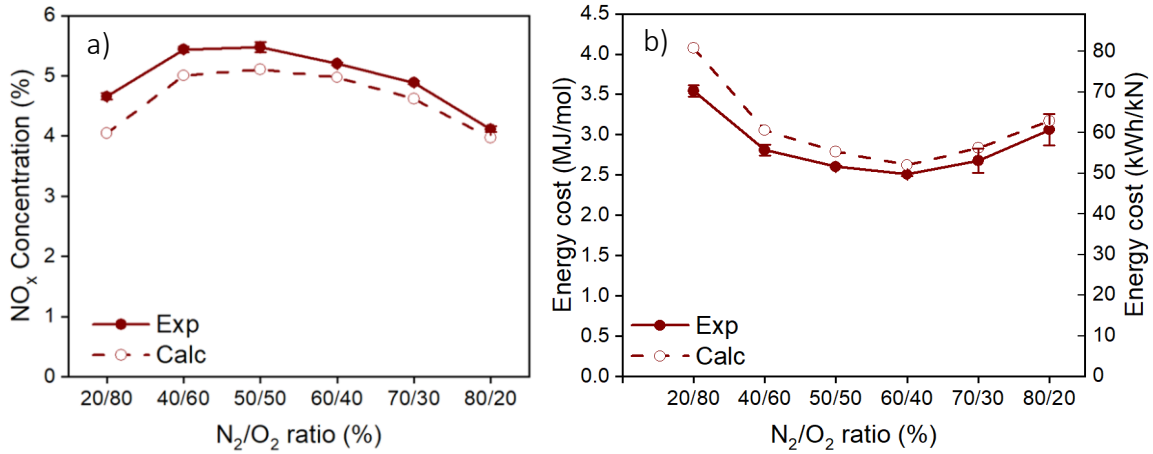

Figure 3.17: Experimental and calculated NO_x concentrations and corresponding energy cost as a function of the N_2/O_2 feed ratio in the steady arc mode of the RGA. The error bars in the experimental data are obtained from the standard deviation of the measurements, and they are sometimes too small to be visible.

3.3.5 Understanding the different performances of both arc operating modes through computational modelling

By applying the same modelling procedure as the rotating arc mode, we can provide a detailed comparison between the two modes, and identify the difference in performance. Figure 3.18(a) presents the calculated temperature distribution for the steady arc regime, showing the gas temperature ranges on the x-axis and the calculated fraction of gas that is found within each range on the y-axis. The same distribution for the rotating regime is also shown again in figure 3.18(b) for easy comparison. A very notable difference between figure 3.18(a) and (b) is that the temperature distribution of the steady regime does not include temperatures below 2500 K. Indeed, as shown by figure 3.16, the steady arc is located in the center of the reactor and fills the whole reactor outlet, essentially treating 100% of the gas that passes through the reactor. This is in strong contrast to other types of GA reactors, where only a small portion of the gas is actually treated by the arc.[91,93] Furthermore, as shown by the temperature distribution in figure 3.18(a), the gas also reaches overall higher temperatures. While figure 3.18 (b) only shows gas temperatures up to 3500 K in the rotating regime, the model predicts gas temperatures even up to 5000 K in the hot center of the steady arc. This is attributed to the increased plasma power associated with the steady arc regime.

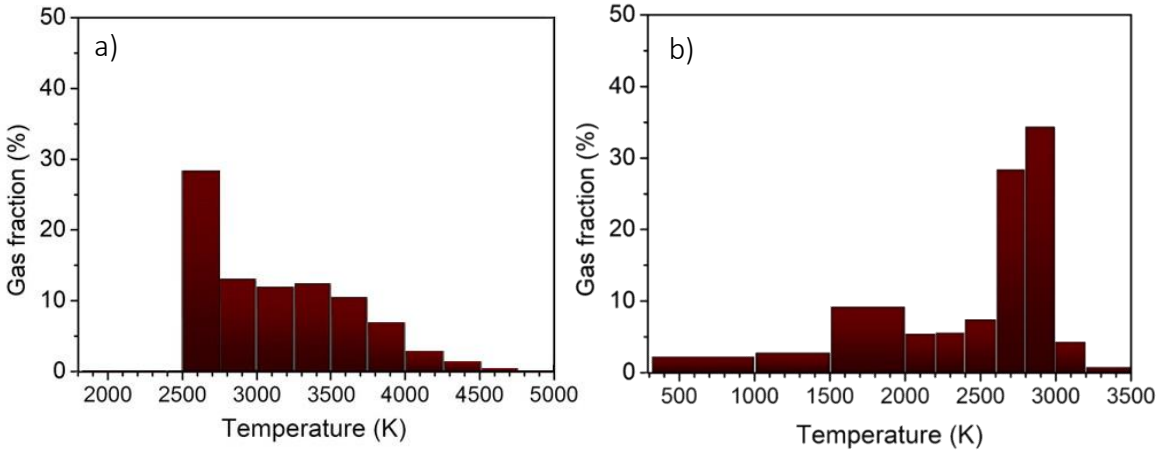

Figure 3.18: Distribution of gas molecules according to the temperature they experience when flowing through the reactor for a) the steady arc mode and b) the rotating arc mode

The steady regime does not only show a clear difference in temperature distribution compared to the rotating regime, it also illustrates a clear difference in its gas and vibrational temperature profiles. Figure 3.19(a) depicts the calculated gas and vibrational temperature profile as a function of time along a streamline in the steady arc regime, while figure 3.19(b) shows the same calculated temperature data along a streamline in the rotating regime, experiencing a similar maximum temperature, for easy comparison. While the rotating arc profile in figure 3.19(b) treats the gas for a short period of time (i.e. about 4 ms), the steady arc in figure 3.19(a) treats the gas for a prolonged duration (up to 10 ms), heating the gas up to 2600 K until it leaves the reactor. At this high gas temperature in the steady arc, VT relaxations occur at a very high rate, and the gas and vibrational temperature reach thermal equilibrium. Indeed, figure 3.19(a) clearly demonstrates that both the gas translational and vibrational temperatures are constant around 2600 K, unlike the temperature profile of the rotating arc in figure 3.19(b), where this VT equilibrium is only reached for less than 4 ms and a thermal non-equilibrium is present between pulses. The uninterrupted treatment of the steady regime pathway produces even more NO_x than in the rotating mode, since the constant vibrational temperature of 2600 K is higher than the average vibrational temperature achieved in the rotating mode. Furthermore, since the gas temperature is also at 2600 K, the thermal Zeldovich mechanism of ground state N_2 is also significant. The extra contribution from the thermal (ground state) pathway in this thermal equilibrium state, in combination with the 100% gas fraction passing through the arc, explains the higher NO_x production in this steady arc mode.

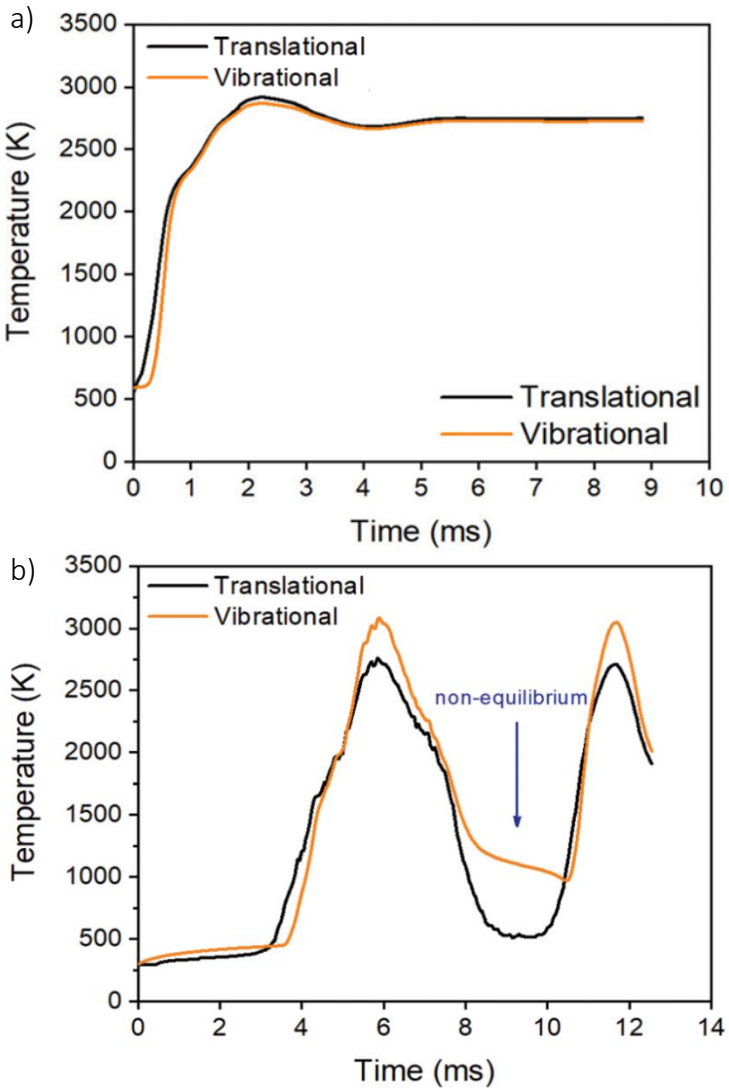

Figure 3.19: Time evolution of the calculated gas and vibrational temperature along a streamline close to the center of the arc for (a) the steady arc mode and b) the rotating arc mode.

3.4 CONCLUSION

New innovative 3D GA reactor designs are gaining increasing interest for plasma-based gas conversion applications. We present here the highly efficient NO_x production in a novel atmospheric-pressure RGA reactor. The reactor can be operated in two distinct plasma arc modes: (i) a rotating arc with variable length, which is the typical mode in the RGA reactor, and (ii) a steady arc with stable length, that could only be achieved at supplied power above 180 W. We measured the NO_x concentrations for different gas feed ratios, exploring the performance of both modes. When the arc is in the rotating mode, we obtained NO_x concentrations up to 3.4%, at an energy cost of 2.4 MJ mol^{-1} , which is generally better than the results obtained up to this research in atmospheric pressure plasma reactors. However, when the arc is in steady mode, even higher NO_x concentrations are achieved, up to 5.5%, i.e., 1.7 times higher than the maximum concentration obtained by the rotating arc mode, with an energy consumption of

2.5 MJ mol^{-1} (or ca. 50 kW h kN^{-1}). To our knowledge, these are by far the highest NO_x concentrations that have so far been achieved in an atmospheric pressure plasma reactor.

To gain deeper insight into the behavior of the arc and the processes taking place in both modes, we developed a combined modelling approach for describing the fluid dynamics, the plasma behavior and the plasma chemistry in a GA reactor in four complementary models. Using this method we can present a very comprehensive description of plasma-based NO_x formation in a RGA reactor.

The model reveals that the characteristic vortex flow formed by the tangential flow inlet drags the arc around in a rotational movement in the rotating mode of the RGA. The model also reveals the underlying plasma chemistry, demonstrating the importance of the vibrationally-promoted NO_x formation through the Zeldovich mechanism in the rotating mode of the RGA. Due to the fast cooling of the gas, each time after the arc rotation, VT relaxation is inhibited, strongly increasing the lifetime of vibrationally excited molecules. Furthermore, these lower temperatures inhibit NO_x destroying back-reactions. As the vibrational energy levels of N_2 remain significantly excited between the arc rotations, N_2 splitting and NO_x formation are shown to continue in between two arc rotations, albeit at a lower rate. For the steady mode, our model reveals that high NO_x concentrations are achieved because the hot plasma zone covers a large portion of the reactor body, permitting all gas molecules to be treated while flowing through the reactor. This is in stark contrast with other GA reactors described in literature, where typically only about 15% of the gas passes through the actual arc, thus explaining the much higher NO_x concentrations achieved in our case. Furthermore, the steady arc mode treats the gas for a prolonged duration, compared to the pulsed treatment of the rotating regime, yielding a thermal equilibrium between the vibrational and gas temperature in which NO_x formation can occur through both the vibrationally-promoted and the thermal Zeldovich mechanisms.

Good agreement with experimental data at different gas ratios demonstrates that our modelling approach can provide a realistic picture of the flow and plasma behavior in the RGA reactor. This approach can also be used for modelling reactor design improvements for other gas conversion applications, when the plasma chemistry is available.

4 EFFUSION NOZZLE FOR ENERGY-EFFICIENT NO_x PRODUCTION IN A ROTATING GLIDING ARC PLASMA REACTOR

The results presented in this chapter were published in:

"Effusion nozzle for energy-efficient NOx production in a rotating gliding arc plasma reactor" Van Alphen S., Ahmadi Eshtehardi H., O'Modhrain C., Bogaerts J., Van Poyer H., Creel J., Delplancke M-P., Snyders R., Bogaerts A., Chem Eng J 443, 136529 (2022)

DOI: 10.1016/j.cej.2022.136529.

4.1 INTRODUCTION

Last chapter showed that operating the RGA in the steady arc mode yielded record-value NO_x concentrations up to 5.5% with an energy consumption of 2.5 MJ mol^{-1} (or ca. 50 kWh kN^{-1}); i.e. the lowest value achieved by atmospheric pressure plasma reactors at that time of the research. While these results are impressive, they are still far from the energy consumption target of 0.7 MJ mol^{-1} defined by Rouwenhorst et al.[48] for a plasma-based N_2 fixation process to be competitive with the electrolysis-based Haber–Bosch process combined with the Ostwald process (see chapter 1.5, page 30-31).

One of the important limitations that is determining the performance of quasi-thermal plasmas like the RGA is that part of the plasma-produced NO_x is destroyed after leaving the plasma reactor. Indeed, the temperature in the RGA, but also in other quasi-thermal GA and MW reactors, reaches a typical value of 3000 K or even higher, [91,94] but the gas cools down slowly after leaving the plasma. As a result, the produced NO will react with N or O atoms, back into N_2 and O_2 molecules, which reduces the overall NO_x production, as revealed by modeling.[70]

Therefore, in this chapter, we present a design modification to the above-mentioned RGA plasma reactor,[94] by coupling it with a specific nozzle, which we call "effusion nozzle". As I will demonstrate by means of modeling, this causes a fast drop in the gas temperature when the gas leaves the reactor, thereby quenching the unwanted recombination reactions, and thus improving the overall reactor performance. My fellow PhD student, H. Ahmadi Eshtehardi, experimentally investigated the performance of this novel plasma reactor/nozzle design in a wide range of operating conditions, i.e., flow rate, input power and N_2/O_2 ratio, and by means of my computational studies, I reveal the

underlying mechanisms of the improvement. The insights obtained by this modeling will also be useful for other plasma reactor designs.

4.2 REACTOR SETUP AND EFFUSION NOZZLE

Figure 4.1 schematically illustrates the RGA plasma reactor, with details of the internal configuration, showing also the rotational gas flow behavior (black arrow line) and the arc plasma (purple) in the center (artist view), in case of steady arc mode (see below). The reactor is the same as in previous chapter. The plasma reactor consists of a nickel anode, and a stainless-steel cathode, coupled to the newly designed effusion nozzle (see below), which acts as the reactor body (Figure 4.1). A spark plug (NGK BP6ES) without its ground pin is used as the powered electrode (the ground pin is replaced by the stainless-steel body of the reactor). The ceramic piece in the center of the reactor (100 mm in length, 6 mm in diameter) encloses the anode pin so that only a cylindrical knob (1.4 mm in length, 2.5 mm in diameter) is exposed (red part in Figure 4.1). The reactor body comprises of a cylinder with diameter of 13 mm and length of 11.2 mm, which is followed by a cone-shape section with diameter decreasing from 13 to 4 mm. The cone-shape section extends to the outlet of the reactor, which is a cylinder of 4 mm diameter and length of 20 mm.

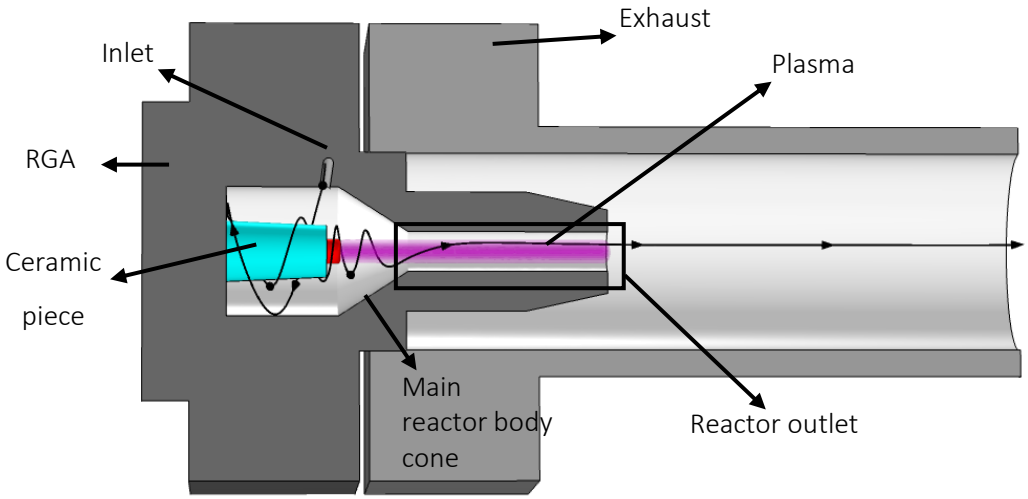

Figure 4.1: Schematic picture of the RGA plasma reactor, illustrating the gas flow behavior (black line) and the plasma in steady arc mode (purple zone). The anode knob is indicated in red at the left, while the entire reactor body is the cathode.

The (stainless-steel) effusion nozzle is coupled to the reactor outlet to enhance the reactor performance by cooling the gas temperature and quenching unwanted recombination reactions, as explained in detail by our model calculations in the results and discussions section. The effusion nozzle consists of a gas-receiving cavity with inner diameter of 15 mm and length of 29.5 mm. At the end, it contains six radially distributed tiny "effusion holes" of 0.8 mm diameter, and a cuboid protruding element, called "gas divider", with 1 mm thickness, perpendicular to the axis of the gas receiving cavity; see Figure 4.2. The

effusion nozzle screws over the plasma reactor outlet, abruptly stopping and dividing the air flow, first by the cuboid and then further by these six small radial holes. The gas divider, indicated in red color in Figure 4.2, serves as anchor for the arc. A stainless-steel cylinder with diameter and length of 25 mm and 295 mm, respectively, is coupled to the whole system to collect the exhaust gas stream and to provide connection to the gas diagnostic device.

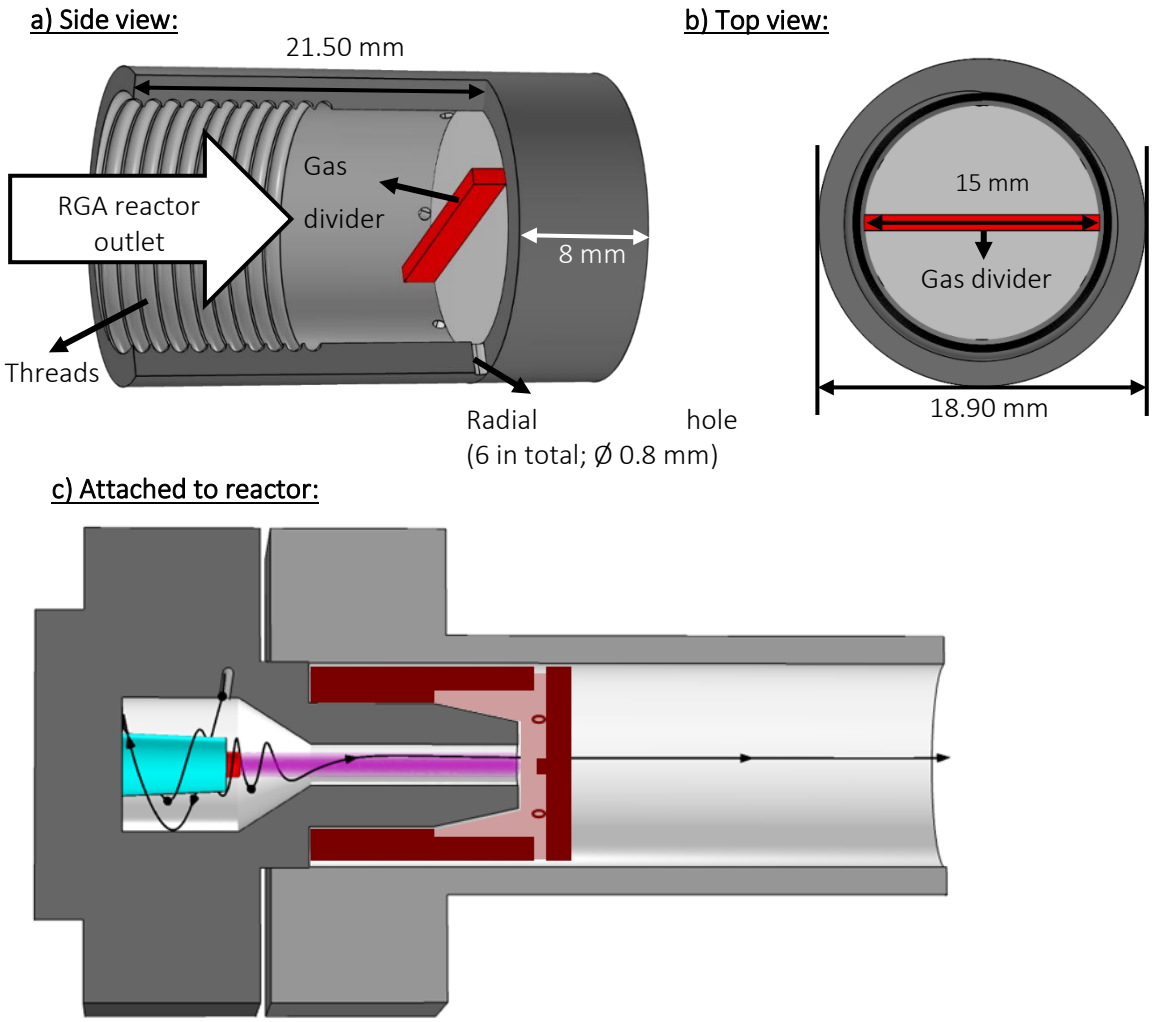

Figure 4.2: Schematic picture of the effusion nozzle with dimensions, in side view (a), top view (b) and attached to the reactor (c). In the latter case, the nozzle is colored in red. The gas divider (red bar in (a) and (b)) serves as anchor when the effusion nozzle is mounted on the RGA, and it has a width of 1 mm, height of 2 mm, and length of 15 mm. It sits on top of the 8 mm steel back wall, across the whole nozzle.

Using the same experimental setup as discussed in previous chapter, H. Ahmadi Eshtehardi measured the total produced NO_x as sum of the NO and NO_2 concentrations (%) in the exhaust stream, by a non-dispersive infrared sensor along with an ultraviolet sensor. Similar to what is described in section 3.3.2 (on page 59) for the RGA without nozzle, N_2O and N_2O_5 are only formed in the ppm range, and therefore do not contribute to the NO_x concentration in a significant way.

The average plasma power (P) is calculated by

$$P[W] = \sum_{j=1}^{N} \frac{V_j I_j}{N} \tag{4.1}$$

Where I_j and V_j are the recorded discharge current and voltage, respectively, and N is the number of records.

Knowing the plasma power and the total measured NO_x concentration, we define the energy cost of the process as:

$$\text{Energy cost}\left[\frac{\text{MJ}}{\text{mol}}\right] = \frac{\text{P}\left[\frac{\text{J}}{\text{s}}\right] \times 24\left[\frac{\text{L}}{\text{mol}}\right] \times 60\left[\frac{\text{s}}{\text{min}}\right] \times 100[\%]}{\text{C}_{\text{NO}_x}[\%] \times \text{Q}\left[\frac{\text{L}}{\text{min}}\right]} \times 10^{-6} \tag{4.2}$$

Where 24 L/mol is the molar volume at the reactor inlet (1 atm and 293.15 K), Q is the total gas volumetric flow rate, and 10^{-6} is the conversion factor from J to MJ.

4.3 MODEL DESCRIPTION

To investigate the performance of the effusion nozzle, we adopt the same computational modelling approach that was described in chapter 2.3 and demonstrated in chapter 3 for the RGA reactor without effusion nozzle. First, a turbulent gas flow model, coupled to the heat balance equation calculates the gas flow behavior inside the reactor. Subsequently, the gas flow behavior and temperature profile are used as input for streamline integration simulations, which describe the trajectory of the gas, and provide a record of the gas temperature and power density "felt" by the gas molecules as they flow through the plasma towards the outlet. This gas temperature and power density profile is then used as an input into a quasi-1D plasma chemical kinetics model, which simulates the plasma chemistry of the N_2/O_2 mixture, and calculates the NO_x concentrations and energy cost of the conversion process. In the following sections, we briefly describe each model in the order in which they are solved..

4.3.1 3D turbulent gas flow and heat transfer model

As the effusion nozzle serves as an obstacle to the gas flow in the outlet, attaching the nozzle might introduce extra turbulence inside the RGA reactor. Therefore the gas flow in the reactor is described by solving the RANS SST[62] turbulence model, as described in detail in section 2.1.1.

$$\rho_g \frac{\partial \vec{u}}{\partial t} + \rho(\vec{u} \cdot \nabla)\vec{u} = \nabla \cdot \left[-p\vec{I} + (\mu + \mu_T)(\nabla\vec{u} + \nabla(\vec{u})^T) - \frac{2}{3}(\mu + \mu_T)(\nabla \cdot \vec{u})\vec{I} - \frac{2}{3}\rho_g k_T \vec{I}\right] + \vec{F} \tag{4.3}$$

$$\rho \frac{\partial \vec{u}}{\partial t} + \nabla \cdot (\rho_g \vec{u}) = 0 \tag{4.4}$$

Where ρ_g stands for the gas density, $\vec{u}$ is the gas flow velocity vector, superscript T stands for transposition, p is the gas pressure, μ is the dynamic viscosity and μ_T the turbulent viscosity of the fluid, k_T is the turbulent kinetic energy, $\vec{I}$ is the unity tensor and $\vec{F}$ is the body force vector.

These equations are coupled to the thermal balance equation to calculate the gas temperature, as described in detail in section 2.1.2 (on page 35).

$$\rho_g C_p \frac{\partial T_g}{\partial t} + \rho_g C_p \vec{u} \cdot \nabla T_g + \nabla \cdot \vec{q} = Q_{heat} \tag{4.5}$$

Where ρ_g stands for the gas density, C_p for the isobaric heat capacity, T_g is the gas temperature, $\vec{u}$ the gas velocity (as calculated in section 1.1), Q_{heat} the heat source term representing the heating from the plasma, and $\vec{q}$ the conductive heat flux vector, which is calculated by:

$$\vec{q} = -(k_g + k_{g,T})\nabla T_g \tag{4.6}$$

Where k_g is the thermal conductivity of the gas and $k_{g,T}$ is the turbulent thermal conductivity of the gas.

In this equation the thermal heat source Q_{heat} is calculated using the plasma volume (V_{plasma}) and power converted to gas heating (P_{heat}).

$$Q_{heat} = \frac{P_{heat}}{V_{plasma}} \tag{4.6}$$

Indeed, as the shape of the plasma arc in the RGA has already been calculated self-consistently in last chapter through a thermal plasma arc model (see section 3.2.3, page 54), we can adopt this same arc shape for calculating the plasma volume, i.e. an arc with an axial length of 20 mm and a Gaussian-shaped radial profile with a width of 2 mm. These arc dimensions are typical for gliding arc reactors [57,92,94,95], but as the arc length serves as an important input parameter for the model, a sensitivity analysis of the arc length on the modelling results is shown in the appendix (section 8.5).

As described in section 2.1.2 (on page 37), P_{heat} can then be calculated using the measured plasma power minus the power needed to produce the measured NO_x concentration in the experiments.

$$\mathrm{P}_{heat} = P_{plasma}(100\% - EE) \tag{4.7}$$

As demonstrated by figure 3.19 in the previous chapter (section 3.3.5, page 74), the steady regime of the RGA is characterized by a quasi-thermal equilibrium, so we can assume that all plasma power that didn't go into chemical reactions goes into gas heating.

Given the important property of the effusion nozzle to conduct heat, thereby influencing the gas temperature within the reactor, the thermal balance equation is not only solved for the gas but also for the solid domains (ceramic and metal parts). This is novel compared to previous chapter. Similar to equation 4.5 for the gas temperature (T_g), The temperature (T_s) of the solid parts of the reactor is calculated through:

$$\rho_s C_{p,s} \frac{\partial T_s}{\partial t} + \nabla \cdot \vec{q} = 0 \tag{4.8}$$

Where ρ_s is the mass density and C_p the heat capacity of the solid materials. In equation 4.8 $\vec{q}$ is the conductive heat flux vector, which is calculated by:

$$\vec{q} = -k_s \nabla T \tag{4.9}$$

Where k_s is the heat conductivity of the solid materials .

At the boundary conditions between the outer wall of the reactor and the ambient air, the heat flux (i.e. heat loss) to the environment is calculated through:

$$\vec{q} = -\vec{n}\varepsilon\beta\left(T_{amb}^4 - {T_s}^4\right) \tag{4.10}$$

Where ε is the surface emissivity, β the Stefan-Boltzmann constant, k is the thermal conductivity, T_{amb} the ambient temperature, h the convective heat transfer coefficient and $\vec{n}$ the unit vector normal to surfaces of the solid domains of the reactor.

4.3.2 Quasi-1D chemical kinetics model and streamline integration

Similar to previous chapter, we use a quasi-1D plasma chemical kinetics model to reveal the chemical formation pathways and calculate the NO_x yields in the RGA reactor. Through the approach described in section 2.3 (on page 43) we calculate the time evolution of all chemical species by solving the continuity equation for all species along the streamlines of the 3D gas turbulent flow model.

$$\frac{dn_i}{dt} = \sum_j \left[\left(a_{ij}^R - a_{ij}^L\right) k_j \prod_l n_l^L \right] \tag{4.11}$$

In which n_i is the density of species i and a_{ij}^R and a_{ij}^L are the stoichiometric coefficients of species i on the right-hand and left-hand side of the reaction j, respectively. n_l is the density of the reacting species l. k_j is the reaction rate coefficient of reaction j.

Through equation 4.12 and 4.13 we integrate 10,000 streamlines, equally spaced over the surface of the inlet boundary, and record the gas temperature and power density that is experienced along the trajectory when flowing through the plasma towards the outlet.

$$q = \int_0^{t_{outlet}} v \, dt \tag{4.12}$$

$$v = \sqrt{{v_x}^2 + {v_y}^2 + {v_z}^2} \tag{4.13}$$

Similar to section 3.2.5 in last chapter (on page 55), we grouped the streamlines based on a similar maximum temperature, and we calculated the average trajectory of each group. As a result, we reduced the 10,000 possible trajectories to only 11 averaged trajectories, which were then used as input for the quasi-1D plasma chemistry model. The overall NO_x concentration is calculated from a weighted average of the 11 simulations, in which the weight is determined by the mass flow in each group.

4.3.3 Plasma chemistry taken into account in the model

Just like last chapter (see section 3.2.6, page 57), we use the N_2/O_2 chemistry set validated by Vervloessem et al.[91] for the quasi-1D chemical kinetics simulation. The reactions and corresponding rate coefficients, and the references where these data were adopted from, are listed in the appendix (section 8.3). However, figure 3.19 in the previous chapter (section 3.3.5 page 74) showed that the steady mode of the RGA is characterized by a quasi-thermal equilibrium, and thus, vibrational-translational relaxation collisions occur fast enough so that vibrational excitation of N_2 and O_2 does not play a significant role in the NO_x formation process.[10] Therefore, to save calculation time, vibrational kinetics are not considered in this model. The remaining set contains 43 different species (see Table 4.1) which react in 1,214 electron impact reactions, 481 ionic reactions, 432 neutral reactions, and are shown in the appendix (section 8.3, table 8.3 to 8.8).

Table 4.1:Plasma species included in the model.

Neutral species	**Radicals**	**Charged species**	**Excited species**
N_2, O_2, O_3,	N, N(2D), N(2P),	e^- N^+, N_2^+, N_3^+, N_4^+,	
NO, NO_2, N_2O,	O, O(1D), O(1S)	O^-, O_2^-, O_3^-, O_4^-,	$N_2(A^3\Sigma_u^+)$, $N_2(B^3\Pi_g)$, $N_2(C^3\Pi_u)$, $N_2(a'^1\Sigma_u^-)$, $O_2(a^1\Delta)$, $O_2(b^1\Sigma^+)$, $O_2(A^3\Sigma^+, C^3\Delta, c^1\Sigma^-)$*
NO_3, N_2O_3,		O^+, O_2^+, O_4^+,	
N_2O_4, N_2O_5		NO^+, NO_2^+, N_2O^+, NO^-, NO_2^-, N_2O^-, NO_3^-, $O_2^+N_2$	

4.4 RESULTS AND DISCUSSION

4.4.1 Improvement in NO_x yield and energy cost due to the effusion nozzle

The effect of the effusion nozzle on the plasma-based NO_x formation was first tested experimentally by H. Ahmadi Eshtehardi, and plotted in figure 4.3. This figure compares the performance of our reactor with and without the effusion nozzle, in terms of NO_x concentration (i.e. NO + NO_2), energy cost and supplied plasma power, as measured using a non-dispersive infrared sensor along with an ultraviolet sensor (see appendix section 8.4 for more experimental details). Similar to last chapter, the results are shown for both rotating and steady arc regime, in a wide range of N_2/O_2 ratios.

In the rotating arc regime, for N_2/O_2 ratios below 50/50, the effusion nozzle allows ignition and sustainment of the plasma arc at lower power values than without nozzle (Figure 4.3e), reaching about the same NO_x concentration (Figure 4.3a). For N_2/O_2 ratios above 50/50, slightly higher power should be supplied as without nozzle, but higher NO_x concentrations are achieved. The effect of either lower power (for the same NO_x concentration) or higher NO_x concentration yields a slightly lower energy cost for each N_2/O_2 ratio, with on average 4.5% improvement, and the largest improvement of 7.3% for an N_2/O_2 ratio of 80/20, mimicking dry air composition (Figure 4.3c).

In the steady arc regime, a lower power can sustain the arc across the entire range of N_2/O_2 ratios when it is operating with the effusion nozzle (Figure 4.3f). Moreover, the effusion nozzle also results in slightly higher NO_x concentrations (improvements up to 8%) (Figure 4.3b). As a consequence of both, the energy cost with the effusion nozzle drops on average by 16.3% over the entire range of N_2/O_2 ratios compared to without nozzle, with the largest improvement of about 22.5% at N_2/O_2 ratio of 80/20. Overall, our best results are obtained in the steady arc regime, at an N_2/O_2 ratio of 50/50, yielding a NO_x concentration of 5.9%, at an energy cost of 2.5 MJ/mol, but an N_2/O_2 ratio of 60/40 yields an even slightly lower energy cost of 2.4 MJ/mol.

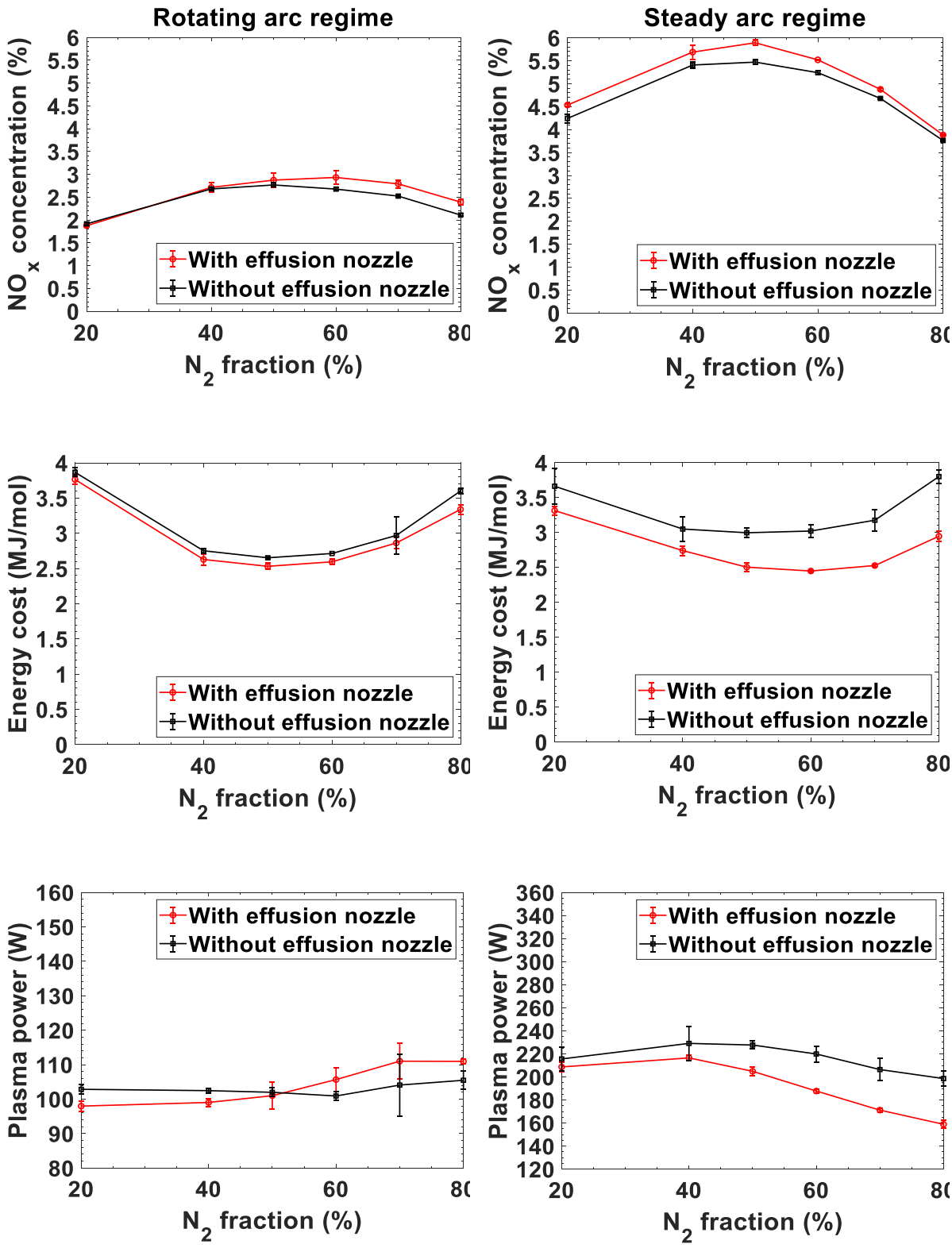

Figure 4.3. Measured NO_x concentration (a, b), energy cost (c, d) and plasma power (e, f) in the RGA plasma reactor operating with and without the effusion nozzle, as function of N_2/O_2 ratio, in rotating (left) and steady (right) arc regimes. The applied current in the rotating arc regime was between 60 and 120 mA, while it was between 120 and 200 mA in the steady arc regime. The total flow rate was fixed at 2 L/min.

As predicted by our models, only NO is initially formed in the plasma, as NO_2 is destroyed at these high gas temperatures. Once out of the plasma, part of the formed NO oxidizes to NO_2 when the gas has

cooled down. By the time the gas reaches our detector, the gas consists of both NO and NO_2. Across the different gas mixtures, the NO/NO_2 ratio varies from 0.2 (at a N_2/O_2 ratio of 20/80) to 0.9 (at a N_2/O_2 ratio of 80/20), hence yielding a higher NO_2 concentration when more O_2 is present in the mixture.

4.4.2 Underlying mechanisms of the improvement: Insights from the models

To explain the improved performance due to the effusion nozzle, we first discuss for both configurations (i.e. with and without the effusion nozzle) the gas flow behavior, arc shape, and temperature profile, as calculated by the fully coupled heat transfer model. Next, we will analyze the molecule trajectories of the streamline integrations and organize them based on their maximum experienced temperature into 11 temperature groups. Finally, we will analyze the obtained NO_x concentrations and reaction rates from each of the temperature groups.

We only show this detailed analysis for the RGA in the steady arc regime, as it yields the best performance, and we will focus on the N_2/O_2 feed ratio of 80/20, which closely mimics dry air, as it is of most interest for practical applications.

4.4.2.1 Gas flow behavior

Figure 4.4(a,b) illustrates the gas flow behavior in the RGA with and without the effusion nozzle, showing a complex rotational flow pattern inside the reactor. Similar to what is described in last chapter, the gas enters the reactor via the tangential gas inlet at a large initial flow velocity of ~60 m/s. Upon entering the main reactor body, the gas velocity drops to ~30 m/s and starts to flow upward along the reactor wall, further decreasing in speed to ~10 m/s. When the gas has reached the top, it will collapse into a smaller inner vortex and flow along the ceramic piece towards the reactor outlet, where the vortex behavior quickly disappears.

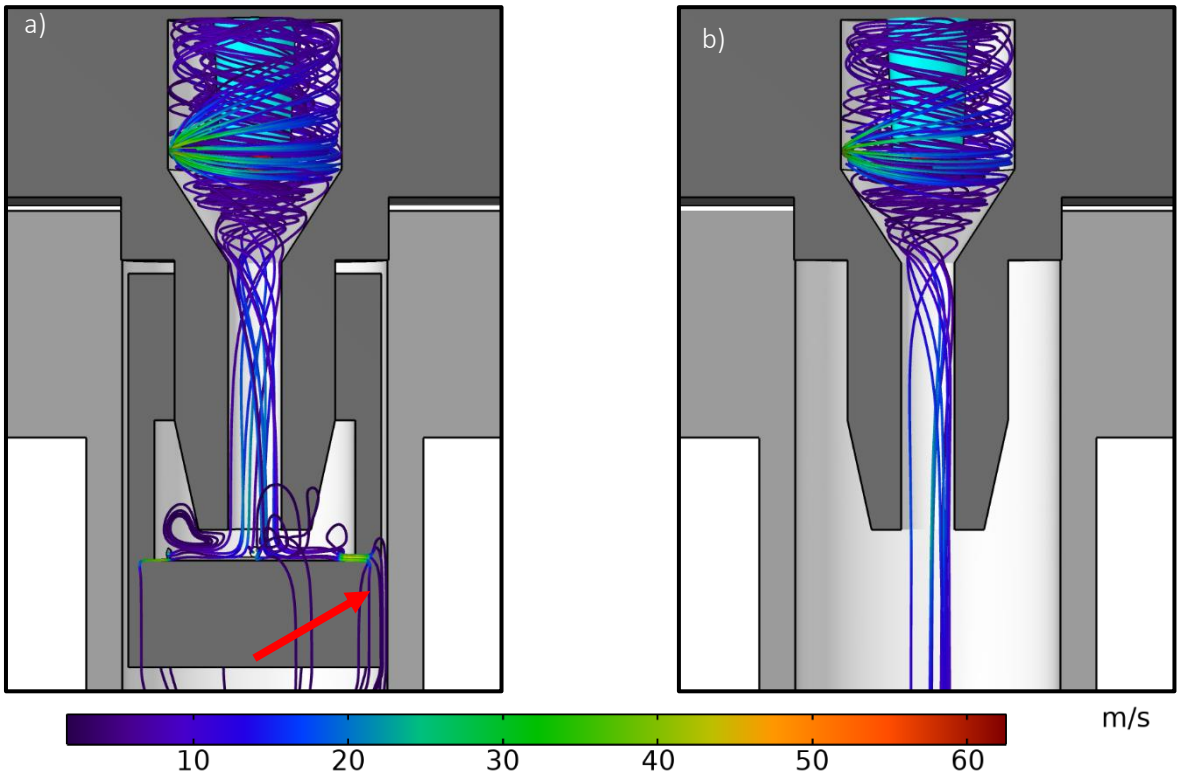

Figure 4.4: Calculated gas flow streamlines for the RGA with (a) and without (b) the effusion nozzle. The color scale denotes the gas velocity.

Up to this position, the flow behavior is the same for the RGA with and without the effusion nozzle. However, the flow in the lower part of the outlet is largely influenced by the nozzle; see Figure 4.4. More specifically, the gas flow is blocked and needs to flow through the small radial holes inside the nozzle to reach the exhaust. This is shown in more detail in Figure 4.5, presenting a close-up of the gas flow behavior inside the effusion nozzle. The gas spreads in all directions when it exits the reactor outlet, because the nozzle blocks the original flow path. The flow does not immediately exit the nozzle through the small radial holes, and some recirculation can occur (red arrow in the figure). Notice that Figure 4.5 does not consider the gas divider that was shown in the nozzle geometry in Figure 4.1. This adaptation was made, based on the experimental observations, because the gas divider partially melted due to the hot temperature of the arc. Once the gas passes through the small radial holes, it shortly accelerates to ~45 m/s, and immediately decelerates to velocities below 10 m/s when it has passed the small holes; see red arrow in Figure 4.4.

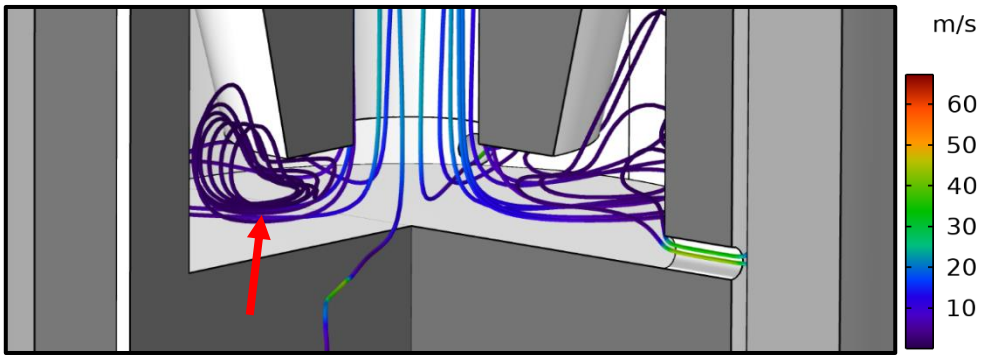

Figure 4.5: Close-up of the gas flow streamlines in the effusion nozzle.

4.4.2.2 Temperature profile

Figure 4.6 shows the temperature profile with and without the effusion nozzle, calculated based on the measured plasma power as input in the model. As observed in Figure 4.3, the plasma power for the 80/20 N_2/O_2 feed ratio was 159 W for the effusion nozzle and 199 W for the set-up without the nozzle. The resulting temperature profiles are compared in Figure 4.6(a) and 4.6(c). We observe two differences. First, we see very fast cooling in the effusion nozzle, cf. the fast transition of red to blue in Figure 4.6(a). This demonstrates that quenching occurs in the set-up with the effusion nozzle, and that it can possibly affect the chemistry (see further). Second, we see that the setup without nozzle exhibits a higher maximum gas temperature inside the plasma region (i.e., 5129 K vs 4615 K), which is of course due to the higher power causing more heating. Therefore, we also compare the temperature profile with and without the effusion nozzle calculated with the same plasma power of 159 W (Figure 4.6(a,b)). Although this simulation does not represent the experimental conditions, it removes the influence of the higher power (and thus temperature) for the RGA without the effusion nozzle, and allows us to see whether quenching affects the temperature inside the arc as well. The maximum temperature inside the arc is now the same, so it is clear that the effusion nozzle only causes very fast cooling when the gas arrives at the wall of it, and escapes through the small holes.

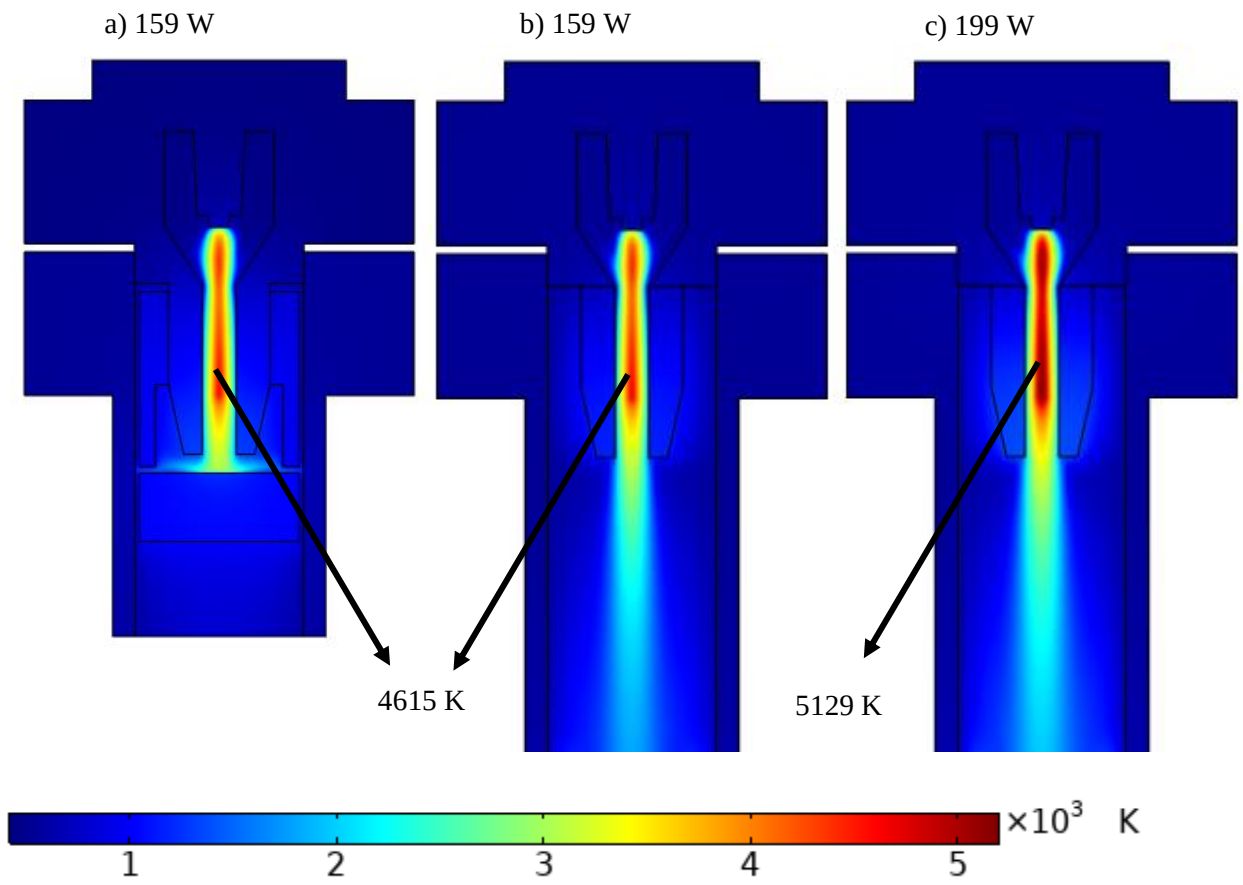

Figure 4.6: Calculated temperature profiles, with the effusion nozzle based on the measured plasma power of 159 W (a), without the effusion nozzle using the same power (b), and using the measured power of 199 W (c).

4.4.2.3 Gas flow trajectories

Because of the non-uniform temperature profile in the reactor outlet, with a maximum in the center and decreasing towards the walls (cf. Figure 4.6), the gas molecules will feel a different temperature when flowing through the reactor, depending on their exact trajectory.

As explained in section 4.3.2, we grouped all flow trajectories into 11 different groups, based on the maximum experienced temperature during their trajectory. Figure 4.7 presents a histogram with the fraction of gas in each group for the three different cases of Figure 4.6 (i.e., with the effusion nozzle and measured plasma power of 159 W, and without nozzle, for the same power, and for the measured power of 199 W).

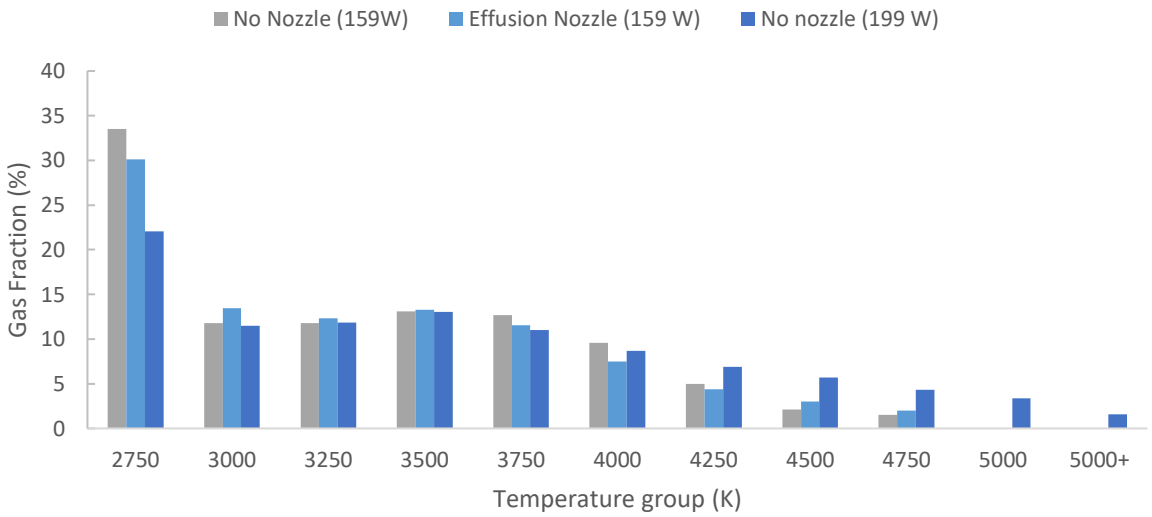

Figure 4.7: Calculated gas fraction in the 11 temperature groups, with and without the effusion nozzle, at the measured plasma power (159 W with, and 199 W without nozzle), as well as without nozzle, for the same power of 159 W. The values in the x-axis denote the maximum of each temperature group (except for the last group).

This figure shows that for all three cases the fraction of gas populating each temperature group roughly decreases as the temperature increases. This is attributed to the fact that the highest gas temperatures are found in the center of the plasma (cf. figure 4.6), which covers only a small volume of the reactor. Furthermore, due to the high gas temperatures, the gas density also decreases towards the hot center of the plasma. The fact that higher gas temperatures are achieved for the higher power case of 199 W, is also represented in this figure, as the distribution indicates that 5% of the gas experiences temperatures higher than 5000 K for the 199 W case, while both the 159 W cases (with and without effusion nozzle) don't reach these high temperatures. The figure also shows that for a reactor with and without nozzle (both 159 W cases), the difference in experienced temperatures are only minimal.

4.4.2.4 NO_x formation

The calculated NO_x concentrations for the 11 temperature groups, obtained from running the quasi-1D chemical kinetics model for each of these groups, are plotted in Figure 4.8. It is clear that the NO_x formation strongly depends on the temperature experienced by the molecules. For gas molecules that experience temperatures below 3250 K, barely any NO_x formation occurs. Hence, only the higher temperature groups, which are found closer to the center of the plasma, contribute to the overall NO_x concentration. In these zones both the gas temperature and electron temperature are very high, i.e. more than 4000 K and ±1 eV, respectively, yielding local high NO_x concentrations up to 10%. Note that these electron temperatures are locally high enough to induce significant NO_x formation. When we compare the NO_x formation with and without the effusion nozzle, we see that the reactor with the effusion produces slightly higher NO_x concentrations in the 3500-4750 K groups. This indicates that the

effusion nozzle clearly affects the chemistry (see next section). Finally, the figure shows that the higher plasma power (199 W instead of 159 W) does not really affect the NO_x formation within each group for the configurations without nozzle (see also next section).

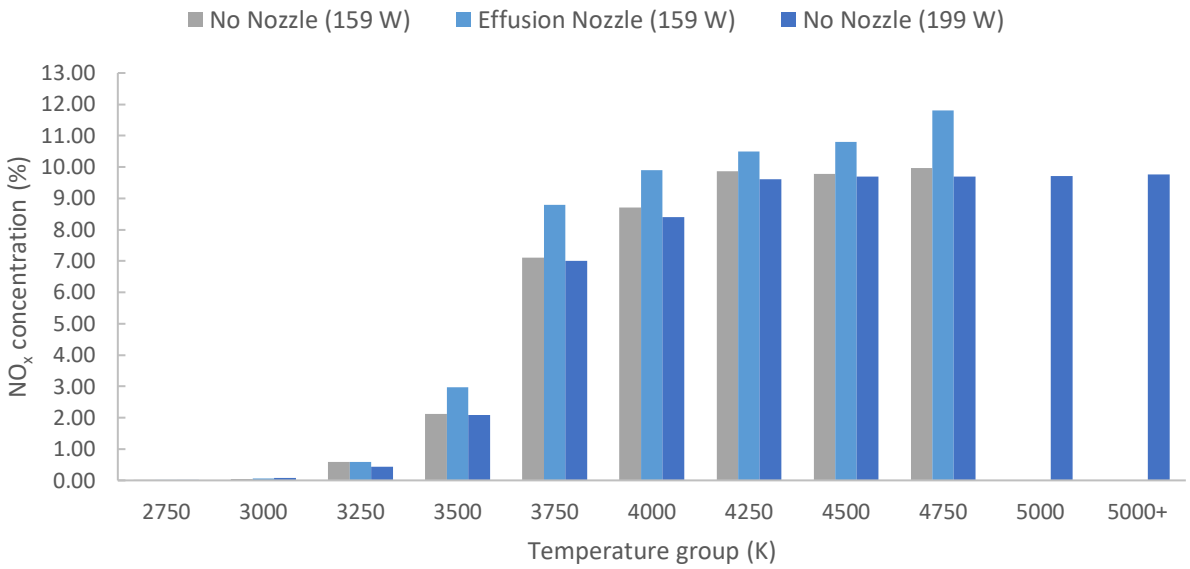

Figure 4.8: Calculated NO_x concentration in the 11 temperature groups, with and without the effusion nozzle, for the same cases as in Figure 4.7.

To calculate the overall NO_x concentration for each configuration, we multiplied the gas fraction from each temperature group (Figure 4.7) with its corresponding NO_x concentration (Figure 4.8), and took the summation over all 11 groups. The results are shown in Table 4.2, and they are compared with the measured NO_x concentrations.

Table 4.2: Summary of the experimental and calculated overall NO_x concentration, with and without the effusion nozzle. The experimental data are obviously only given at the measured plasma power, while the calculations without nozzle were performed both for the measured plasma power (199 W) and the same plasma power as with nozzle (159 W), for a theoretical comparison.

Plasma power	NO_x concentration (%) without nozzle		NO_x concentration (%) with effusion nozzle	
	Experimental	Model	Experimental	Model
159 W	/	2.76	3.88 ± 0.01	3.30
199 W	3.77± 0.02	3.95	/	/

First, to evaluate whether quenching affects the overall formed NO_x concentration, we compare in Table 4.2 the overall concentration with and without nozzle, calculated at the same plasma power (159 W). The concentration with the effusion nozzle is higher than without (3.30% vs. 2.76%). As both configurations show a similar gas fraction distribution over the different temperature groups (see Figure 4.7), the higher overall NO_x concentration with the effusion nozzle is clearly due to the larger NO_x formation in the higher temperature groups, especially in the group above 3500 K (see Figure 4.8). This is indeed due to the quenching, as explained in next section.

Second, Table 4.2 shows that the higher plasma power (199 W vs. 159 W) for the configuration without effusion nozzle results in a higher overall NO_x concentration (3.95% vs. 2.76%), due to the higher temperature, enhancing the chemistry.

Last but not least, we see that the model underestimates the overall NO_x concentration with the effusion nozzle. This is probably attributed to the heat source approximation made in the model, i.e., based on the plasma power minus power used for the chemistry, and not accounting for details, like local power density hot spots near the cathode and anode of the reactor. As a result, our simulations show lower temperatures in these regions than would be expected in reality, thus potentially leading to an underestimation of the achieved NO_x concentration. Indeed, the calculations are quite sensitive to small changes in temperature (due to the temperature dependence of all rate coefficients). We could "tune" our calculations until better quantitative agreement with the experiments is achieved, but we believe this would not bring more physical insight. We prefer to keep the modelling strategy entirely transparent, and we believe the agreement is reasonable enough to explain the observed improvement due to the effusion nozzle; see next section.

4.4.2.5 Reaction rate analysis

It is clear from Figure 4.8 that the higher temperature groups determine the NO_x formation. Hence, to understand why the effusion nozzle enhances the NO_x formation in these higher temperature groups, we plot in Figure 4.9 the change in NO_x concentration as a function of time for the gas molecules in the 3750 K temperature group, with and without the effusion nozzle. We only discuss the details for this temperature group, as a representative example, because the same behavior was observed for the other temperature groups.

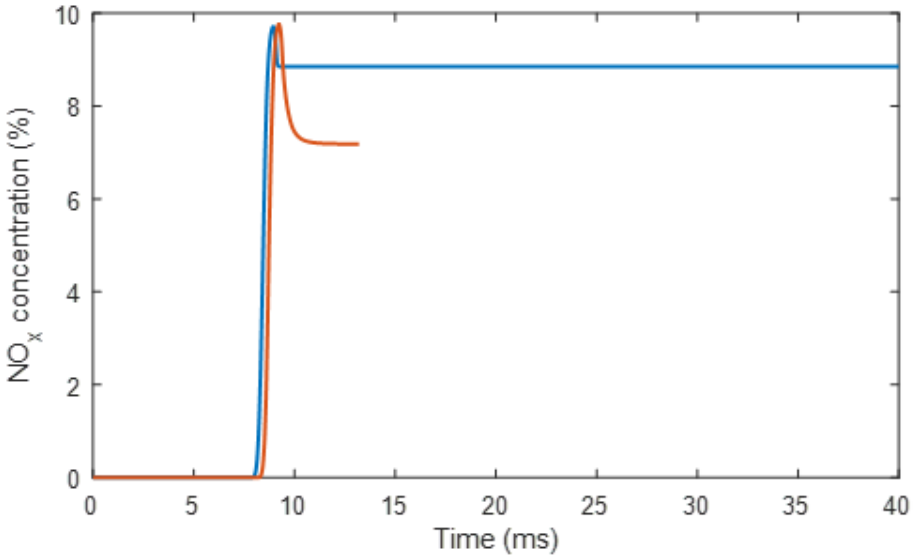

Figure 4.9: Calculated NO_x concentration in the 3750 K temperature group as a function of time, with (blue) and without (orange) the effusion nozzle.

First of all, the difference in time scale between both reactor configurations is because the effusion nozzle blocks the flow path of the gas when it exits the reactor outlet (see figure 4.5), such that the gas takes longer to reach the exhaust due to recirculation inside the effusion nozzle before it flows through the radial holes. Next, the small offset between both peaks in NO_x concentration is because the gas flow a little longer in the vortex of the main reactor body without the effusion nozzle. This small difference is however not significant and was not the result of changing anything in the reactor body geometry. Furthermore, the time spent in the plasma was the same for both configurations, and thus the offset has no effect on the model outcome.

It is clear from Figure 4.9 that both with and without the effusion nozzle, the NO_x concentration first rises to a similar value, due to the NO_x formation inside the plasma, but then the concentration drops when the gas leaves the plasma, until it stabilizes to a constant value, which is clearly higher with than without effusion nozzle.

Indeed, the NO_x concentration without the effusion nozzle drops more significantly, and this can be explained by reaction analysis of the most important formation and destruction reactions (see details in appendix section 8.5.2). From this analysis, it is clear that the drop in NO_x concentration is due to the backward reactions of the Zeldovich mechanism, which convert NO back into N_2 and O_2:

$$N + NO \rightarrow O + N_2 \qquad \text{(R4.1)}$$

$$O + NO \rightarrow N + O_2 \qquad \text{(R4.2)}$$

These reactions reduce the overall NO_x concentration if the rates of the destruction reactions (as written in reaction R4.1 and reaction R4.2) are higher than the formation rates of NO; i.e. the Zeldovich

mechanism (reverse of reaction (R4.1, R4.2)). Therefore, we plot the sum of both formation and destruction reactions (i.e., forward and backward reactions of the Zeldovich mechanism) as a function of time in Figure 4.10. We also plot the average gas temperature profile experienced by these molecules (in the 3750 K group) to explain the behavior seen in Figure 4.9. We are not interested in the time before the plasma, which is when the gas enters the RGA reactor and circulates upwards. Some chemistry can already occur, but it is negligible compared to the conversion in the plasma (cf. the log scale in Figure 4.10, and see also Figure 4.9: significant NO_x formation only starts around 7-8 ms).

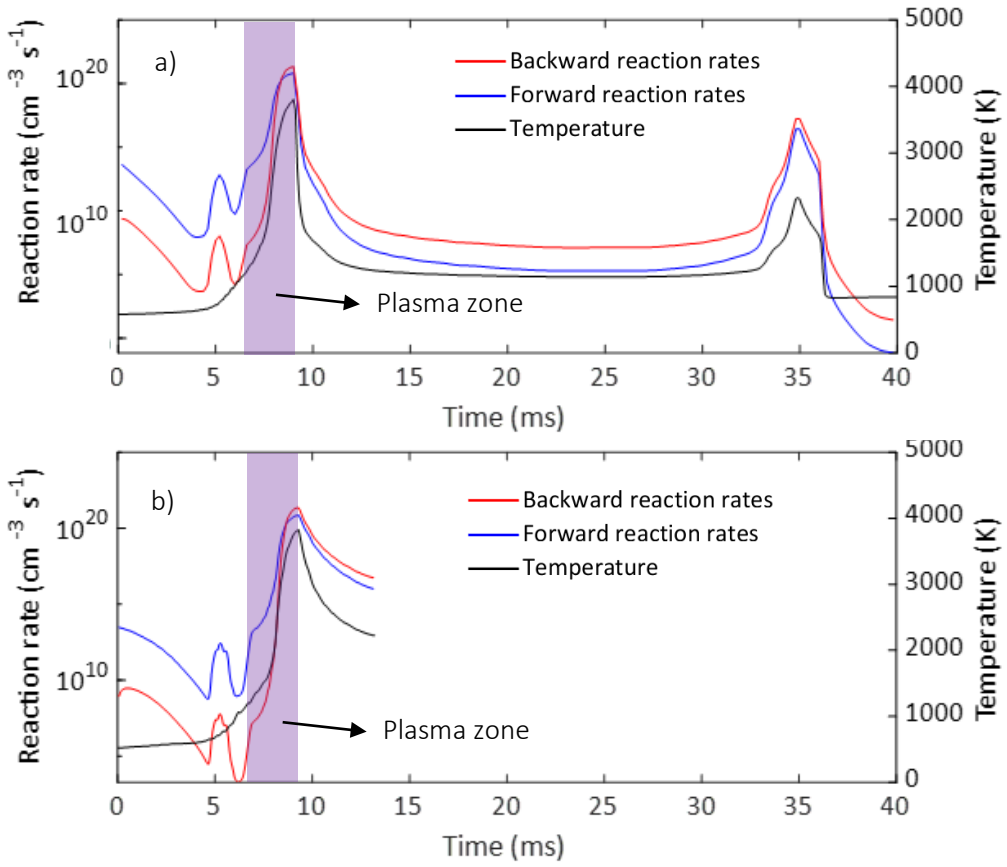

Figure 4.10: Calculated total forward and backward reaction rates of NO formation/destruction as a function of time, with (a) and without (b) the effusion nozzle, for the 3750 K temperature group. The black curve is the gas temperature, and the purple region is the plasma zone. Note that the gas takes longer to reach the exhaust in the case of the effusion nozzle (a), as it experiences some recirculation inside the effusion nozzle before it flows through the radial holes.

For the RGA with the effusion nozzle (Figure 4.10a), the reaction rates for both forward and backward reactions rise upon rising temperature when the gas passes through the plasma, but the total forward reaction rate is higher than the total backward reaction rate, thus resulting in net NO_x formation (see Figure 4.9). When the gas reaches the maximum temperature at the end of the plasma, the rates of both total forward and backward reactions also reach their maximum, and they are equal to each other,

hence leading to no further NO_x formation, explaining the maximum NO_x concentration in Figure 4.9 at this time point.

When the gas exits the plasma, the temperature drops quickly, because the effusion nozzle acts as heat sink (see Figure 4.6). Hence, both forward and backward reaction rates drop quickly, but the total backward reaction rate is slightly higher than the total forward reaction rate, explaining the drop in NO_x concentration of Figure 4.9. However, this drop is limited, because the quenching due to the effusion nozzle (fast drop in temperature) leads to such a fast drop in reaction rates that after 2 ms they are already low enough to not influence the NO_x concentration further, explaining why the latter remains constant until reaching the exhaust (see Figure 4.9).

Note that after this fast cooling, the gas recirculate in the effusion nozzle, characterized by lower temperatures, and the reaction rates stay low. However, as seen in Figure 4.10(a), the gas feel a second peak in temperature. This is due to the recirculation which brings the gas close again to the exit of the reactor outlet that is characterized by higher temperatures (see Figure 4.5). This higher temperature is accompanied by a rise in both forward and backward reaction rates, and the rate of the backward reactions is slightly higher than for the forward reactions. However, we do not observe a drop in NO_x concentration in Figure 4.9, because the reaction rates are too low, as the gas temperature is only ~2000 K at maximum. Nevertheless, this second temperature peak results in a (small) drop in NO concentration, while the NO_2 concentration slightly rises, which is shown in figure 11, displaying the NO and NO_2 concentration as a function of time during second temperature peak in figure 4.10(a). Indeed, this temperature is high enough for the conversion of NO to NO_2, but not high enough for the reverse reaction, as NO_2 is more stable than NO. However, as shown in figure 11, the effect is small (increase/decrease in concentration by only 0.08%), and it does not affect the total NO_x concentration. Finally, after this second temperature peak, the gas leaves the effusion nozzle, and the temperature drops further, to such low values that both forward and backward reactions are negligible and the NO_x concentration further remains constant.

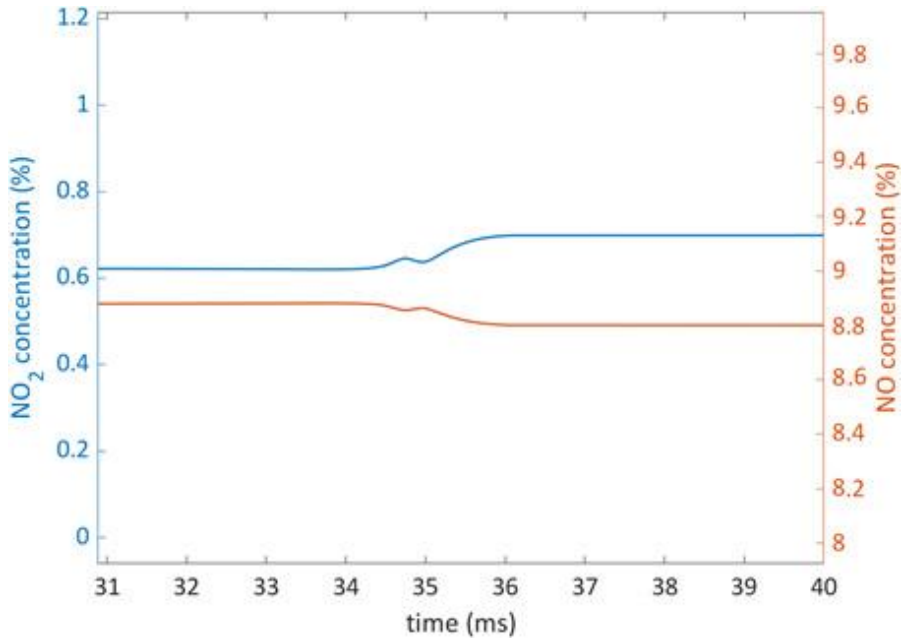

Figure 4.11: Calculated NO (orange) and NO_2 (blue) concentrations as a function of time, during the second temperature peak in figure 4.10(a).

For the RGA without the effusion nozzle (Figure 4.10b), we see the same behavior as with the nozzle, up to when the gas exits the plasma. At this stage, the gas cools down much more slowly than with the effusion nozzle (cf. Figure 4.10b vs 4.10a). Indeed, the effusion nozzle acts as heat sink; see Figure 4.6 above. During this cooling, the total backward reaction rate is again higher than the total forward reaction rate, but importantly, both rates drop more slowly than for the RGA with effusion nozzle, due to the slower temperature drop. As a result, the higher total backward reaction rate is more significant than for the RGA with effusion nozzle, which explains the larger drop in the NO_x concentration in Figure 4.9, and thus also the lower NO_x concentration in this temperature group in Figure 4.8.

In summary, the effusion nozzle acts as heat sink once the molecules collide with it, causing a fast drop in temperature which "freezes" the gas composition. Hence, the backward reactions of the Zeldovich mechanism, i.e., recombination of NO with N and O atoms into N_2 and O_2, which occur at somewhat higher rate than the forward reactions, become rapidly negligible. We showed this behavior in detail for the 3750 K group, but the same was observed for the other high temperature groups (that contribute to NO_x production). This explains the slightly higher NO_x concentrations observed experimentally with the effusion nozzle. In addition, because the effusion nozzle allows ignition and sustainment of a stable plasma at slightly lower power, the (same or slightly higher) NO_x formation occurs at lower plasma power, explaining the lower energy cost, observed experimentally.

Knowing that the effusion nozzle enhances the NO_x production by removing heat from the gas and quenching the back reactions, its shape could be subjected to reactor design optimization to maximize

this effect. A possible approach would be to increase the contact area between the metal and the gas by adding more radial holes to the nozzle and making these holes smaller. This way the surface-to-volume ratio of the nozzle increases, increasing the number of collisions between gas molecules and the nozzle wall and thus increasing the heat transfer. Another approach would aim to change the material of the nozzle, to maximize the heat conductivity and heat capacity of the metal, so that more heat can be absorbed by the nozzle.

4.5 CONCLUSION

Plasma-based NO_x production is gaining increasing interest as a sustainable N_2 fixation process, but the energy cost is not yet competitive with the combined Haber-Bosch and Ostwald process [48]. Hence, efforts are needed to improve the performance of plasma-based NO_x production. We present here a novel design, called "effusion nozzle", to improve the performance of an RGA plasma reactor for NO_x production. My fellow PhD student, H. Ahmadi Eshtehardi, performed experiments in a wide range of applied power, gas flow rates and N_2/O_2 ratios, and his results indicate an enhancement in NO_x concentration by 8%, as well as a reduction in energy cost by 22.5%. In absolute terms, we obtain NO_x concentrations up to 5.9%, at an energy cost down to 2.1 MJ/mol, which to our knowledge are the best values obtained up to now in atmospheric pressure plasmas. Note that he has also tested more conventional cooling options of the outflowing gas after the plasma reactor, but they did not improve the performance. The reason is that the cooling happened too late, after the recombination reactions had occurred already, as could also be explained by our modeling work. Hence, the strength of our effusion nozzle is the immediate and fast cooling right at the end of the plasma, yielding a temperature drop of almost 3500 K, and therefore avoiding the recombination reactions. This makes it superior to other, more conventional cooling options.

To understand why the effusion nozzle yields improved performance, we developed a modelling strategy, combining a 3D CFD model with quasi-1D plasma chemical kinetics simulations. Our models can explain the improved performance of the effusion nozzle observed experimentally, even though we do not reach quantitative agreement with the measured NO_x concentrations. Indeed, our models reveal that fast cooling (quenching) occurs as soon as the gas molecules collide with the effusion nozzle, which acts as very efficient heat sink. This fast drop in temperature limits the recombination of NO with N and O atoms into N_2 and O_2, i.e., the backward reactions of the so-called Zeldovich mechanism, and thus it limits the drop in NO_x concentration after the plasma, which is much more pronounced without the effusion nozzle, due to the slow drop in temperature after the plasma. Hence, this explains the higher NO_x concentrations observed experimentally in case of the effusion nozzle. Furthermore, because the effusion nozzle allows ignition and sustainment of the plasma at somewhat lower power, still producing

the same (or even slightly higher) NO_x concentrations, this also explains the lower energy cost which was observed experimentally.

The insights obtained by this detailed analysis are not only useful to explain the better performance of the effusion nozzle, but can also help us in further improving plasma-based NO_x production, not limited to this RGA or other GA plasmas, but also other plasma types. First of all, our simulations clearly reveal that the higher temperature groups mainly contribute to NO_x formation, so a higher plasma power may cause a further rise in NO_x production, but only if the NO_x production rises faster than the power, because otherwise it would negatively affect the energy cost. Second, and even more important, the obtained insights on the effect of quenching on the detailed chemistry of the Zeldovich mechanism are very useful for designing new nozzles or other quenching options (like an additional gas or liquid flow), that can lead to fast cooling of the gas after leaving the plasma, and thus avoiding the back reactions.

5 EFFECT OF N_2 ON CO_2-CH_4 CONVERSION IN A GLIDING ARC PLASMATRON: CAN THIS MAJOR COMPONENT IN INDUSTRIAL EMISSIONS IMPROVE THE ENERGY EFFICIENCY?

The results presented in this chapter were published in:

"Effect of N_2 on CO_2-CH_4 conversion in a gliding arc plasmatron: Can this major component in industrial emissions improve the energy efficiency?" Van Alphen S., Slaets J., Ceulemans S., Aghaei M., Snyders R., Bogaerts A., J. CO2 Utiliz. 54 101767 (2021)

DOI: 10.1016/j.jcou.2021.101767

5.1 INTRODUCTION

While last chapter showed a plasma process being optimized purely from a reactor design standpoint, i.e. by attaching an effusion nozzle to the reactor, this is not the only optimization route. Another way of increasing the performance of plasma-based gas conversion applications is to optimize the gas mixture from a chemical standpoint, i.e. using admixtures to enhance beneficial chemical pathways or suppress undesired chemical pathways. Some studies explored the addition of N_2 to CO_2 or CO_2-CH_4 plasmas, either to create a more stable plasma or to mimic realistic emissions from industrial plants.[90,95–98] Vice versa, CH_4 addition to CO_2/N_2 plasma has also been shown to have beneficial effects, as CH_4 acts as a chemical oxygen scavenger, suppressing undesired NO_x and N_2O formation.[99]

Most industrial gas emissions contain significant amounts of N_2, and separation is financially costly.[100] The addition of N_2 thus represents a more realistic situation in view of the industrial application of plasma-based DRM.[101] For this purpose, more insight is needed in the effect of N_2 on the plasma chemistry and the performance of plasma-based DRM, and its content in the feed gas needs to be optimized. While adding N_2 inevitably leads to electric power being wasted into excitation, ionization and dissociation of N_2, it has already been demonstrated for pure CO_2 conversion that N_2 assists the CO_2 splitting process,[95,96,98] raising the question if N_2 could also be a useful admixture for DRM.

In the present chapter we investigate the effect of N_2 on plasma-based DRM and we optimize the N_2 content in the gas feed to achieve maximal performance for a gliding arc plasmatron (GAP) reactor. This novel type of gliding arc reactor was developed at Drexel University by Nunnally et al.[27] to overcome the

non-uniform gas treatment of a classical two-dimensional (2D) gliding arc. The GAP has already delivered promising results for pure CO_2 splitting,[26] as well as for DRM in CO_2-CH_4[80] and CO_2-CH_4-O_2[90] mixtures. In the latter case, N_2 was also present, but in large amounts (60-80 %) to create a more stable plasma, and the focus was on the effect of O_2 addition, while the effect of N_2 on the chemistry and performance was not investigated. N_2 addition to pure CO_2 plasma showed promising results,[95] but the effect of N_2 addition for DRM in the GAP has not been studied yet. Therefore, together with S. Ceulemans and J. Slaets from our group, we focus here on optimizing the performance of the GAP for DRM in a wide range of N_2 fractions. We present an in-depth study, both by experiments and computational models. Experimentally S. Ceulemans and J. Slaets evaluated the energy cost, energy efficiency, the conversion of CO_2 and CH_4, and the product yields and selectivities in the GAP for N_2 fractions ranging from 80% to 0%, in which the CO_2:CH_4 ratio is kept at 1:1, as this was found to be the optimal ratio in our previous study.[90] In addition, I used the computational modelling approach similar to previous chapters (section 3.2, page 52 and section 4.3, page 79, and explained in detail in section 2.3, page 43) to simulate the gas flow, plasma dynamics and plasma chemistry for the exact same conditions as the experiments. This allows us to explain the experimental results and provide insight in both the physical and chemical effects of varying the N_2 fraction in the plasma.

5.2 EXPERIMENTAL DETAILS

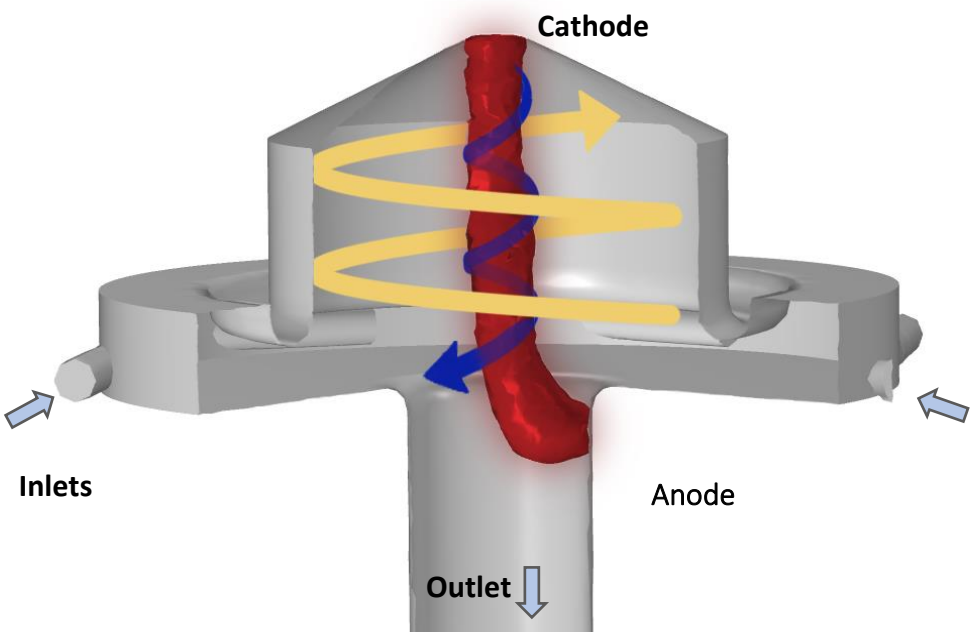

Figure 5.1: Schematic picture of the GAP reactor, with illustration of the outer and inner vortex gas flows (yellow and blue arrows), and the plasma arc (red). The reactor body is at cathode potential while the outlet functions as anode. The arc is formed between the top of the cathode (top of the reactor body) and anode (outlet). The tangential gas inlets and the outlet of the reactor are indicated with arrows.

The experimental setup consists of three main parts, the reactor, the electric circuit, and the gas analysis system. The gas flow of the different inlet gasses (i.e. CO_2, CH_4 and N_2) is regulated by mass flow controllers (MFC) (Bronkhorst), that are controlled by a computer. These gasses mix in the inlet tube leading to the reactor and enter the reactor through six tangential inlets, of which two are depicted in figure 5.1. This creates an initial vortex flow in the reactor body (at cathode potential) that moves upwards along the reactor walls (yellow arrow in figure 5.1). At the top of the reactor the vortex reverses and turns inwards (blue arrow in figure 5.1) moving the gas downwards to the outlet (at anode potential), after which the gas is transported to a gas chromatograph (GC) (Thermo Scientific trace 1310 GC) with a thermal conductivity detector for gas analysis. The plasma arc first ignites at the shortest distance between the cathode and anode, but is carried by the gas flow to the center of the reactor, and at steady state it forms a long arc between the top of the reactor (cathode) and outlet (anode), as depicted in red in figure 5.1. In the ideal case, the gas in the inner vortex all moves through the arc, although in reality the arc is typically not wide enough to cover the whole inner vortex flow. The outer gas vortex causes thermal insulation between the hot plasma arc and reactor walls.

The power supply (Advanced Plasma Solutions, PA, USA) is connected to the electrodes. The electrical current is controlled and held at 0.3 A, while the voltage is regulated by the power supply itself, to deliver a certain power. The plasma power is measured using an oscilloscope (Tektronix TDS2012C), by integrating the product of voltage and current over a certain period of time. The voltage is measured using a high voltage probe (Testec) connected to the cathode. The current is measured over a resistor (3 Ohm) that is placed in the grounding wire. The oscilloscope registers this as a voltage, which is converted to a current using Ohm's law.

Before each experiment the setup is flushed for 10 min with the gas mixture, after which the plasma is ignited, and another 10 min is given to stabilize. The exhaust gasses are stored in sample loops, each with a 100 µL volume. After the filling process, the content of the sample loops is injected in the set of three columns with helium as carrier gas. For statistical analysis, every experiment is repeated three times, with four sample loops analyzed for each repeat, thus creating 12 data points. For every gas mixture a blank measurement without plasma is performed, needed to calculate the CO_2 and CH_4 conversion.

The experiments were performed by S. Ceulemans and J. Slaets during, respectively, their bachelor's and master's thesis at PLASMANT. They measured the CO_2 and CH_4 conversion, as well as the H_2 and CO yield, the energy cost and energy efficiency of the conversion process. The formulas to calculate these properties are explained in detail in the appendix (section 8.6).

5.3 COMPUTATIONAL DETAILS

To explain both the physical and chemical effects of the addition of N_2, we apply a similar modelling approach that we used to describe the RGA in last chapters (see section 3.2, page 52 and section 4.3, page 79) to the GAP reactor in figure 5.1. Using a combination of a 3D CDF model, a 3D thermal plasma arc model and a quasi-1D chemical kinetics model, we will simulate the gas flow, the arc dynamics, and the plasma chemistry in the same $N_2/CO_2/CH_4$ mixtures as in the experiment. Note that, unlike the description of the RGA in chapter 3, we don't apply a 2D non-thermal model for the GAP. A 2D non-thermal model for the GAP has already been developed in our group for CO_2 conversion,[92] showing that the arc in the GAP is a quasi-thermal plasma, such that the temperature can be calculated without a non-thermal plasma model, as will be discussed more in detail in section 5.3.2.

In following sections we briefly discuss the models that are solved.

5.3.1 CFD model

We describe the behavior of the gas flow in the reactor by a turbulent gas flow model. Given the complex dual vortex flow in the reactor, some turbulence is expected in the flow. The gas flow velocity is described through solving the RANS equations for turbulent flow using the SST model :

$$\rho_g \frac{\partial \vec{u}}{\partial t} + \rho(\vec{u} \cdot \nabla)\vec{u} = \nabla \cdot \left[-p\vec{I} + (\mu + \mu_T)(\nabla\vec{u} + \nabla(\vec{u})^T) - \frac{2}{3}(\mu + \mu_T)(\nabla \cdot \vec{u})\vec{I} - \frac{2}{3}\rho_g k_T \vec{I}\right] + \vec{F} \quad (5.1)$$

$$\rho \frac{\partial \vec{u}}{\partial t} + \nabla \cdot (\rho_g \vec{u}) = 0 \quad (5.2)$$

Where ρ_g stands for the gas density, $\overrightarrow{u}$is the gas flow velocity vector, superscript T stands for transposition, p is the gas pressure, μ is the dynamic viscosity and μ_T the turbulent viscosity of the fluid, k_T is the turbulent kinetic energy, $\vec{I}$ is the unity tensor and $\vec{F}$ is the body force vector.

Solving these equation yields the flow velocity $\overrightarrow{u_g}$, which is used as input for solving the thermal balance equation:

$$\rho_g C_p \frac{\partial T_g}{\partial t} + \rho_g C_p \vec{u} \cdot \nabla T_g + \nabla \cdot \vec{q} = Q_{heat} \quad (5.3)$$

Where ρ_g stands for the gas density, C_p for the isobaric heat capacity, T_g is the gas temperature, $\vec{u}$ the gas velocity, Q_{heat} the heat source term representing the heating from the plasma, and $\vec{q}$ the conductive heat flux vector, which is calculated by:

$$\vec{q} = -(k_g + k_{g,T})\nabla T_g \quad (5.4)$$

Where k_g is the thermal conductivity of the gas and $k_{g,T}$ is the turbulent thermal conductivity of the gas.

5.3.2 Thermal plasma arc model

Similar to chapter 3 (section 3.2.3, page 54), the arc formation between the cathode and anode, as well as the arc shape and arc dynamics is simulated using a 3D thermal arc model. Our group already developed non-equilibrium 2D models for pure CO_2 conversion,[73,74,92] but due to the complexity of the combined chemistry of the three input gasses CO_2-CH_4-N_2 , resulting in 15987 reactions, a thermal plasma arc model is chosen instead of a non-equilibrium plasma fluid model, due to its shorter calculation times (i.e. several hours instead of several days) and because it can easily be solved in 3D. This way the model can be solved for all gas feed ratios within a reasonable time. To simulate the formation and movement of the arc in the dual vortex gas flow, we model the reactor as a part of the electric circuit, similar to previous chapters, and as shown in figure 5.2. The cathode is connected to a ballast resistor, which in turn is connected to a voltage source supplying 3 kV, while the anode is grounded. The current is limited by a ballast 200 Ω resistor (Rb), and a 10 pF capacitor (Cb) forms an RC filtering circuit. The total current for the system is varied by changing the value for the ballast resistor.

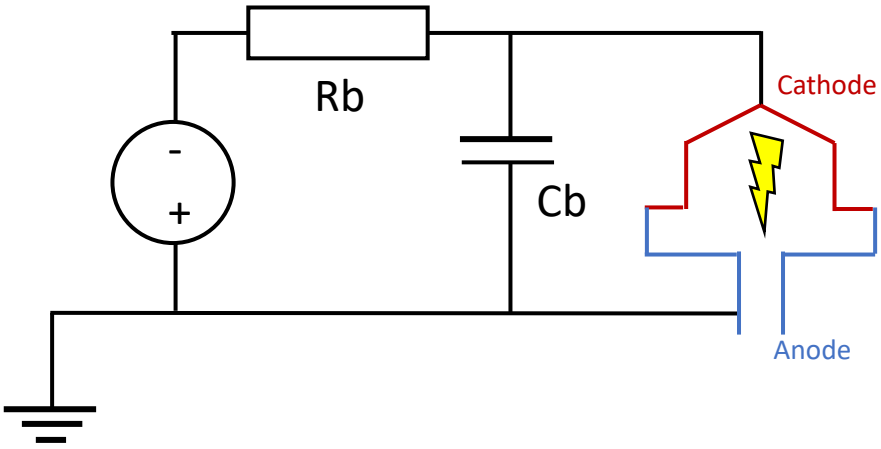

Figure 5.2: Representative electrical scheme of the GAP reactor in the thermal plasma arc model.

Similar to the description of the thermal arc model in the RGA in section 3.2.3 (on page 54), the movement of the arc in the dual vortex gas flow is simulated by solving a current conservation equation based on Ohm's law, using the electric potential (V) and the electric conductivity of the gas mixture (σ) as dependent variables.

$$\nabla \cdot \vec{J} = 0 \tag{5.5}$$

$$\vec{J} = \sigma \vec{E} \tag{5.6}$$

$$\vec{E} = -\nabla V \tag{5.7}$$

Here $\vec{J}$ is the current density and $\vec{E}$ is the electric field.

The electrical conductivity of the gas mixtures is calculated using a 0D chemical kinetic model (see 2.2 on page 41). We run the model for a range of temperatures and calculate the plasma conductivity through equation 5.8 and 5.9 for each condition, creating a database of lookup tables for the 3D plasma arc model.

$$\sigma = \frac{\mu}{n_{tot}} \cdot n_e \cdot e \tag{5.8}$$

$$\mu = -\frac{\sqrt{\frac{2e}{m_e}}}{3} \int_0^\infty \frac{\varepsilon}{Q} \frac{\partial f}{\partial \varepsilon} d\varepsilon \tag{5.9}$$

In which n_{tot} is the total density of all plasma species, e is the elementary charge, m_e the electron mass, ε the electron energy, and f the electron energy distribution function, calculated by the Boltzmann solver of the 0D model (see section 2.2 on page 41)

Using the thermal plasma arc model, we can determine the shape and volume of the arc (V_{plasma}) to calculate the plasma heat source term Q_{heat} of the thermal balance equation through:

$$Q_{heat} = \frac{P_{heat}}{V_{plasma}} \tag{5.10}$$

As described in section 2.1.2 (on page 37), P_{heat} can be calculated using the experimental plasma power and energy efficiency, by assuming that all power that did not go into chemistry is lost to gas heating.

$$P_{heat} = P_{plasma}(100\% - EE) \tag{5.11}$$

This is a reasonable assumption, as just like the RGA the arc in the GAP reactor is a quasi-thermal plasma,[80,81,90] meaning that we can assume that all plasma power that didn't go into chemical reaction goes into gas heating.

5.3.3 Gas properties of CO_2-CH_4-N_2 gas mixture

The 3D CFD and thermal plasma models require several physical properties of the CO_2-CH_4-N_2 mixture as input for the calculations, i.e. heat capacity, ratio of specific heat, dynamic viscosity and thermal conductivity. As these thermodynamic and transport properties are not available in literature for the CO_2-CH_4-N_2 mixtures, they are calculated based on the gas properties of a CO_2-CH_4 mixture, taken from Wu et al.[102], Niu et al.,[103] and the properties of N_2 gas, taken from Tanaka et al.[104]

The heat capacity at constant pressure (C_p) of the mixture is calculated using:

$$C_p = m_{CO_2} C_{p\,CO_2} + m_{CH_4} C_{p\,CH_4} + m_{N_2} C_{p\,N_2} \tag{5.12}$$

In which m_{CO_2}, m_{CH_4} and m_{N_2} are the mass fractions of CO_2, CH_4 and N_2 and $C_{p\,CO_2}$, $C_{p\,CH_4}$, $C_{p\,N_2}$ the heat capacity at constant pressure of pure CO_2, CH_4 and N_2.

The ratio of specific heat (γ) is calculated as follows:

$$\gamma = \frac{C_p}{C_v} \tag{5.13}$$

In which C_v is the heat capacity at constant volume, which equals $C_p - R$, with R the gas constant in J/mol*K.

The dynamic viscosity (μ) is calculated following the method of Wilke[105]:

$$\mu = \frac{n_{CO_2}\mu_{CO_2}}{n_{CO_2} + n_{CH_4}\varphi_{CO_2\cdot CH_4} + n_{N_2}\varphi_{CO_2\cdot N_2}} + \frac{n_{CH_4}\mu_{CH_4}}{n_{CH_4} + n_{CO_2}\varphi_{CH_4\cdot CO_2} + n_{N_2}\varphi_{CH_4\cdot N_2}} + \frac{n_{N_2}\mu_{N_2}}{n_{N_2} + n_{CO_2}\varphi_{N_2\cdot CO_2} + n_{CH_4}\varphi_{N_2\cdot CH_4}} \tag{5.14}$$

Where μ_{CO_2}, μ_{CH_4} and μ_{N_2} are the pure component viscosities of CO_2, CH_4 and N_2, and n_{CO_2}, n_{CH_4} and n_{N_2} the molar fractions of CO_2, CH_4 and N_2.

$\varphi_{CO_2\cdot CH_4}$ is a placeholder for the following term: $\frac{\left[1+(\mu_{CO_2}/\mu_{CH_4})^{1/2}(M_{CH_4}/M_{CO_2})^{1/4}\right]^2}{\left[8(1+M_{CO_2}/M_{CH_4})\right]^{1/2}}$

Using the molar masses of the pure components M_{CO_2}, M_{CH_4} and M_{N_2}

$\varphi_{CO_2\cdot N_2}, \varphi_{CH_4\cdot CO_2}, \varphi_{CH_4\cdot N_2}, \varphi_{N_2\cdot CO_2}$ and $\varphi_{N_2\cdot CH_4}$ are calculated similarly.

The thermal conductivity (k) is calculated using the method by Mason and Saxena.[105] As this property is used in the plasma model, the method is also applied for the high temperature regimes in the plasma. Literature reports errors around 10% for the method even at high temperature[106], which we believe is reasonable for the purpose of this study.

$$k = \frac{n_{CO_2}k_{CO_2}}{n_{CO_2} + n_{CH_4}A_{CO_2\cdot CH_4} + n_{N_2}A_{CO_2\cdot N_2}} + \frac{n_{CH_4}k_{CH_4}}{n_{CH_4} + n_{CO_2}A_{CH_4\cdot CO_2} + n_{N_2}A_{CH_4\cdot N_2}} + \frac{n_{N_2}\mu_{N_2}}{n_{N_2} + n_{CO_2}A_{N_2\cdot CO_2} + n_{CH_4}A_{N_2\cdot CH_4}} \tag{5.15}$$

Where k_{CO_2}, k_{CH_4} and k_{N_2} are the pure component thermal conductivities of CO_2, CH_4 and N_2, and n_{CO_2}, n_{CH_4} and n_{N_2} the molar fractions of CO_2, CH_4 and N_2.

$A_{CO_2\cdot CH_4}$ is a placeholder for the following term: $\frac{\left[1+(k_{CO_2}/k_{CH_4})^{1/2}(/M_{CO_2}/M_{CH_4})^{1/4}\right]^2}{\left[8(1+M_{CO_2}/M_{CH_4})\right]^{1/2}}$

$A_{CO_2 \cdot N_2}, A_{CH_4 \cdot CO_2}, A_{CH_4 \cdot N_2}, A_{N_2 \cdot CO_2}$ and $A_{N_2 \cdot CH_4}$ are calculated similarly.

5.3.4 Quasi-1D chemical kinetics model

Similar to previous chapters and as explained in detail in section 2.3 (on page 43), we solve a quasi-1D chemical kinetics model to reveal chemical reaction pathways of the DRM chemistry and calculate the CO_2 and CH_4 conversions along the streamlines calculated by the 3D CFD model, using the species balance equation :

$$\frac{dn_i}{dt} = \sum_j \left[(a_{ij}^R - a_{ij}^L) k_j \prod_l n_l^L \right] \tag{5.16}$$

In which n_i is the density of species i and a_{ij}^R and a_{ij}^L are the stoichiometric coefficients of species i on the right-hand and left-hand side of the reaction j, respectively. n_l is the density of the reacting species l. k_j is the reaction rate coefficient of reaction j.

Through equation 5.17 and 5.18 we integrate 10,000 streamlines, equally spaced over the surface of the inlet boundary, and record the temperature and power density, as calculated by the 3D CFD model, that is experienced along the trajectory.

$$q = \int_0^{t_{outlet}} v \, dt \tag{5.17}$$

$$v = \sqrt{{v_x}^2 + {v_y}^2 + {v_z}^2} \tag{5.18}$$

Unlike previous chapters in the RGA, we don't group the streamlines based on temperature, but based on their position in the GAP reactor. This way the reactor is divided into four different zones, as illustrated in figure 5.3, i.e. the steady part of the arc within the reactor body (yellow), the rotating part, gliding over the anode (outlet) wall (red), the hot afterglow, where no power is applied but the gas is still hot enough for thermal CO_2 and CH_4 conversion (blue), and the rest of the reactor, where the conversion is negligible, i.e. < 1% (grey). For each individual zone, we calculate the average trajectory and record the temperature and power density along this average trajectory, which are then used as input for the quasi-1D plasma chemistry model. The overall conversion is then calculated as the weighted average of the four simulations, in which the weight is based on the mass flow in each zone in the reactor. These weights are shown in table 5.1.

Table 5.1: Fraction of the gas flowing through each of the four zones as calculated by the streamline integration.

Zone	Calculated weight
Steady arc (yellow)	15 %
Rotating arc (red)	23 %
Hot afterglow (blue)	0 - 11.78 % (depending on gas mixture)
Rest of the reactor (grey)	50 – 61% (depending on gas mixture)

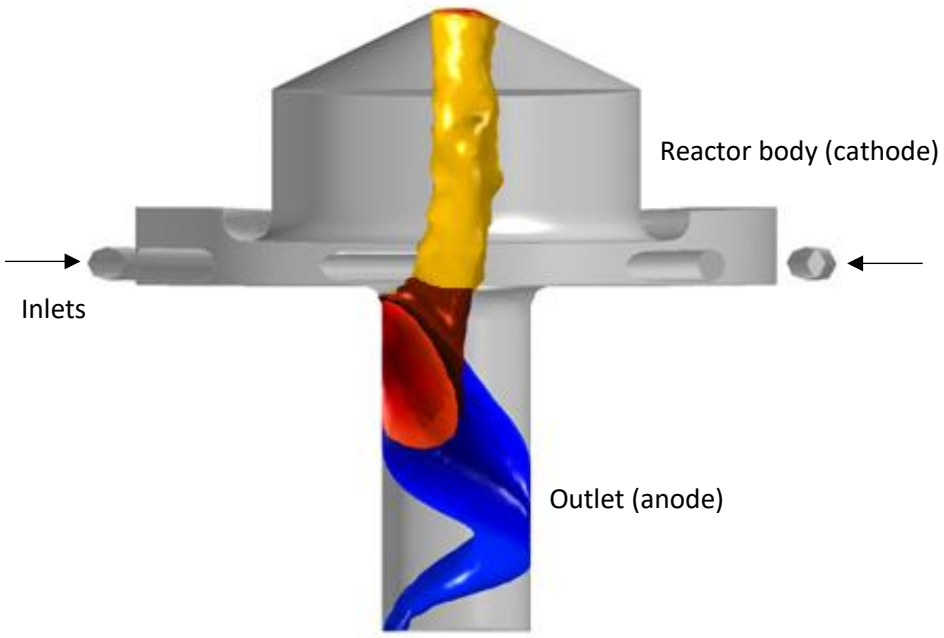

Figure 5.3: Schematic representation of the four zones of the GAP reactor where the 0D chemical kinetics model is applied: the steady part of the arc within the reactor body (yellow), the rotating part of the arc near the anode (outlet) (red), the hot afterglow (blue) and the rest of the reactor (grey).

The species taken into account in the quasi-1D simulation, which can be formed from the gas mixture of N_2, CO_2, CH_4, are listed in Table 5.2. This chemistry set was developed by J. Slaets in our group and includes 15,987 reactions, i.e., various electron impact reactions, electron-ion recombination reactions, ion-ion, ion-neutral, and neutral-neutral reactions, as well as vibrational-translational and vibrational-vibrational relaxation reactions.

The reactions (and corresponding rate coefficients) between CH_4 and CO_2 derived species (hence including also those between CH_4 and O_2 derived species) were taken from Cleiren et al.[80], the reactions between CO_2 and N_2 derived species (including also those between O_2 and N_2 derived species) were adopted from Ramakers et al.[95], and those between CH_4 and N_2 from Snoeckx et al.[107]

Note that the number of species and chemical reactions in this model is much larger than what is actually needed for the purpose of this study, as we are in first instance interested in the conversion of CH_4 and CO_2, and the effect of N_2 on these conversions, but not in the formation of all possible reaction products. However, this chemistry set was developed to be as complete as possible, because it is not *a priori* known which species and chemical reactions are important in the conversion process. For instance, the model contains a large number of (electronically and vibrationally) excited levels, which can be important for energy-efficient CO_2 conversion.[82]

Table 5.2: Species included in the chemical kinetics model, sorted by type.

Molecules	Ions	Radicals	Excited species
	electrons		
C_3H_8, C_3H_6		C_3H_7, C_3H_5	
C_2H_6, C_2H_4, C_2H_2	$C_2H_6^+$, $C_2H_5^+$, $C_2H_4^+$, $C_2H_3^+$, $C_2H_2^+$, C_2H^+	C_2H_5, C_2H_3, C_2H	
CH_4	CH_5^+, CH_4^+, CH_3^+, CH_2^+, CH^+	CH_3, CH_2, CH	
H_2	H_2^+		$H_2(V_1\text{-}V_{14})$
	H^+, H^-, H_3^+	H	
N_2	N_2^+		$N_2(V_1\text{-}V_{24})$, $N_2(A^3\Sigma_u^+)$, $N_2(B^3\Pi_g)$, $N_2(a^1\Sigma_u^-)$, $N_2(C^3\Pi_u)$
	N^+, N_3^+, N_4^+	N	N(2D), N(2P)
N_2O	NO^+, N_2O^+, NO_2^+, NO^-, N_2O^-, NO_2^-, NO_3^-	NO, NO_2, NO_3	
		CN, NCN	
		NCO	
CO_2	CO_2^+		$CO_2(V_a\text{-}V_d)$, $CO_2(V_1\text{-}V_{21})$, $CO_2(E_1)$
CO	CO^+, CO_3^-, CO_4^-		$CO(V_1\text{-}V_{10})$, $CO(E_1\text{-}E_4)$
O_2	O^-, O_2^-	O	$O_2(V_1\text{-}V_4)$, $O_2(E_1\text{-}E_2)$
CH_2O, CH_3OH		CHO, CH_2OH	
CH_3OOH		CH_3O, CH_3O_2	
		C_2HO, CH_3CO	
CH_3CHO, CH_2CO			
H_2O, H_2O_2	H_2O^+, H_3O^+, OH^-, OH^+	HO_2, OH	
NH_3		NH, NH_2, N_2H_3	
N_2H_4			
HNO			

5.4 RESULTS AND DISCUSSIONS

5.4.1 Absolute and effective CO_2 and CH4 conversion

To analyze the effect of N_2 on the performance of DRM, five different N_2 fractions were evaluated (i.e. 0, 20, 40, 60 and 80 %), while the CO_2:CH_4 ratio was kept constant at 1:1. The total flow rate and electrical current were kept at 10 L min^{-1} and 0.3 A. To quantify the CO_2 and CH_4 conversion, we define both the absolute and the effective conversion. The absolute conversion, or simply "conversion", allows easy comparison between different mixtures, while the effective conversion takes into account the dilution of CO_2 and CH_4 in N_2. It is obtained by multiplying the absolute conversion with the CO_2 or CH_4 fraction in the mixture.

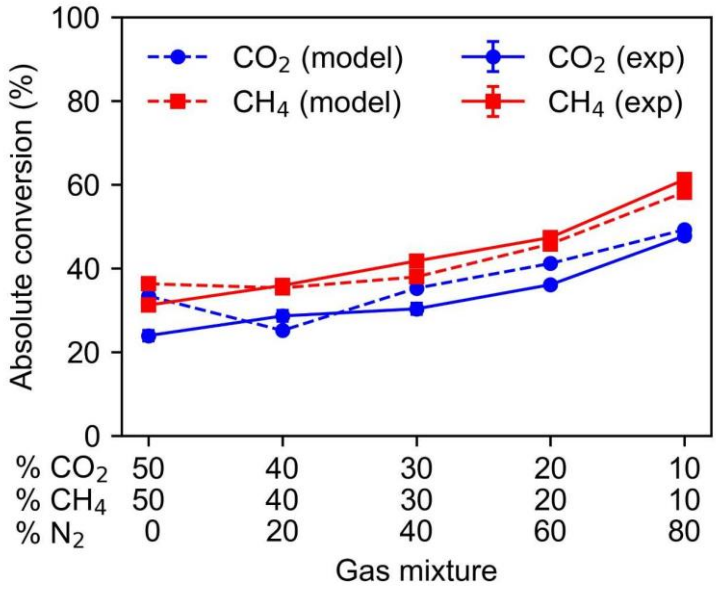

Figure 5.4: Experimental and calculated absolute CO_2 and CH_4 conversion as a function of N_2 fraction.
The experiments in both figures were performed in triplicate, but the error bars on the experimental results are mostly too small to be visible.

Figure 5.4 presents the (absolute) CO_2 and CH_4 conversion as a function of N_2 fraction in the mixture, obtained in the experiments and the models. Without N_2, a conversion of 23.9 % is achieved for CO_2 and 31.4 % for CH_4. These values rise notably upon N_2 addition, up to 47.7 % for CO_2 and 61.2 % for CH_4 at 80% N_2. The calculated conversions are in satisfying agreement with the experimental values. Hence, our results demonstrate that the addition of N_2 benefits the conversion of CO_2 and CH_4. The reason is that N_2 does not actively participate in the DRM chemistry and essentially remains unconverted (i.e. less than 0.05% conversion) in the plasma. As the energy acquired by N_2 molecules through inelastic collisions with electrons does not lead to chemical reactions, this energy eventually relaxes to gas

heating, which accelerates the DRM reactions. This will be explained in more detail by the computational models in section 5.4.5.

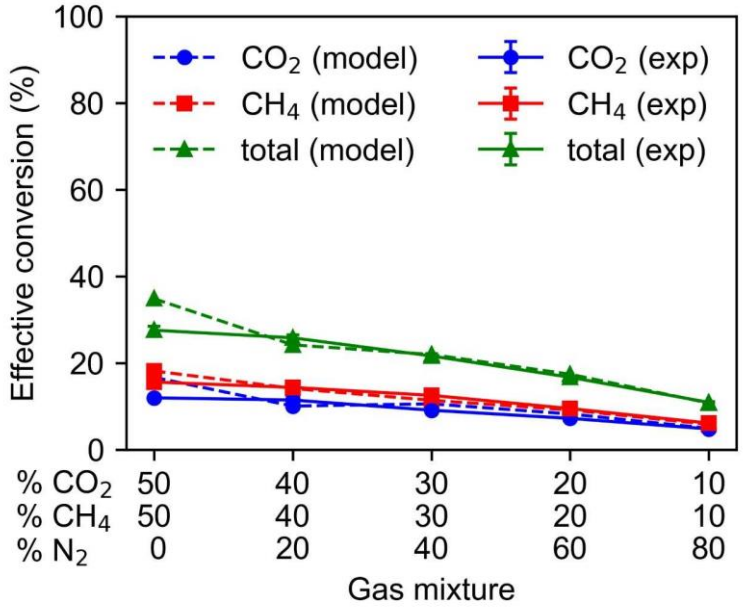

Figure 5.5: Effective CO_2 and CH_4 conversion, as well as the total conversion, as a function of N_2 fraction. The experiments in both figures were performed in triplicate, but the error bars on the experimental results are mostly too small to be visible.

Note that by adding N_2, the total amount of CO_2 and CH_4 present in the gas mixture is lowered from 100% (50%-50%) to 20% (10%-10%). This means that the effective conversion of CO_2 and CH_4, which is calculated based on the initial fraction of each gas in the mixture is expected to decrease upon adding more N_2. This is shown in figure 5.5, displaying the effective CO_2, CH_4 and total (overall) conversion as a function of N_2 fraction. The values drop from 12.0 to 4.8 % for CO_2, from 15.6 to 6.1 % for CH_4, and from 27.6 to 10.9% for the total conversion, upon increasing N_2 fraction. Hence, while the absolute conversion increases upon N_2 addition, the effective and total conversion decreases, meaning that less CO_2 and CH_4 can be converted overall upon dilution, simply because there is less CO_2 and CH_4 present in the mixture. However, the drop in conversions is not linear: it is less steep at low N_2 fractions and becomes a bit more significant as more N_2 is added. This implies that at low N_2 fractions, the dilution effect is less important than the beneficial effect of N_2 on the (absolute) conversion, observed in figure 5.4.

5.4.2 **Product yields**

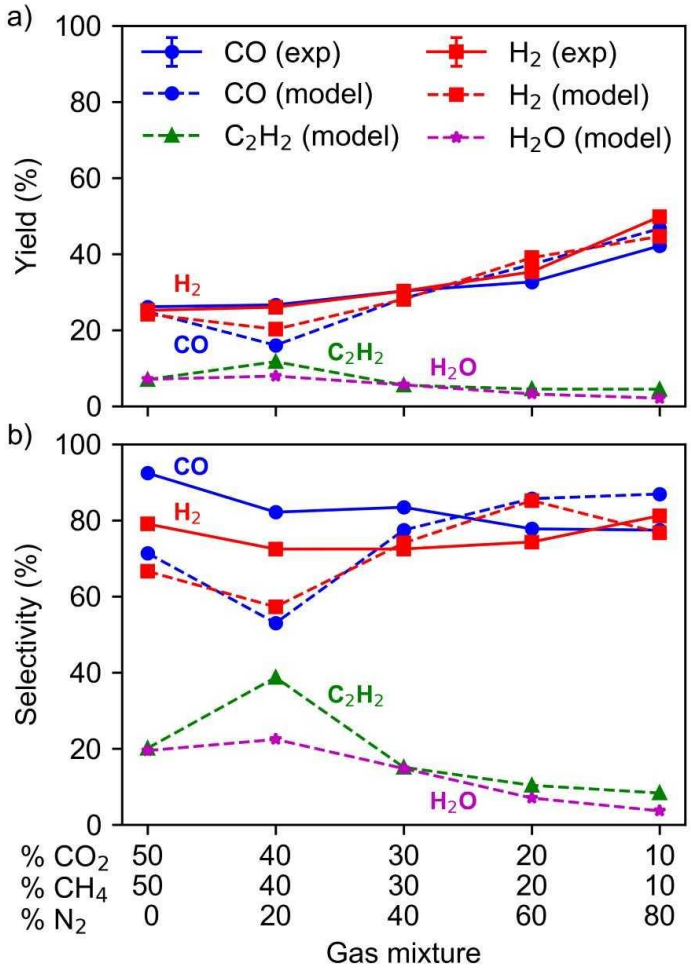

Figure 5.6: Experimental and calculated product (a) yields and (b) selectivities, as a function of N_2 fraction. The experiments in both figures were performed in triplicate, but the error bars on the experimental results are too small to be visible.

The measured and calculated product yields for different N_2 fractions are presented in figure 5.6(a). The CO yield rises from 26.1 to 42.1%, while the H_2 yield rises from 25.2 to 49.8 %, upon increasing N_2 fraction. The calculated values are in satisfying agreement with the experiments. The model also predicts H_2O and C_2H_2 as important products, but they could not be measured by our GC. The CO and H_2 yields follow the same trend as the (absolute) conversion, which is logical. Figure 5.6(b) illustrates the measured and calculated product selectivities. While the CO selectivity drops from 92.4 to 77.4 % upon increasing N_2 fraction, the H_2 selectivity first drops from 79.0 to 72.4 % when 20% N_2 is added and then increases again to 81.2 % upon 80% N_2 addition. Our model also predicts the drop in selectivity when 20% N_2 is added, but the drops is much more pronounced and occurs for both CO and H_2. Our model suggests that for this mixing ratio, the selectivity towards C_2H_2 increases, which lowers the

selectivity towards CO and H_2. As this drop is not so pronounced in the experiments, some reaction towards C_2H_2 may be slightly overestimated in the model at these low N_2 fractions.

5.4.3 Energy cost and energy efficiency

Besides conversion, product yields and selectivities, the other important criteria in defining the optimal gas composition for plasma-based DRM are the energy cost and energy efficiency, as they also define the performance of the process in an industrial context, where processes must be cost- and energy-efficient to be competitive. The energy efficiency is calculated from the effective conversion (shown in figure 5.5) and the specific energy input (SEI) of the process, the latter being defined by the ratio of the plasma power over the gas flow rate (see appendix section 8.6, equation 8.32). The experimental SEI across the different gas mixtures is presented in figure 5.7(a).

It is clear that the SEI significantly decreases when N_2 is initially added to the gas mixture, from 0.82 to 0.55 eV/molec (or from 3.2 to 2.2 kJ/L) when only 20% N_2 is added to a pure CO_2-CH_4 mixture. Further addition of N_2 only induces a slight drop in SEI. The fact that less power is required to achieve a stable plasma at a fixed plasma current when N_2 is added, explains why N_2 is often added to pure CO_2, CH_4 or CO_2-CH_4 mixtures to achieve a more stable plasma discharge. While the origin of this effect will be explained further by the computational models in section 4.5, we will now discuss the implication of this effect on the energy cost and energy efficiency.

Figure 5.7(b) depicts the energy cost (both in eV/molec and kJ/L) as a function of the N_2 fraction, obtained in the experiments and the models. Across the different gas mixtures, the energy cost ranges from 2.2 to 5.0 eV/molec (or 8.7 to 19.8 kJ/L) and is minimal for an N_2 fraction of 20 %. The latter is attributed to the limited reduction in effective conversion at 20 % N_2 (i.e. only 2 % loss), as seen in the figure 5.5, while it corresponds to a significantly lower SEI for stable plasma operation, as observed in figure 5.7(a), thus resulting in an overall lower energy cost. This minimum energy cost at the 20% N_2 fraction corresponds to the maximum energy efficiency of 58 % as shown in figure 5.7(c), where the energy efficiency is plotted across the different gas mixtures, calculated using equation 8.36 in the appendix (section 8.6).

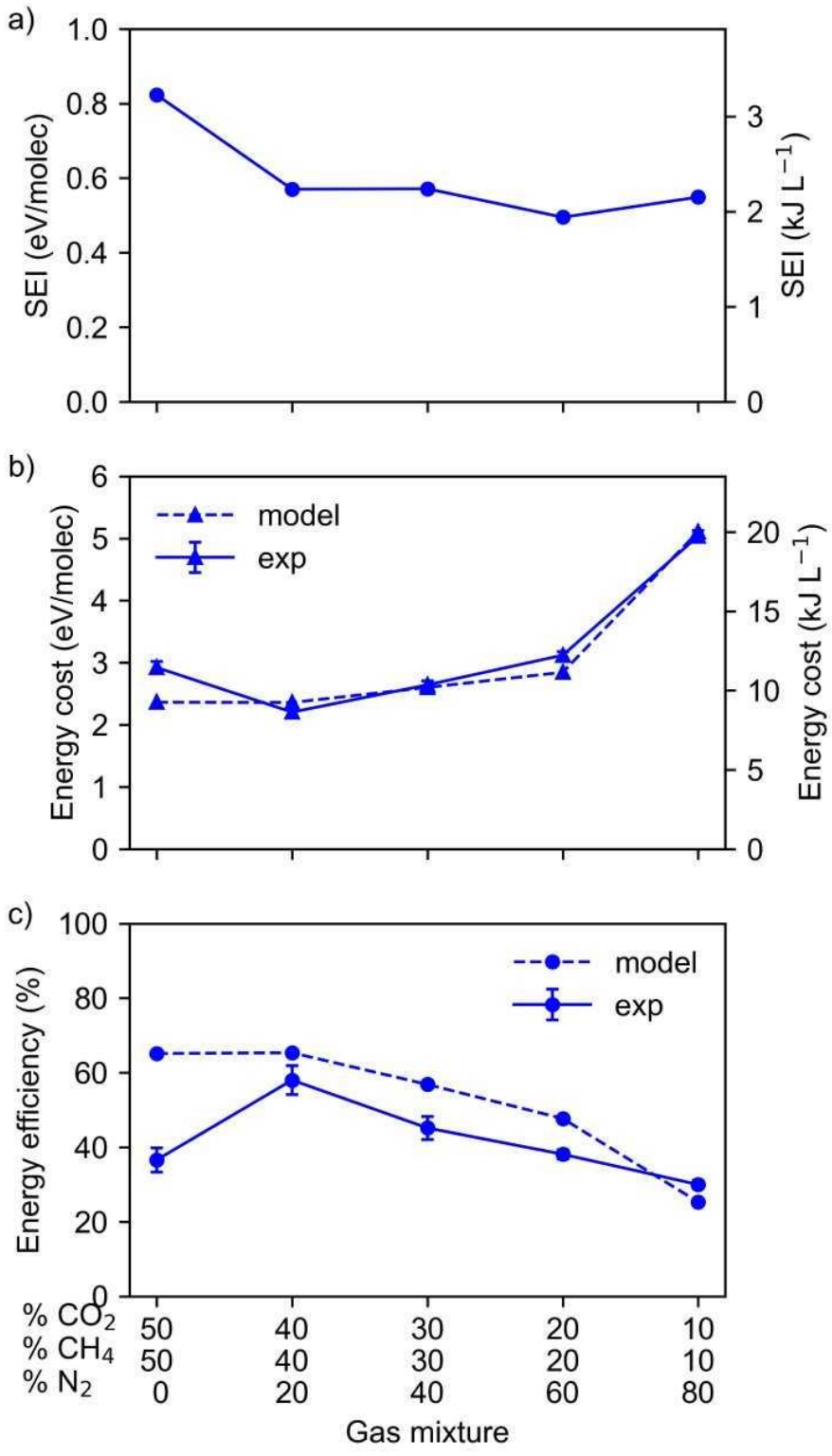

Figure 5.7: a) Experimental SEI at a constant plasma current of 0.3 A, (b) experimental and calculated energy cost, and (c) experimental and calculated energy efficiency, as a function of N_2 fraction. For all three figures, the experiments were performed in triplicate, but the error bars on the experimental results are mostly too small to be visible.

Taking it all together, our results indicate that 20 % N_2 addition yields the best performance, i.e., the lowest energy cost of 2.2 eV/molec (or 8.7 kJ/L) and highest energy efficiency of 58 %, for a CO_2 and CH_4 (absolute) conversion of 28.7 and 35.9 %, and a total conversion of 25.8 %.

5.4.4 Explanation of the performance by means of the computational models

As the calculated conversions, product yields and selectivies, and the energy cost and energy efficiency are all in satisfying agreement with the experiments, we can use our models to explain the experimental trends upon addition of N_2 to the CO_2-CH_4 mixture. The physical properties of the plasma are captured by the 3D models, while the chemical reaction pathways are calculated by the quasi-1D model.

5.4.4.1 N_2 addition enhances the plasma arc temperature

To calculate the physical properties of the plasma, the arc formation and stabilization in the vortex gas flow of the GAP are simulated in 3D by the arc plasma model. The arc is initially formed at the shortest distance between cathode and anode and is dragged to the center of the reactor by the rotational vortex flow.[108] The result of this stabilization is depicted in figure 5.8, showing the arc position (in red) within the velocity streamlines, as calculated by our turbulent gas flow model and plasma arc model. The gas flow forms two vortexes: an outer vortex displaying gas velocities up to 14 m/s, and an inner vortex, in which the gas slows down to 4 m/s. The arc is indeed stabilized by the vortex flow in the middle of the reactor, gliding over the anode outlet wall, while it remains connected to the top of the cathode. As shown by table 5.1 in section 5.3.4, our model predicts that 38 % of the gas gets treated directly by the plasma, either by the steady part of the arc (15 %) or by the rotating part of the arc (23 %), which glides along the outlet wall, while up to 11.8 % of the gas is treated by the hot afterglow of the plasma. It also means that at least 50 % of the gas is not yet treated by the plasma (or hot afterglow), showing the clear room for further improvement in conversion, by smart reactor design, as mentioned in previous section.

The calculated arc dimensions in figure 5.8 very strongly resemble the arc dimensions calculated by Trenchev et al.[92] in a two-dimensional non-thermal plasma model for pure CO_2 in the GAP, which indicates that our approach of the 3D thermal plasma (with corrected gas temperature) correctly predicts the shape of the arc.

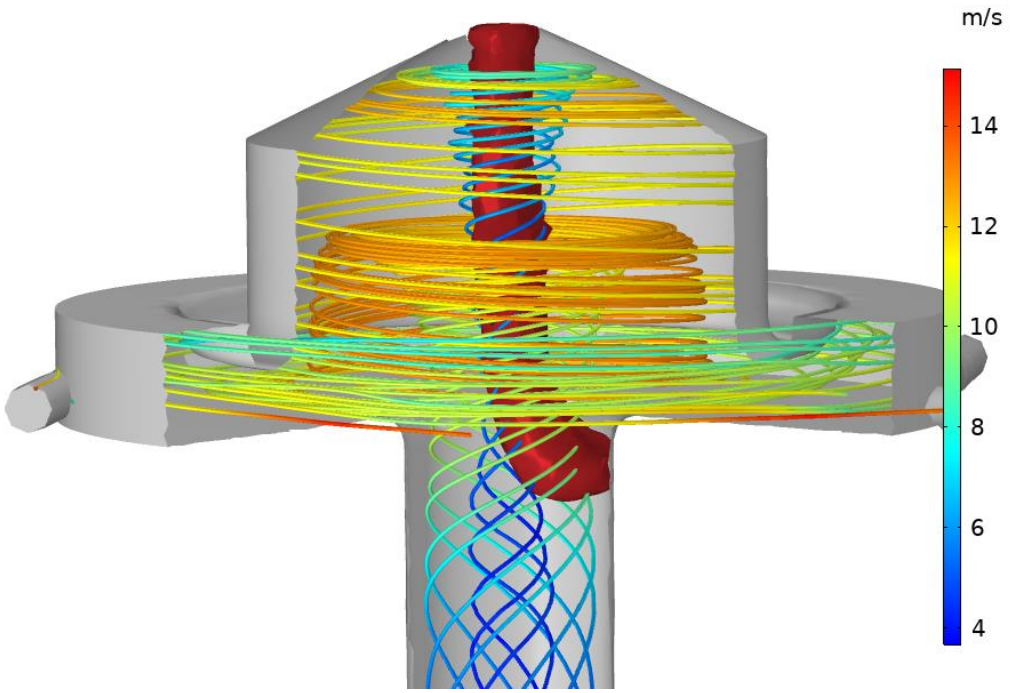

Figure 5.8: Calculated gas velocity streamlines (see colour scale at the right) and arc formation in the GAP reactor for a 10 L/min 50/50 CO_2/CH_4 flow. The results look the same for all gas mixtures investigated.

Figure 5.9 illustrates the 2D gas temperature profile, calculated by the thermal plasma model for a pure CO_2-CH_4 mixture and corrected using the experimental plasma power and energy efficiency (see section 3.2, page 52). Inside the arc the gas temperature builds up to 3200 K in the center of the arc. This value is very close to the temperature calculated for a pure CO_2 plasma in the GAP by Trenchev et al.,[92] which indicates that our approach of using the experimental energy efficiency to determine how much power is put into gas heating, delivers realistic temperature values. Note that the gas temperature plays a crucial role in DRM, since the production rate of reactive plasma species, and thus also the overall rate of the conversion process, increases significantly upon higher gas temperatures.

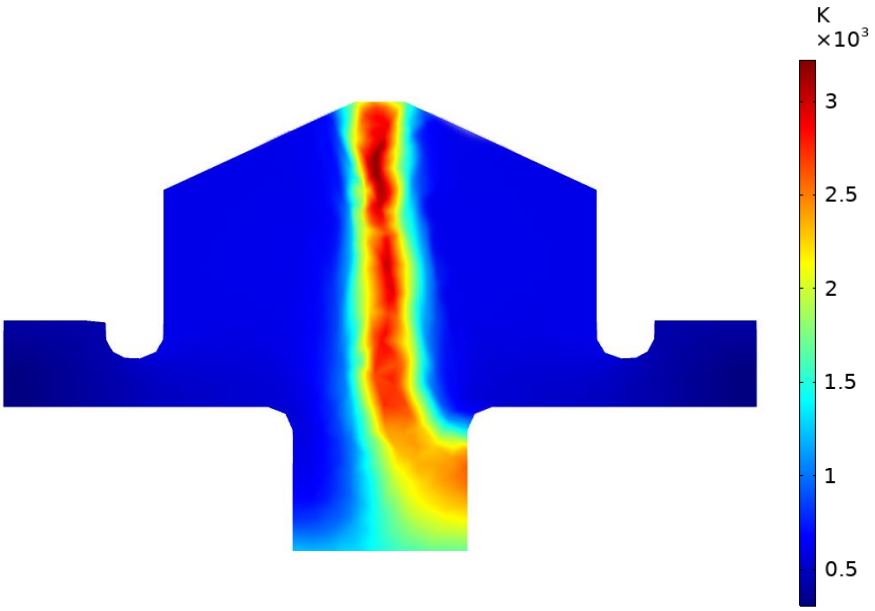

Figure 5.9: Calculated 2D gas temperature profile in the GAP for a pure (50/50) CO_2-CH_4 plasma, at 10 L/min and 0.3 A electric current.

Our models reveal that the gas temperature is heavily influenced by the composition of the gas mixture. This is illustrated in figure 5.10 for the maximum gas temperatures achieved in the arc across the different gas mixtures, as calculated by the arc plasma model. In general, the temperature in the arc increases upon N_2 addition, reaching up to 4400 K for a N_2 fraction of 80 %. Firstly, this is attributed to the higher overall heat capacity upon N_2 addition, as illustrated by the isobaric heat capacity of the different CO_2-CH_4-N_2 mixtures at 3000 K (i.e. a typical plasma gas temperature) in figure 5.10 (right y-axis). Indeed, the addition of N_2 lowers the overall heat capacity of the mixture, meaning that less energy is required to heat the gas mixture at higher N_2 fractions. The reason is that a diatomic molecule (like N_2) has less internal degrees of freedom (rotational, vibrational) than polyatomic molecules (like CO_2 and CH_4) and thus stores more of its energy in its translational degrees of freedom, making it easier to heat up the gas when N_2 is present in the mixture, for the same input (plasma) power.

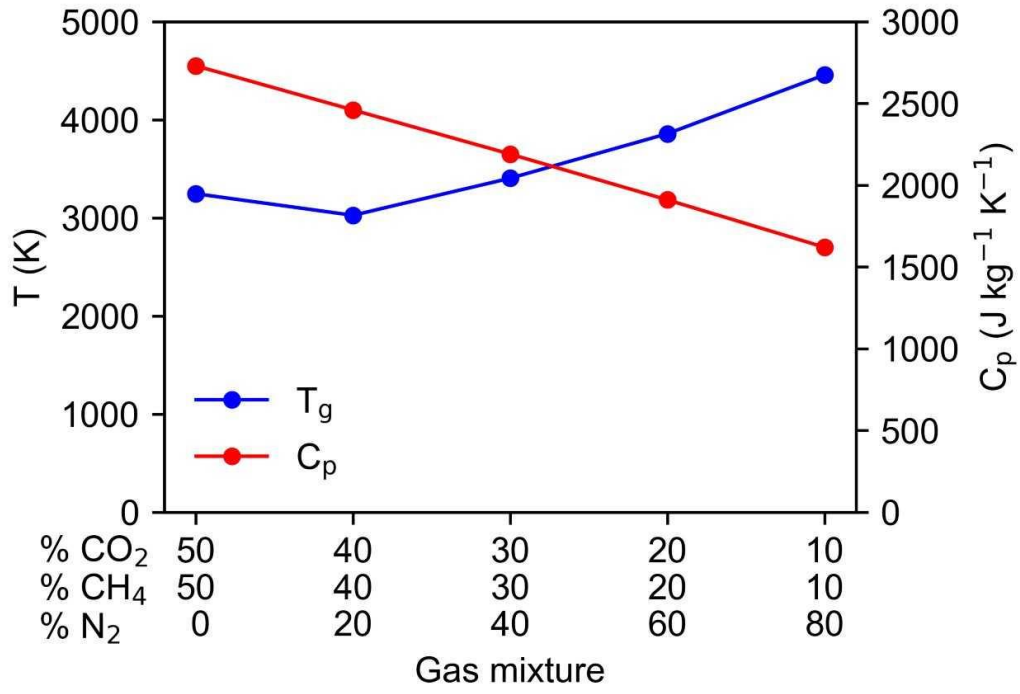

Figure 5.10: Maximum calculated gas temperature in the plasma (arc center) (blue) and isobaric heat capacity of the CO_2-CH_4-N_2 gas mixture at 3000 K (red), as a function of the N_2 fraction.

Next to the lower heat capacity of the mixture, the more efficient gas heating upon N_2 addition is also because N_2 channels more of the applied (plasma) energy into gas heating. While some N_2 molecules acquire enough energy through inelastic collisions with electrons to be ionized or to dissociate, most molecules do not undergo chemical reactions because of the strong triple bond, and only become (vibrationally) excited, after which they eventually relax their acquired energy, increasing the gas temperature in the plasma. Note that in figure 5.10 the gas temperature for the pure CO_2-CH_4 mixture is higher than when 20 % N_2 is added, which does not align with the trend observed in the other gas mixtures. This is due to the fact that at the fixed plasma current of 0.3 A, this gas mixture operates at a significantly higher SEI (see figure 5.7 (a)) compared to the other mixtures, so that more power is available to put in to gas heating, which outweighs the effect of the N_2 addition.

The higher gas temperature resulting from N_2 addition has also been observed experimentally in a CH_4 plasma by Zhang et al. for a rotating gliding arc reactor.[109] Using optical emission spectroscopy the authors observed an increase of more than 300 K when the molar CH_4/N_2 ratio was reduced from 1.20 to 0.05. A similar observation has been reported by Gröger et al. when studying a pure N_2 plasma in the GAP reactor using optical emission spectroscopy.[69] Gas temperatures up to 5500 K were measured, which is much higher that the gas temperatures between 3000 and 4000 K calculated by Trenchev et al. for a pure CO_2 plasma in the same GAP reactor.[92]

The higher gas temperature speeds up the plasma kinetics of the DRM reactions, and this explains the higher (absolute) CO_2 and CH_4 conversions at higher N_2 fractions (see figure 5.4). These results provide valuable new insights, in addition to previous computational studies that analyzed the beneficial effect of N_2 addition to CO_2 or CO_2/CH_4 plasmas in various plasma reactor types.[95–98] In a dielectric barrier discharge (DBD) reactor, modelling revealed that N_2 improved the CO_2 conversion through reaction with metastable electronically excited $N_2(\Sigma_u^+)$ molecules[96], while in a microwave (MW) plasma reactor at reduced pressure, N_2 enhanced the CO_2 conversion by transferring its vibrational energy to CO_2 molecules through vibration-vibrational relaxation reactions.[98] The DBD and MW plasma operate at lower gas temperatures than our GAP (300 K for the DBD and 1000 K for the MW plasma at reduced pressure) and, as a consequence, thermal conversion of CO_2 or CH_4 is not so prominent, unlike in our GAP reactor. Our study thus perfectly complements previous modeling results, providing new insights for warm plasmas, where thermal conversion and the effects of the gas temperature are crucial.

5.4.4.2 N_2 addition enhances the electron density, affecting the plasma conductivity, plasma power and SEI

As illustrated in figure 5.6(a) above, the measured SEI in the CO_2-CH_4 mixture drops significantly when 20 % N_2 is added, due to the lower power needed to ignite and sustain the plasma at a fixed plasma current. Our computational models reveal that this is attributed to the increasing electron density upon adding N_2 to the mixture, as illustrated in figure 5.11 (black line, left y-axis). This figure also presents the dominant electron formation reactions in the mixture (colored bars, right y-axis), as calculated by the quasi-1D model. Note that this model was run for a constant temperature of 3500 K and power density of 4.5 kW cm^{-3}, to clearly isolate the effect of the changing gas composition (independent from the effect of the gas temperature) on the plasma chemistry. Without N_2, electron formation mainly occurs through recombination of H_2 and O^- to H_2O (reaction 5), and of CO and O^- to CO_2 (reaction 4), as well as by electron impact ionization of CO_2 (reaction 1). When N_2 is added, ionization of N_2 (especially electron impact ionization of ground state N_2 (reactions 7 and 8), but also associative ionization by two electronically excited molecules, $N_2(A^1\Sigma_u)$ (reaction 9) and $N_2(A^3\Sigma_u)$) (reaction 10) take over as the main electron formation processes, explaining the rising electron density in the plasma. In other words, through the addition of N_2 a new gas is introduced to the plasma, which, unlike CO_2 and CH_4, does not react away easily by other (chemical) reactions due to its strong triple bond, and is thus always available for ionization. The electron density enhances the conductivity of the plasma, thus reducing the power needed to achieve a certain plasma current. Hence, this explains the drop in plasma power, and thus in SEI (cf. figure 5.6(a)) upon N_2 addition, contributing to the low energy cost of the 20 % N_2 mixture.

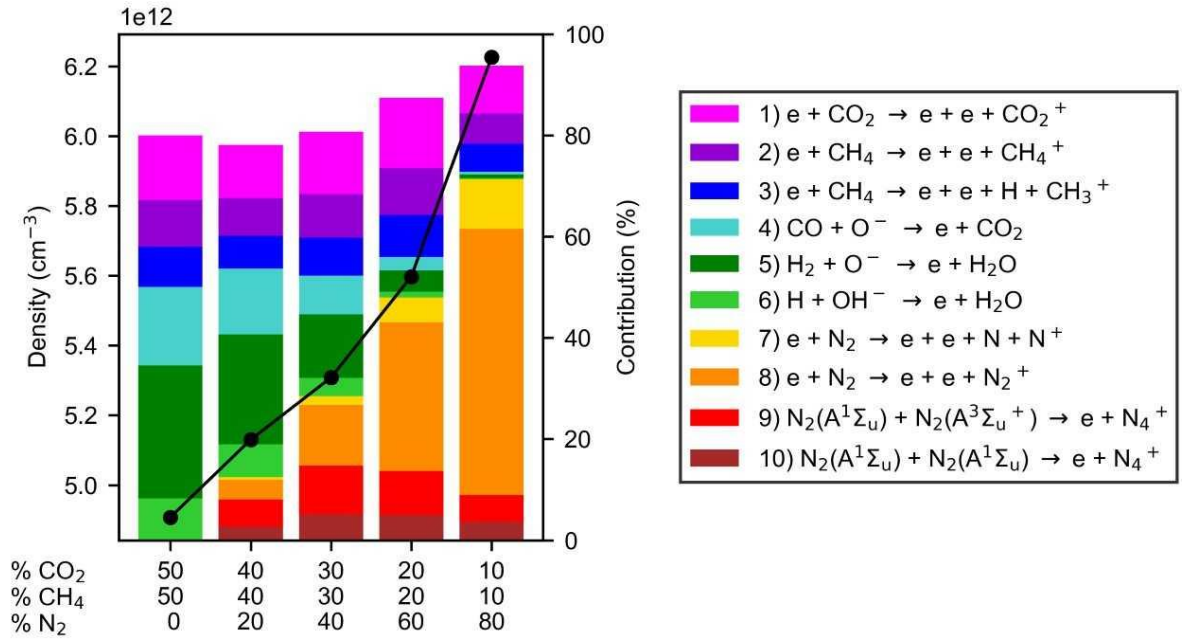

Figure 5.11: Calculated electron density (black line, left y-axis) as a function of N_2 fraction, at a constant gas temperature of 3500 K and power density of 4.5 kW cm^{-3}. The coloured bars (right y-axis) show the contribution of the dominant electron formation reactions across the different gas mixtures. The values are determined for a plasma residence time of 1 ms, which is comparable to the residence time in the plasma obtained in the 3D simulations based on the experimental conditions.

5.5 CONCLUSIONS

In this chapter, we investigated the effect of N_2 on plasma-based DRM in a gliding arc plasmatron, by means of experiments and a combination of three different computational models. Overall, a N_2 content of 20 % was found to be optimal in terms of overall performance, achieving a total conversion of 25.8 %, and (absolute) conversions of 28.6 % for CO_2 and 35.9 % for CH_4 at a total energy cost of 2.2 eV/molec (or 8.7 kJ/L) and energy efficiency of 58 %. The syngas components (CO and H_2) are the major products, but the model reveals that some C_2H_2 (and H_2O) are also formed.

Our computational models yield good agreement with the experimental conversions, product yields and selectivities, energy cost and energy efficiency, and can thus be used to elucidate the underlying mechanisms, and explain the trends of N_2 addition. The models reveal that the addition of N_2 significantly increases the gas temperature in the plasma. This is attributed to the lower isobaric heat capacity, and because N_2 remains largely unconverted in the plasma, so virtually all plasma energy that is taken up by N_2 molecules through inelastic collisions with electrons is eventually distributed to the translational degrees of freedom. Hence, the maximum gas temperature reached in the plasma significantly increases, from around 3200 K without N_2, up to 4400 K upon 80 % N_2 addition. This higher temperature accelerates the DRM reactions, enhancing the (absolute) conversions of CO_2 and CH_4.

Indeed, our models reveal that the addition of N_2 promotes the conversion of CO_2 and CH_4 through thermal conversion reactions, rather than through electron impact reactions. Due to the higher gas temperature at higher N_2 fractions, the rates of the thermal chemistry reactions increase significantly, so these reaction pathways have the highest contribution in the conversion process.

Next to increasing the gas temperature, the addition of N_2 also reduces the power that is needed to achieve a certain plasma current, and thus the plasma can operate at lower SEI, for a constant gas flow rate. Indeed, the N_2 molecules are virtually not dissociated (and thus converted in chemical reactions), but they only undergo ionization (and excitation). This enhances the electron production rate due to the extra ionization channels, thus increasing the electron density. A higher electron density leads to a higher plasma conductivity, so less power is required to achieve the plasma current of 0.3 A when more N_2 is present, thereby reducing the SEI of the process.

Hence, both the higher absolute conversion and lower SEI at increasing N_2 fractions are beneficial, but on the other hand, diluting the CO_2-CH_4 fraction reduces the effective conversion of CO_2 and CH_4. However, at N_2 fractions around 20 %, the advantages of adding N_2 outweigh the dilution effect, improving the energy efficiency of the process with respect to pure CO_2-CH_4 mixtures, by 21 %, i.e., from 37 to 58 %, and reducing the energy cost from 2.9 to 2.2 eV/molec (or from 11.5 to 8.7 kJ/L).

In conclusion, we have shown that the addition of N_2, a ubiquitous component in many industrial emissions, can significantly improve the energy efficiency of plasma-based DRM, thus bringing this plasma-based process a step closer towards real applications.

6 MODELLING POST-PLASMA QUENCHING NOZZLES FOR IMPROVING THE PERFORMANCE OF CO_2 MICROWAVE PLASMAS

The results presented in this chapter are accepted for publication in:

"Modelling post-plasma quenching nozzles for improving the performance of CO_2 microwave plasmas"

Van Alphen S., Hecimovic A., Kiefer C. K. , Fantz U., Snyders R., Bogaerts A. In press at Chem Eng J (2023)

6.1 INTRODUCTION

Previous chapters investigated how to enhance the performance of plasma-based gas conversion applications in different GA reactors. However, just like GA reactors, MW plasma reactors have proven to be especially interesting for gas conversion applications like CO_2 dissociation, being electrode-free, thus avoiding electrode degradation over time, and achieving very high conversion and energy efficiency.[14,24,25,110] MW plasmas display different characteristics depending on the operating pressure. At low pressures, i.e. below 100 mbar, the plasma is radially expanded to almost fill up the whole quartz tube, operating in the so-called diffuse mode.[13] At higher pressure, the plasma is confined in a narrow filament in the center of the reactor, operating in the contracted mode.[13] Recent studies strongly suggest that the CO_2 dissociation process in both modes heavily relies on the thermal dissociation pathway.[111] Especially in the contracted mode, where the discharge is confined in a small volume, thermal dissociation is the dominant pathway. The small plasma volume results in a high power density and a high local specific energy input (SEI), yielding gas temperatures up to 6000 K.[13,24] While at these high temperatures CO_2 is fully dissociated, only conversions around 10% at energy efficiencies around 30% are measured at pressures close to 1 atm.[24,25] Just like the limitation observed for N_2 fixation in GA reactors in chapter 4, this is attributed to recombination reactions, in this case of CO back into CO_2, once the gas slowly cools down after leaving the plasma:

$$CO + O + M \rightleftarrows CO_2 + M$$

$$CO + O_2 \rightleftarrows CO_2 + O$$

As observed for N_2 fixation into NO_x in chapter 4, it has been suggested that fast cooling of the gas after the plasma can quench the recombination reactions, effectively "freezing" the conversion that was achieved in the hot plasma.[25] Modelling work by Vermeiren and Bogaerts showed that for warm plasmas with high specific energy input (SEI ≥ 2 eV/molecule) quenching at the point of maximum conversion inside the plasma could enhance the conversion and energy efficiency by up to a factor 3.[84] Next to limiting the recombination reactions, and thus freezing the formed reaction products (so-called ideal quenching), it is also possible to even further dissociate CO_2 upon quenching. This is called super-ideal quenching and was predicted by Vermeiren and Bogaerts to occur at low SEI (ca. 0.5 eV/molecule) when a vibrational non-equilibrium, created or enhanced by the sudden drop in gas temperature, promotes further dissociation of CO_2:[84]

$$CO_2(v) + O \rightleftarrows CO + O_2$$

in which $CO_2(v)$ represents a vibrationally excited CO_2 molecule.

Recently, the beneficial effect of quenching was experimentally shown by Hecimovic et al.[112] by using nozzles of varying diameter in the effluent of a MW plasma torch. The aim of the nozzle was to force mixing of the hot plasma gas with the surrounding colder gas to induce cooling and reduce the recombination reactions. Significant improvements of the conversion and energy efficiency were observed, especially at higher pressures (900 mbar) and low CO_2 flow rates (< 10 slm), which corresponds to an SEI above 2 eV/molecule. At 5 slm, 1500 W and 900 mbar, the conversion in a reactor without nozzle was measured to be about 5%, while attaching a 2.5 mm nozzle enhanced the conversion to 35%, which is a 7-fold increase.

Given the exceptional performance of the nozzle configuration demonstrated by Hecimovic et al., we aim in this paper to reveal in detail the gas flow behavior and quenching mechanism of the nozzle by means of computational modelling. Through computational fluid dynamics (CFD), we will simulate the gas flow and heat transfer within the reactor that was operated by Hecimovic et al. and how this is influenced by attaching a nozzle in the effluent. Subsequently, we will use a quasi-1D chemical kinetics model to reveal the effect of the nozzle on the underlying chemistry. The most significant results of Hecimovic et al. were found at the highest investigated pressure, i.e. 900 mbar. This pressure was used for the measurements, but experiments performed at 900 mbar and at atmospheric pressure yield identical CO_2 conversion,[113] thus results presented at 900 mbar are representative for atmospheric pressure operating conditions as well. As atmospheric pressure regimes are also most interesting for practical (industrial) applications, we will focus on this pressure regime in the present study as well, but to be consistent with the experiments, the CFD model is also performed at 900 mbar.

6.2 METHODOLOGY

6.2.1 Calculating the gas flow and heat transfer in a 3D fluid dynamics model

To reveal the effect of a nozzle in the effluent of the MW plasma reactor, we developed a three-dimensional (3D) CFD model that calculates the flow behavior and heat transfer within the gas flowing through the plasma torch in COMSOL Multiphysics.[114] The 3D model geometry of the MW reactor, as described by Hecimovic et al., is shown in figure 6.1.

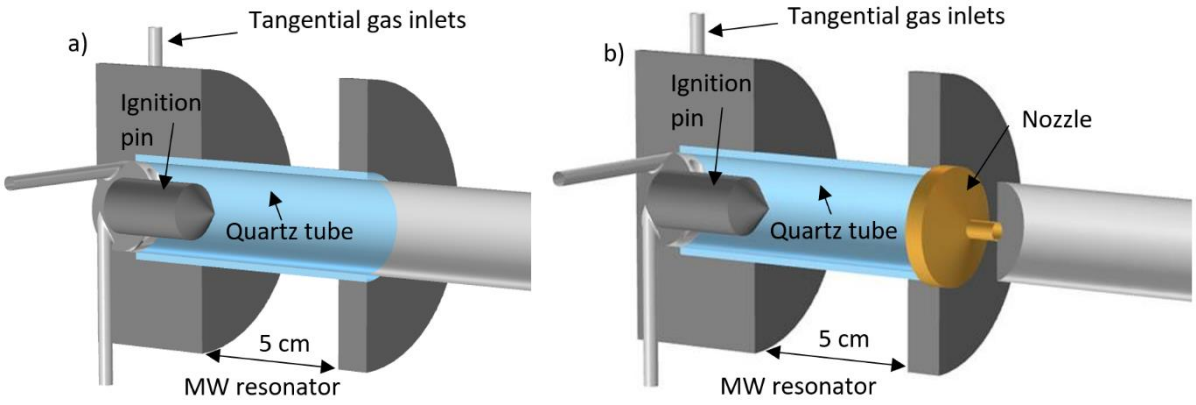

Figure 6.1: 3D model geometry of the MW reactor a) without and b) with nozzle attached, as described by Hecimovic et al.[1]

The gas flow behavior is described using the RANS SST turbulent gas flow model that solves the mass continuity and momentum continuity equations for a Newtonian fluid in equations 6.1 and 6.2:

$$\rho_g \frac{\partial \vec{u}}{\partial t} + \rho(\vec{u} \cdot \nabla)\vec{u} = \nabla \cdot \left[-p\vec{I} + (\mu + \mu_T)(\nabla\vec{u} + \nabla(\vec{u})^T) - \frac{2}{3}(\mu + \mu_T)(\nabla \cdot \vec{u})\vec{I} - \frac{2}{3}\rho_g k_T \vec{I}\right] + \vec{F} \quad (6.1)$$

$$\rho \frac{\partial \vec{u}}{\partial t} + \nabla \cdot (\rho_g \vec{u}) = 0 \quad (6.2)$$

where ρ_g stands for the gas density, $\overrightarrow{u_g}$ is the gas flow velocity vector, superscript T stands for transposition, p is the gas pressure, μ is the dynamic viscosity, and μ_T the turbulent viscosity of the fluid, k is the turbulent kinetic energy, $\vec{I}$ the unity tensor and $\vec{F}$ the body force vector (which includes forces like gravity or surface tension, but is considered zero as they are not the driving force of the fluid flow in this model).

The gas temperature is calculated by representing the plasma as a heat source Q_{heat}, using the following thermal balance equation:

$$\rho_g C_p \frac{\partial T_g}{\partial t} + \rho_g C_p \vec{u} \cdot \nabla T_g + \nabla \cdot \vec{q}_{cond} = Q_{heat} \quad (6.3)$$

Where ρ_g stands for the gas density, C_p for the isobaric heat capacity, T_g is the gas temperature, $\vec{u}_g$ the gas velocity field vector, and $\vec{q}_{cond}$ the conductive heat flux vector, which is calculated by:[63]

$$\vec{q}_{cond} = -(k_g + k_{g,T})\nabla T \tag{6.4}$$

Where k_g is the thermal conductivity and $k_{g,T}$ is the turbulent thermal conductivity of the gas, calculated by:

$$k_{g,T} = \frac{C_p \mu_T}{Pr_T} \tag{6.5}$$

In which μ_T is the turbulent dynamic viscosity and Pr_T the turbulent Prandtl number, as calculated by the Kays-Crawford model.[64] The material properties μ, C_p and k_g in equation 6.1, 6.3 and 6.4, respectively, are adopted from the work of Magin et al.[87], where these properties are calculated for a wide range of temperatures assuming thermodynamic equilibrium. This means that changes in gas composition and energy balance due to chemical reactions are taken into account within these properties, e.g. the endothermic characteristic of CO_2 splitting, as well as the formation of CO and O_2 and the destruction of CO_2 are represented in the heat capacity and thermal conductivity.

In equation 6.3, the second term ($\rho_g C_p \vec{u}_g \cdot \nabla \mathrm{T}$) accounts for convective cooling and the third term ($\nabla \cdot \vec{q}_{cond}$) accounts for conductive cooling. While the second term directly yields the conductive heat flux $\vec{q}_{cond}$, as defined in equation 6.4, the convective heat flux is calculated using:

$$\vec{q}_{conv} = \rho_g \vec{u}_g \left(H - \frac{p}{\rho_g}\right) \tag{6.6}$$

In which H is related to C_p through:

$$\left(\frac{\partial H}{\partial T}\right)_T = C_p \tag{6.7}$$

The total heat flux is then described by:

$$\vec{q}_{tot} = \vec{q}_{cond} + \vec{q}_{conv} \tag{6.8}$$

The final term in equation 6.3 (Q_{heat}) represents the absorbed MW power that is converted into gas heating. This heat source term is then defined as:

$$Q_{heat} = N * rad(x) * rad(y) * ax(z) \tag{6.9}$$

In which rad and ax are the radial and axial power profiles of the MW power, respectively, and N is a normalization factor, such that the integrated value of Q_{heat} to be calculated using the experimental plasma power.

$$\iiint Q_{heat}\, dx\, dy\, dz = P_{MW} \tag{6.10}$$

Where P_{MW} is the microwave power that is absorbed by the plasma, measured in the experiments. Indeed, as atmospheric pressure MW plasmas are known for very fast vibrational-translational relaxation, making them quasi-thermal or "warm" plasmas,[13,66] it is reasonable to assume that the absorbed MW power is nearly fully transferred to gas heating.

The radial and axial power profiles (rad and ax) are defined using analytical functions that approximate the radial and axial profile of a contracted plasma filament, as measured by D'Isa et al.[24] and Wolf et al.[13] The radial power profile used in the model, is shown in figure 6.2(a), resembling closely the profile measured by D'Isa et al., shown in figure 6.2(b). The axial power profile used in the model, is shown in figure 6.3(a), resembling closely the profile measured by D'Isa et al., shown in figure 6.3(b). Furthermore, as concluded in the work from D'Isa et al., the plasma diameter and length of the plasma is independent from the flow,[24] allowing us to use the same power profile for every flow rate.

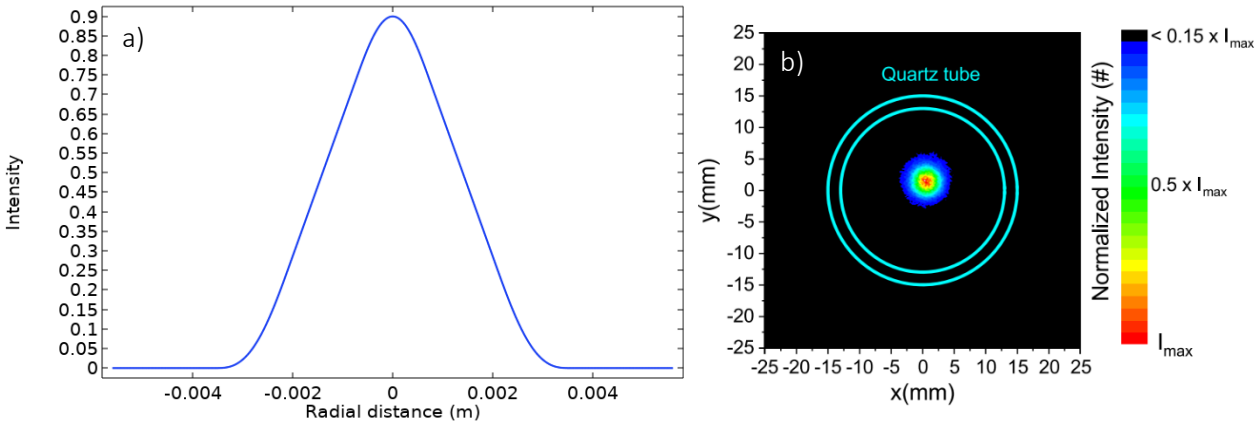

Figure 6.2: a) Radial power density profile of the plasma assumed in the model
b) Radial ICCD image taken by D'Isa et al

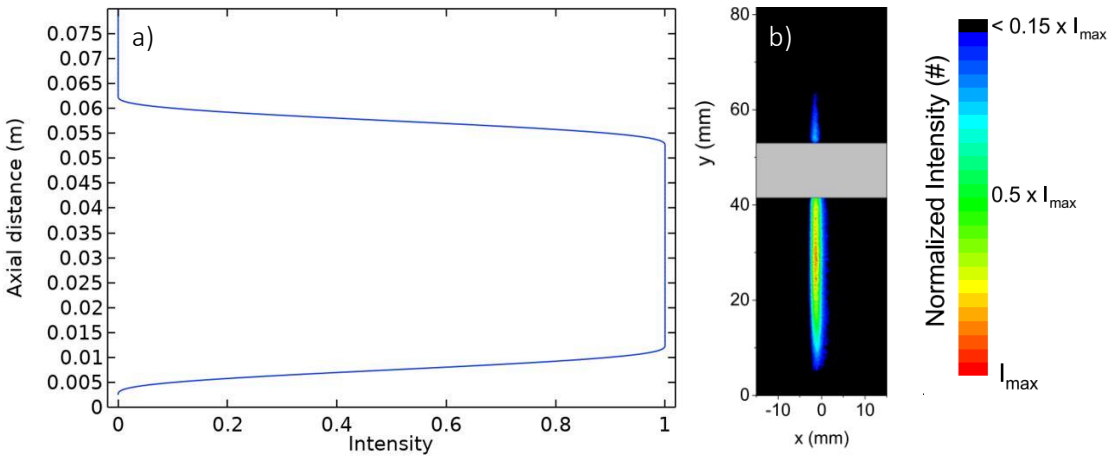

Figure 6.3: a) Axial power density profile of the plasma assumed in the model
b) Axial ICCD image taken by D'Isa et al.

6.2.2 Calculating the underlying chemistry in a quasi-1D chemical kinetics model

To reveal the underlying chemistry at different locations in the reactor, we developed a chemical kinetics model that simulates the CO_2 chemistry over a one-dimensional straight line in the reactor. Similar to previous chapter, the model calculates the density evolution of the most important plasma species as a function of time, using the spatial profile of the calculated gas temperature and gas flow velocity from the 3D CFD model as input, resulting in a quasi-1D simulation. The evolution of the species densities as a function of time is described by:

$$\frac{\partial c_i}{\partial t} = \sum_j a_{ij} r_j \tag{6.11}$$

in which c_i is the concentration of species *i* (mol.m^{-3}), and *j* is the number of reactions included in the model. The stoichiometric coefficients are denoted as a_{ij}, and are defined as being negative for reactants and positive for products. The reaction rates (r_j, mol/(m^3·s)$^{-1}$) can be described by the mass action law:

$$r_j = k_j^f \prod_i c_i^{-a_{ij}} - k_j^r \prod_i c_i^{a_{ij}} \tag{6.12}$$

Here, k_j^f and k_j^r represent the forward and reverse rate coefficients, respectively. The reactions included in the model are shown in *Table 6.1*. This set only includes thermal reactions of species that play a significant role in the thermal dissociation and recombination pathway of CO_2. The rate coefficients of the forward reactions, shown in *Table 6.1*, are taken from the Gri-mech 3.0 database,[115] while the rate coefficients of the reverse reactions are calculated assuming thermodynamic equilibrium:

$$k^r = \frac{k^f}{K_{eq}} \tag{3.13}$$

In which K_{eq} is the equilibrium constant of the reaction, calculated using thermodynamic constants of the NASA-Glenn database.[116]

Table 6.1: List of reactions and reaction rate coefficients of the forward reactions used in the model, as adopted from the Gri-mech 3.0 database.[115] The rate coefficients of the backward reactions are calculated assuming thermodynamic equilibrium. M in the reactions below represents any neutral species, R is defined as 8.314 J(K.mol)-1, c_M is given in mol.cm-3, and T in K.

Reaction	Reaction rate coefficient of forward reaction
$CO + O + M \rightleftarrows CO_2 + M$	$k = \frac{k_{inf}}{\frac{1 + k_{inf}}{k_o c_M}}$ $k_{inf} = 1.80 \text{ x } 10^{10} \left[\text{cm}^3\text{mol}^{-1}s^{-1}\right] \exp\left(\frac{-9978.8 \left[\frac{J}{mol}\right]}{RT}\right)$ $k_o = 6.02 \text{ x } 10^{14} \left[\text{cm}^6\text{mol}^{-2}s^{-1}\right] \exp\left(\frac{-12552 \left[\frac{J}{mol}\right]}{RT}\right)$
$CO + O_2 \rightleftarrows CO_2 + O$	$k = 2.50 \text{ x } 10^{12} \left[\text{cm}^3\text{mol}^{-1}s^{-1}\right] \exp\left(\frac{-2 \text{ x } 10^5 \left[\frac{J}{mol}\right]}{RT}\right)$
$O + O + M \rightleftarrows O_2 + M$	$k = \frac{1.20 \text{ x } 10^{17} \left[\text{cm}^6\text{mol}^{-2}s^{-1}\right]}{T} c_M$
$C + O + M \rightleftarrows CO + M$	$k = 7.76 \text{ x } 10^6 \left[\text{cm}^6\text{mol}^{-2}s^{-1}\right] \left(\frac{T}{300 \left[K\right]}\right)^{-3.08} \exp\left(\frac{-2114 \left[K\right]}{T}\right) c_M$

6.3 RESULTS AND DISCUSSION

6.3.1 Experimental performance of the nozzle

Figure 6.4 presents the experimental results acquired by Hecimovic et al.[112], showing the conversion as a function of flow rate in the MW reactor without and with nozzles of varying diameters, for a plasma power of 1500 W and an operating pressure of 900 mbar (which, as mentioned, is representative for atmospheric pressure operating conditions). In addition, the inverse relation between flow rate and conversion, that holds in the case of constant energy efficiency, is marked with a grey dashed line. In general, figure 6.4 shows a significantly higher conversion and energy efficiency when a nozzle is attached to the reactor. Interestingly, the performance enhancement of the nozzle is most significant at lower flow rates: while the rise in conversion at 20 slm is only a few % for a nozzle with diameter of 2.5 mm, at 5 slm the same nozzle enhances the conversion by a factor 7, i.e., from 5 to 35 %. Furthermore, the best improvements are observed at smaller diameter nozzles. Through computational modelling we aim to fully explain these trends and identify the quenching mechanisms of the nozzle, using the following steps: in section 6.3.2, we simulate the gas flow and heat transfer inside the MW reactor without nozzle attached as a reference case, varying the gas flow rates as shown by the black data points in figure 6.4. Subsequently, in section 6.3.3 we describe the gas flow and heat transfer inside the MW reactor with a nozzle attached at different flow rates and different nozzle diameters, as shown by the blue data points in figure 6.4. Then, in section 6.3.4 we validate our model results to experimental temperature data, measured using optical emission spectroscopy (OES). Finally, in section 6.3.5, using the calculated temperature data from these 3D models, we describe the effect of the nozzle on the recombination reactions and the net conversion, using a quasi-1D chemical kinetics model.

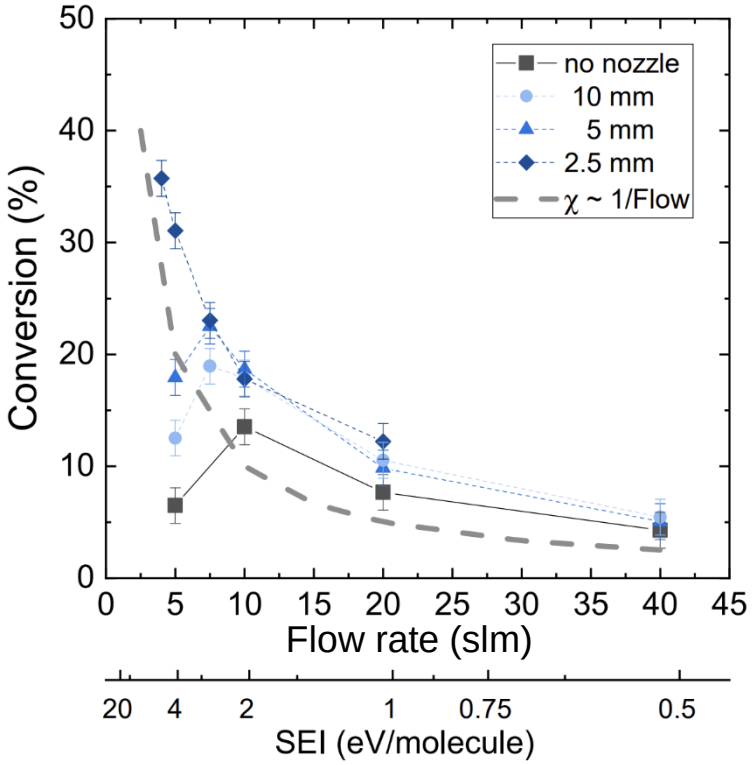

Figure 6.4: Measured conversion in the MW CO_2 plasma as a function of flow rate and SEI. The black line represents conversion without the nozzle, and the blue symbols are for different nozzle diameters, as indicated in the legend. The gray dashed line indicates the inverse relation between conversion and flow rate. The operating pressure is 900 mbar and the plasma power is 1500 W.

6.3.2 Behavior of the MW reactor without nozzle

The flow pattern inside the MW reactor, as calculated by our 3D CFD model, is shown in figure 6.5. The figure shows that the tangential gas injection creates a swirling gas flow in the reactor, which results in two distinct regions in the reactor, i.e. a cold edge and a hot center: gas swirling near the reactor walls flows at a high gas flow velocity around the hot plasma filament (indicated in the figure by the red cone), thus remaining cold and untreated by the plasma. This cool, high velocity swirling gas flow is vital to stabilize the plasma in the center of the reactor and to shield the quartz tube walls from overheating. Gas near the center of the reactor swirls at a lower flow velocity and is heated by the plasma filament (red cone) that is formed above the ignition pin. The gas temperature in this region increases significantly towards the center of the reactor, reaching temperatures up to 6000 K for gas flowing through the core of the plasma filament (see below).

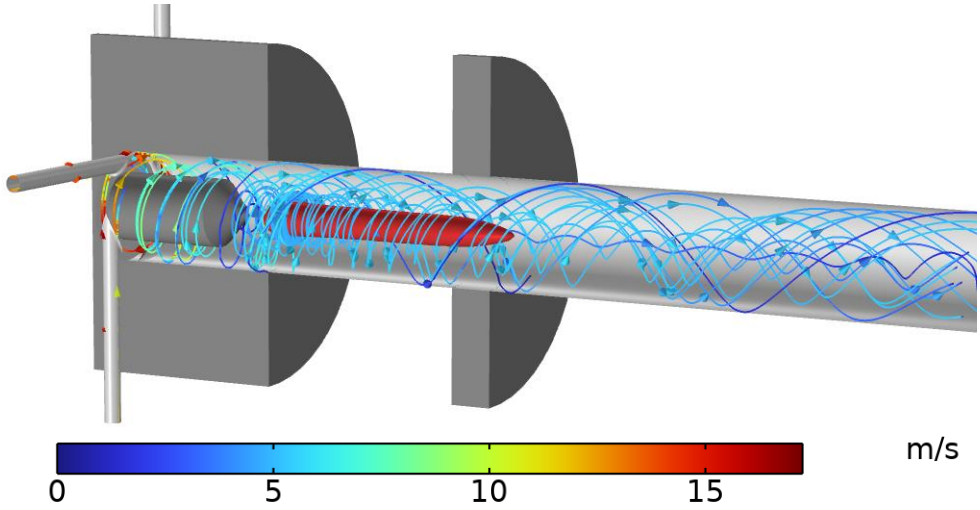

Figure 6.5: Calculated gas flow velocity streamlines in the MW reactor without a nozzle attached, operating at a flow rate of 20 slm and a pressure of 900 mbar. The contracted plasma filament is schematically illustrated in red.

Figure 6.6 illustrates the calculated gas temperature profiles inside the MW reactor operating at different flow rates. As the flow rate increases, the core plasma temperature remains more or less the same, i.e. between 5500-6000 K, which is in good agreement with the axial temperature profiles measured OES, which are discussed further in section 6.3.4. The shape and temperature of the afterglow, however, strongly change upon increasing flow rate, resulting in a cooler, narrower and shorter afterglow upon higher flow rates.

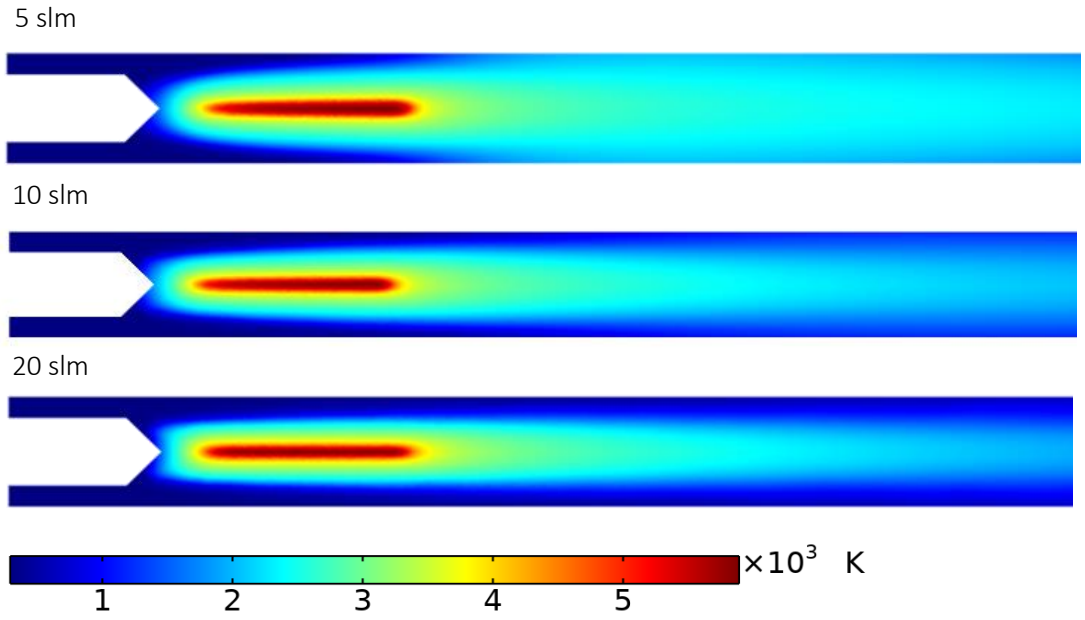

Figure 6.6: Calculated temperature profiles in the MW reactor without a nozzle attached, for flow rates of 5, 10 and 20 slm, operating at a pressure of 900 mbar and a plasma power of 1500 W

Figure 6.7 presents the magnitude and the direction of the calculated heat flux (as defined in equation 6.4, 6.6 and 6.8) at the different flow rates, while outlining the shape of the plasma filament in black. The direction of the convective cooling is represented by the black arrows, while the direction of the conductive cooling is represented by the red arrows. The figure shows that the cooling gradually increases upon higher flow rate, as the most significant cooling present is convective cooling, which increases at higher flow rates. The model shows that conductive cooling also occurs near the edges of the plasma filament where the highest temperature gradient is present (as indicated by the red arrows), but this cooling is an order of magnitude lower than the convective cooling of the gas flow. The figure clearly demonstrates that little heat transfer is present between the hot plasma core and the cool periphery gas flow around the plasma, due to the lack of mixing between these two regions. Given the increased convective cooling inherently present at higher flow rates, these higher flow rates tend to more effectively quench recombination reactions, which destroy the formed CO in the plasma afterglow. This will be further explained in section 6.3.5.

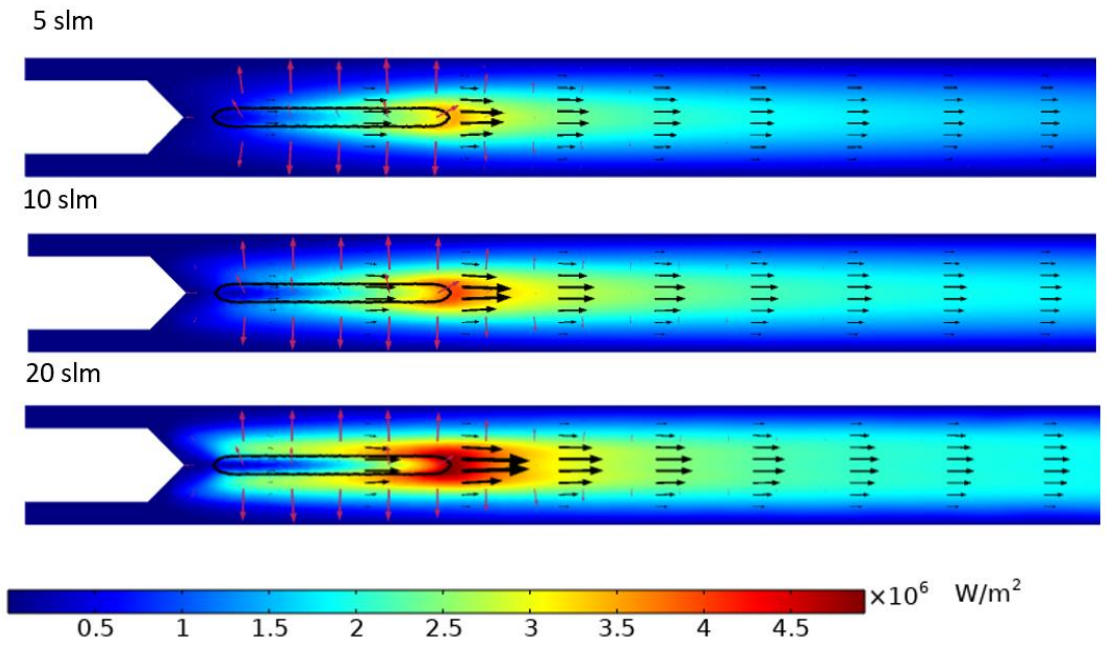

Figure 6.7: Calculated heat flux magnitude profile in the MW reactor without a nozzle attached, for flow rates of 5, 10 and 20 slm, operating at a pressure of 900 mbar and a plasma power of 1500 W. The direction of the convective heat flux is represented by the black arrows, while the direction of the conductive heat flux is represented by the red arrows. The shape of the plasma filament is outlined in black.

6.3.3 Revealing the effect of the nozzle

When a nozzle is attached in the reactor's effluent, the flow pattern in the reactor significantly changes, as shown by the calculated streamlines in figure 6.8 (a). This figure demonstrates that the nozzle disturbs the swirling flow pattern, forcing the rotating flow to converge and mix the hot gas in the center with the cool periphery gas flow, right at the end of the plasma. The flow is then highly accelerated by the

small opening in the nozzle. Figure 6.8 b) shows the same calculated streamlines as figure 6.8a) but using the color scale of figure 6.5, for an easy comparison of the flow behavior between a reactor with and without nozzle attached. As discussed and shown more clearly in section 6.3.5, the influence of the nozzle on the flow is already present before the gas has reached the nozzle, as the converging movement of the gas is dragged upstream by the gas viscosity. This causes a slight increase in gas flow velocity in the center of the reactor already before the nozzle when a nozzle is attached.

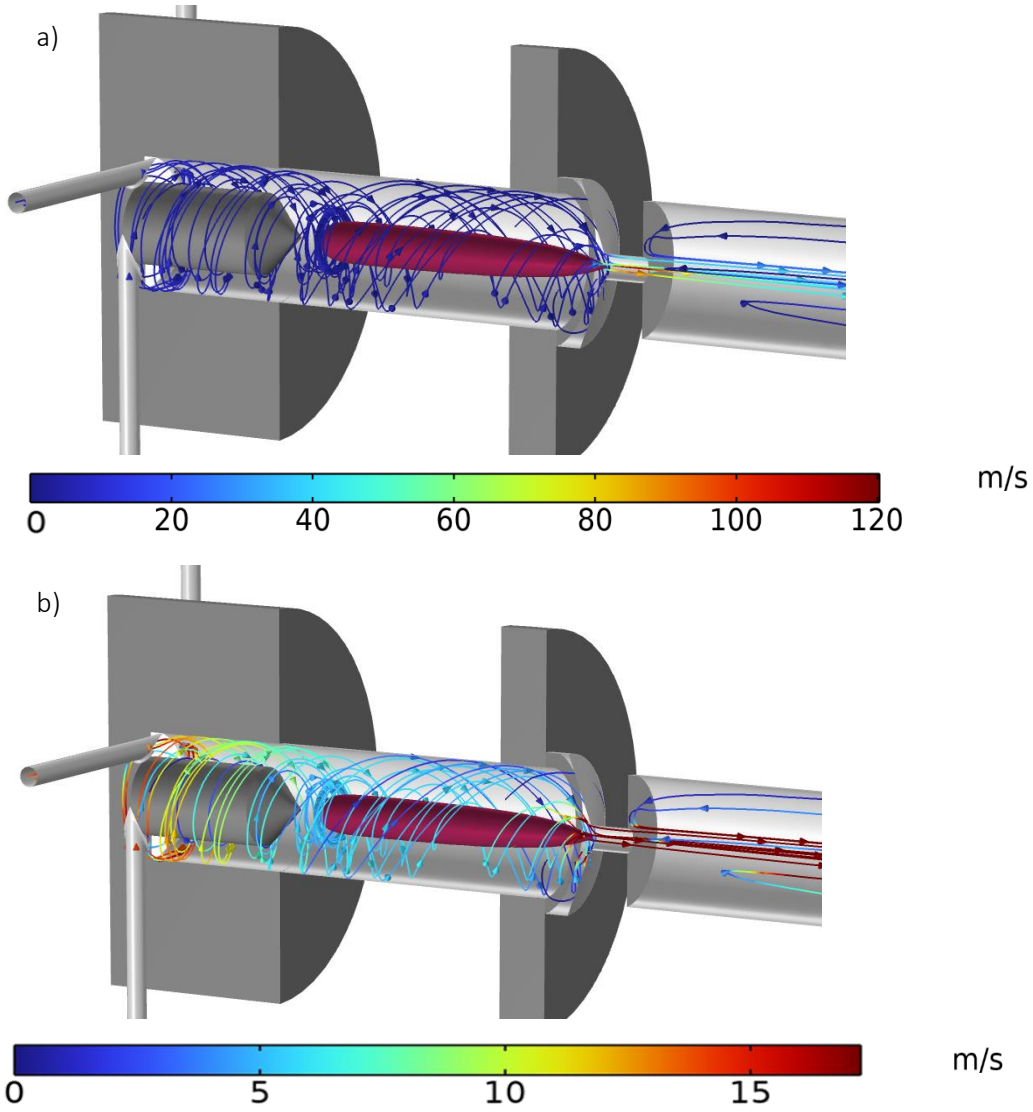

Figure 6.8: Calculated gas velocity streamlines in the MW reactor with a 5 mm nozzle attached, operating at a flow rate of 20 slm and a pressure of 900 mbar. The plasma filament is schematically illustrated in red. Figure b shows the same streamlines as figure a, but with the color scale of figure 3, to allow easy comparison between a reactor with and without nozzle.

The effect of the nozzle on the temperature profile in the plasma torch when using the nozzle is presented in Figure 6.9, where the calculated temperature profile in the reactor with a 5 mm nozzle for different flow rates is shown. It is clear that the nozzle greatly affects the temperature in the afterglow, which drops by more than 4000 K compared to the plasma region, and is different for the different flow

rates. Again, good agreement is reached between the calculated temperature profiles and the experimentally measured temperatures, which will be discussed further in section 6.3.4. Compared to figure 6.6, the plasma's hot afterglow is significantly shortened: after the nozzle, the gas temperature quickly cools down below 2000 K. Similar to the reactor without nozzle, the fastest cooling is observed at the higher flow rate, which will be discussed in more detail in section 6.3.5.

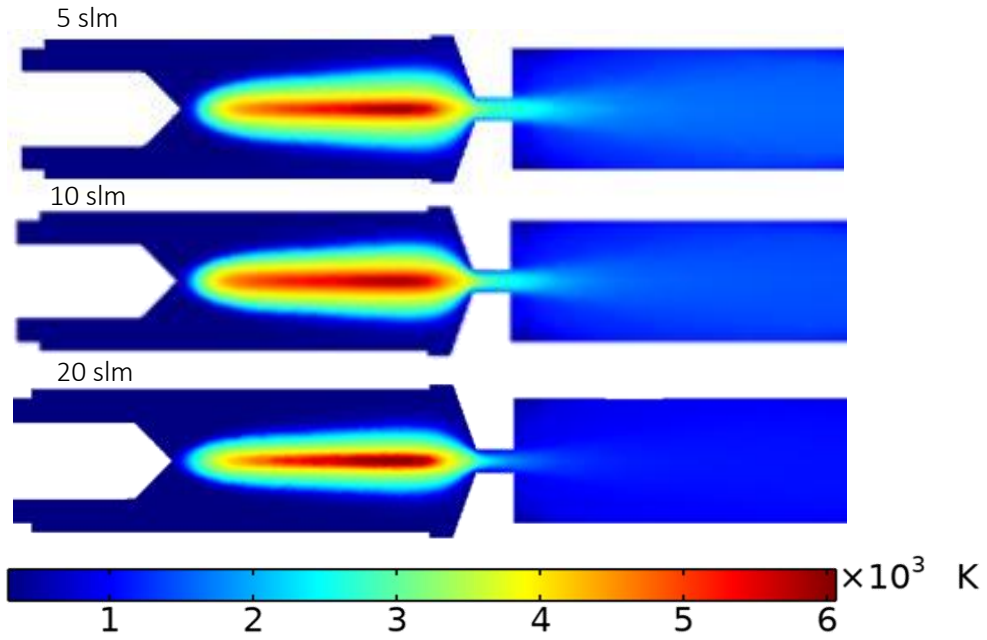

Figure 6.9: Calculated temperature profiles in the MW reactor with a 5 mm nozzle attached, for a flow rate of 5, 10 and 20 slm, operating at a pressure of 900 mbar and a plasma power of 1500 W

The heat transfer in the plasma torch with the nozzle becomes very concentrated in the throat of the nozzle as shown in Figure 6.10 which shows the magnitude and direction of the calculated heat flux in the MW reactor with 5 mm nozzle for different flow rates. The black arrows represent the direction of the convective heat flux and the red arrows the direction of the conductive heat flux. Compared to figure 6.7, the heat flux magnitude has increased by two orders of magnitude and is now mainly located in the throat of the nozzle. Our model shows that the cooling effect of the nozzle has two origins. First, the nozzle forces the cool, untreated gas near the walls to mix with the hot gas in the center. The second effect is due to the nozzle itself being externally cooled with cooling water. This is primarily done to prevent the copper nozzle from melting, as it is placed close to the hot plasma, but the model shows that, in addition, this greatly enhances the quenching capabilities of the nozzle. The effect of the cooled nozzle is demonstrated in figure 6.11, comparing the axial temperature profile in the center of the MW reactor between a 5 mm nozzle, cooled by room temperature water, and a hypothetical case where the nozzle is not cooled (and the heat loss is only defined by the limited heat dissipation through the reactor walls, like the rest of the reactor walls), for (a) a flow rate of 5 slm and (b) a flow rate of 20 slm. For both flow rates the figure shows that both nozzles display a very similar cooling curve, but the cooled nozzle

allows to eventually reach a temperature that is slightly lower (i.e. ± 500 K for 5 slm and ± 300 K for 20 slm) than the nozzle without water cooling. Hence, in addition to the convective cooling resulting from gas mixing inside the nozzle, conductive cooling through the nozzle walls allows for a significant portion of heat (i.e. ca. 275 W for 5 slm and 200 W for 20 slm) to be transferred out of the system, thus reaching lower overall temperatures in the afterglow. Note that more heat is transferred at 5 slm, as the lower flow rate allows the gas to spend more time in contact with the nozzle, resulting in more time to exchange heat with the cooled nozzle walls. Surface integration of the total calculated heat flux across the nozzle walls shows that the conductive cooling through the nozzle walls increases the overall heat transfer, and thus the overall cooling capacity of the nozzle, by ca. 35%. As illustrated by figure 6.11(a), the temperature would remain around 2500 K if no cooling is applied in the 5 slm regime, but it lowers to below 2000 K when the nozzle is cooled. As will be shown in section 6.3.5, this is an important temperature threshold for the recombination chemistry that is reached thanks to the nozzle cooling. In the 20 slm regime, however, figure 6.11(b) demonstrates that the temperature reaches the 2000 K threshold either way, both when the nozzle is and isn't cooled, thanks to the increased convective cooling present at this higher flow rate. Hence, the fact that the nozzle walls are cooled is expected only to influence the CO retention at lower flow rates (i.e. 5 slm).

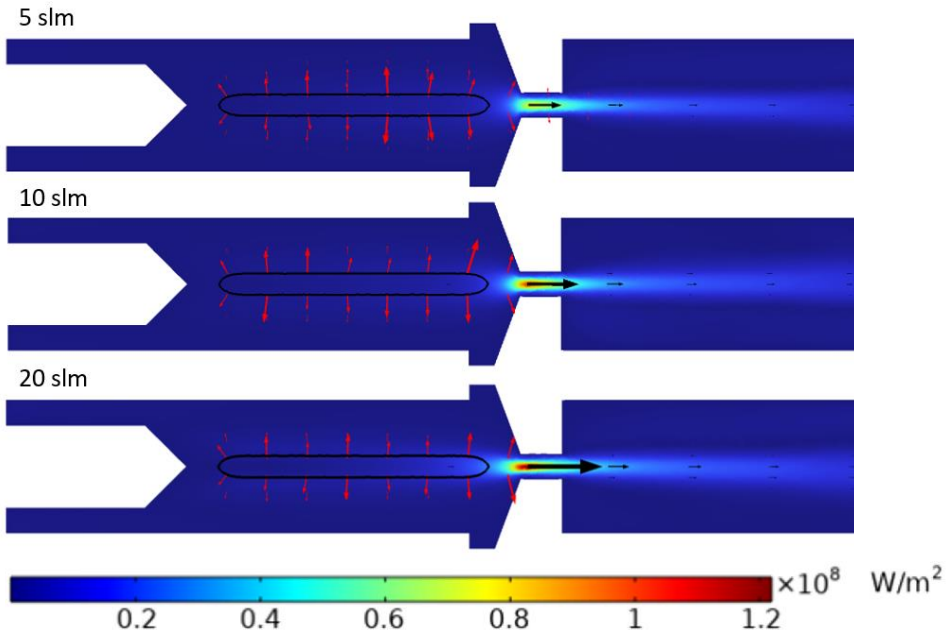

Figure 6.10: Calculated heat flux magnitude profile in the MW reactor with a 5 mm nozzle attached, for a flow rate of 5, 10 and 20 slm , operating at a pressure of 900 mbar and a plasma power of 1500 W. The direction of the convective heat flux is represented by the black arrows, while the direction of the conductive heat flux is represented by the red arrows. The shape of the plasma filament is outlined in black.

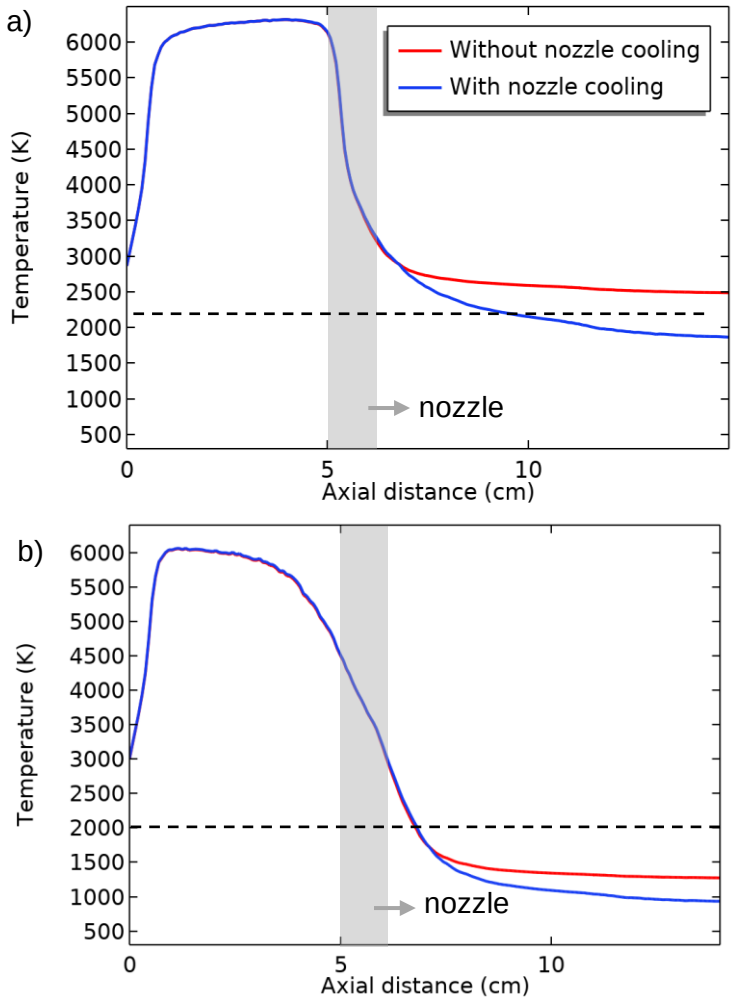

Figure 6.11: Calculated axial temperature profile in the center of the MW reactor for a reactor quipped with a cooled 5 mm nozzle attached and for a hypothetical case when the nozzle isn't cooled, for a) a flow rate of 5 slm and b) a flow rate of 20 slm

Finally, the magnitude of the heat transfer is also influenced by the nozzle diameter. Figure 6.12 shows the magnitude and direction of the calculated heat flux with nozzles of different diameters attached to a reactor operating at 10 slm. The black arrows represent the direction of the convective heat flux and the red arrows the direction of the conductive heat flux. As the nozzle diameter decreases, the cooling effect of the nozzle increases. Forcing the gas through a smaller opening induces more gas mixing and higher gas flow velocities, which increases convective cooling. Furthermore, it also induces more contact with the cooled nozzle walls, resulting in more conductive cooling. Note that reducing the nozzle diameter yields a higher pressure inside the reactor. For the 2.5 mm nozzle, the model predicts the pressure difference over the nozzle (i.e. before and after the narrow nozzle gap) to be about 250 mbar, which is comparable to the pressure differences observed experimentally by Hecimovic et al.[112] In the simulation the pressure difference was observed as the increase of the pressure in the resonator, with respect to the 900 mbar boundary conditions in the effluent. In the experiment the 900 mbar was

maintained inside the resonator and the low pressures are observed in the effluent. While this pressure build-up is not enough to yield supersonic flow velocities, we can expect this to occur when the pressure on the outlet is reduced below 900 mbar.

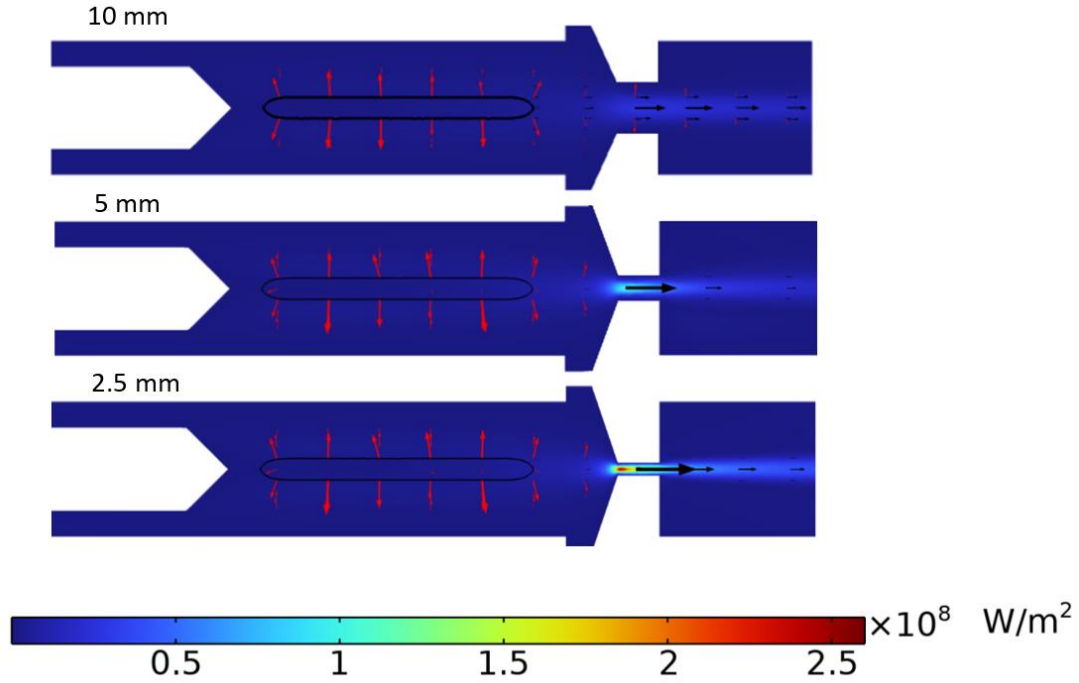

Figure 6.12: Calculated heat flux magnitude profile in the MW reactor with a 10, 5 and 12.5 mm nozzle attached, for a flow rate of 10 slm, operating at a pressure of 900 mbar and a plasma power of 1500 W

6.3.4 Validation of the calculated gas temperature profiles

Figure 6.13(a) presents the axial profile of the gas temperature in the plasma, measured using OES (C_2 swan band) by D'Isa et al.,[24] as well as the gas temperature calculated by our 3D CFD model for a MW reactor without a nozzle, operating at a flow rate of 10 slm. Figure 6.13(b) presents the same data for a MW reactor with a 2.5 mm nozzle attached, and in addition shows the axial profile of the vibrational temperature, also measured using OES, making use of the database developed by Carbone et al.[117] Figure 6.13(b) shows that the MW plasma is in quasi-thermal equilibrium, as the vibrational temperature is more or less equal to the gas temperature. Furthermore, the figures show that the gas temperature calculated by the model is in satisfying agreement with the experimental data.

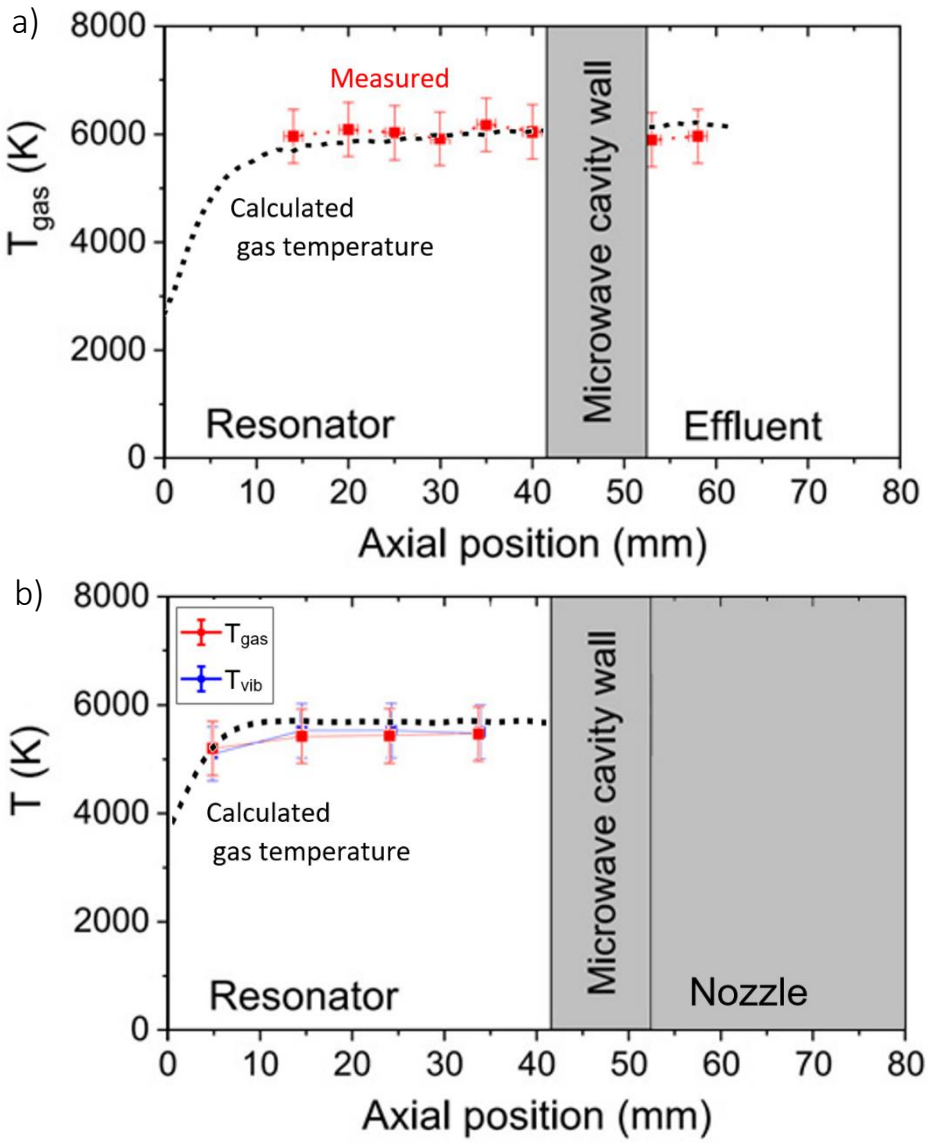

Figure 6.13: Axial profile of the measured gas (rotational) temperature, as well as the gas temperature calculated by our 3D CFD model, for a MW reactor, a) without nozzle attached, as adopted from D'Isa et al.[10] and b) with a 2.5 mm nozzle attached, operating at 10 slm, at a pressure of 900 mbar and a plasma power of 1500 W. In (b), also the vibrational temperature is plotted.

Figure 6.14 presents the radial temperature profiles of the calculated gas temperatures and the gas temperature measured with a thermocouple at different distances from the waveguide, for a MW reactor with 5 mm nozzle, operating at different flow rates. Note that at lower flow rates, the temperature could only be measured at longer distances from the waveguide due to the temperature becoming too high for thermocouple measurements. The figures display satisfying agreement between the calculated gas temperatures and the experimental data.

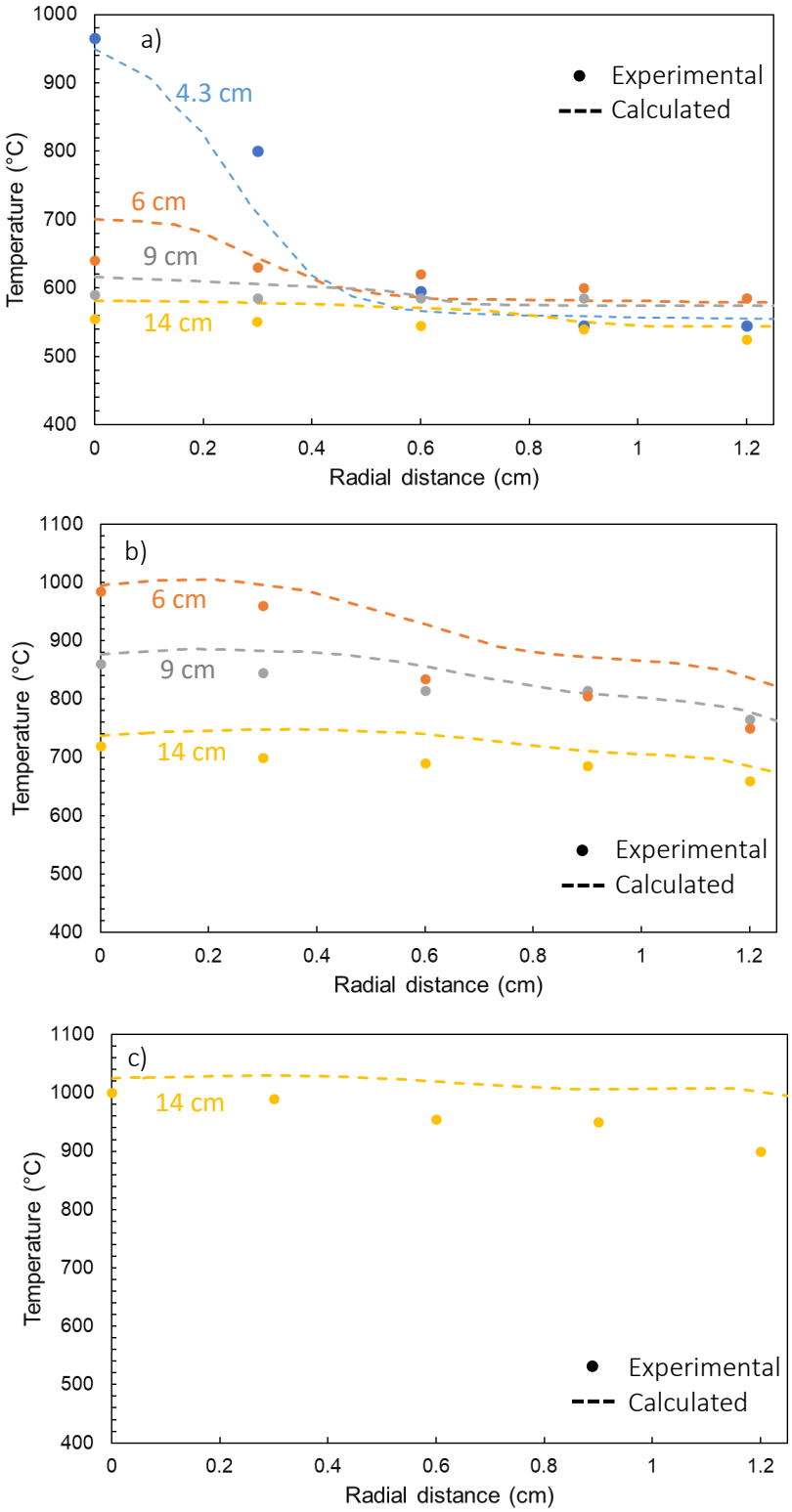

Figure 6.14: Calculated and experimental radial temperature profiles at different distances from the waveguide, for a MW reactor with a 5 mm nozzle attached, for a flow rate of a) 20 slm, b) 10 slm and c) 5 slm, at a pressure of 900 mbar and a plasma power of 1500 W.

6.3.5 Effect on the conversion and underlying chemistry

In this section we reveal how the cooling capabilities of the nozzle affect the recombination reactions and why this quenching effect is more significant for lower flow rates. To investigate the mechanisms of the CO recombination reactions and to reveal important temperature thresholds in the thermal CO_2 dissociation process, we modeled the CO_2 chemistry in the reactor with a quasi-1D chemical kinetics model. This model simulates the thermal CO_2 dissociation process over a one-dimensional straight line in the reactor, based on the gas flow velocity and temperature profile, as calculated by the 3D CFD model. Figure 6.15 shows the result of the quasi-1D chemical kinetics model for a reactor operating at a flow rate of 20 slm without nozzle, for a temperature profile taken in the center of the reactor. These simulation results thus represent the evolution of gas flowing through the center of the plasma filament, starting at the beginning of the waveguide. The left y-axis of figure 6.15 corresponds to the gas temperature profile, illustrating that in the plasma core the gas heats up to 6000 K, but at the end of the waveguide (corresponding to 0.17 s), the gas quickly cools back down, to 1500 K after 0.23 s. The right y-axis of figure 6.15 shows the corresponding calculated CO production rate. A positive value for the production rate indicates the formation of CO (mainly by the $CO_2 + O \rightarrow CO + O_2$ reaction), while a negative value for the formation rate indicates the destruction of CO (mainly by the $CO + O + M \rightarrow CO_2 + M$ reaction).

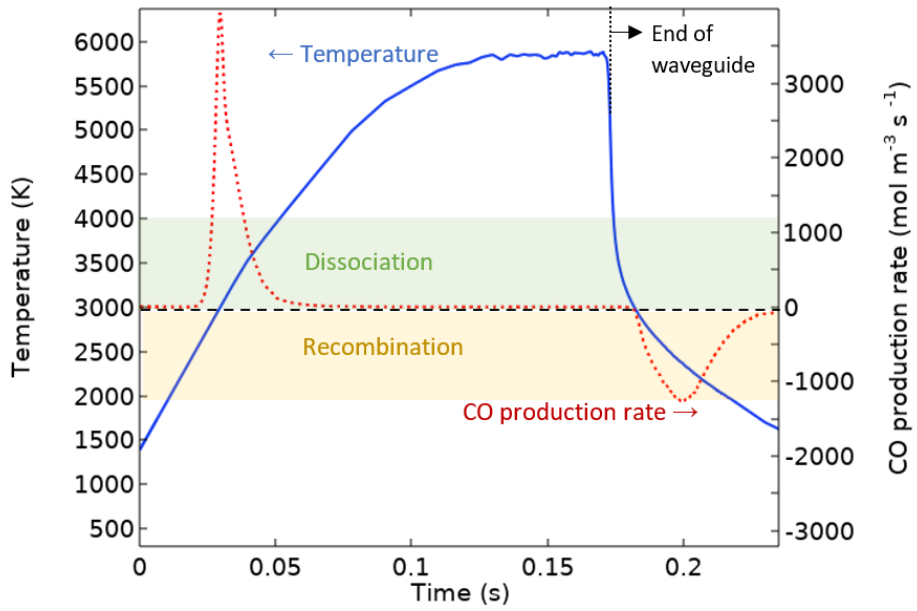

Figure 6.15: Calculated gas temperature profile (left y-axis) and CO production rate (right y-axis) over a straight line in the center of the MW reactor without a nozzle attached, for a flow rate of 20 slm. The temperature threshold for net thermal CO_2 dissociation above 3000 K and the zone of recombination between 2000 and 3000 K are also highlighted in the figure.

The figure shows that as the gas approaches the plasma filament and the gas temperature rises above 1800-2000 K, the formation rate of CO increases, eventually reaching a peak value around a

temperature of 3000 K. As highlighted in the figure, this temperature value is considered the threshold for efficient thermal CO_2 conversion. While the exact values of these temperature thresholds can vary slightly upon changing flow rate, they are in good agreement with what is expected in literature for thermal CO_2 chemistry at atmospheric pressure.[9] Once the gas temperature increases further, the CO formation rate decreases again, eventually reaching zero at around 0.05 s, when the temperature has reached ca. 4000 K. At these temperatures the rate of CO recombination balances the dissociation rate, reaching a steady state situation where there is no net formation or destruction of CO. Note that at temperatures around 6000 K, CO dissociation into C and O is also present, although in a very limited amount. Once the gas has passed through the plasma filament and cools back down to below the 3000 K threshold, the efficient thermal CO_2 dissociation diminishes, while the recombination reactions still occur. This translates into a negative CO formation rate, because CO recombines with O (+ M) into CO_2 (+ M). Hence, 3000 K is considered the threshold for the recombination reactions (as indicated by the horizontal dashed line in figure 6.15). Once the gas temperature decreases below ca. 2000 K, the CO formation rates becomes zero again, as the temperature is now too low for either of the recombination or dissociation reactions to occur. To avoid recombination reactions and reduce the overall CO destruction, the gas temperature should thus, once cooled down below the 3000 K threshold, drop as quickly as possible below 2000 K to quench the recombination reactions. Integration of the positive and negative CO production peaks in figure 6.15 shows that the time-integrated CO destruction rate is 72 % of the time-integrated CO production rate, meaning that 72 % of the CO that is formed in the center of the plasma is destroyed after the plasma by recombination.

Similar to figure 6.15, figure 6.16 illustrates the calculated temperature profile and CO production rate in the center of the reactor, again for a reactor without nozzle, but operating at 5 slm. At this lower flow rate, the gas takes more time to reach the plasma filament and heat up to the 3000 K and 4000 K thresholds. Likewise, the gas spends a longer time at the temperature for net thermal conversion, making the initial CO production peak broader compared to at 20 slm, although the maximum value is clearly lower (cf. figure 6.16 vs. figure 6.15). However, after the plasma the gas also cools down more slowly, due to the limited convective cooling shown previously in figure 6.7. As a result, the gas also spends more time in the recombination zone below 3000 K, broadening the CO destruction peak, and resulting in a higher loss in CO due to recombination reactions. Indeed, while for a flow rate of 20 slm, 72 % of the produced CO was destroyed in the negative CO production peak in figure 6.16, time-integration of the CO production peaks in figure 15 shows that for a flow rate of 5 slm, 83 % of the produced CO is destroyed by recombination after the plasma.

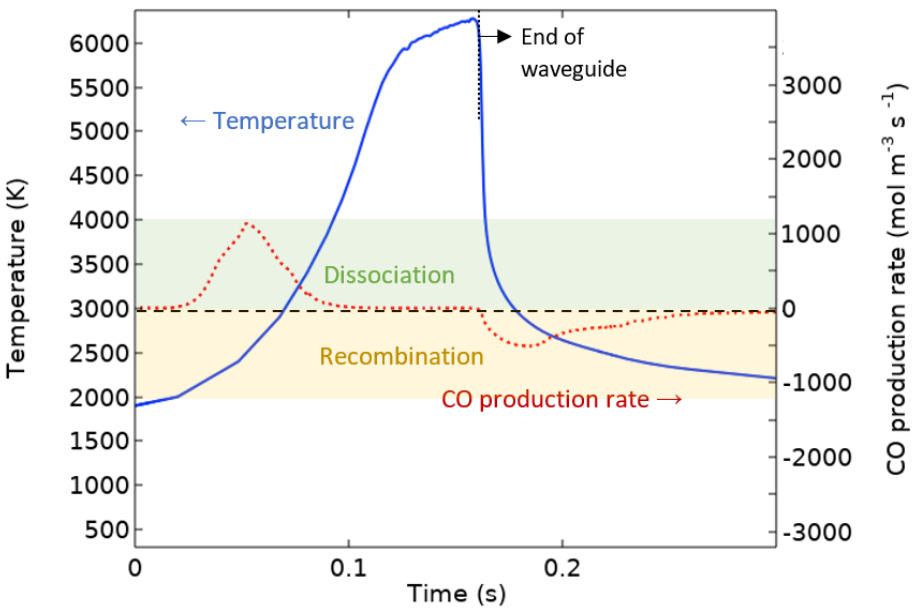

Figure 6.16: Calculated gas temperature profile (left y-axis) and CO production rate (right y-axis) over a straight line in the center of the MW reactor without a nozzle attached, for a flow rate of 5 slm. The temperature threshold for net thermal CO_2 dissociation above 3000 K and the zone of recombination between 2000 and 3000 K are also highlighted in the figure.

Figure 6.17 shows the results for running the quasi-1D chemical kinetics model in the center of the reactor for 20 slm (a) and 5 slm (b) with a 5 mm nozzle attached to the reactor. The results from figure 6.15 and 6.16 without nozzle are also depicted (as dashed lines) to more easily distinguish the effect of the nozzle. The figures show that for both high and low flow rate, adding a nozzle drastically changes the cooling curve after the plasma in two distinct ways: (i) while the temperature is slightly higher inside the plasma, it reaches a lower value after the plasma compared to when no nozzle is attached, and (ii) the average cooling rate in the effluent is much higher, i.e., it rises from 9.1×10^4 to 6.0×10^5 K/s for 20 slm, and from 6.4×10^4 to 4.8×10^5 K/s for 5 slm. Locally, in the steepest part of the cooling curve, the cooling rate even exceeds 10^7 K/s, which is indeed high enough to efficiently suppress recombination reactions according to literature.[10] Due to these high quenching rates, the time spent after the plasma in the recombination zone between 2000 and 3000 K (i.e. 0.03 s for 20 slm and 0.12 s for 5 slm) is drastically reduced compared to the reactor without quenching nozzle, especially for the 5 slm case, where the gas took a long time to cool down below 2000 K without nozzle attached. As a result, recombination only occurs for a very short time, which is represented by the very narrow negative peaks in the CO production rate. Note that these destruction peaks are high in intensity, reaching almost -10,000 mol $m^{-3}s^{-1}$ at 20 slm. This is due to the high concentration of O atoms that are still present for a short amount of time when the gas is quickly quenched from 6000 K. However, these peaks are very short in duration (i.e. less than 0.5 ms), resulting in very low overall CO recombination during this timeframe. For 20 slm, the time-integrated value of the CO destruction peaks in figure 6.17 (a) is reduced from 72 % to 24 % of the time-integrated CO production peak, while for 5 slm in figure 6.17

(b), the time-integrated CO destruction is reduced from 83 % to 64 % of the time-integrated CO production peak. Note that attaching a nozzle not only impacts the cooling curve of the temperature profile, but also has a limited influence on the heating curve: both for the 20 slm and 5 slm regime, the temperature profile reaches its maximal value slightly faster when a nozzle is attached. As mentioned earlier in section 6.3.3, this is attributed to the flow velocity field in the reactor that has slightly adapted to the converging shape of the nozzle, making the gas flow slightly faster in the center of the reactor.

While this reduced CO destruction due to fast quenching explains the overall improvement seen in figure 6.4 when the nozzle is attached, it does not yet explain the significantly higher improvement at lower flow rates compared to higher flow rates. However, figures 6.15 – 6.17 only represent gas flowing through the center of the plasma, and do not capture the overall effect in the whole reactor. Indeed, a significant portion of the treated gas will not experience the maximum temperature of 6000 K in the center of the plasma filament, but will flow closer near the edges of the plasma, where the gas temperature lies between 2000 – 4000 K.

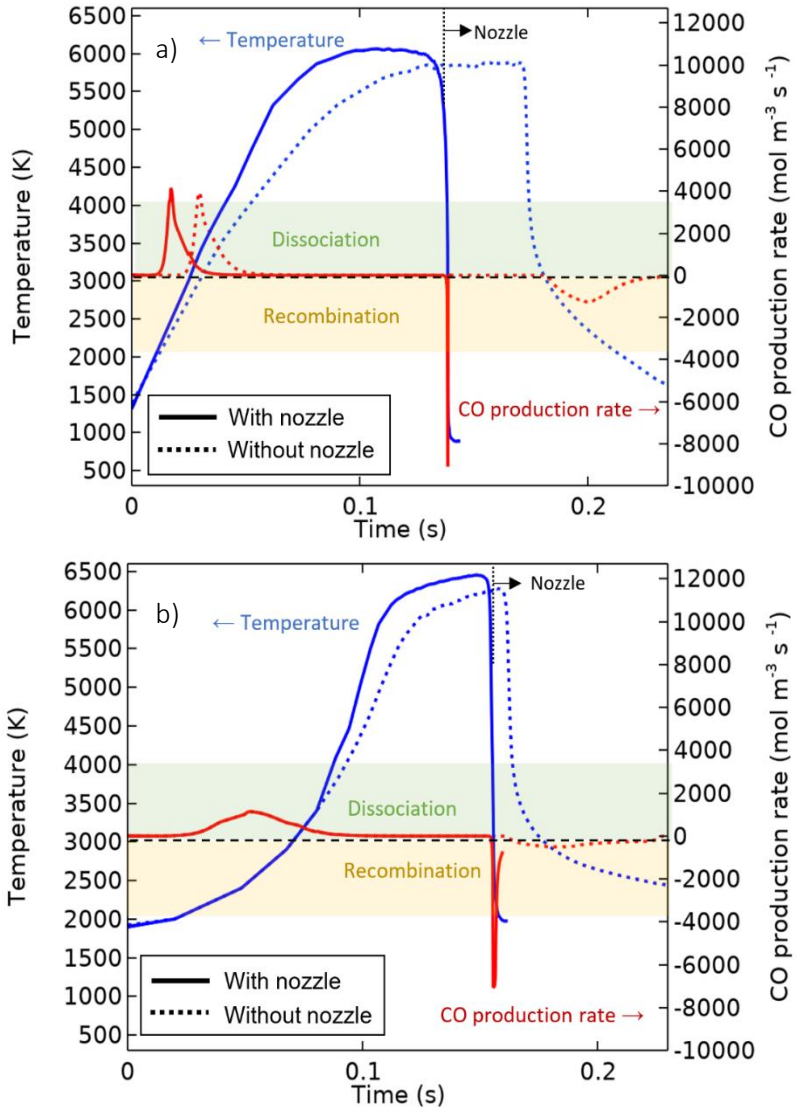

Figure 6.17: Calculated gas temperature profile (left y-axis) and CO production rate (right y-axis) over a straight line in the center of the MW reactor with and without a 5 mm nozzle attached, for a flow rate of a) 20 slm and b) 5 slm. The temperature threshold for net thermal CO_2 dissociation above 3000 K and the zone of recombination between 2000 and 3000 K are also highlighted in the figure.

Figure 6.18 shows the calculated temperature profile and CO production rate over a straight line at a radial distance of 6.5 mm from the center of the reactor, for a flow rate of 20 and 5 slm without nozzle attached. The temperature profiles indicate that due to the increased convective cooling, the temperature in this part of the reactor is clearly lower at 20 slm compared to 5 slm. At 5 slm the temperature reaches up to 2500 K, while at 20 slm, the gas temperature barely exceeds 2100 K. This was also represented in figure 6.6, where the high temperature zone extends to a somewhat larger radial distance at 5 slm compared to at 20 slm. At 5 slm, the temperature is high enough for some CO_2 dissociation to occur in this region (i.e., radial distance of 6.5 mm), although at a lower rate than in the center of the reactor, as the threshold temperature of 3000 K for efficient thermal conversion is not reached. After the plasma, CO recombination still occurs, as indicated by the negative CO production

rate, although also at a lower rate than in the center. This indicates that also in this part of the reactor, an improvement in conversion would occur if the gas is quenched after the plasma, as the negative peak of the CO production rate is positioned behind where the nozzle would be placed (as indicated in figure 16). At 20 slm, however, the temperature only reaches up to 2100 K, so that very limited thermal CO_2 dissociation occurs, as shown by the very small peak in CO production rate. Furthermore, the gas temperature does not peak high enough above 2000 K to induce significant recombination reactions. Hence, in this part of the reactor at 20 slm, the limiting factor of the CO_2 conversion process is not CO recombination, but rather the short residence time in the hotter regions of the plasma. As a result, this part of the reactor will not display a significant improvement in CO retention due to quenching, making the overall effect of quenching on the MW reactor performance as a whole less impactful for 20 slm. This is in great contrast to the reactor operating at 5 slm, where CO_2 conversion is limited by recombination also beyond the center of the reactor, where most of the gas flows, and quenching could thus impact the conversion in large parts of the gas stream.

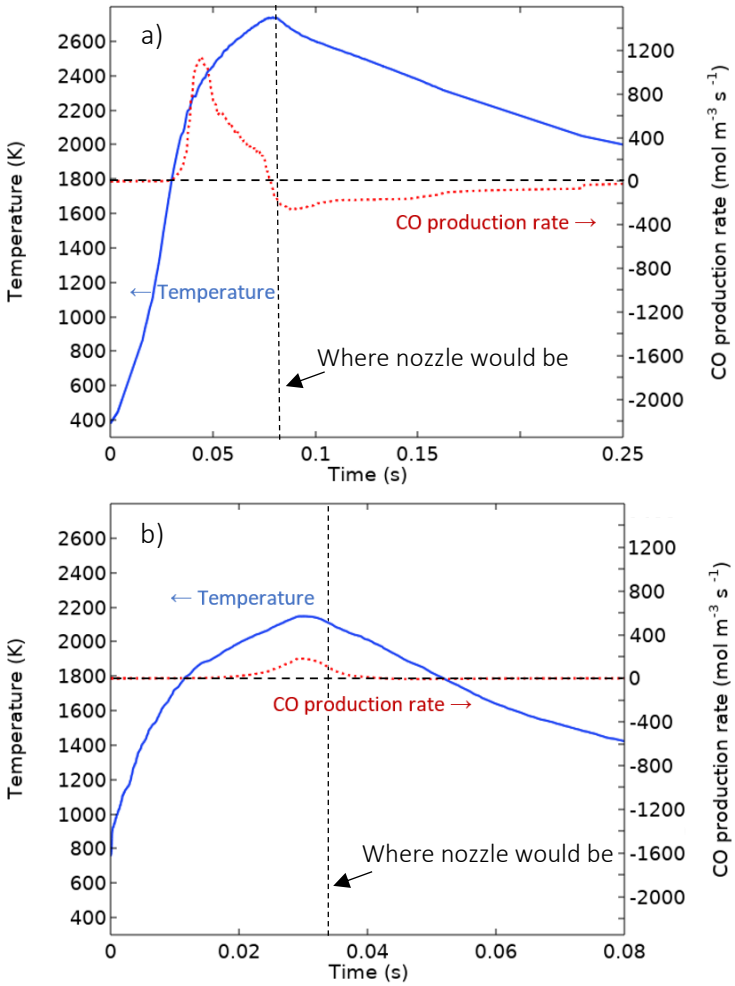

Figure 6.18: Calculated gas temperature profile (left y-axis) and CO production rate (right y-axis) over a straight line at 6.5 mm from the center of the MW reactor without a nozzle attached, for a flow rate of a) 5 slm and b) 20 slm.

The fact that the CO_2 conversion in the outer layers of the plasma is mainly limited by the residence time at high flow rates (e.g., 20 slm), and mainly by recombination at low flow rates (e.g., 5 slm), is also represented in the experimental results in figure 6.4. For a reactor without nozzle (black data points), lowering the flow rate from 40 slm down to 10 slm improves the conversion, indicating that conversion could be limited by the residence time, and lowering the flow rate, thus increasing the residence time, the conversion could be enhanced. In general, given the inverse relation between flow rate and SEI, this can be summarized as the SEI being the limiting factor, as at high flow rates the SEI is simply too low to provide enough power to the gas within the short time frame that the gas spends flowing through the active parts of the plasma. Indeed, these data points align with the inverse relation between flow rate and conversion (which is the same as the directly proportional relation between SEI and conversion), indicated by the grey dashed line. Reducing the flow rate to 5 slm, however, does not follow this relation, as the overall conversion drops. Indeed, lowering the flow rate even more (to 5 slm) reduces the convective cooling and increases the significance of back reactions in the whole reactor. Figure 6.4 indicates that below 10 slm, the conversion is mainly limited by recombination, rather than by residence time.

This is further demonstrated in figure 6.4 when a nozzle is attached to the reactor (blue data points). The greatest improvement is seen at 5 slm, which is most limited by recombination, while smaller improvements are observed at higher flows, when already in the standard case without nozzle there are less recombination reactions. As shown by figure 6.4, the improvement due to quenching by the 2.5 mm nozzle at 5 slm is so significant, that this case also becomes residence time-limited. Indeed, the recombination reactions are suppressed to the extent that lowering the flow rate from 10 slm to 5 slm enhances the conversion, aligning again with the inverse flow rate-conversion relation.

6.4 CONCLUSION

We developed a 3D CFD model and a quasi-1D chemical kinetics model to simulate the effect of quenching nozzles developed by Hecimovic et al., for enhancing the CO_2 conversion in a MW plasma reactor by quenching the recombination reactions in the effluent. Our models show that due to the tangential gas injection, two distinct regions are formed in the reactor: (i) hot gas that swirls in the center of the reactor and (ii) cool gas swirling near the walls, which forms a cool periphery gas flow around the hot center. Without nozzle attached, there is very limited heat transfer between these two regions, and the only cooling present is due to convective cooling from the gas stream, which is more significant at higher flow rates. When a nozzle is attached, the cooling drastically increases in two ways: (i) the small nozzle opening forces the hot gas in the center and the cool gas near the walls to mix, while (ii) the nozzle walls (being water-cooled) induce additional conductive cooling. In this way, the effluent

gas can be cooled faster, and to lower temperatures. Our quasi-1D chemical kinetics model shows that the nozzle allows to quickly cool below some important temperature thresholds, i.e. the recombination zone between 2000 and 3000 K. The fast cooling capabilities of the nozzle allow the gas to spend less time in the “recombination zone”, thus limiting the amount of CO lost to recombination reactions.

While the fastest cooling in general (i.e., with nozzle as well as without quenching nozzle) is observed at the higher flow rates, due to the more pronounced convective cooling, the largest improvement due to the quenching nozzles is observed at the lowest flow rate of 5 slm. Due to the strong cooling capabilities of the smallest nozzle of 2.5 mm, we have shown that recombination reactions are suppressed to such an extent that also the low flow rate regime of 5 slm becomes limited by residence time, rather than by recombination, and due to the great reduction of recombination reactions, the conversion enhances by even a factor seven, i.e., from 5% without nozzle, to 35% with quenching nozzle.

7 GENERAL CONCLUSION AND FUTURE OUTLOOK

In this thesis I used computational modelling as a tool to describe the underlying mechanisms of various plasma reactors for plasma-based gas conversion. Throughout the different chapters, I described three different reactors, i.e. the RGA, GAP and MW reactor, and three different gas conversion applications, i.e. N_2 fixation, combined CO_2-CH_4 conversion and CO_2 splitting. Each time I used a combination of various computational models to propose an answer to research questions that were generated by interesting initial experimental observations, made by fellow colleagues. The experiments could significantly improve upon existing literature data in terms of reactor performance. For N_2 fixation into NO_x, the RGA (first without, and then with effusion nozzle) achieved the best performance for atmospheric pressure reactors reported up to the time of these studies, yielding NO_x concentrations up to 5.9%, at an energy cost down to 2.1 MJ mol^{-1}, while at the start of my PhD, the record values up to that point were only 2% at an energy cost of 2.8 MJ mol^{-1}.[55,56] It should be noted that during/after these RGA studies, other experiments were also performed with other plasma types, yielding very good results. Indeed, Kelly and Bogaerts obtained NO_x concentrations up to 3.8%, at an energy cost down to 2.0 MJ/mol in an atmospheric pressure MW plasma, operating at higher power and flow rate, thus reaching record-high NO_x production rates of 0.77 L/min.[15] Likewise, Vervloessem et al. used a pulsed spark atmospheric pressure plasma jet, and obtained a record-low energy cost of 0.42 MJ/mol, albeit at very low NO_x concentrations of 200 ppm, due to the low power used.[54] Nevertheless, the RGA still yields among the best results reported ever. For CO_2-CH_4 conversion with N_2 admixtures, the GAP reactor performance was among the best in literature, achieving a total conversion of 25.8 %, and (absolute) conversions of 28.6 % for CO_2 and 35.9 % for CH_4 at a total energy cost of 2.2 eV/molec (or 8.7 kJ/L) and energy efficiency of 58 %. Finally, using quenching nozzles in a MW reactor also yielded CO_2 conversions that are amongst the highest at atmospheric pressure, achieving a CO_2 conversion of 35 % at an energy efficiency of 26%. While I did not contribute to these experiments myself, I was able to reveal the underlying mechanisms of the process and thus pinpoint the reason for the excellent results, thanks to my computational models. This way I was able to reveal the underlying chemistry of the rotating and steady arc regime of the RGA reactor and explain why the two modes delivered different results in terms of NO_x formation. Subsequently I could reveal through computational modelling the quenching effect of the effusion nozzle for suppressing the reverse Zeldovich mechanism, and explain the significant improvements it brought to the performance of the RGA reactor. For plasma-based DRM, my computational model could reveal that the addition of 20% N_2 increased the electron density and gas temperature inside the plasma, leading to an increased absolute conversion and lower SEI that outweigh

the diluting effect of adding N_2. Finally, my models could also reveal the convective and conductive cooling effect of quenching nozzles in CO_2 MW plasmas, suppressing recombination reactions the increase the CO retention in the reactor. Furthermore, it was revealed that the suppression of recombination reactions has more impact at low flow rates, where recombination is the most limiting factor in the conversion process.

The modelling insights acquired in this thesis open up the way to improve further upon these and other plasma-based processes. Indeed, while we have not yet reached the point at which plasma-based gas conversion applications are competitive with their current fossil fuel-based counterparts, if we extrapolate the improvements that could be achieved in only the four years of this PhD, the future does seem promising for plasma technology playing a prominent role in the electrification of the chemical industry. In the following section, we discuss on how this improvement process can continue in the upcoming years.

While originally the best performances for plasma-based gas conversions were achieved by non-thermal plasmas at reduced pressure,[21] inducing a pronounced vibrational non-equilibrium, and thereby promoting the vibrational dissociation pathway, has proven not to be straightforward to realize in practice. Recent insights based on both modeling and experiments have revealed that the CO_2 conversion in (sub)atmospheric pressure MW and GA plasmas, i.e. quasi-thermal plasmas, proceeds by thermal reactions[22,23,34,68,111] and this can also give rise to quite high energy efficiencies (up to 40– 50%). The same can be said about plasma-based N_2 fixation, as Kelly and Bogaerts recently obtained NO_x concentrations up to 3.8%, at an energy cost down to 2.0 MJ/mol in a quasi-thermal MW reactor working at atmospheric pressure.[15] Indeed, also throughout all chapters of this thesis, the thermal dissociation channel in our quasi-thermal plasmas always presented itself as the most efficient chemical pathway for both CO_2 conversion and N_2 fixation. While quasi-thermal plasmas are too hot to sustain a vibrational non-equilibrium, and thus lack the vibrationally-promoted dissociation pathway, the reaction rates of the thermal reactions between various plasma species rise drastically upon higher gas temperature, thus enhancing the conversion. Furthermore, the atmospheric pressure conditions of these plasmas are much more industry-friendly, making quasi-thermal plasmas more suitable for industrial applications, which is eventually the desired end-goal.

To optimize quasi-thermal plasmas, chapters 4 and 6 demonstrated that most impact is not made by optimizing the plasma process itself, but by what happens after the plasma. Indeed, as demonstrated in chapter 6, the CO_2 conversion within the contracted MW plasma filament, where the gas temperature lies around 6000 K, is near 100%. Also in chapter 4, we reveal that within the hot arc, NO_x concentrations up to 10% are found, which lies very close to the thermal production limit. The big losses only occur

after the plasma due to recombination reactions, breaking down the formed plasma products. Therefore, both chapter 4 and chapter 6 demonstrate that fast quenching of the gas after passing through the plasma, from temperatures above 3000 K to below 2000 K, can drastically improve the performance of quasi-thermal plasmas, and should thus be extensively investigated as an optimization strategy. Various quenching methods have already been proposed, such as supersonic quenching in a converging nozzle yielding adiabatic expansion and conductive cooling through cooling tubes.[7] At very high quenching rates, a vibrational non-equilibrium, created or enhanced by the sudden drop in gas temperature can promote further dissociation of CO_2 or N_2, which is called super-ideal quenching. Ideally, the heat removed from the outflowing gas mixture due to the quenching/cooling process can be recovered to preheat the incoming gas so that the less plasma power is needed for heating the gas, and making the whole process more energy-efficient.

Besides improving the conversion and energy efficiency through quenching, there is also room for improvement in the field of plasma catalysis.[118] As catalyst have already proven to be successful in conventional thermal processes, the use of post-plasma catalysis in the afterglow of quasi-thermal plasmas is also a promising research route.

Finally, up until now, plasma research focused mainly on scientific rather than on technological aspects of the plasma process. For plasma reactors to be applied on an industrial scale, more research is needed considering scaling up the technology, involving issues related to downstream processing, safety, reliability of operations, possibility of management of fluctuations in space-velocity, temperature, and compositions, etc. The most straightforward way is by placing a large number of plasma reactors in parallel, as demonstrated already for ozone synthesis in DBD plasma reactors.[11] However, before numbering up, current lab-scale plasma reactors may also be scaled up in size to some extent, to allow higher flow rates and power. Recently, these aspects of the research are gaining more interests, as the performance of the plasma-based gas conversion reactors approach the efficiency target to be competitive. For instance, detailed life cycle assessments (LCA) have been carried out on an upscaled plasma-based N_2 fixation process to prove the environmental benefits by comparison to existing fixation processes for the synthesis of nitric acid[119], and the first wind-powered pilot plant for plasma-based ammonia production has already been tested, proving the integration of plasma technology with renewable electricity.[120]

8 APPENDIX

8.1 TURBULENT FLOW SHEAR STRESS TENSOR (SST) MODEL

The turbulent model applied in our study is the RANS (Reynolds-Averaged-Navier-Stokes) SST (Shear Stress Tensor) model, which uses the common k-ε model in the free stream and combines it with the more accurate k-ω model near the walls.[61] In this k-ω model the viscous layer at the boundaries is fully resolved, i.e. the model is more accurate for the flow near the walls than in models where so-called wall functions are used that employ analytical solutions for the behavior near the walls. This approach includes the following equations for the turbulent kinetic energy k and the specific dissipation ω:

$$\rho(\overrightarrow{u_g}.\nabla)k = \nabla \cdot [(\mu + \mu_T \sigma_k)\nabla k] + P - \beta_0 \rho \omega k \tag{8.1}$$

$$\rho(\overrightarrow{u_g}.\nabla)\omega = \nabla \cdot [(\mu + \mu_T \sigma_\omega)\nabla \omega] + \frac{\gamma}{\mu_T}\rho P - \beta_0 \rho \omega^2 + 2(1 - f_{v1})\frac{\sigma_{\omega 2}\rho}{\omega}\nabla k \cdot \nabla \omega \tag{8.2}$$

Where ρ stands for the gas density, $\overrightarrow{u_g}$ is the gas flow velocity vector, μ is the dynamic viscosity, σ_k, σ_ω and γ are model coefficients defined in equation 8.12, 8.13 and 8.14, and β_0 and $\sigma_{\omega 2}$ are dimensionless model constants defined in table 2.1. The other symbols are explained below.

At the inlet the initial values of the turbulent kinetic energy k and the specific dissipation ω are defined as:

$$k = \frac{3}{2}(u_0 I_T)^2 \tag{8.3}$$

$$\omega = \frac{k^{\frac{1}{2}}}{(\beta_0)^{\frac{1}{4}} L_T} \tag{8.4}$$

Where u_0 is the input flow rate, I_T the expected turbulence intensity (0.01 for low, 0.05 for medium and 0.1 for high intensity) and L_T the turbulence length scale.

In equation 8.1 and 8.2, μ_T is the turbulent viscosity of the fluid and is defined as:

$$\mu_T = \frac{a_1 k}{max(a_1 \omega, S f_{v2})} \tag{8.5}$$

In which S is the absolute strain rate and a_1 is a dimensionless model constant defined in table 2.1.

In equation 8.2 and 8.5, f_{v1} and f_{v2} are two blending functions that control the switch from the k-ω model to the k-ε model in the free stream (where f_{v1} = 1)

$$f_{v1} = \tanh\left(\min\left(\theta_2^2, \frac{4\sigma_{\omega 2} k}{CD_{k\omega} y^2}\right)\right)^4 \tag{8.6}$$

$$f_{v2} = \tanh(\theta_2^2) \tag{8.7}$$

In which y is the y-component of the position vector, and θ_2 and $CD_{k\omega}$ are placeholders for the following terms:

$$CD_{k\omega} = max\left(2\rho\sigma_{\omega 2}\frac{1}{\omega}\frac{\partial k}{\partial x}\frac{\partial \omega}{\partial x},\ 10^{-10}\right) \tag{8.8}$$

$$\theta_2 = max\left(\frac{2\sqrt{k}}{\beta_0 \omega l_W^2}, \frac{500\mu}{y^2\omega}\right) \tag{8.9}$$

In which l_W is the wall distance.

In equation 8.1 and 8.2, P serves as a product limiter coefficient and is defined as:

$$P = \min(P_k 10\rho\beta_0 k\omega) \tag{8.10}$$

In which P_k is a placeholder for the following term:

$$P_k = \mu_T\left(\nabla\overrightarrow{u_g}:\left(\nabla\overrightarrow{u_g} + \left(\nabla\overrightarrow{u_g}\right)^T\right) - \frac{2}{3}\cdot\left(\nabla\cdot\overrightarrow{u_g}\right)^2\right) - \frac{2}{3}\rho k\nabla\cdot\overrightarrow{u_g} \tag{8.11}$$

The model coefficients in equation 8.1 and 8.2 are defined as

$$\sigma_k = f_{v1}\cdot\sigma_{k1} + (1 - f_{v1})\sigma_{k2} \tag{8.12}$$

$$\sigma_\omega = f_{v1}\cdot\sigma_{\omega 1} + (1 - f_{v1})\sigma_{\omega 2} \tag{8.13}$$

$$\gamma = f_{v1}\cdot\gamma_1 + (1 - f_{v1})\gamma_2 \tag{8.14}$$

In which σ_{k1}, σ_{k2}, $\sigma_{\omega 1}$,$\sigma_{\omega 2}$, γ_1 and γ_2 are dimensionless model constants defined in table 8.1.

Table 8.1: Dimensionless model constants used in the SST turbulent flow model.

σ_{k1}	0.85
σ_{k2}	1
$\sigma_{\omega 1}$	0.5
$\sigma_{\omega 2}$	0.856
γ_1	0.5556
γ_2	0.44
a_1	0.31
β_0	0.09

8.2 GAS PROPERTIES OF THE 3D TURBULENT FLOW MODEL AND THERMAL PLASMA MODEL.

The material properties used in the 3D turbulent flow model and the thermal plasma model are adopted from the COMSOL 5.5 material database for air.[121] The temperature dependencies of these properties are considered by interpolation of the property values listed in table 8.2. In this table T is the temperature, ρ the gas density, C_p the heat capacity at constant pressure, μ the dynamic viscosity, k the thermal conductivity, and σ the electrical conductivity.

Table 8.2: Temperature dependency of the properties considered in the 3D turbulent flow model and thermal plasma model.

$T\ (K)$	$\rho\ \left(\frac{kg}{m^3}\right)$	$C_p\left(\frac{J}{kg\ K}\right)$	$\mu(Pa.s)$	$k\left(\frac{W}{m\ K}\right)$	$\sigma\left(\frac{S}{m}\right)$
500	7.020E-01	1.047E+03	2.710E-05	4.100E-02	0.000
600	5.850E-01	1.069E+03	3.080E-05	4.800E-02	0.000
700	5.010E-01	1.086E+03	3.440E-05	5.500E-02	0.000
800	4.390E-01	1.103E+03	3.790E-05	6.200E-02	0.000
900	3.900E-01	1.119E+03	4.120E-05	6.800E-02	0.000
1000	3.510E-01	1.135E+03	4.450E-05	7.500E-02	0.000
1100	3.190E-01	1.151E+03	4.760E-05	8.100E-02	0.000
1200	2.930E-01	1.167E+03	5.070E-05	8.800E-02	0.000
1300	2.700E-01	1.184E+03	5.370E-05	9.400E-02	0.000
1400	2.510E-01	1.201E+03	5.660E-05	1.010E-01	0.000
1500	2.340E-01	1.219E+03	5.950E-05	1.070E-01	0.000
1600	2.190E-01	1.237E+03	6.240E-05	1.140E-01	0.000
1700	2.070E-01	1.257E+03	6.520E-05	1.210E-01	0.000
1800	1.950E-01	1.278E+03	6.790E-05	1.280E-01	0.000
1900	1.850E-01	1.301E+03	7.060E-05	1.360E-01	0.000
2000	1.760E-01	1.328E+03	7.330E-05	1.450E-01	0.000
2100	1.670E-01	1.361E+03	7.590E-05	1.550E-01	0.000
2200	1.590E-01	1.403E+03	7.860E-05	1.680E-01	0.000
2300	1.520E-01	1.456E+03	8.120E-05	1.830E-01	0.000
2400	1.460E-01	1.527E+03	8.370E-05	2.030E-01	0.000
2500	1.400E-01	1.620E+03	8.630E-05	2.280E-01	0.000
2600	1.340E-01	1.741E+03	8.880E-05	2.600E-01	0.000
2700	1.290E-01	1.894E+03	9.140E-05	3.010E-01	1.000E-03
2800	1.240E-01	2.084E+03	9.390E-05	3.500E-01	2.000E-03
2900	1.190E-01	2.310E+03	9.650E-05	4.070E-01	4.000E-03
3000	1.140E-01	2.569E+03	9.900E-05	4.720E-01	9.000E-03
3100	1.100E-01	2.855E+03	1.017E-04	5.420E-01	3.600E-02
3200	1.050E-01	3.151E+03	1.043E-04	6.100E-01	6.400E-02
3300	1.010E-01	3.435E+03	1.070E-04	6.720E-01	1.100E-01
3400	9.700E-02	3.679E+03	1.097E-04	7.190E-01	1.820E-01
3500	9.300E-02	3.852E+03	1.125E-04	7.460E-01	2.900E-01

3600	8.900E-02	3.927E+03	1.152E-04	7.500E-01	4.440E-01
3700	8.600E-02	3.891E+03	1.179E-04	7.310E-01	6.620E-01
3800	8.200E-02	3.750E+03	1.205E-04	6.930E-01	9.580E-01
3900	7.900E-02	3.528E+03	1.231E-04	6.460E-01	1.351E+00
4000	7.600E-02	3.264E+03	1.257E-04	5.980E-01	1.861E+00
4100	7.400E-02	2.997E+03	1.282E-04	5.550E-01	2.510E+00
4200	7.200E-02	2.758E+03	1.307E-04	5.220E-01	3.325E+00
4300	7.000E-02	2.567E+03	1.331E-04	5.010E-01	4.332E+00
4400	6.800E-02	2.432E+03	1.356E-04	4.930E-01	5.563E+00
4500	6.600E-02	2.353E+03	1.379E-04	4.970E-01	7.051E+00
4600	6.400E-02	2.330E+03	1.403E-04	5.150E-01	8.831E+00
4700	6.300E-02	2.357E+03	1.426E-04	5.440E-01	1.094E+01
4800	6.100E-02	2.433E+03	1.450E-04	5.870E-01	1.343E+01
4900	6.000E-02	2.556E+03	1.473E-04	6.420E-01	1.633E+01
5000	5.800E-02	2.725E+03	1.496E-04	7.110E-01	1.968E+01
5100	5.700E-02	2.940E+03	1.519E-04	7.940E-01	2.355E+01
5200	5.600E-02	3.202E+03	1.543E-04	8.920E-01	2.798E+01
5300	5.400E-02	3.515E+03	1.566E-04	1.006E+00	3.301E+01
5400	5.300E-02	3.818E+03	1.589E-04	1.137E+00	3.871E+01
5500	5.200E-02	4.295E+03	1.612E-04	1.286E+00	4.511E+01
5600	5.000E-02	4.767E+03	1.636E-04	1.452E+00	5.230E+01
5700	4.900E-02	5.295E+03	1.660E-04	1.636E+00	6.035E+01
5800	4.800E-02	5.880E+03	1.683E-04	1.837E+00	6.928E+01
5900	4.600E-02	6.520E+03	1.707E-04	2.053E+00	7.918E+01
6000	4.500E-02	7.212E+03	1.731E-04	2.283E+00	9.019E+01
6100	4.300E-02	7.952E+03	1.755E-04	2.522E+00	1.024E+02
6200	4.200E-02	8.730E+03	1.778E-04	2.767E+00	1.159E+02
6300	4.100E-02	9.534E+03	1.802E-04	3.011E+00	1.309E+02
6400	3.900E-02	1.035E+04	1.825E-04	3.248E+00	1.475E+02
6500	3.800E-02	1.115E+04	1.848E-04	3.471E+00	1.659E+02
6600	3.700E-02	1.192E+04	1.870E-04	3.670E+00	1.865E+02
6700	3.500E-02	1.262E+04	1.892E-04	3.837E+00	2.095E+02
6800	3.400E-02	1.323E+04	1.913E-04	3.963E+00	2.352E+02
6900	3.300E-02	1.371E+04	1.933E-04	4.043E+00	2.641E+02
7000	3.200E-02	1.403E+04	1.952E-04	4.070E+00	2.965E+02
7100	3.000E-02	1.416E+04	1.970E-04	4.043E+00	3.327E+02
7200	2.900E-02	1.411E+04	1.988E-04	3.964E+00	3.731E+02
7300	2.800E-02	1.386E+04	2.005E-04	3.837E+00	4.178E+02
7400	2.700E-02	1.343E+04	2.021E-04	3.670E+00	4.670E+02
7500	2.700E-02	1.284E+04	2.037E-04	3.473E+00	5.208E+02
7600	2.600E-02	1.213E+04	2.053E-04	3.256E+00	5.790E+02
7700	2.500E-02	1.134E+04	2.069E-04	3.031E+00	6.417E+02
7800	2.400E-02	1.051E+04	2.086E-04	2.806E+00	7.085E+02
7900	2.400E-02	9.678E+03	2.102E-04	2.591E+00	7.794E+02
8000	2.300E-02	8.871E+03	2.119E-04	2.390E+00	8.540E+02
8100	2.300E-02	8.113E+03	2.136E-04	2.208E+00	9.321E+02

8200	2.200E-02	7.426E+03	2.153E-04	2.046E+00	1.014E+03
8300	2.200E-02	6.806E+03	2.171E-04	1.907E+00	1.098E+03
8400	2.200E-02	6.268E+03	2.189E-04	1.788E+00	1.185E+03
8500	2.100E-02	5.807E+03	2.207E-04	1.690E+00	1.275E+03
8600	2.100E-02	5.428E+03	2.225E-04	1.611E+00	1.367E+03
8700	2.000E-02	5.103E+03	2.243E-04	1.550E+00	1.462E+03
8800	2.000E-02	4.857E+03	2.261E-04	1.504E+00	1.558E+03
8900	2.000E-02	4.647E+03	2.279E-04	1.471E+00	1.657E+03
9000	2.000E-02	4.497E+03	2.297E-04	1.451E+00	1.756E+03
9100	1.900E-02	4.408E+03	2.315E-04	1.443E+00	1.858E+03
9200	1.900E-02	4.327E+03	2.332E-04	1.443E+00	1.961E+03
9300	1.900E-02	4.318E+03	2.349E-04	1.454E+00	2.064E+03
9400	1.900E-02	4.302E+03	2.366E-04	1.471E+00	2.169E+03
9500	1.800E-02	4.353E+03	2.382E-04	1.497E+00	2.275E+03
9600	1.800E-02	4.418E+03	2.398E-04	1.529E+00	2.382E+03
9700	1.800E-02	4.463E+03	2.413E-04	1.565E+00	2.489E+03
9800	1.800E-02	4.605E+03	2.421E-04	1.609E+00	2.597E+03
9900	1.700E-02	4.689E+03	2.441E-04	1.656E+00	2.706E+03
10000	1.700E-02	4.867E+03	2.453E-04	1.709E+00	2.814E+03

8.3 N_2-O_2 CHEMISTRY SET IN THE QUASI-1D CHEMICAL KINETICS MODEL AND 2D NON-THERMAL PLASMA MODEL

The full chemistry set used in the quasi-1D chemical kinetics model was recently developed and validated for a GA plasmatron by Vervloessem et al.[91] Table 8.3 lists all electron impact reactions. Most of these reactions are treated by energy-dependent cross sections. Table 8.4 lists the neutral-neutral reactions and the corresponding rate coefficient expressions. For certain reactions, the rate coefficients of the vibrationally excited species are determined according to the Fridman-Macheret model in which the activation energy is lowered by $\alpha\, E_v$, where α is the vibrational efficiency to lower the activation barrier and E_v is the vibrational energy. For those reactions, the α parameter is given in the last column of Table 8.4. We realize that the Fridman-Macheret model is only an approximation for describing vibrationally promoted dissociation, but for now, there is no better alternative available. Tables 8.5 to 8.7 list the electron-ion recombination, the ion-neutral and the ion-ion reactions and the corresponding rate coefficients, respectively. Table 8.8 displays the optical transitions. Reactions included in the reduced chemistry set of the 2D non-thermal plasma model are highlighted in blue bold face.

Table 8.3 Electron impact reactions implemented in the model for atomic and molecular nitrogen and oxygen species as well as NO_x species. The list includes vibrational excitation and de-excitation, electronic excitation and de-excitation, direct and dissociative ionization, dissociation, as well as direct and dissociative attachment reactions. These reactions are treated by energy-dependent cross sections when the rate coefficient is not specified in column 2. When indicated, rate coefficients are expressed in $cm^3\ s^{-1}$ or $cm^6\ s^{-1}$ for binary or ternary reactions, respectively.

Reaction	Rate Coefficient	Ref.	Note
$\mathbf{e^- + N_2 \rightleftarrows e^- + N_2(v)}$		122	
$\mathbf{e^- + N_2(v) \rightleftarrows e^- + N_2(v')}$		122	
$\mathbf{e^- + N_2(g,v) \rightarrow e^- + N_2(E_x)}$		123	a, b, c
$\mathbf{e^- + N_2(E_x) \rightarrow e^- + N_2}$		123	b
$\mathbf{e^- + N_2(g,v) \rightarrow 2e^- + N_2^+}$		124	a
$\mathbf{e^- + N_2(E_x) \rightarrow 2e^- + N_2^+}$		124	b
$\mathbf{e^- + N \rightarrow 2e^- + N^+}$		125	
$\mathbf{e^- + N_2(g,v) \rightarrow 2e^- + N^+ + N}$		126	a
$\mathbf{e^- + N_2(g,v) \rightarrow e^- + N + N}$		123	a, c
$\mathbf{e^- + N_2(E_x) \rightarrow e^- + N + N}$		123	b
$\mathbf{e^- + N \rightarrow e^- + N(E_x)}$		123	d
$\mathbf{e^- + O_2 \rightleftarrows e^- + O_2(v)}$		122	

$\mathbf{e^- + O_2(v) \rightleftarrows e^- + O_2(v')}$		127	
$\mathbf{e^- + O_2(g,v) \rightarrow e^- + O_2(E_x)}$		123	a, c, e
$\mathbf{e^- + O_2(E_x) \rightarrow e^- + O_2}$		123	e
$\mathbf{e^- + O_2(g,v) \rightarrow 2e^- + O_2^+}$		124	a, c
$\mathbf{e^- + O_2(E_x) \rightarrow 2e^- + O_2^+}$		128	e
$e^- + O \rightarrow 2e^- + O^+$		123	
$e^- + O_2(g,v) \rightarrow 2e^- + O + O^+$		128	a, c
$e^- + O_2(E_x) \rightarrow 2e^- + O + O^+$		128	e
$\mathbf{e^- + O_3 \rightarrow 2e^- + O + O_2^+}$		129	
$e^- + O_3 \rightarrow e^- + O^+ + O^- + O$		77	
$\mathbf{e^- + O_2(g,v) \rightarrow e^- + O + O}$		123	a
$\mathbf{e^- + O_3 \rightarrow e^- + O_2 + O}$		129	
$e^- + O_2(g,v) \rightarrow O + O^-$		123	a, c
$e^- + O_2(g,v) + M \rightarrow O_2^- + M$		130	a, c, f
$e^- + O_3 \rightarrow O^- + O_2$		124	
$e^- + O_3 \rightarrow O + O_2^-$		124	
$e^- + O_3 + M \rightarrow O_3^- + M$	5×10^{-31}	131	f
$e^- + O + M \rightarrow O^- + M$	1×10^{-31}	132	f
$\mathbf{e^- + NO \rightarrow 2e^- + NO^+}$		133	
$e^- + NO_2 \rightarrow 2e^- + NO_2^+$		134	
$e^- + N_2O \rightarrow 2e^- + N_2O^+$		135	
$e^- + N_2O \rightarrow e^- + N_2 + O$		136	
$e^- + N_2O \rightarrow e^- + N_2 + O(1D)$		136	
$e^- + N_2O \rightarrow e^- + NO + N$		136	

$e^- + NO \rightarrow O^- + N$		133	
$e^- + N_2O \rightarrow N_2 + O^-$		135	
$\mathbf{e^- + NO_2 \rightarrow NO_2^-}$	1×10^{-11}	97	
$e^- + NO_2 \rightarrow O^- + NO$	1×10^{-11}	137	
$e^- + NO + M \rightarrow NO^- + M$	8×10^{-31}	137	f
$e^- + N_2O + M \rightarrow N_2O^- + M$	6×10^{-33}	137	f

[a] For any species indicated with (g, v), g and v stand for its ground and vibrationally excited state, respectively.

[b] $N_2(E_x)$ represents the electronically excited states: $N_2(A^3\Sigma_u^+)$, $N_2(B^3\Pi_g)$, $N_2(C^3\Pi_u)$ and $N_2\left(a'^1\Sigma_u^-\right)$.

[c] The cross sections of the reactions involving excited species on the left hand side are shifted over the difference in the threshold energies.

[d] $N(E_x)$ represents the electronically excited states of atomic N: $N(2D)$ and $N(2P)$.

[e] $O_2(E_x)$ represents the electronically excited states: $O_2(a^1\Delta)$, $O_2(b^1\Sigma^+)$ and a combination of three states, i.e. $O_2(A^3\Sigma^+, C^3\Delta, c^1\Sigma^-)$ at a threshold energy of 4.5 eV.

[f] M represents any neutral species.

Table 8.4 Neutral-neutral reactions included in the model and the corresponding rate coefficient expressions. Tg is the gas temperature in K. The rate coefficients are expressed in $cm^3\ s^{-1}$ or $cm^6\ s^{-1}$ for binary or ternary reactions, respectively. For certain reactions, the rate coefficients of the vibrationally excited species are determined according to the Fridman-Macheret model in which the activation energy is lowered by $\alpha\ E_v$, where α is the vibrational efficiency to lower the activation barrier and E_v is the vibrational energy. For those reactions, the α parameter is given in the last column.

Reaction	Rate coefficient	Ref.	Note
$\mathbf{N_2(g,v) + M \rightarrow N + N + M}$	$8.37 \times 10^{-4} \times \left(\frac{T_g}{298}\right)^{-3.5} \times \exp\left(-\frac{113710}{T_g}\right)$	138	a, b $\alpha = 1$
$\mathbf{N + N + M \rightarrow N_2 + M}$	$1.38 \times 10^{-33} \times \exp\left(\frac{502.978}{T_g}\right)$	139	b
$\mathbf{N + N \rightarrow N_2^+ + e^-}$	$2.7 \times 10^{-11} \times \exp\left(-\frac{6.74\times10^4}{T_g}\right)$	137	
$\mathbf{N + N + N \rightarrow N_2(A^3\Sigma_u^+) + N}$	1.0×10^{-32}	137	
$\mathbf{N + N + N \rightarrow N_2(B^3\Pi_g) + N}$	1.4×10^{-32}	137	
$\mathbf{N + N + N_2 \rightarrow N_2(A^3\Sigma_u^+) + N_2}$	1.7×10^{-33}	137	
$\mathbf{N + N + N_2 \rightarrow N_2(B^3\Pi_g) + N_2}$	2.4×10^{-33}	137	
$N(2D) + M \rightarrow N + M$	2.4×10^{-14}	140	b
$N(2P) + N \rightarrow N(2D) + N$	1.8×10^{-12}	137	
$N(2P) + N_2 \rightarrow N + N_2$	2.0×10^{-18}	137	
$\mathbf{N_2\left(a'^1\Sigma_u^-\right) + N \rightarrow N_2 + N}$	2.0×10^{-11}	140	
$\mathbf{N_2\left(a'^1\Sigma_u^-\right) + N_2 \rightarrow N_2 + N_2}$	3.7×10^{-16}	140	
$\mathbf{N_2\left(a'^1\Sigma_u^-\right) + N_2 \rightarrow N_2(B^3\Pi_g) + N_2}$	1.9×10^{-13}	137	
$\mathbf{N_2\left(a'^1\Sigma_u^-\right) + N_2\left(a'^1\Sigma_u^-\right) \rightarrow N_2^+ + N_2 + e^-}$	5.0×10^{-13}	140	

$N_2\left(a'^1\Sigma_u^-\right) + N_2\left(a'^1\Sigma_u^-\right) \rightarrow N_4^+ + e^-$	1.0×10^{-11}	[137]	
$N_2\left(a'^1\Sigma_u^-\right) + N_2(A^3\Sigma_u^+) \rightarrow N_4^+ + e^-$	4.0×10^{-12}	[137]	
$N_2(A^3\Sigma_u^+) + N \rightarrow N_2 + N(2P)$	$4.0 \times 10^{-11} \times \left(\frac{300}{T_g}\right)^{0.667}$	[137]	
$\mathbf{N_2(A^3\Sigma_u^+) + N \rightarrow N_2 + N}$	2.0×10^{-12}	[137]	
$\mathbf{N_2(A^3\Sigma_u^+) + N_2 \rightarrow N_2 + N_2}$	3.0×10^{-16}	[137]	
$\mathbf{N_2(A^3\Sigma_u^+) + N_2\left(a'^1\Sigma_u^-\right) \rightarrow N_2^+ + N_2 + e^-}$	1.0×10^{-12}	[140]	
$\mathbf{N_2(A^3\Sigma_u^+) + N_2(A^3\Sigma_u^+) \rightarrow N_2 + N_2(A^3\Sigma_u^+)}$	2.0×10^{-12}	[140]	
$\mathbf{N_2(A^3\Sigma_u^+) + N_2(A^3\Sigma_u^+) \rightarrow N_2 + N_2\left(B^3\Pi_g\right)}$	3.0×10^{-10}	[137]	
$\mathbf{N_2(A^3\Sigma_u^+) + N_2(A^3\Sigma_u^+) \rightarrow N_2 + N_2(C^3\Pi_u)}$	1.5×10^{-10}	[137]	
$\mathbf{N_2\left(B^3\Pi_g\right) + N_2 \rightarrow N_2 + N_2}$	2.0×10^{-12}	[137]	
$\mathbf{N_2\left(B^3\Pi_g\right) + N_2 \rightarrow N_2(A^3\Sigma_u^+) + N_2}$	3×10^{-11}	[137]	
$\mathbf{N_2(C^3\Pi_u) + N_2 \rightarrow N_2 + \left(a'^1\Sigma_u^-\right)}$	1.0×10^{-11}	[137]	
$\mathbf{O_2(g, v) + M \rightarrow O + O + M}$	$\left(\frac{3.0\times10^{-6}}{T_g}\right) \times \exp\left(\frac{-59380}{T_g}\right)$		a $\alpha =$ 1
$\mathbf{O + O + M \rightarrow O_2 + M}$	$5.21 \times 10^{-35} \times \exp\left(\frac{900}{T_g}\right)$	[141]	b

$\mathbf{O + O_3 \rightarrow O_2 + O_2}$	$8.0 \times 10^{-12} \times \exp\left(-\frac{2056}{T_g}\right)$	[142]	
$\mathbf{O + O_2(g, v) + M \rightarrow O_3 + M}$	$1.34 \times 10^{-34} \times \left(\frac{T_g}{298}\right)^{-1.0}$	[143]	a, b
$\mathbf{O_3 + M \rightarrow O_2 + O + M}$	$7.16 \times 10^{-10} \times \exp\left(-\frac{98120}{R_g T_g}\right)$	[144]	b, c
$\mathbf{O + O_2(E_x) + M \rightarrow O_3 + M}$	$1.34 \times 10^{-34} \times \left(\frac{T_g}{298}\right)^{-1.0}$	[143]	b, d, e
$\mathbf{O + O_3 \rightarrow O_2 + O_2(a^1\Delta)}$	$2.0 \times 10^{-11} \times \exp\left(-\frac{2280}{T_g}\right)$	[137]	
$\mathbf{O_2(a^1\Delta) + O \rightarrow O_2 + O}$	7.0×10^{-16}	[137]	
$\mathbf{O_2(a^1\Delta) + O_2 \rightarrow O_2 + O_2}$	$3.8 \times 10^{-18} \times \exp\left(-\frac{205}{T_g}\right)$	[137]	
$\mathbf{O_2(b^1\Sigma^+) + O \rightarrow O_2(a^1\Delta) + O}$	8.1×10^{-14}	[137]	
$O_2(b^1\Sigma^+) + O \rightarrow O_2 + O(1D)$	$3.4 \times 10^{-11} \times \left(\frac{T_g}{300}\right)^{-0.1} \times \exp\left(-\frac{4200}{T_g}\right)$	[137]	
$\mathbf{O_2(b^1\Sigma^+) + O_2 \rightarrow O_2 + O_2(a^1\Delta)}$	$4.3 \times 10^{-22} \times (T_g)^{2.4} \times \exp\left(-\frac{281}{T_g}\right)$	[137]	
$\mathbf{O_2(b^1\Sigma^+) + O_3 \rightarrow O_2 + O_2 + O}$	2.2×10^{-11}	[137]	
$\mathbf{O_2(a^1\Delta) + O_3 \rightarrow O_2 + O_2 + O(1D)}$	$5.2 \times 10^{-11} \times \exp\left(-\frac{2840}{T_g}\right)$	[137]	
$\mathbf{O_2(a^1\Delta) + O_2(a^1\Delta) \rightarrow O_2 + O_2(b^1\Sigma^+)}$	$7.0 \times 10^{-28} \times (T_g)^{3.8} \times \exp\left(\frac{700}{T_g}\right)$	[137]	
$O(1D) + O \rightarrow O + O$	8.0×10^{-12}	[137]	

$O(1D) + O_2 \rightarrow O + O_2$	$6.4 \times 10^{-12} \times \exp\left(-\frac{67}{T_g}\right)$	[137]	
$O(1S) + O \rightarrow O(1D) + O(1D)$	$5.0 \times 10^{-11} \times \exp\left(-\frac{300}{T_g}\right)$	[137]	
$O(1S) + O_2 \rightarrow O + O_2$	$1.3 \times 10^{-12} \times \exp\left(-\frac{850}{T_g}\right)$	[137]	
$O(1S) + O_2 \rightarrow O + O + O$	3.0×10^{-12}	[137]	
$O(1S) + O_2(a^1\Delta) \rightarrow O + O + O$	3.2×10^{-11}	[137]	
$O(1S) + O_2(a^1\Delta) \rightarrow O(1D) + O_2(b^1\Sigma^+)$	2.9×10^{-11}	[137]	
$O(1S) + O_2 \rightarrow O + O_2(A^3\Sigma^+, C^3\Delta, c^1\Sigma^-)$	$3.0 \times 10^{-12} \times \exp\left(-\frac{850}{T_g}\right)$	[137]	f
$\mathbf{N + O_2(g, v) \rightarrow O + NO}$	$2.36 \times 10^{-11} \times \exp\left(-\frac{44230}{R_g T_g}\right)$	[145]	a, c $\alpha =$ 0.24
$\mathbf{O + N_2(g, v) \rightarrow N + NO}$	$3.01 \times 10^{-10} \times \exp\left(-\frac{318000}{R_g T_g}\right)$	[146]	a, c $\alpha =$ 1
$\mathbf{O_3 + N \rightarrow NO + O_2}$	$5.0 \times 10^{-12} \times \exp\left(-\frac{650}{T_g}\right)$	[142]	
$\mathbf{O_3 + NO \rightarrow O_2 + NO_2}$	$2.5 \times 10^{-13} \times \exp\left(-\frac{765}{T_g}\right)$	[137]	
$\mathbf{O_3 + NO_2 \rightarrow O_2 + NO_3}$	$1.2 \times 10^{-13} \times \exp\left(-\frac{2450}{T_g}\right)$	[97]	
$\mathbf{NO_3 + O_3 \rightarrow NO_2 + O_2 + O_2}$	1.0×10^{-17}	[147]	
$\mathbf{N + NO \rightarrow O + N_2}$	1.66×10^{-11}	[148]	
$\mathbf{N + NO_2 \rightarrow O + O + N_2}$	9.1×10^{-13}	[137]	

$\mathbf{N + NO_2 \rightarrow O + N_2O}$	3.0×10^{-12}	137	
$\mathbf{N + NO_2 \rightarrow N_2 + O_2}$	7.0×10^{-13}	137	
$\mathbf{N + NO_2 \rightarrow NO + NO}$	2.3×10^{-12}	137	
$\mathbf{O + NO \rightarrow N + O_2}$	$7.5 \times 10^{-12} \times \left(\frac{T_g}{300}\right) \times \exp\left(-\frac{19500}{T_g}\right)$	137	
$\mathbf{O + NO_2 \rightarrow NO + O_2}$	$9.05 \times 10^{-12} \times \left(\frac{T_g}{298}\right)^{-0.52}$	149	
$O + N_2O \rightarrow NO + NO$	$1.5 \times 10^{-10} \times \exp\left(-\frac{14090}{T_g}\right)$	137	
$O + N_2O \rightarrow N_2 + O_2$	$8.3 \times 10^{-12} \times \exp\left(-\frac{14000}{T_g}\right)$	137	
$O + NO_3 \rightarrow O_2 + N_2$	1.0×10^{-11}	137	
$\mathbf{NO + NO \rightarrow N + NO_2}$	$3.3 \times 10^{-16} \times \left(\frac{300}{T_g}\right)^{0.5} \times \exp\left(-\frac{39200}{T_g}\right)$	137	
$NO + NO \rightarrow O + N_2O$	$2.2 \times 10^{-12} \times \exp\left(-\frac{32100}{T_g}\right)$	137	
$\mathbf{NO + NO \rightarrow N_2 + O_2}$	$5.1 \times 10^{-13} \times \exp\left(-\frac{33660}{T_g}\right)$	137	
$NO + N_2O \rightarrow N_2 + NO_2$	$4.6 \times 10^{-10} \times \exp\left(-\frac{25170}{T_g}\right)$	137	
$NO + NO_3 \rightarrow NO_2 + NO_2$	1.7×10^{-11}	137	
$NO_2 + NO_2 \rightarrow NO + NO_3$	$4.5 \times 10^{-10} \times \exp\left(-\frac{18500}{T_g}\right)$	137	
$\mathbf{NO_2 + NO_2 \rightarrow NO + NO + O_2}$	$3.3 \times 10^{-12} \times \exp\left(-\frac{13500}{T_g}\right)$	137	
$NO_2 + NO_3 \rightarrow NO + NO_2 + O_2$	$2.3 \times 10^{-13} \times \exp\left(-\frac{1600}{T_g}\right)$	137	

$NO_3 + NO_3 \rightarrow O_2 + NO_2 + NO_2$	$4.3 \times 10^{-12} \times \exp\left(-\frac{3850}{T_g}\right)$	137	
$\mathbf{NO + O_2(g,v) \rightarrow O + NO_2}$	$2.8 \times 10^{-12} \times \exp\left(-\frac{23400}{T_g}\right)$	137	a $\alpha =$ 1
$\mathbf{NO + NO + O_2(g,v) \rightarrow NO_2 + NO_2}$	$3.3 \times 10^{-39} \times \exp\left(-\frac{4410}{R_g T_g}\right)$	150	a, c $\alpha =$ 0.2
$\mathbf{NO_2 + O_2(g,v) \rightarrow NO + O_3}$	$2.8 \times 10^{-12} \times \exp\left(-\frac{25400}{T_g}\right)$	137	a $\alpha =$ 0.2
$NO_3 + O_2(g,v) \rightarrow O_3 + NO_2$	$1.5 \times 10^{-12} \times \exp\left(-\frac{15020}{T_g}\right)$	137	a $\alpha =$ 0.8
$\mathbf{NO + O \rightarrow NO_2}$	$3.01 \times 10^{-11} \times \left(\frac{T_g}{300}\right)^{-0.75}$	151	
$NO_2 + NO + M \rightarrow N_2O_3 + M$	$3.09 \times 10^{-34} \times \left(\frac{T_g}{300}\right)^{-7.70}$	142	b
$NO_2 + NO_2 + M \rightarrow N_2O_4 + M$	$1.4 \times 10^{-33} \times \left(\frac{T_g}{300}\right)^{-3.8}$	142	b
$NO_2 + NO_3 + M \rightarrow N_2O_5 + M$	$3.7 \times 10^{-30} \times \left(\frac{300}{T_g}\right)^{4.10}$	150	b
$\mathbf{N + O + M \rightarrow NO + M}$	$1.0 \times 10^{-32} \times \left(\frac{300}{T_g}\right)^{0.5}$	137	b
$N_2(g,v) + O + M \rightarrow N_2O + M$	$3.9 \times 10^{-35} \times \exp\left(-\frac{10400}{T_g}\right)$	137	b

$N_2O + M \rightarrow N_2 + O + M$	$1.20 \times 10^{-9} \times \exp\left(-\frac{240000}{R_g T_g}\right)$	[137]	b, c
$\mathbf{NO_2 + M \rightarrow NO + O + M}$	$9.4 \times 10^{-5} \times \left(\frac{T_g}{298}\right)^{-2.66} \times \exp\left(-\frac{311000}{R_g T_g}\right)$	[151]	b, c
$NO_3 + M \rightarrow NO + O_2 + M$	$2.51 \times 10^{-14} \times \exp\left(-\frac{10230}{R_g T_g}\right)$	[152]	b, c
$\mathbf{NO + M \rightarrow N + O + M}$	$8.7 \times 10^{-9} \times \exp\left(-\frac{75994}{T_g}\right)$	[137]	b
$N_2O_3 + M \rightarrow NO + NO_2 + M$	$1.91 \times 10^{-7} \times \left(\frac{T_g}{298}\right)^{-8.7} \times \exp\left(-\frac{40570}{R_g T_g}\right)$	[142]	b, c
$N_2O_4 + M \rightarrow NO_2 + NO_3 + M$	$1.3 \times 10^{-5} \times \left(\frac{T_g}{298}\right)^{-3.8} \times \exp\left(-\frac{53210}{R_g T_g}\right)$	[142]	b, c
$N_2O_5 + M \rightarrow NO_2 + NO_3 + M$	$2.1 \times 10^{-11} \times \left(\frac{300}{T_g}\right)^{-3.5} \times \exp\left(-\frac{91460}{R_g T_g}\right)$	[137]	b, c
$NO + O_2(g, v) + M \rightarrow NO_3 + M$	$5.65 \times 10^{-41} \times \exp\left(-\frac{1750}{R_g T_g}\right)$	[153]	a, b, c
$NO + O_2(E_x) + M \rightarrow NO_3 + M$	$5.65 \times 10^{-41} \times \exp\left(-\frac{1750}{R_g T_g}\right)$	[153]	b, d
$\mathbf{N + N + NO \rightarrow N_2(A^3\Sigma_u^+) + NO}$	1.7×10^{-33}	[137]	
$\mathbf{N + N + NO \rightarrow N_2(B^3\Pi_g) + NO}$	2.4×10^{-33}	[137]	
$\mathbf{N + N + O \rightarrow N_2(A^3\Sigma_u^+) + O}$	1.0×10^{-32}	[137]	
$\mathbf{N + N + O \rightarrow N_2(B^3\Pi_g) + O}$	1.4×10^{-32}	[137]	

$\mathbf{N + N + O_2 \rightarrow N_2(A^3\Sigma_u^+) + O_2}$	1.7×10^{-33}	[137]	
$\mathbf{N + N + O_2 \rightarrow N_2(B^3\Pi_g) + O_2}$	2.4×10^{-33}	[137]	
$N(2D) + N_2O \rightarrow NO + N_2$	3.5×10^{-12}	[137]	
$N(2D) + NO \rightarrow N_2 + O$	1.8×10^{-10}	[137]	
$N(2D) + O \rightarrow N + O(1D)$	4.0×10^{-13}	[137]	
$N(2D) + O_2(g, v) \rightarrow NO + O$	5.2×10^{-12}	[137]	a
$N(2P) + NO \rightarrow N_2(A^3\Sigma_u^+) + O$	3.0×10^{-11}	[137]	
$N(2P) + O \rightarrow N + O$	1.0×10^{-12}	[137]	
$N(2P) + O_2(g, v) \rightarrow NO + O$	2.6×10^{-15}	[137]	a
$\mathbf{N_2\left(a'^1\Sigma_u^-\right) + NO \rightarrow N_2 + N + O}$	3.6×10^{-10}	[137]	
$\mathbf{N_2\left(a'^1\Sigma_u^-\right) + O \rightarrow NO + N}$	3.0×10^{-10}	[146]	
$\mathbf{N_2\left(a'^1\Sigma_u^-\right) + O_2(g, v) \rightarrow N_2 + O + O}$	2.8×10^{-11}	[137]	a
$N_2(A^3\Sigma_u^+) + N_2O \rightarrow N_2 + N + NO$	1.0×10^{-11}	[137]	
$\mathbf{N_2(A^3\Sigma_u^+) + NO \rightarrow N_2 + NO}$	6.9×10^{-11}	[137]	
$\mathbf{N_2(A^3\Sigma_u^+) + NO_2 \rightarrow N_2 + O + NO}$	1.0×10^{-12}	[137]	
$N_2(A^3\Sigma_u^+) + O \rightarrow N_2 + O(1S)$	2.1×10^{-11}	[137]	
$N_2(A^3\Sigma_u^+) + O \rightarrow NO + N(2D)$	7.0×10^{-12}	[137]	
$\mathbf{N_2(A^3\Sigma_u^+) + O_2(g, v) \rightarrow N_2 + O + O}$	$2.0 \times 10^{-12} \times \left(\frac{T_g}{300}\right)^{0.55}$	[137]	a
$\mathbf{N_2(A^3\Sigma_u^+) + O_2 \rightarrow N_2 + O_2(a^1\Delta)}$	$2.0 \times 10^{-13} \times \left(\frac{T_g}{300}\right)^{0.55}$	[137]	
$\mathbf{N_2(A^3\Sigma_u^+) + O_2 \rightarrow N_2 + O_2}$	2.54×10^{-12}	[137]	
$N_2(A^3\Sigma_u^+) + O_2(g, v) \rightarrow N_2O + O$	$2.0 \times 10^{-14} \times \left(\frac{T_g}{300}\right)^{0.55}$	[137]	a

$N_2(B^3\Pi_g) + N_2O \rightarrow N_2 + N + NO$	0.58×10^{-10}	[154]	
$N_2(B^3\Pi_g) + N_2O \rightarrow N_2 + N_2 + O$	0.58×10^{-10}	[154]	
$\mathbf{N_2(B^3\Pi_g) + O \rightarrow NO + N}$	3.0×10^{-10}	[146]	
$\mathbf{N_2(C^3\Pi_u) + O \rightarrow NO + N}$	3.0×10^{-10}	[146]	
$\mathbf{N_2(C^3\Pi_u) + O_2(g,v) \rightarrow N_2 + O + O}$	3.0×10^{-10}	[137]	a
$\mathbf{NO + O_2(E_x) \rightarrow O + NO_2}$	$2.8 \times 10^{-12} \times \exp\left(-\frac{23400}{T_g}\right)$	[137]	d, g
$NO_3 + O_2(E_x) \rightarrow O_3 + NO_2$	$1.5 \times 10^{-12} \times \exp\left(-\frac{15020}{T_g}\right)$	[137]	d, h
$O(1D) + N_2 \rightarrow N_2 + O$	2.3×10^{-11}	[137]	
$O(1S) + N \rightarrow O + N$	1.0×10^{-12}	[137]	
$O(1S) + N_2(g,v) \rightarrow O + N_2(g,v)$	1.0×10^{-17}	[137]	
$\mathbf{O_2(a^1\Delta) + N \rightarrow NO + O}$	$2.0 \times 10^{-14} \times \exp\left(-\frac{600}{T_g}\right)$	[137]	
$\mathbf{O_2(a^1\Delta) + N_2(g,v) \rightarrow O_2 + N_2(g,v)}$	3.0×10^{-21}	[137]	
$\mathbf{O_2(a^1\Delta) + NO \rightarrow O_2 + NO}$	2.5×10^{-11}	[137]	
$\mathbf{O_2(b^1\Sigma^+) + N_2 \rightarrow O_2(a^1\Delta) + N_2}$	$1.7 \times 10^{-15} \times \left(\frac{T_g}{300}\right)^{1.0}$	[137]	
$\mathbf{N_2(B^3\Pi_g) + NO \rightarrow N_2(A^3\Sigma_u^+) + NO}$	2.4×10^{-10}	[137]	
$\mathbf{N_2(B^3\Pi_g) + O_2(g,v) \rightarrow N_2 + O + O}$	3.0×10^{-10}	[137]	a

[a] For any species indicated with (g,v), g and v stand for its ground and vibrationally excited state, respectively.

[b] M represents any neutral species.

[c] $R_g = 8.3144598\ J.K^{-1}.mol^{-1}$ is the universal gas constant.

[d] $O_2(E_x)$ represents the two electronically excited states: $O_2(a^1\Delta)$ and $O_2(b^1\Sigma^+)$.

[e] The rate coefficient is assumed to be equal to the rate of $O + O_2 + M \rightarrow O_3 + M$.

[f] $O_2(A^3\ \Sigma^+, C^3\ \Delta, c^1\ \Sigma^-)$ is a combination of three electronic excited states at a threshold energy of 4.5 eV.

[g] The rate coefficient is assumed to be equal to the rate of $NO + O_2 \rightarrow O + NO_2$.

[h] The rate coefficient is assumed to be equal to the rate of $NO_3 + O_2 \rightarrow O_3 + NO_2$.

Table 8.5 Electron-ion recombination reactions included in the model and the corresponding rate coefficient expressions. Te is the electron temperature in K and Tg is the gas temperature in K. The rate coefficients are expressed in $cm^3\ s^{-1}$ or $cm^6\ s^{-1}$ for binary or ternary reactions, respectively.

Reaction	Rate coefficient	Ref.	Note
$\mathbf{e^- + N_2^+ \rightarrow N + N(g, E_x)}$	$R \times 1.8 \times 10^{-7} \times \left(\frac{300}{T_e}\right)^{0.39}$	137	a
$e^- + N_3^+ \rightarrow N_2 + N$	$2 \times 10^{-7} \times \left(\frac{300}{T_e}\right)^{0.5}$	155	
$e^- + N_3^+ \rightarrow N_2(E_x) + N$	$6.91 \times 10^{-8} \times \left(\frac{T_e}{11604.5}\right)^{-0.5}$	155	c
$e^- + N_4^+ \rightarrow N_2 + N_2$	$2.3 \times 10^{-6} \times \left(\frac{300}{T_e}\right)^{0.53}$	137	
$e^- + N_4^+ \rightarrow N_2 + N + N$	$3.13 \times 10^{-7} \times \left(\frac{T_e}{11604.5}\right)^{-0.41}$	155	
$e^- + N^+ + e^- \rightarrow e^- + N$	$7 \times 10^{-20} \times \left(\frac{300}{T_e}\right)^{4.5}$	155	
$e^- + N^+ + M \rightarrow N + M$	$6 \times 10^{-27} \times \left(\frac{300}{T_e}\right)^{1.5}$	156	b
$\mathbf{e^- + N_2^+ + e^- \rightarrow e^- + N_2}$	$1 \times 10^{-19} \times \left(\frac{T_e}{300}\right)^{-4.5}$	155	
$\mathbf{e^- + N_2^+ + M \rightarrow N_2 + M}$	$2.49 \times 10^{-29} \times \left(\frac{T_e}{11604.5}\right)^{-1.5}$	155	b
$e^- + O^+ + O_2 \rightarrow O + O_2$	$6 \times 10^{-27} \times \left(\frac{300}{T_e}\right)^{1.5}$	156	
$e^- + O^+ + e^- \rightarrow e^- + O$	$7 \cdot 10^{-20} \cdot \left(\frac{300}{T_e}\right)^{4.5}$	137	
$\mathbf{e^- + O_2^+ + M \rightarrow O_2 + M}$	1×10^{-26}	132	b
$\mathbf{e^- + O_2^+ + e^- \rightarrow e^- + O_2}$	$1 \times 10^{-19} \times \left(\frac{T_e}{300}\right)^{-4.5}$	156	
$\mathbf{e^- + O_2^+ \rightarrow O + O}$	$6.46 \times 10^{-5} \times T_e^{-0.5} \times T_g^{-0.5}$	157	
$e^- + O_2^+ \rightarrow O + O(1D)$	$1.08 \times 10^{-7} \left(\frac{T_e}{300}\right)^{-0.7}$	137	
$e^- + O_2^+ \rightarrow O + O(1S)$	$0.14 \times 10^{-7} \left(\frac{T_e}{300}\right)^{-0.7}$	137	

$e^- + O_4^+ \rightarrow O_2 + O_2$	$1.4 \times 10^{-6} \times \left(\frac{300}{T_e}\right)^{0.5}$	137	
$\mathbf{e^- + NO^+ + e^- \rightarrow e^- + NO}$	$\mathbf{1.0 \times 10^{-19} \left(\frac{T_e}{300}\right)^{-4.5}}$	156	
$\mathbf{e^- + NO^+ + M \rightarrow NO + M}$	$\mathbf{2.49 \times 10^{-29} \times \left(\frac{T_e}{11604.5}\right)^{-1.5}}$	155	b
$e^- + NO^+ \rightarrow O + N(g, E_x)$	$R \times 4.2 \times 10^{-7} \times \left(\frac{300}{T_e}\right)^{0.85}$	137	d
$e^- + N_2O^+ \rightarrow N_2 + O$	$2.0 \times 10^{-7} \times \left(\frac{300}{T_e}\right)^{0.5}$	137	
$e^- + NO_2^+ \rightarrow NO + O$	$2.0 \times 10^{-7} \times \left(\frac{300}{T_e}\right)^{0.5}$	137	
$e^- + O_2^+N_2 \rightarrow O_2 + N_2$	$1.3 \times 10^{-6} \times \left(\frac{300}{T_e}\right)^{0.5}$	137	

[a] In $N(g, E_x)$, g stands for the ground state of atomic N and E_x represents two of its electronically excited states: $N(2D)$ and $N(2P)$; R is equal to 0.5, 0.45 and 0.05 for N, $N(2D)$ and $N(2P)$, respectively.

[b] M represents any neutral species.

[c] $N_2(E_x)$ represents $N_2(A^3\Sigma_u^+)$ and $N_2(B^3\Pi_g)$.

[d] In $N(g, E_x)$, g stands for the ground state of atomic N and E_x represents the electronic excited state $N(2D)$; R is equal to 0.2 and 0.8 for N and $N(2D)$, respectively.

Table 8.6 Ion-neutral reactions included in the model and the corresponding rate coefficient expressions. T_g is the gas temperature in K. For certain reactions, T_{ion} is the effective temperature of the reacting ion in K. The rate coefficients are expressed in $cm^3\ s^{-1}$ or $cm^6\ s^{-1}$ for binary or ternary reactions, respectively.

Reaction	Rate coefficient	Ref.	Note
$N_2^+ + N \rightarrow N^+ + N_2$	$7.2 \times 10^{-13} \times \left(\frac{T_{ion}}{300}\right)$	[137]	
$N_2^+ + N + N_2 \rightarrow N_3^+ + N_2$	$9.0 \times 10^{-30} \times \left(\frac{400}{T_{ion}}\right)$	[137]	
$N_4^+ + N_2 \rightarrow N_2^+ + N_2 + N_2$	$2.1 \times 10^{-16} \times \left(\frac{Tion}{121}\right)$	[137]	
$N^+ + N_2 + N_2 \rightarrow N_3^+ + N_2$	$1.7 \times 10^{-29} \times \left(\frac{300}{Tion}\right)^{2.1}$	[137]	
$N_2^+ + N_2 + N_2 \rightarrow N_4^+ + N_2$	$5.2 \times 10^{-29} \times \left(\frac{300}{T_{ion}}\right)^{2.2}$	[137]	
$N^+ + N + N_2 \rightarrow N_2^+ + N_2$	1.0×10^{-29}	[137]	
$N^+ + N \rightarrow N_2^+$	1.0×10^{-29}	[158]	
$N_3^+ + N \rightarrow N_2^+ + N_2$	6.6×10^{-11}	[137]	
$N_4^+ + N \rightarrow N^+ + N_2 + N_2$	1.0×10^{-11}	[137]	
$N_2^+ + N_2(A^3\Sigma_u^+) \rightarrow N_3^+ + N$	3.0×10^{-10}	[97]	
$O^- + M \rightarrow O + M + e^-$	4.0×10^{-12}	[97]	a
$O^- + O \rightarrow O_2 + e^-$	2.3×10^{-10}	[159]	
$O^- + O_2(g,v) + M \rightarrow O_3^- + M$	$1.1 \times 10^{-30} \times \exp\left(\frac{300}{T_g}\right)$	[159]	a, b
$O^- + O_2(g,v) \rightarrow O_3 + e^-$	5.0×10^{-15}	[137]	b
$O^- + O_3 \rightarrow O_2 + O_2 + e^-$	3.0×10^{-10}	[160]	
$O^- + O_3 \rightarrow O_3^- + O$	5.3×10^{-10}	[161]	
$O^+ + O + M \rightarrow O_2^+ + M$	1.0×10^{-29}	[156]	a
$O^+ + O_2(g,v) \rightarrow O + O_2^+$	$1.9 \times 10^{-11} \times \left(\frac{T_g}{300}\right)^{-0.5}$	[162]	b
$O^+ + O_3 \rightarrow O_2^+ + O_2$	1.0×10^{-10}	[156]	

$O_2^- + M \rightarrow O_2 + M + e^-$	$2.7 \times 10^{-10} \times \left(\frac{T_g}{300}\right)^{0.5} \times \exp\left(-\frac{5590}{T_g}\right)$	[162]	a
$O_2^- + O \rightarrow O_2 + O^-$	3.31×10^{-10}	[159]	
$O_2^- + O_2(g,v) + M \rightarrow O_4^- + M$	$3.5 \times 10^{-31} \times \left(\frac{T_g}{300}\right)^{-1.0}$	[156,159,161]	a, b
$O_2^- + O_2 \rightarrow O_2 + O_2 + e^-$	2.18×10^{-18}	[163]	
$O_2^- + O_3 \rightarrow O_3^- + O_2$	4.0×10^{-10}	[159]	
$O_2^+ + O_2(g,v) + M \rightarrow O_4^+ + M$	$2.4 \times 10^{-30} \times \left(\frac{T_g}{300}\right)^{-3.2}$	[156]	a, b
$O_3^- + M \rightarrow O_3 + M + e^-$	2.3×10^{-11}	[162]	a
$O_3^- + O \rightarrow O_2 + O_2 + e^-$	1.0×10^{-13}	[161]	
$O_3^- + O \rightarrow O_2^- + O_2$	2.5×10^{-10}	[131]	
$O_3^- + O \rightarrow O_3 + O^-$	1.0×10^{-13}	[159]	
$O_3^- + O_3 \rightarrow O_2 + O_2 + O_2 + e^-$	3.0×10^{-10}	[161]	
$O_4^- + O \rightarrow O^- + O_2 + O_2$	3.0×10^{-10}	[156]	
$O_4^- + O \rightarrow O_3^- + O_2$	4.0×10^{-10}	[156]	
$O_4^- + O_2 \rightarrow O_2^- + O_2 + O_2$	$1.0 \times 10^{-10} \times \exp\left(-\frac{1044}{T_g}\right)$	[137]	
$O_4^+ + O \rightarrow O_2^+ + O_3$	3.0×10^{-10}	[156]	
$O_4^+ + O_2 \rightarrow O_2^+ + O_2 + O_2$	$3.3 \times 10^{-6} \times \left(\frac{300}{T_g}\right)^{4.0} \times \exp\left(-\frac{5030}{T_g}\right)$	[156]	
$O^- + O_2(a^1\Delta) \rightarrow O_3 + e^-$	3.0×10^{-10}	[137]	
$O_2^- + O_2(a^1\Delta) \rightarrow O_2 + O_2 + e^-$	2.0×10^{-10}	[137]	
$O_2^- + O_2(b^1\Sigma^+) \rightarrow O_2 + O_2 + e^-$	3.6×10^{-10}	[137]	

$O_2^+ + O_2(E_x) + M \rightarrow O_4^+ + M$	$2.4 \times 10^{-30} \times \left(\frac{T_g}{300}\right)^{-3.2}$	137	a, c, d
$O_4^+ + O_2(a^1\Delta) \rightarrow O_2^+ + O_2 + O_2$	1.0×10^{-10}	137	
$O_4^- + O_2(E_x) \rightarrow O_2^- + O_2 + O_2$	1.0×10^{-10}	137	c
$O^- + O_2(a^1\Delta) \rightarrow O_2^- + O$	1.0×10^{-10}	137	
$O^- + O_2(E_x) + M \rightarrow O_3^- + M$	$1.1 \times 10^{-30} \times \exp\left(\frac{300}{T_g}\right)$	137	a, c, e
$O_2^- + O_2(E_x) + M \rightarrow O_4^- + M$	$3.5 \times 10^{-31} \times \exp\left(\frac{T_g}{300}\right)^{-1.0}$	156	a, c, f
$N^+ + N + O_2 \rightarrow N_2^+ + O_2$	1.0×10^{-29}	137	
$N^+ + N_2O \rightarrow NO^+ + N_2$	5.5×10^{-10}	137	
$N^+ + NO \rightarrow N_2^+ + O$	3.0×10^{-12}	137	
$N^+ + NO \rightarrow NO^+ + N$	8.0×10^{-10}	137	
$N^+ + NO \rightarrow O^+ + N_2$	1.0×10^{-12}	137	
$N^+ + O + M \rightarrow NO^+ + M$	1.0×10^{-29}	137	a
$N^+ + O \rightarrow N + O^+$	1.0×10^{-12}	137	
$N^+ + O_2 \rightarrow NO^+ + O$	2.5×10^{-10}	137	
$N^+ + O_2 \rightarrow O^+ + NO$	2.8×10^{-11}	137	
$N^+ + O_2 \rightarrow O_2^+ + N$	2.8×10^{-10}	137	
$N^+ + O_3 \rightarrow NO^+ + O_2$	5.0×10^{-10}	137	
$N_2^+ + N_2O \rightarrow N_2O^+ + N_2$	5.0×10^{-10}	137	
$N_2^+ + N_2O \rightarrow NO^+ + N + N_2$	4.0×10^{-10}	137	
$N_2^+ + NO \rightarrow NO^+ + N_2$	3.3×10^{-10}	137	
$N_2^+ + O \rightarrow NO^+ + N$	$1.3 \times 10^{-10} \times \left(\frac{300}{T_{ion}}\right)^{0.5}$	137	
$N_2^+ + O_2 \rightarrow O_2^+ + N_2$	$6.0 \times 10^{-11} \times \left(\frac{300}{T_{ion}}\right)^{0.5}$	137	

$N_2^+ + O_3 \rightarrow O_2^+ + O + N_2$	1.0×10^{-10}	[137]	
$N_2O^- + N \rightarrow NO + N_2 + e^-$	5.0×10^{-10}	[97]	
$N_2O^- + O \rightarrow NO + NO + e^-$	1.5×10^{-10}	[97]	
$N_2O^+ + NO \rightarrow NO^+ + N_2O$	2.9×10^{-10}	[137]	
$N_3^+ + NO \rightarrow N_2O^+ + N_2$	7.0×10^{-11}	[137]	
$N_3^+ + NO \rightarrow NO^+ + N + N_2$	7.0×10^{-11}	[137]	
$N_3^+ + O_2 \rightarrow NO_2^+ + N_2$	4.4×10^{-11}	[137]	
$N_3^+ + O_2 \rightarrow O_2^+ + N + N_2$	2.3×10^{-11}	[137]	
$N_4^+ + NO \rightarrow NO^+ + N_2 + N_2$	4.0×10^{-10}	[137]	
$N_4^+ + O \rightarrow O^+ + N_2 + N_2$	2.5×10^{-10}	[137]	
$N_4^+ + O_2 \rightarrow O_2^+ + N_2 + N_2$	2.5×10^{-10}	[137]	
$NO^- + N_2O \rightarrow NO + N_2O + e^-$	$4.26 \times 10^{-10} \times \exp\left(-\frac{107.2}{T_g}\right)$	[164]	
$NO^- + NO \rightarrow NO + NO + e^-$	$3.28 \times 10^{-10} \times \exp\left(-\frac{105.1}{T_g}\right)$	[164]	
$NO^- + N \rightarrow N_2O + e^-$	5.0×10^{-10}	[137]	
$NO^- + N_2O \rightarrow NO_2^- + N_2$	2.8×10^{-14}	[137]	
$NO^- + NO_2 \rightarrow NO_2^- + NO$	7.4×10^{-10}	[137]	
$NO^- + O \rightarrow NO_2 + e^-$	1.5×10^{-10}	[97]	
$NO^- + O_2 \rightarrow O_2^- + NO$	5.0×10^{-10}	[137]	
$NO_2^- + N \rightarrow NO + NO + e^-$	5.0×10^{-10}	[97]	
$NO_2^- + N_2O_5 \rightarrow NO_3^- + NO_2 + NO_2$	7.0×10^{-10}	[137]	
$NO_2^- + NO_2 \rightarrow NO_3^- + NO$	4.0×10^{-12}	[137]	

$NO_2^- + NO_3 \rightarrow NO_3^- + NO_2$	5.0×10^{-10}	[137]	
$NO_2^- + O_3 \rightarrow NO_3^- + O_2$	1.8×10^{-11}	[137]	
$NO_2^+ + NO \rightarrow NO^+ + NO_2$	2.9×10^{-10}	[137]	
$NO_3^- + N \rightarrow NO + NO_2 + e^-$	5.0×10^{-10}	[97]	
$NO_3^- + NO \rightarrow NO_2^- + NO_2$	3.0×10^{-15}	[137]	
$NO_3^- + O \rightarrow NO + O_3 + e^-$	1.5×10^{-10}	[97]	
$O^- + N \rightarrow NO + e^-$	2.6×10^{-10}	[137]	
$O^- + N_2(g, v) \rightarrow N_2O + e^-$	0.5×10^{-13}	[137]	b
$O^- + N_2(A^3\Sigma_u^+) \rightarrow O + N_2 + e^-$	2.2×10^{-9}	[137]	
$O^- + N_2(B^3\Pi_g) \rightarrow O + N_2 + e^-$	1.9×10^{-9}	[137]	
$O^- + N_2O \rightarrow N_2O^- + O$	2.0×10^{-12}	[137]	
$O^- + N_2O \rightarrow NO^- + NO$	2.0×10^{-10}	[137]	
$O^- + NO + M \rightarrow NO_2^- + M$	1.0×10^{-29}	[137]	a
$O^- + NO \rightarrow NO_2 + e^-$	2.6×10^{-10}	[137]	
$O^- + NO_2 \rightarrow NO_2^- + O$	1.2×10^{-9}	[137]	
$O^+ + N + M \rightarrow NO^+ + M$	1.0×10^{-29}	[137]	a
$O^+ + N \rightarrow N^+ + O$	1.3×10^{-10}	[137]	
$O^+ + N_2(g, v) + M \rightarrow NO^+ + N + M$	$6.0 \times 10^{-29} \times \left(\frac{300}{T_{ion}}\right)^2$	[137]	a, b
$O^+ + N_2(g, v) \rightarrow NO^+ + N$	$(1.5 - 2.0 \times 10^{-3} \times T_{ion} + 9.6 \times 10^{-7} \times T_{ion}^2) \times 1.0 \times 10^{-12}$	[137]	b
$O^+ + N_2O \rightarrow N_2O^+ + O$	2.2×10^{-10}	[137]	
$O^+ + N_2O \rightarrow NO^+ + NO$	2.3×10^{-10}	[137]	

$O^+ + N_2O \rightarrow O_2^+ + N_2$	2.0×10^{-11}	[137]	
$O^+ + NO \rightarrow NO^+ + O$	2.4×10^{-11}	[137]	
$O^+ + NO \rightarrow O_2^+ + N$	3.0×10^{-12}	[137]	
$O^+ + NO_2 \rightarrow NO_2^+ + O$	1.6×10^{-9}	[137]	
$O_2^- + N \rightarrow NO_2 + e^-$	5.0×10^{-10}	[137]	
$O_2^- + N_2(B^3\Pi_g) \rightarrow O_2 + N_2 + e^-$	2.5×10^{-9}	[137]	
$O_2^- + N_2(A^3\Sigma_u^+) \rightarrow O_2 + N_2 + e^-$	2.1×10^{-9}	[137]	
$O_3^- + N_2(B^3\Pi_g) \rightarrow O_3 + N_2 + e^-$	2.5×10^{-9}	[97]	
$O_3^- + N_2(A^3\Sigma_u^+) \rightarrow O_3 + N_2 + e^-$	2.1×10^{-9}	[97]	
$NO^- + N_2(B^3\Pi_g) \rightarrow NO + N_2 + e^-$	2.5×10^{-9}	[97]	
$NO^- + N_2(A^3\Sigma_u^+) \rightarrow NO + N_2 + e^-$	2.1×10^{-9}	[97]	
$N_2O^- + N_2(B^3\Pi_g) \rightarrow N_2O + N_2 + e^-$	2.5×10^{-9}	[97]	
$N_2O^- + N_2(A^3\Sigma_u^+) \rightarrow N_2O + N_2 + e^-$	2.1×10^{-9}	[97]	
$NO_2^- + N_2(B^3\Pi_g) \rightarrow NO_2 + N_2 + e^-$	2.5×10^{-9}	[97]	
$NO_2^- + N_2(A^3\Sigma_u^+) \rightarrow NO_2 + N_2 + e^-$	2.1×10^{-9}	[97]	
$NO_3^- + N_2(B^3\Pi_g) \rightarrow NO_3 + N_2 + e^-$	2.5×10^{-9}	[97]	

$NO_3^- + N_2(A^3\Sigma_u^+) \rightarrow NO_3 + N_2 + e^-$	2.1×10^{-9}	97	
$O_2^- + NO_2 \rightarrow NO_2^- + O_2$	7.0×10^{-10}	137	
$O_2^- + NO_3 \rightarrow NO_3^- + O_2$	5.0×10^{-10}	137	
$\mathbf{O_2^+ + N \rightarrow NO^+ + O}$	1.2×10^{-10}	137	
$O_2^+ + N_2(g,v) + N_2 \rightarrow O_2^+N_2 + N_2$	$9.0 \times 10^{-31} \times \left(\frac{300}{T_{ion}}\right)^2$	137	b
$\mathbf{O_2^+ + N_2(g,v) \rightarrow NO^+ + NO}$	1.0×10^{-17}	137	b
$\mathbf{O_2^+ + NO \rightarrow NO^+ + O_2}$	6.3×10^{-10}	137	
$\mathbf{O_2^+ + NO_2 \rightarrow NO^+ + O_3}$	1.0×10^{-11}	137	
$\mathbf{O_2^+ + NO_2 \rightarrow NO_2^+ + O_2}$	6.6×10^{-10}	137	
$O_2^+N_2 + N_2 \rightarrow O_2^+ + N_2 + N_2$	$1.1 \times 10^{-6} \times \left(\frac{300}{T_{ion}}\right)^{5.3} \times \exp\left(-\frac{2360}{T_{ion}}\right)$	137	
$O_2^+N_2 + O_2 \rightarrow O_4^+ + N_2$	1.0×10^{-9}	137	
$O_3^- + N \rightarrow NO + O_2 + e^-$	5.0×10^{-10}	97	
$O_3^- + NO \rightarrow NO_2^- + O_2$	2.6×10^{-12}	137	
$O_3^- + NO \rightarrow NO_3^- + O$	1.0×10^{-11}	137	
$O_3^- + NO_2 \rightarrow NO_2^- + O_3$	7.0×10^{-11}	137	
$O_3^- + NO_2 \rightarrow NO_3^- + O_2$	2.0×10^{-11}	137	
$O_3^- + NO_3 \rightarrow NO_3^- + O_3$	5.0×10^{-10}	137	
$O_4^- + N_2 \rightarrow O_2^- + O_2 + N_2$	$1 \times 10^{-10} \times \exp\left(-\frac{1044}{T_g}\right)$	137	
$O_4^- + NO \rightarrow NO_3^- + O_2$	2.5×10^{-10}	137	

$O_4^+ + N_2(g,v) \rightarrow O_2^+N_2 + O_2$	$4.6 \times 10^{-12} \times \left(\frac{T_{ion}}{300}\right)^{2.5} \times \exp\left(-\frac{2650}{T_{ion}}\right)$	[137]	b
$O_4^+ + NO \rightarrow NO^+ + O_2 + O_2$	1.0×10^{-10}	[137]	

[a] M represents any neutral species.

[b] For any species indicated with (g,v), g and v stand for its ground and vibrationally excited state, respectively.

[c] $O_2(E_x)$ represents the electronically excited states: $O_2(a^1\Delta)$and $O_2(b^1\Sigma^+)$.

[d] The rate coefficient is assumed to be equal to the rate of $O_2^+ + O_2 + M \rightarrow O_4^+ + M$.

[e] The rate coefficient is assumed to be equal to the rate of $O^- + O_2 + M \rightarrow O_3^- + M$.

[f] The rate coefficient is assumed to be equal to the rate of $O_2^- + O_2 + M \rightarrow O_4^- + M$.

Table 8.7 Ion-ion reactions included in the model, the corresponding rate coefficient expressions and the references. T_g is the gas temperature in K. The rate coefficients are expressed in $cm^3\ s^{-1} or\ cm^6\ s^{-1}$ for binary or ternary reactions, respectively.

Reaction	Rate coefficient	Ref.	Note
$O^- + O^+ + M \rightarrow O_2 + M$	$1.0 \times 10^{-25} \times \left(\frac{300}{T_g}\right)^{2.5}$	162	a
$O^- + O_2^+ + M \rightarrow O_3 + M$	$1.0 \times 10^{-25} \times \left(\frac{300}{T_g}\right)^{2.5}$	162	a
$O_2^- + O^+ + M \rightarrow O_3 + M$	$1.0 \times 10^{-25} \times \left(\frac{300}{T_g}\right)^{2.5}$	162	a
$O_2^- + O_2^+ + M \rightarrow O_2 + O_2 + M$	$1.0 \times 10^{-25} \times \left(\frac{300}{T_g}\right)^{2.5}$	162	a
$O_3^- + O^+ + M \rightarrow O_3 + O + M$	$2.0 \times 10^{-25} \times \left(\frac{300}{T_g}\right)^{2.5}$	97	a
$O_3^- + O_2^+ + M \rightarrow O_3 + O_2 + M$	$2.0 \times 10^{-25} \times \left(\frac{300}{T_g}\right)^{2.5}$	97	a
$O^- + O_2^+ \rightarrow O + O + O$	$2.60 \times 10^{-8} \times \left(\frac{300}{T_g}\right)^{0.44}$	159	a
$O_3^- + O_2^+ \rightarrow O + O + O_3$	$1.0 \times 10^{-7} \times \left(\frac{300}{T_g}\right)^{0.5}$	159	a
$O^- + O^+ \rightarrow O + O$	$4.0 \times 10^{-8} \times \left(\frac{300}{T_g}\right)^{0.43}$	159	
$O^- + O_2^+ \rightarrow O_2 + O$	$2.6 \times 10^{-8} \times \left(\frac{300}{T_g}\right)^{0.44}$	159	
$O_2^- + O^+ \rightarrow O + O_2$	$2.7 \times 10^{-7} \times \left(\frac{300}{T_g}\right)^{0.5}$	159	
$O_2^- + O_2^+ \rightarrow O_2 + O_2$	$2.01 \times 10^{-7} \times \left(\frac{300}{T_g}\right)^{0.5}$	159	
$O_2^- + O_2^+ \rightarrow O_2 + O + O$	$1.01 \times 10^{-13} \times \left(\frac{300}{T_g}\right)^{0.5}$	159	

$O_3^- + O^+ \rightarrow O_3 + O$	$1.0 \times 10^{-7} \times \left(\frac{300}{T_g}\right)^{0.5}$	163	
$O_3^- + O_2^+ \rightarrow O_2 + O_3$	$2.0 \times 10^{-7} \times \left(\frac{300}{T_g}\right)^{0.5}$	159	
$NO^- + A^+ + M \rightarrow NO + A + M$	$2.0 \times 10^{-25} \times \left(\frac{300}{T_g}\right)^{2.5}$	97	a, b
$NO_2^- + A^+ + M \rightarrow NO_2 + A + M$	$2.0 \times 10^{-25} \times \left(\frac{300}{T_g}\right)^{2.5}$	97	a, b
$N_2O^- + A^+ + M \rightarrow N_2O + A + M$	$2.0 \times 10^{-25} \times \left(\frac{300}{T_g}\right)^{2.5}$	97	a, b
$NO_3^- + A^+ + M \rightarrow NO_3 + A + M$	$2.0 \times 10^{-25} \times \left(\frac{300}{T_g}\right)^{2.5}$	97	a, b
$O_3^- + B^+ + M \rightarrow O_3 + B + M$	$2.0 \times 10^{-25} \times \left(\frac{300}{T_g}\right)^{2.5}$	97	a, c

[a] M represents any neutral species.

[b] A represents N, O, N_2, O_2, NO, NO_2 and N_2O species.

[c] B represents N, N_2, NO, NO_2 and N_2O species.

Table 8.8 Optical transitions of N_2 and O_2 species. The rate coefficients are expressed in s^{-1}.

Reaction	Rate coefficient	Ref.	Note
$\mathbf{N_2(A^3\Sigma_u^+) \rightarrow N_2}$	0.5	[137]	
$\mathbf{N_2(B^3\Pi_g) \rightarrow N_2(A^3\Sigma_u^+)}$	1.35×10^5	[137]	
$\mathbf{N_2(a'^1\Sigma_u^-) \rightarrow N_2}$	1.0×10^2	[137]	
$\mathbf{N_2(C^3\Pi_u) \rightarrow N_2(B^3\Pi_g)}$	2.45×10^7	[137]	
$\mathbf{O_2(a^1\Delta) \rightarrow O_2}$	2.6×10^{-4}	[137]	
$\mathbf{O_2(b^1\Sigma^+) \rightarrow O_2}$	8.5×10^{-2}	[137]	
$\mathbf{O_2(b^1\Sigma^+) \rightarrow O_2(a^1\Delta)}$	1.5×10^{-3}	[137]	
$\mathbf{O_2(A^3\Sigma^+, C^3\Delta, c^1\Sigma^-) \rightarrow O_2}$	11	[137]	a

[a] $O_2(A^3\Sigma^+, C^3\Delta, c^1\Sigma^-)$ is a combination of three electronic excited states at a threshold energy of 4.5 eV.

The reaction rate coefficient expressions of the VT relaxations and VV exchanges between N_2 - N_2, N_2 - O_2 and O_2 - O_2 are calculated using the Forced Harmonic Oscillator (FHO) model proposed by Adamovich et al.[165] This method offers a semi-classical non-perturbative analytical solution for VT and VV transitions of diatomic molecules by averaging the VT and VV probabilities (P_{VT} and P_{VV}) over the one-dimensional Boltzmann distribution.

$$P_{VT}(i \rightarrow f) = \frac{(n_s)^s}{(s!)^2} \cdot \varepsilon^s \cdot \exp\left(-\frac{2n_s}{s+1}\varepsilon\right) \tag{8.15}$$

$$P_{VV}(i_1, i_2 \rightarrow f_1, f_2) \cong \frac{\left[n_s^{(1)} n_s^{(2)}\right]^s}{(s!)^2} \cdot \left(\frac{\rho_\varepsilon^2}{4}\right)^s \cdot \exp\left[-\frac{2n_s^{(1)} n_s^{(2)}}{s+1}\frac{\rho_\varepsilon^2}{4}\right] \tag{8.16}$$

with $s = |i - f|$, $n_s = \left[\frac{\max(i,f)!}{\min(i,f)!}\right]^{1/s}$. ρ_ε and ε are collision and potential specific parameters.

Table 8.9 Vibrational –vibrational exchanges and vibrational-translational relaxations for N_2 (as an example) and the rate coefficient expression.

Reaction	Rate coefficient
$\mathbf{N_2(v_i) + M \rightarrow N_2(v_i - 1) + M}$	$Z \cdot \left(\frac{m}{kT}\right) \int_0^\infty P_{VT}(\bar{v}) \cdot \exp\left(\frac{-mv^2}{2kT}\right) vdv$
$\mathbf{N_2(v_i) + N_2(v_j) \rightarrow N_2(v_i - 1) + N_2(v_j + 1)}$	$Z \cdot \left(\frac{m}{kT}\right) \int_0^\infty P_{VV}(\bar{v}) \cdot \exp\left(\frac{-mv^2}{2kT}\right) vdv$

M represents any neutral particle in the plasma.

v_i and v_j are the vibrational levels of N_2 (0-24).

Z is the collision frequency and v is the particle velocity.

The reaction rate coefficients of the VT relaxations between N_2 – N are based on quasi-classical calculations that have been reproduced through a fit as proposed by Esposito et al.[166], for the following general reaction:

$N_2(v) + N \rightarrow N_2(w) + N$, with $v > w$

All the relevant trends in the rate coefficients were taken into consideration by using an additive model into the exponential argument of the reaction rate coefficient, as shown in the following expression (valid for $v = 1 - 66$ and $\Delta v = 1 - 30$):

$$K(v, T, \Delta v) = \exp\left(a_1(v, \Delta v) + \frac{a_2(v, \Delta v)}{T} + \frac{a_3(v, \Delta v)}{T^2} + \frac{a_4(v, \Delta v)}{T^3} + a_5(v, \Delta v) \cdot \ln(T)\right) \quad (8.17)$$

where

$$a_i(v, \Delta v) = z_{i0}(\Delta v) + z_{i1}(\Delta v)v + z_{i2}(\Delta v)v^2 + z_{i3}(\Delta v)v^3 + z_{i4}(\Delta v)v^4 \quad (8.18)$$

$$z_{ij}(\Delta v) = b_{ij} + c_{ij}\Delta v \quad (8.19)$$

For which the parameters are reported in [166].

Similarly, the reaction rate coefficients of the VT relaxations between O_2 – O are based on quasi-classical calculations that have been reproduced through a fit as proposed by Esposito et al.[167], for the following general reaction:

$O_2(v) + O \rightarrow O_2(w) + O$, with $v > w$

The reaction rate coefficient is then determined based on the following expression:

$$K(T, v, \Delta v) = DegF \cdot \exp\left(a_1(v, \Delta v) + \frac{a_2(v, \Delta v)}{\ln(T)} + a_3(v, \Delta v) \cdot \ln(T)\right) \tag{8.20}$$

where Δv is $(v - w)$

$$a_i(v, \Delta v) = b_{i1}(\Delta v) + b_{i2}(\Delta v) \cdot \ln(v) + \frac{b_{i3}(\Delta v) + b_{i4}(\Delta v)v + b_{i5}(\Delta v)v^2}{10^{21} + \exp(v)} \tag{8.21}$$

$$b_{ij}(\Delta v) = c_{ij1} + c_{ij2} \cdot \ln(\Delta v) + c_{ij3} \cdot \Delta v \cdot \exp(-\Delta v) + c_{ij4} \cdot \Delta v \cdot \Delta v \tag{8.22}$$

The coefficients c_{ijk} have been generated using a linear least squares method and are reported in[167] where the degeneracy factor (DegF) is also explained.

8.4 EXPERIMENTAL SETUP OF THE RGA REACTOR

Figure 8.1 shows the experimental setup of our RGA plasma. The arc discharge is generated by a 10 kV DC power supply (Topower TN-XXZ02). A 25 kΩ ballast resistor is connected to the circuit to compensate for changes in the discharge current and to prevent over-heating of the plasma, allowing for a maximum current of 280 mA. The discharge voltage is measured by a high-voltage probe (TESTEC 1000:1), and the discharge current is determined from the voltage drop across a 25 Ω resistor. The time-resolved waveforms of the discharge voltage and current are recorded by an oscilloscope (Keysight DSOX1102A, 70 MHz bandwidth, 2GSa/s sample rate). The flow rates of the N_2 and O_2 feed gases (99.999% in purity) are controlled by mass flow controllers (Bronkhorst model F-201CV). The total flow rate is fixed at 2 L min^{-1}, and the gas feed ratio between N_2 and O_2 is varied from 20/80 to 80/20. The exhaust gas (comprising the product and unconverted feed gas) is analysed using a non-dispersive infra-red (NDIR) sensor, along with an ultra-violet sensor, for quantitative analysis of the species concentration (EMERSON Rosemount X-STREAM Enhanced XEGP continuous Gas Analyzer). The X-STREAM system is configured with four gases, two of which were used for this work: NO and NO_2. Exhaust gas from the RGA was input into the system at a flow rate of 500 mL/min through the use of a Bronkhorst mass flow controller; the specific flow rate of 500 mL/min was used as the system needed an input flow rate range between 50 mL/min and 1.5 L/min, although the choice of flow rate had no effect on the concentrations. The X-STREAM system was calibrated at the factory for NO_2 (UV sensor) and NO (NDIR sensor), and the calibration was again checked before measurements of the exhaust gas components, using known concentrations from 1% to 8%.

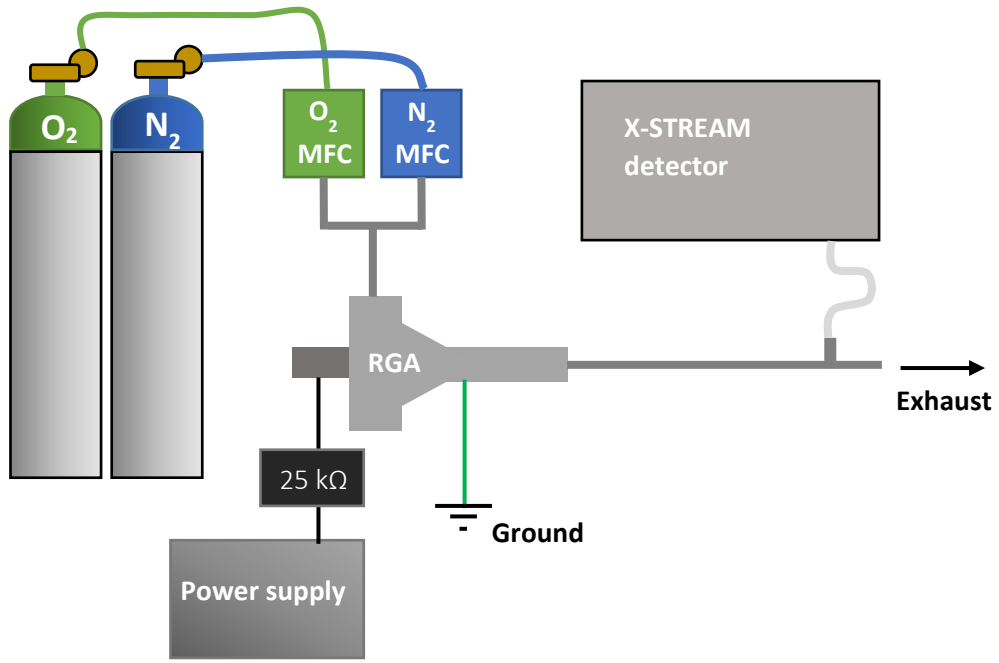

Figure 8.1: Experimental setup of the RGA reactor and X-STREAM detection device.

8.5 MODELLING DETAILS OF THE RGA

8.5.1 Sensitivity analysis of the arc length

In equation 4.5 the heat source term Q_{heat}, is calculated by a step function in the axial direction, representing the arc length (i.e. 20 mm), and a Gaussian function in the radial direction representing the width of the arc (i.e. 2 mm). These arc dimensions are typical for gliding arc reactors [57,92,94,95], but as the arc length serves as an important input parameter for the model, a sensitivity analysis of the arc length on the modelling results is performed. Figure 8.2 illustrates the effect of the arc length on the calculated gas temperature as obtained by the fully coupled heat transfer model for a reactor with an arc length of 20 and 10 mm for a plasma power of 199 W. This figure shows that a shorter arc concentrates the 199 W of plasma power in a smaller volume, leading to more gas heating and thus a higher gas temperature in the plasma. Figure 8.3 shows the effect of this increased gas temperature on the calculated NO_x concentration, as obtained by the quasi-1D chemical kinetics model for an arc length of 10, 12.5, 15, 17.5, 20, 22.5 and 25 mm. This figure shows that due to the higher gas temperatures in shorter arcs, a higher NO_x concentration is achieved. However, the figure also shows that the gain in NO_x formation becomes less significant as the arc length decreases. In short arcs the gas temperature in the center of the arc becomes so high that thermal NO_x decomposition becomes more dominant than NO_x formation reactions. The figure also shows that for the chosen arc length of 20 mm, an error of ± 0.5% in NO_x concentration is implemented in the model if the arc length is actually 2.5 mm longer or shorter, which is an acceptable sensitivity for the purpose of this model.

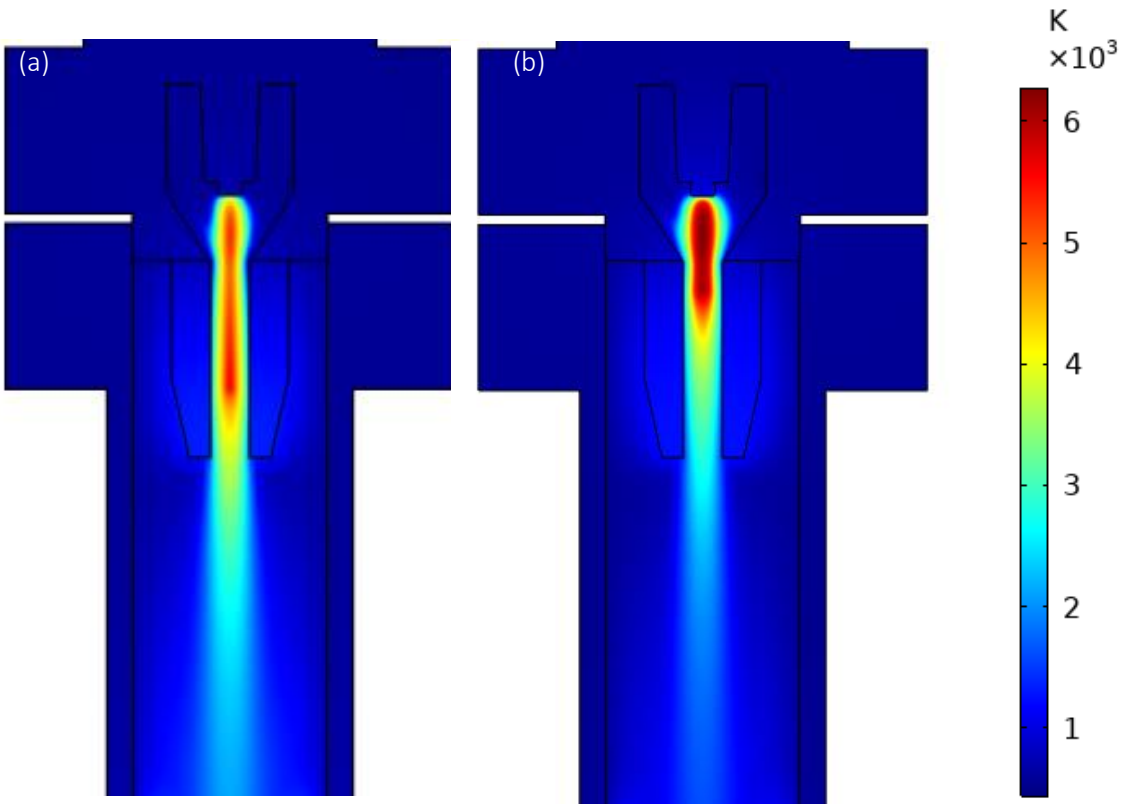

Figure 8.2: Calculated gas temperature in the reactor without effusion nozzle for a plasma power of 199 W, and for an arc length of a) 20 mm and b) 10 mm, as obtained from the 3D CFD model.

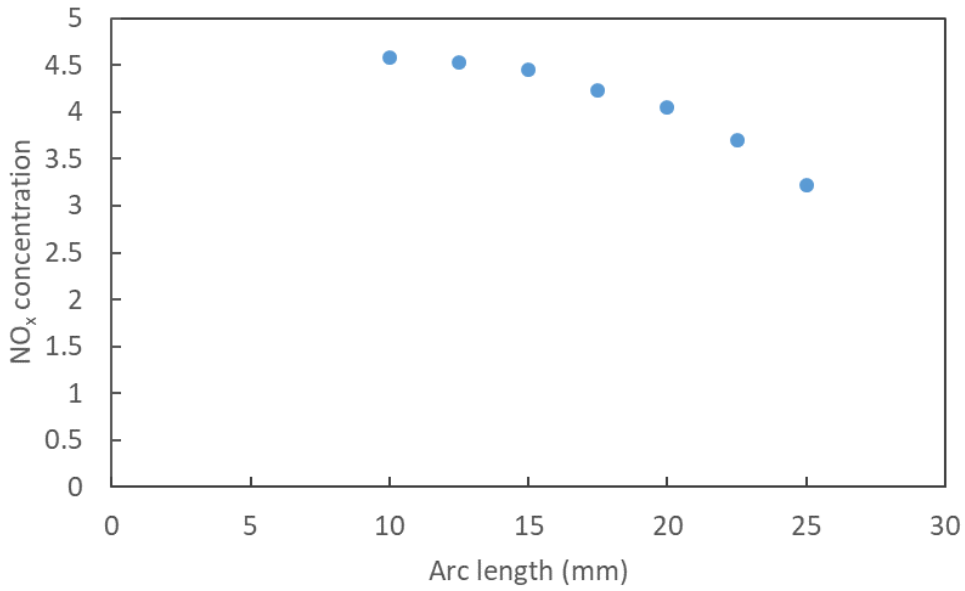

Figure 8.3: Calculated NOx concentration as a function of the arc length for a reactor without effusion nozzle at a plasma power of 199 W, as obtained by the quasi-1D chemical kinetics model.

8.5.2 Detailed reaction analysis

Table 8.10 presents the reaction analysis of the most important formation and destruction reactions at the time step where the NO_x concentration decreases (cf. Figure 4.10 in section 4.4.2), for the 3500 K temperature group. We calculated the contribution of each reaction that forms or destroys NO or NO_2, based on its reaction rate divided by the sum of the rates of all the reactions leading to the destruction or formation of NO or NO_2:

$$Contribution = \frac{Reaction\ rate\ of\ reaction\ A\ for\ destruction\ of\ NO}{Sum\ of\ reaction\ rates\ of\ all\ reactions\ that\ destroy\ NO} \quad (8.23)$$

For NO_2, the most important loss channel is the conversion of NO_2 back into NO, but as no significant contributions were found for reactions that would convert NO_2 back into N_2 and O_2, NO_2 is not the reason for the drop in total NO_x concentration. The latter is clearly attributed to NO. While part of NO is destroyed to NO_2 and hence does not decrease the total NO_x concentration, the recombination reactions of NO with N or O atoms, back into N_2 and O_2 (i.e., the reverse processes of the Zeldovich mechanism) are responsible for the drop in NO_x concentration.

Table 8.10: Most important formation and loss reactions for NO and NO2 and their relative contributions during cooling of the gas for an N2/O2 feed ratio of 80/20, for the 3500 K temperature group (see details in main paper). M stands for any neutral molecule.

Formation reactions of NO	
Reaction	Contribution (%)
$NO_2 + M \rightarrow NO + O + M$	87.79
$O + N_2 \rightarrow N + NO$	6.15
$O + NO_2 \rightarrow NO + O_2$	2.29
$N + O_2 \rightarrow O + NO$	1.93
$N + O_2 \rightarrow O + NO$	1.30
$NO_2 + NO_2 \rightarrow NO + NO_3$	0.38

Destruction reactions of NO	
Reaction	Contribution (%)
$NO + O \rightarrow NO_2$	88.09
$N + NO \rightarrow O + N_2$	6.12
$O + NO \rightarrow N + O_2$	3.29
$NO + O_2 \rightarrow O + NO_2$	2.09
$NO + NO_3 \rightarrow NO_2 + NO_2$	0.34

Formation reactions of NO_2	
Reaction	Contribution (%)
$NO + O \rightarrow NO_2$	96.91
$NO + O_2 \rightarrow O + NO_2$	2.30
$NO + NO_3 \rightarrow NO_2 + NO_2$	0.74

Destruction reactions of NO_2	
Reaction	Contribution (%)
$NO_2 + M \rightarrow NO + O + M$	96.47
$O + NO_2 \rightarrow NO + O_2$	2.52
$NO_2 + NO_2 \rightarrow NO + NO_3$	0.82

8.6 ANALYSIS OF THE EXPERIMENTAL RESULTS OF THE GAP REACTOR

The absolute conversion (X_{abs}) was calculated for CO_2 and CH_4 using equation 8.24, in which i is the molecule (CO_2 or CH_4 in this case), c_i^{blanc} is the concentration of i in the blank measurement, c_i^{plasma} is the concentration of i in the plasma measurement and α is a correction factor for gas expansion.[168] The concentrations are determined from the average of the peak areas from the four sample loops that were analyzed by the GC.

$$X_{abs_i}(\%) = \left(1 - \frac{\alpha \cdot c_i^{out}}{c_i^{in}}\right) \cdot 100\ \% \tag{8.24}$$

A correction factor α was used in the conversion equation to correct for gas expansion.[168] Indeed, DRM leads to an expansion of gas due to the increasing number of molecules after the reaction (see equation in the Introduction of the main paper). As a result, the volumetric flow rate also increases. The sample loops in the GC, however, have a constant volume, and therefore gas expansion will result in a pressure rise. However, the GC operates at atmospheric pressure, meaning that part of the gas is lost before injecting in the GC. This results in a lower number of molecules (e.g., of CO_2 or CH_4) being detected compared to the number of molecules in the outlet of the reactor, which leads to an overestimation of the conversion.

The expansion factor can be determined by adding an internal standard, such as N_2, He or Ar, to the outflow gas stream after the gas has passed through the reactor. The factor α equation 8.25 is defined as the ratio of the peak area of this internal standard from the blank to the plasma measurement, and factor β equation 8.26 is introduced to account for the increased gas flow rate because of the internal standard.[168]

In our setup He cannot be used as this is the carrier gas in the GC and neither can Ar, because the peak overlaps with the one of O_2. Therefore, a N_2 flow of 1 L/min is added after the plasma as internal standard for pure CO_2-CH_4 mixtures. For the gas mixtures already containing N_2, no extra N_2 flow is added after the plasma. The N_2 in the mixture is barely converted in the GAP (< 0.05%) and can therefore be used as internal standard. In those cases, the formulas still apply with the β factor taken as zero.

$$\alpha = \frac{A_{blanc}}{A_{plasma}}(1 + \beta) - \beta \tag{8.25}$$

$$\beta = \frac{Q_{N_2}\ (L\ min^{-1}\ )}{Q_{plasma}(L\ min^{-1}\ )} \tag{8.26}$$

This gas expansion is also taken into account when calculation the concentrations equation 8.27 and 8.28, in which c_m is the measured concentration obtained from the GC.[168]

$$c^{blanc} = c_m^{blanc}(1+\beta) \tag{8.27}$$

$$c^{plasma} = c_m^{plasma}\left(1+\frac{\beta}{\alpha}\right) \tag{8.28}$$

The absolute conversion (of both CO_2 and CH_4) defines the amount of converted gas by comparing the blank and the plasma measurements.

In addition, due to dilution with N_2 in the mixture, we also define the effective conversion, which accounts for the fraction of component $\mathbf{i}$ in the initial gas mixture equation 8.29.[80]

$$\chi_{\mathrm{eff_i}}(\%) = \chi_{\mathrm{abs_i}}(\%) \cdot \mathrm{fraction_i} \tag{8.29}$$

The total conversion (χ_{total}) equation 8.30 is calculated as the sum of the effective conversions of CO_2 and CH_4.[80]

$$X_{\mathrm{total}}(\%) = X_{\mathrm{eff_{CO_2}}}(\%) + X_{\mathrm{eff_{CH_4}}}(\%) \tag{8.30}$$

The yields (Y; in %) of the different products is calculated from the absolute conversions of CH_4 and CO_2 and the product selectivity. The selectivity (S; in %) is calculated based on C for all the products (equation 8.31), except for H_2 and H_2O, for which we calculated the H-based selectivity (equation 8.32). In these equations, general notations are used for the products ($C_xH_yO_z$ and H_yO_z) in which x, y and z are the number of C, H and O atoms in the products, c is the concentration (in %) and α is the correction factor for gas expansion (discussed above, see equation 8.25). The yields are calculated using Equations 8.33 and 8.34.[168]

$$\mathrm{S_{C,C_xH_yO_z}}(\%) = \frac{\mathrm{x}\cdot \mathrm{c}^{\mathrm{out}}_{\mathrm{C_xH_yO_z}}\cdot\alpha}{\left(\mathrm{c}^{\mathrm{in}}_{\mathrm{CH_4}} - \mathrm{c}^{\mathrm{out}}_{\mathrm{CH_4}}\cdot\alpha\right) + \left(\mathrm{c}^{\mathrm{in}}_{\mathrm{CO_2}} - \mathrm{c}^{\mathrm{out}}_{\mathrm{CO_2}}\cdot\alpha\right)} \cdot 100\ \% \tag{8.31}$$

$$\mathrm{S_{H,H_yO_z}}(\%) = \frac{\mathrm{y}\cdot \mathrm{c}^{\mathrm{out}}_{\mathrm{H_yO_z}}\cdot\alpha}{4\cdot\left(\mathrm{c}^{\mathrm{in}}_{\mathrm{CH_4}} - \mathrm{c}^{\mathrm{out}}_{\mathrm{CH_4}}\cdot\alpha\right)} \cdot 100\ \% \tag{8.32}$$

$$\mathrm{Y_{C,C_xH_yO_z}} = \frac{fraction_{CH_4}\cdot \mathrm{X_{abs,CH_4}} + fraction_{CO_2}\cdot \mathrm{X_{abs,CO_2}}}{fraction_{CH_4} + fraction_{CO_2}} \cdot \mathrm{S_{C,C_xH_yO_z}} \tag{8.33}$$

$$\mathrm{Y_{H,H_yO_z}} = \mathrm{X_{abs,CH_4}}\cdot \mathrm{S_{H,H_yO_z}} \tag{8.34}$$

The specific energy input (SEI) is calculated using Equations 8.35 and 8.36, in which P_{plasma} is the plasma power calculated from the oscilloscope data, V_{mol} is the molar volume (24.5 L mol^{-1} at 293 K) and Φ_{flow} is the total gas flow rate (kept constant in our experiments at 10 L min^{-1}).[80]

$$\mathrm{SEI\ (kJ\ L^{-1})} = \frac{\mathrm{P_{plasma}(kW)}\cdot 60(\mathrm{s\ min^{-1}})}{\Phi_{\mathrm{flow}}(\mathrm{L\ min^{-1}})} \tag{8.35}$$

$$\mathrm{SEI\ (eV\ molecule^{-1})} = \mathrm{SEI(kJ\ L^{-1})}\ \cdot \frac{6.24 \cdot 10^{21}(\mathrm{eV\ kJ^{-1}}) \cdot \mathrm{V_{mol}(L\ mol^{-1})}}{6.022 \cdot 10^{23}(\mathrm{molecule\ mol^{-1}})} \tag{8.36}$$

The energy cost of the conversion (EC) is calculated for the total conversion, using Equations 8.37 and 8.38.[80]

$$\mathrm{EC\ (kJ\ L^{-1})} = \frac{\mathrm{SEI\ (kJ\ L^{-1})}}{\mathrm{X_{total}}} \tag{8.37}$$

$$\mathrm{EC\ (eV\ molecule^{-1})} = \mathrm{EC\ (kJ\ L^{-1})} \cdot \frac{6.24 \cdot 10^{21}(\mathrm{eV\ kJ^{-1}}) \cdot \mathrm{V_{mol}(L\ mol^{-1})}}{6.022 \cdot 10^{23}(\mathrm{molecule\ mol^{-1}})} \tag{8.38}$$

The energy efficiency (EE) is calculated with Equation 5.39, with H_f the enthalpy of formation ($H_{f,CO}$= -110,5 kJ mol^{-1}; H_{f,CH_4}= -74,8 kJ mol^{-1}; H_{f,CO_2}= -393,5 kJ mol^{-1}).).[80] This formula only considers the main DRM products CO and H_2 ($H_{f,H}$ = 0, thus it is not included in the formula), however a more accurate value could be calculated when side products could be considered, e.g. H_2O, C_2H_2 or other hydrocarbons. These were not included because they could not be quantified with the current experimental setup, but based on the model, they are not formed in large amounts, so the effect of neglecting them in the formula would be minor anyway.

$$EE = \frac{\alpha \cdot \mathrm{c_{CO}^{in}} \cdot H_{f,CO} - \left(X_{CH_4} \cdot c_{CH_4}^{in} \cdot H_{f,CH_4} + X_{CO_2} \cdot c_{CO_2}^{in} \cdot H_{f,CO_2}\right)}{SEI(kJ\ L^{-1}) \cdot V_{mol}(L\ mol^{-1})} \tag{8.39}$$

REFERENCES

(1) Hayes, E. T. Energy Implications of Materials Processing (USA). *Dev. Dig.* 1980, *18*, 101–111.

(2) Pirani, S. *Burning Up: A Global History of Fossil Fuel Consumption*; Pluto Press: London, 2018.

(3) IEA. *Chemicals*; Paris, 2022.

(4) IEA. *World Energy Outlook 2021*; Paris, 2021.

(5) Sorknæs, P.; Johannsen, R. M.; Korberg, A. D.; Nielsen, T. B.; Petersen, U. R.; Mathiesen, B. V. Electrification of the Industrial Sector in 100% Renewable Energy Scenarios. *Energy* 2022, *254*, 124339.

(6) Van Geem, K. M.; Weckhuysen, B. M. Toward an E-Chemistree: Materials for Electrification of the Chemical Industry. *MRS Bull.* 2021, *46*, 1187–1196.

(7) Bogaerts, A.; Centi, G. Plasma Technology for CO2 Conversion: A Personal Perspective on Prospects and Gaps. *Front. Energy Res.* 2020, *8*, 1–23.

(8) Bogaerts, A.; Neyts, E. C. Plasma Technology: An Emerging Technology for Energy Storage. *ACS Energy Lett.* 2018, *3*, 1013–1027.

(9) Snoeckx, R.; Bogaerts, A. Plasma Technology-a Novel Solution for CO2 Conversion? *Chem. Soc. Rev.* 2017, *46*, 5805–5863.

(10) Fridman, A. *Plasma Chemistry*; Cambridge University Press: Cambridge, U.K., 2008.

(11) Kogelschatz, U. Dielectric-Barrier Discharges: Their History, Discharge Physics, and Industrial Applications. *Plasma Chem. Plasma Process.* 2003, *23*, 1–46.

(12) Kogelschatz, U.; Eliasson, B.; Egli, W. From Ozone Generators to Flat Television Screens: History and Future Potential of Dielectric-Barrier Discharges. *Pure Appl. Chem.* 1999, *71*, 1819–1828.

(13) Wolf, A. .; Righart, T. W.; Peeters, F. J.; Bongers, W. .; van de Sanden, M. C. Implications of Thermo-Chemical Instability on the Contracted Modes in CO2 Microwave Plasmas. *Plasma Sources Sci. Technol.* 2020, *29*, 025005.

(14) Silva, T.; Britun, N.; Godfroid, T.; Snyders, R. Optical Characterization of a Microwave Pulsed Discharge Used for Dissociation of CO2. *Plasma Sources Sci. Technol.* 2014, *23*, 025009.

(15) Kelly, S.; Bogaerts, A. Nitrogen Fixation in an Electrode-Free Microwave Plasma. *Joule* 2021, *5*, 3006–3030.

(16) Nunnaly, T.; Gutsol, K.; Rabinovich, A.; Fridman, A.; Gutsol, A.; Kemoun, A. A Gutsol, A Kemoun, Dissoaciation of CO2 in a Low Current Gliding Arc Plasmatron. *J. Phys. D Appl. Phys* 2011, *44*, 274009.

(17) Li, K.; Liu, J. L.; Li, X. S.; Zhu, X.; Zhu, A. M. Warm Plasma Catalytic Reforming of Biogas in a Heat-Insulated Reactor: Dramatic Energy Efficiency and Catalyst Auto-Reduction. *Chem. Eng. J.* 2016, *288*, 671–679.

(18) Prentice, I.; Farquhar, G.; Fasham, M. The Carbon Cycle and Atmospheric Carbon Dioxide. *Clim. Chang. 2001 Sci. Basis* 2001, 183–237.

(19) IEA. *Net Zero by 2050*; Paris, 2021.

(20) Bogaerts, A.; Kozák, T.; Van Laer, K.; Snoeckx, R. Plasma-Based Conversion of CO2: Current Status and Future Challenges. *Faraday Discuss.* 2015, *183*, 217–232.

(21) Asisov, R. I.; Vakar, A. K.; Jivitov, V. K.; Krotov, M. F.; Zinoviev, O. A.; Potapkin, B. V.; Rusanov, A. A.; Rusanov, V. D.; Fridman, A. A. Non-Equilibrium Plasma-Chemical Process of CO2 Decomposition in a Supersonic Microwave Discharge. *Proc. USSR Acad. Sci.* 1983, *271*, 94–97.

(22) van Rooij, G. J.; van den Bekerom, D. C. M.; den Harder, N.; Minea, T.; Berden, G.; Bongers, W. W.; Engeln, R.; Graswinckel, M. F.; Zoethout, E.; van de Sanden, M. C. M. Taming Microwave Plasma to Beat Thermodynamics in CO2 Dissociation. *Faraday Discuss.* 2015, *183*, 233–248.

(23) Bongers, W. Bouwmeester, H.; Wolf, B.; Peeters, F.; Welzel, S.; van den Bekerom, D.; den Harder, N.; Goede, A. .; Graswinckel, M. .; Groen, P. W.; Kopecki, J.; et al. Plasma-Driven Dissociation of CO2 for Fuel Synthesis. *Plasma Process. Polym.* 2017, *14*, 1600126.

(24) D'Isa, F. A.; Carbone, E. A. D.; Hecimovic, A.; Fantz, U. Performance Analysis of a 2.45 GHz Microwave Plasma Torch for CO2decomposition in Gas Swirl Configuration. *Plasma Sources Sci. Technol.* 2020, *29*, 105009.

(25) Wolf, A. J.; Peeters, F. J. J.; Groen, P. W. C.; Bongers, W. A.; van de Sanden, M. C. M. CO 2 Conversion in Nonuniform Discharges: Disentangling Dissociation and Recombination Mechanisms. *J. Phys. Chem. C* 2020, *124*, 16806–16819.

(26) Ramakers, M.; Trenchev, G.; Heijkers, S.; Wang, W.; Bogaerts, A. Gliding Arc Plasmatron: Providing an Alternative Method for Carbon Dioxide Conversion. *ChemSusChem* 2017, *10*, 2642–2652.

(27) Nunnally, T. P.; Gutsol, K.; A., R.; Fridman, A.; Gutsol, A. F.; Kemoun, A. Dissociation of CO2 in a Low Current Gliding Arc Plasmatron. *J. Phys. D. Appl. Phys.* 2011, *44*, 274009.

(28) Wang, W.; Mei, D.; Tu, X.; Bogaerts, A. Gliding Arc Plasma for CO2 Conversion: Better Insights by a Combined Experimental and Modelling Approach. *Chem. Eng. J.* 2017, *330*, 11–25.

(29) Aerts, R.; Somers, W.; Bogaerts, A. Carbon Dioxide Splitting in a Dielectric Barrier Discharge Plasma: A Combined Experimental and Computational Study. *ChemSusChem* 2015, *8*, 702–716.

(30) Van Laer, K.; Bogaerts, A. Improving the Conversion and Energy Efficiency of Carbon Dioxide Splitting in a Zirconia-Packed Dielectric Barrier Discharge Reactor. *Energy Technol.* 2015, *3*, 1038–1044.

(31) Mei, D.; Zhu, X.; Wu, C.; Ashford, B.; Williams, P. T.; Tu, X. Plasma-Photocatalytic Conversion of CO2 at Low Temperatures: Understanding the Synergistic Effect of Plasma-Catalysis. *Appl. Catal. B Environ.* 2016, *182*, 525–532.

(32) Aerts, R.; Somers, W.; Bogaerts, A. Carbon Dioxide Splitting in a Dielectric Barrier Discharge Plasma: A Combined Experimental and Computational Study. *ChemSusChem* 2015, *8*, 702–716.

(33) Rusanov, V. D.; Fridman, A. A.; Sholin, G. V. The Physics of a Chemically Active Plasma with Nonequilibrium Vibrational Excitation of Molecules. *Usp. Fiz. Nauk* 1981, *134*, 185–235.

(34) Berthelot, A.; Bogaerts, A. Modeling of CO_2 Splitting in a Microwave Plasma: How to Improve the Conversion and Energy Efficiency. *J. Phys. Chem. C* 2017, *121*, 8236–8251.

(35) Scapinello, M.; Martini, L. M.; Tosi, T. CO2 Hydrogenation by CH4 in a Dielectric Barrier Discharge: Catalytic Effect of Ni and Cu. *Plasma Process. Polym.* 2014, *11*, 624–628.

(36) Wu, A.; Yan, J.; Zhang, H.; Zhang, M.; Du, C.; Li, X. Study of the Dry Methane Reforming Process Using a Rotating Gliding Arc Reactor. *Int. J. Hydrogen Energy* 2014, *39*, 17656–17670.

(37) Dinh, D. K.; Trenchev, G.; Lee, D. H.; Bogaerts, A. Arc Plasma Reactor Modification for Enhancing Performance of Dry Reforming of Methane. *J. CO2 Util.* 2020, *42*, 101352.

(38) Canfield, D. E.; Glazer, A. N.; Falkowski, P. G. The Evolution and Future of Earth's Nitrogen Cycle. *Science (80-.).* 2010, *330*, 192–196.

(39) Cherkasov, N.; Ibhadon, A. O.; Fitzpatrick, P. A Review of the Existing and Alternative Methods for Greener Nitrogen Fixation. *Chem. Eng. Process. Process Intensif.* 2015, *90*, 24–33.

(40) Hong, J.; Prawer, S.; Murphy, A. B. Production of Ammonia by Heterogeneous Catalysis in a Packed-Bed Dielectric-Barrier Discharge: Influence of Argon Addition and Voltage. *IEEE Trans. Plasma Sci.* 2014, *42*, 2338–2339.

(41) Rouwenhorst, K. H. R.; Engelmann, Y.; van 't Veer, K.; Postma, R. S.; Bogaerts, A.; Lefferts, L. Plasma-Driven Catalysis: Green Ammonia Synthesis with Intermittent Electricity. *Green Chem.* 2020, *22*, 6258–6287.

(42) Mindi Bai; Wang Ning; Zhitao Zhang; Mindong Bai; Xiyao Bai. Plasma Synthesis of Ammonia with a Microgap Dielectric Barrier Discharge at Ambient Pressure. *IEEE Trans. Plasma Sci.* 2004, *31*, 1285–1291.

(43) Wang, Y.; Craven, M.; Yu, X.; Ding, J.; Bryant, P.; Huang, J.; Tu, X. Plasma-Enhanced Catalytic Synthesis of Ammonia over a Ni/Al2O3 Catalyst at Near-Room Temperature: Insights into the Importance of the Catalyst Surface on the Reaction Mechanism. *ACS Catal.* 2019, *9*, 10780–10793.

(44) van 't Veer, K.; Engelmann, Y.; Reniers, F.; Bogaerts, A. Plasma-Catalytic Ammonia Synthesis in a DBD Plasma: Role of Microdischarges and Their Afterglows. *J. Phys. Chem. C* 2020, *124*, 22871–22883.

(45) Ingels, R.; Graves, D. B. Improving the Efficiency of Organic Fertilizer and Nitrogen Use via Air Plasma and Distributed Renewable Energy. *Plasma Med.* 2015, *5*, 257–270.

(46) Birkeland, K. On the Oxidation of Atmospheric Nitrogen in Electric Arcs. *Trans. Faraday Soc.* 1906, *2*, 98–116.

(47) Eyde, S. Oxidation of Atmospheric Nitrogen and Development of Resulting Industries in Norway. *J. Ind. Eng. Chem.* 1912, *4*, 771–774.

(48) Rouwenhorst, K. H. R.; Jardali, F.; Bogaerts, A.; Lefferts, L. From the Birkeland-Eyde Process towards Energy-Efficient Plasma-Based NO: Xsynthesis: A Techno-Economic Analysis. *Energy Environ. Sci.* 2021, *14*, 2520–2534.

(49) Patil, B. S.; Cherkasov, N.; Lang, J.; Ibhadon, A. O.; Hessel, V.; Wang, Q. Low Temperature Plasma-Catalytic NOx Synthesis in a Packed DBD Reactor: Effect of Support Materials and Supported Active Metal Oxides. *Appl. Catal. B Environ.* 2016, *194*, 123–133.

(50) Krop, J.; Pollo, I. Chemical Reactors for Synthesis of Nitrogen Oxide in a Stream of Low-Temperature Plasma. III. Reactor to Freeze Reaction Products by Injection of Water. *Chemia* 1981, *678*, 51–59.

(51) Namihira, T.; Katsuki, S.; Hackam, R.; Akiyama, H.; Okamoto, K. Production of Nitric Oxide Using a Pulsed Arc Discharge. *IEEE Trans. Plasma Sci.* 2002, *30*, 1993–1998.

(52) Mutel, B.; Dessaux, O.; Goudmand, P. Energy Cost Improvement of the Nitrogen Oxides Synthesis in a Low Pressure Plasma. *Rev. Phys. Appliquée* 1984, *19*, 461–464.

(53) Azizov R.I., Zhivotov V.K., Krotov M.F., Rusanov V.D., Tarasov Yu.V., Fridman A.A., S. G. V.

Synthesis of Nitrogen Oxides in a Nonequilibrium UHF Discharge under Electron-Cyclotron Resonance Conditions. *High Energy Chem.* 1980, *14*, 366.

(54) Vervloessem, E.; Gorbanev, Y.; Nikiforov, A.; De Geyter, N.; Bogaerts, A. Sustainable NO x Production from Air in Pulsed Plasma: Elucidating the Chemistry behind the Low Energy Consumption . *Green Chem.* 2022, *24*, 916–929.

(55) Patil, B. S.; Peeters, F. J. J.; van Rooij, G. J.; Medrano, J. A.; Gallucci, F.; Lang, J.; Wang, Q.; Hessel, V. Plasma Assisted Nitrogen Oxide Production from Air: Using Pulsed Powered Gliding Arc Reactor for a Containerized Plant. *AIChE J.* 2018, *64*, 526–537.

(56) Wang, W.; Patil, B.; Heijkers, S.; Hessel, V.; Bogaerts, A. Nitrogen Fixation by Gliding Arc Plasma: Better Insight by Chemical Kinetics Modelling. *ChemSusChem* 2017, *10*, 2110.

(57) Vervloessem, E.; Aghaei, M.; Jardali, F.; Hafezkhiabani, N.; Bogaerts, A. Plasma-Based N2 Fixation into NOx: Insights from Modeling toward Optimum Yields and Energy Costs in a Gliding Arc Plasmatron. *ACS Sustain. Chem. Eng.* 2020, *8*, 9711–9720.

(58) Van Rooij, G. J.; Akse, H. N.; Bongers, W. A.; Van De Sanden, M. C. M. Plasma for Electrification of Chemical Industry: A Case Study on CO2 Reduction. *Plasma Phys. Control. Fusion* 2018, *60*, 14019.

(59) Morgan, E. R.; Manwell, J. F.; McGowan, J. G. Sustainable Ammonia Production from U.S. Offshore Wind Farms: A Techno-Economic Review. *ACS Sustain. Chem. Eng.* 2017, *5*, 9554–9567.

(60) Smith, C.; Hill, A. K.; Torrente-Murciano, L. Current and Future Role of Haber-Bosch Ammonia in a Carbon-Free Energy Landscape. *Energy Environ. Sci.* 2020, *13*, 331–344.

(61) Menter, F. R.; Kuntz, M.; Langtry, R. Ten Years of Industrial Experience with the SST Turbulence Model Turbulence Heat and Mass Transfer. *Turbul. Heat Mass Transf.* 2003, *4*, 625–632.

(62) Menter, F. R. Zonal Two Equation κ-ω Turbulence Models for Aerodynamic Flows. *AIAA 23rd Fluid Dyn. Plasmadynamics, Lasers Conf. 1993* 1993.

(63) Jones, W. .; Launder, B. E. The Prediction of Laminarization with a Two-Equation Model of Turbulence. *Int. J. Heat Mass Transf.* 1972, *15*, 301–314.

(64) Weigand, B.; Ferguson, J. R.; Crawford, M. E. An Extended Kays and Crawford Turbulent Prandtl Number Model. *Int. J. Heat Mass Transf.* 1997, *40*, 4191–4196.

(65) Vortmeyer, D.; Kabelac, S. *VDI Heat Atlas, Chapter 3: Gas Radiation: Radiation from Gas Mixtures*; 2006.

(66) Van Den Bekerom, D. C. M.; Linares, J. M. P.; Verreycken, T.; Van Veldhuizen, E. M.; Nijdam, S.; Berden, G.; Bongers, W. A.; Van De Sanden, M. C. M.; Van Rooij, G. J. The Importance of Thermal Dissociation in CO2 Microwave Discharges Investigated by Power Pulsing and Rotational Raman Scattering. *Plasma Sources Sci. Technol.* 2019, *28*, 055015.

(67) den Harder, N.; van den Bekerom, D. C. M.; Al, R. S.; Graswinckel, M. F.; Palomares, J. M.; Peeters, F. J. J.; Ponduri, S.; Minea, T.; Bongers, W. A.; van de Sanden, M. C. M.; et al. Homogeneous CO2 Conversion by Microwave Plasma: Wave Propagation and Diagnostics. *Plasma Process. Polym.* 2017, *14*, 1600120.

(68) Wolf, A. J.; Righart, T. W. H.; Peeters, F. J. J.; Bongers, W. A.; Van De Sanden, M. C. M. Implications of Thermo-Chemical Instability on the Contracted Modes in CO2 Microwave Plasmas. *Plasma Sources Sci. Technol.* 2020, *29*, 25005.

(69) Gröger, S.; Ramakers, M.; Hamme, M.; Medrano, J. A.; Bibinov, N.; Gallucci, F.; Bogaerts, A.;

Awakowicz, P. Characterization of a Nitrogen Gliding Arc Plasmatron Using Optical Emission Spectroscopy and High-Speed Camera. *J. Phys. D. Appl. Phys.* 2019, *52*.

(70) Patil, B. S.; van Rooij, G. J.; Peeters, F. J. J.; Medrano, J. A.; Gallucci, F.; Lang, J.; Wang, Q.; Hessel, V. Plasma Assisted Nitrogen Oxide Production from Air: Using Pulsed Powered Gliding Arc Reactor for a Containerized Plant. *AIChE J.* 2017, *64*, 526–537.

(71) Berthelot, A.; Bogaerts, A. Modeling of Plasma-Based CO2 Conversion: Lumping of the Vibrational Levels. *Plasma Sources Sci. Technol.* 2016, *25*, 045022.

(72) Kolev, S.; Sun, S.; Trenchev, G.; Wang, W.; Wang, H.; Bogaerts, A. Quasi-Neutral Modeling of Gliding Arc Plasmas. *Plasma Process. Polym.* 2017, *14*, 8–11.

(73) Trenchev, G.; Nikiforov, A.; Wang, W.; Kolev, S.; Bogaerts, A. Atmospheric Pressure Glow Discharge for CO2 Conversion: Model-Based Exploration of the Optimum Reactor Configuration. *Chem. Eng. J.* 2019, *362*, 830–841.

(74) Trenchev, G.; Bogaerts, A. Dual-Vortex Plasmatron – A Novel Plasma Source for CO2 Conversion. *J. CO2 Util.* 2020, *39*, 101152.

(75) Pancheshnyi, S.; Eismann, B.; Hagelaar, G. J. M.; Pitchford, L. C. Computer code ZDPlasKin, http://www.zdplaskin.laplace.univ-tlse.fr (University of Toulouse, LAPLACE, CNRS-UPSINP, Toulouse, France, 2008).

(76) Hagelaar, G. J. M.; Pitchford, L. C. Solving the Boltzmann Equation to Obtain Electron Transport Coefficients and Rate Coefficients for Fluid Models. *Plasma Sources Sci. Technol.* 2005, *14*, 722–733.

(77) IST-Lisbon database, www.lxcat.net, retrieved in february 2018.

(78) Phys4entry database, CNR IMIP Bari and SER&Practices, retrieved in february 2019.

(79) Colonna, G.; Laporta, V.; Celiberto, R.; Capitelli, M.; Tennyson, J. Non-Equilibrium Vibrational and Electron Energy Distributions Functions in Atmospheric Nitrogen Ns Pulsed Discharges and Ms Post-Discharges: The Role of Electron Molecule Vibrational Excitation Scaling-Laws. *Plasma Sources Sci. Technol.* 2015, *24*.

(80) Cleiren, E.; Heijkers, S.; Ramakers, M.; Bogaerts, A. Dry Reforming of Methane in a Gliding Arc Plasmatron: Towards a Better Understanding of the Plasma Chemistry. *ChemSusChem* 2017, *10*, 3864–3864.

(81) Heijkers, S.; Bogaerts, A. CO2Conversion in a Gliding Arc Plasmatron: Elucidating the Chemistry through Kinetic Modeling. *J. Phys. Chem. C* 2017, *121*, 22644–22655.

(82) Kozàk, T.; Bogaerts, A. Splitting of CO2 by Vibrational Excitation in Non-Equilibrium Plasmas: A Reaction Kinetics Model. *Plasma Sources Sci. Technol.* 2014, *23*.

(83) Van Alphen, S.; Vermeiren, V.; Butterworth, T.; Van Den Bekerom, D. C. M.; Van Rooij, G. J.; Bogaerts, A. Power Pulsing to Maximize Vibrational Excitation Efficiency in N2 Microwave Plasma: A Combined Experimental and Computational Study. *J. Phys. Chem. C* 2020, *124*, 1765–1779.

(84) Vermeiren, V.; Bogaerts, A. Plasma-Based CO2 Conversion: To Quench or Not to Quench? *J. Phys. Chem. C* 2020, *124*, 18401–18415.

(85) Vermeiren, V.; Bogaerts, A. Improving the Energy Efficiency of CO2 Conversion in Non-Equilibrium Plasmas through Pulsing. *J. Phys. Chem. C* 2019.

(86) Celli, V. Streamlines and streamtubes on http://galileo.phys.virginia.edu/.

(87) Magin, T.; Degrez, G.; Sokolova, I. Thermodynamic and Transport Properties of Martian Atmosphere for Space Entry Application. *33rd Plasmadynamics Lasers Conf.* 2002, No. May.

(88) Wang, W.; Patil, B.; Heijkers, S.; Hessel, V.; Bogaerts, A. Nitrogen Fixation by Gliding Arc Plasma: Better Insight by Chemical Kinetics Modelling. *ChemSusChem* 2017, *10*, 2110.

(89) Liu, J.; Park, H.; Chung, W.; Park, D. High-Efficient Conversion of CO2 in AC-Pulsed Tornado Gliding Arc Plasma. *Plasma Chem. Plasma Process.* 2015, *09*, 437–449.

(90) Slaets, J.; Aghaei, M.; Ceulemans, S.; Van Alphen, S.; Bogaerts, A. CO2 and CH4 Conversion in "Real" Gas Mixtures in a Gliding Arc Plasmatron: How Do N2 and O2 Affect the Performance? *Green Chem.* 2020, *22*, 1366–1377.

(91) Vervloessem, E.; Aghaei, M.; Jardali, F.; Hafezkhiabani, N.; Bogaerts, A. Plasma-Based N 2 Fixation into NO X : Insights from Modeling toward Optimum Yields and Energy Costs in a Gliding Arc Plasmatron. *ACS Sustain. Chem. Eng.* 2020, *8*, 9711–9720.

(92) Trenchev, G.; Kolev, S.; Wang, W.; Ramakers, M.; Bogaerts, A. CO2 Conversion in a Gliding Arc Plasmatron: Multidimensional Modeling for Improved Efficiency. *J. Phys. Chem. C* 2017, *121*, 24470–24479.

(93) Wang, Q.; Patil, B.; Anastasopoulou, A.; Butala, S.; Rovira, J.; Hessel, V.; Lang, J. Plasma Assisted Nitrogen Fixation Process. *22nd Int. Symp. Plasma Chem.* 2015, No. July, 1–2.

(94) Jardali, F.; Van Alphen, S.; Creel, J.; Ahmadi Eshtehardi, H.; Axelsson, M.; Ingels, R.; Snyders, R.; Bogaerts, A. NOxproduction in a Rotating Gliding Arc Plasma: Potential Avenue for Sustainable Nitrogen Fixation. *Green Chem.* 2021, *23*, 1748–1757.

(95) Ramakers, M.; Heijkers, S.; Tytgat, T.; Lenaerts, S.; Bogaerts, A. Combining CO2 Conversion and N2 Fixation in a Gliding Arc Plasmatron. *J. CO2 Util.* 2019, *33*, 121–130.

(96) Snoeckx, R.; Heijkers, S.; Van Wesenbeeck, K.; Lenaerts, S.; Bogaerts, A. CO2 Conversion in a Dielectric Barrier Discharge Plasma: N2 in the Mix as a Helping Hand or Problematic Impurity? *Energy Environ. Sci.* 2016, *9*, 999–1011.

(97) Wang, W.; Snoeckx, R.; Zhang, X.; Cha, M. S.; Bogaerts, A. Modeling Plasma-Based CO2 and CH4 Conversion in Mixtures with N2, O2, and H2O: The Bigger Plasma Chemistry Picture. *J. Phys. Chem. C* 2018, *122*, 8704–8723.

(98) Heijkers, S.; Snoeckx, R.; Kozák, T.; Silva, T.; Godfroid, T.; Britun, N.; Snyders, R.; Bogaerts, A. CO<inf>2</Inf> Conversion in a Microwave Plasma Reactor in the Presence of N<inf>2</Inf>: Elucidating the Role of Vibrational Levels. *J. Phys. Chem. C* 2015, *119*, 12815–12828.

(99) Snoeckx, R.; Van Wesenbeeck, K.; Lenaerts, S.; Cha, M. S.; Bogaerts, A. Suppressing the Formation of NO: X and N2O in CO2/N2 Dielectric Barrier Discharge Plasma by Adding CH4: Scavenger Chemistry at Work. *Sustain. Energy Fuels* 2019, *3*, 1388–1395.

(100) Yeo, Z. Y.; Chew, T. L.; Zhu, P. W.; Mohamed, A. R.; Chai, S. P. Conventional Processes and Membrane Technology for Carbon Dioxide Removal from Natural Gas: A Review. *J. Nat. Gas Chem.* 2012, *21*, 282–298.

(101) Aresta, M.; Dibenedetto, A.; Angelini, A. Catalysis for the Valorization of Exhaust Carbon: From CO2 to Chemicals, Materials, and Fuels. Technological Use of CO2. *Chem. Rev.* 2014, *114*, 1709–1742.

(102) Wu, Y.; Chen, Z.; Rong, M.; Cressault, Y.; Yang, F.; Niu, C.; Sun, H. Calculation of 2-Temperature Plasma Thermo-Physical Properties Considering Condensed Phases: Application to CO2-CH4 Plasma: Part 1. Composition and Thermodynamic Properties. *J. Phys. D. Appl. Phys.* 2016, *49*.

(103) Niu, C.; Chen, Z.; Rong, M.; Wang, C.; Wu, Y.; Yang, F.; Wang, X.; Pang, Q. Calculation of 2-Temperature Plasma Thermo-Physical Properties Considering Condensed Phases: Application to CO2-CH4 Plasma: Part 2. Transport Coefficients. *J. Phys. D. Appl. Phys.* 2016, *49*.

(104) Tanaka, Y.; Paul, K. C.; Sakuta, T. Thermodynamic and Transport Properties of N2/O2 Mixtures at Different Admixture Ratios. *IEEJ Trans. Power Energy 120*, 24–30.

(105) Poling, B. E.; Prausnitz, J. M.; O'Connell, J. P. *The Properties of Gases and Liquids*, 5th ed.; 2000.

(106) Vesovic, V. Prediction of the Thermal Conductivity of Gas Mixtures at Low Pressures. *Int. J. Thermophys.* 2001, *22*, 801–828.

(107) Snoeckx, R.; Setareh, M.; Aerts, R.; Simon, P.; Maghari, A.; Bogaerts, A. Influence of N2 Concentration in a CH4/N2 Dielectric Barrier Discharge Used for CH4 Conversion into H2. *Int. J. Hydrogen Energy* 2013, *38*, 16098–16120.

(108) Trenchev, G.; Kolev, S.; Bogaerts, A. A 3D Model of a Reverse Vortex Flow Gliding Arc Reactor. *Plasma Sources Sci. Technol.* 2016, *25*, 035014.

(109) Zhang, H.; Wang, W.; Li, X.; Han, L.; Yan, M.; Zhong, Y.; Tu, X. Plasma Activation of Methane for Hydrogen Production in a N2 Rotating Gliding Arc Warm Plasma: A Chemical Kinetics Study. *Chem. Eng. J.* 2018, *345*, 67–78.

(110) Qin, Y.; Niu, G.; Wang, X.; Luo, D.; Duan, Y. Status of CO 2 Conversion Using Microwave Plasma. *J. CO2 Util.* 2018, *28*, 283–291.

(111) van den Bekerom, D. C. M.; Palomares Linares, J. M.; Verreycken, T.; van Veldhuizen, E. M.; Nijdam, S.; Bongers, W.; Van de Sanden, R.; Van Rooij, G. J. The Importance of Thermal Dissociation in CO2 Microwave Discharges Investigated by Power Pulsing and Rotational Raman Scattering. *Plasma Sources Sci. Technol.* 2019, *28*, 055015.

(112) Hecimovic, A.; D'Isa, F. A.; Carbone, E.; Fantz, U. Enhancement of CO2 Conversion in Microwave Plasmas Using a Nozzle in the Effluent. *J. CO2 Util.* 2022, *57*, 101870.

(113) Viegas, P.; Vialetto, L.; Wolf, A. J.; Peeters, F. J. J.; Groen, P. W. C.; Righart, T. W. H.; Bongers, W. A.; van de Sanden, M. C. M.; Diomede, P. Insight into Contraction Dynamics of Microwave Plasmas for CO2 Conversion from Plasma Chemistry Modelling. *Plasma Sources Sci. Technol.* 2020, *29*, 105014.

(114) COMSOL Multiphysics® v. 6.0, COMSOL AB: Stockholm, Sweden.

(115) Smith, G. P.; Golden, D. M.; Frenklach, M.; Moriarty, N. W.; Eiteneer, B.; Goldenberg, M.; Bowman, T. C.; Hanson, R. K.; Song, S.; Gardiner, W. C. J.; et al. GRI-MECH 3.0.

(116) McBride, B. J.; Zehe, M. J.; Gordon, S. *NASA Glenn Coefficients for Calculating Thermodynamic Properties of Individual Species: National Aeronautics and Space Administration*; 2002.

(117) Carbone, E.; D'Isa, F.; Hecimovic, A.; Fantz, U. Analysis of the C2 (D3 Πg-A3 Πu) Swan Bands as a Thermometric Probe in CO2 Microwave Plasmas. *Plasma Sources Sci. Technol.* 2020, *29*, 055003.

(118) Bogaerts, A.; Tu, X.; Whitehead, J. C.; Centi, G.; Lefferts, L.; Guaitella, O.; Azzolina-Jury, F.; Kim, H.-H.; Murphy, A. B.; Schneider, W. F.; et al. The 2020 Plasma Catalysis Roadmap. *J. Phys. D. Appl. Phys.* 2020, *53*, 443001.

(119) Anastasopoulou, A.; Butala, S.; Lang, J.; Hessel, V.; Wang, Q. Life Cycle Assessment of the Nitrogen Fixation Process Assisted by Plasma Technology and Incorporating Renewable Energy. *Ind. Eng. Chem. Res.* 2016, *55*, 8141–8153.

(120) Anastasopoulou, A.; Wang, Q.; Hessel, V.; Lang, J. Energy Considerations for Plasma-Assisted N-

Fixation Reactions. *Processes* 2014, *2*, 694–710.

(121) COMSOL Multiphysics® v. 5.5. Www.Comsol.Com. COMSOL AB, Stockholm, Sweden.

(122) Laporta, V.; Little, D. A.; Celiberto, R.; Tennyson, J. Electron-Impact Resonant Vibrational Excitation and Dissociation Processes Involving Vibrationally Excited N2molecules. *Plasma Sources Sci. Technol.* 2014, *23*, 065002.

(123) Alves, L. L. E + N2 => N2^+ + 2e Exc to B3PG C3PU A3Suv4 A1Su and N(Ex). *J. phys. Conf. Ser.* 2014, *656*, 1.

(124) Morgan database, www.lxcat.net, retrieved in february 2018.

(125) Alves, L. L. The IST-Lisbon Database on LXCat. *J. phys. Conf. Ser.* 2014, *565*.

(126) Phelps Database, www.lxcat.net, Phelps, A.V.; Pitchford, L. C. Anisotropic Scattering of Electrons by N2 and Its Effect on Electron Transport. *Phys. Rev.* 1985, *31*, 2932.

(127) Tennyson, V.; Laporta, R. . C. J. O2 Vibrational Excitation CS. *plasma sources sci. Technol.* 2013, *22*, 025001.

(128) Itikawa, Y. Cross Sections for Electron Collisions with Oxygen Molecules. *J. Phys. Chem. Ref. Data* 2009, *38*, 1–20.

(129) Eliasson, B.; Kogelschatz, U. *Basic Data for Modelling of Electrical Discharges in Gases: Oxygen*; Baden: ABB Asea Brown Boveri, 1986.

(130) Lawton, S. A.; Phelps, A. V. Excitation of the b^1 sigma_g^+ state of O_2 by low energy electrons.

(131) Khvorostovskaya, L. E.; Yankovsky, V. A. Negative Ions, Ozone, and Metastable Components in Dc Oxygen Glow Discharge. *Contrib. to Plasma Phys.* 1991, *31*, 71–88.

(132) Hokazono, H.; Obara, M.; Midorikawa, K.; Tashiro, H. Theoretical Operational Life Study of the Closed-Cycle Transversely Excited Atmospheric CO2laser. *J. Appl. Phys.* 1991, *69*, 6850–6868.

(133) Itikawa database, www.lxcat.net, retrieved in february 2018.

(134) Quantemol database, www.lxcat.net, retrieved in february 2018.

(135) Hayashi database, www.lxcat.net, retrieved in february 2018.

(136) Gordillo-V'azquez, F. J. Air Plasma Kinetics under the Influence of Sprites. *J. Phys. D. Appl. Phys.* 2008, *41*, 234016.

(137) Capitelli, M.; Ferreira, C. M.; Gordiets, B. F.; Osipov, A. I. *Plasma Kinetics in Atmospheric Gases*; 2000.

(138) Kewley, D. J.; Hornung, H. G. Free-Piston Shock-Tube Study of Nitrogen Dissociation. *Chem. Phys. Lett.* 1974, *25*, 531–536.

(139) Clyne, M. A. A. .; Stedman, D. H. Rate of Recombination of Nitrogen Atoms. *J. Phys. Chem.* 1967, *71*, 3071–3073.

(140) Van Gaens, W.; Bogaerts, A. Erratum: Kinetic Modelling for an Atmospheric Pressure Argon Plasma Jet in Humid Air (J. Phys. D: Appl. Phys. 46 (2013) 275201)). *J. Phys. D. Appl. Phys.* 2014, *47*.

(141) Tsang, W.; Hampson, R. F. Chemical Kinetic Data Base for Combustion Chemistry. Part I. Methane and Related Compounds. *J. Phys. Chem. Ref. Data* 1986, *15*, 1087–1279.

(142) Atkinson, R.; Baulch, D. L.; Cox, R. A.; Hampson, R. F.; Kerr Chairman, J. A.; Troe, J. Evaluated

Kinetic and Photochemical Data for Atmospheric Chemistry: Supplement III. IUPAC Subcommittee on Gas Kinetic Data Evaluation for Atmospheric Chemistry. *J. Phys. Chem. Ref. Data* 1997, *18*, 881–1097.

(143) Hippler, H.; Rahn, R.; Troe, J. Temperature and Pressure Dependence of Ozone Formation Rates in the Range 1-1000 Bar and 90-370 K. *J. Chem. Phys.* 1990, *93*, 6560–6569.

(144) Heimerl, J. M.; Coffee, T. P. The Unimolecular Ozone Decomposition Reaction. *Combust. Flame* 1979, *35*, 117–123.

(145) Suzzi Valli, G.; Orrú, R.; Clementi, E.; Laganà, A.; Crocchianti, S. Rate Coefficients for the N+O2reaction Computed on an Ab Initio Potential Energy Surface. *J. Chem. Phys.* 1995, *102*, 2825–2832.

(146) Baulch, D.L.; Cobos, C.J.; Cox, R.A.; Frank, P.; Hayman, G.; Just, Th.; Kerr, J.A.; Murrells, T.; Pilling, M.J.; Troe, J.; Walker, R.W.; Warnatz, J. Evaluated Kinetic Data for Combusion Modelling. Supplement I. *J. Phys. Chem. Ref. Data* 1994, *23*, 847–1033.

(147) Hjorth, J. No Title. *Int. J. Chem. Kinet.* 1992, *24*, 51–65.

(148) Herron, J. T. Rate of the Reaction NO+N. *J. Chem. Phys.* 1961, *35*, 1138–1139.

(149) Bemand, P. P.; Clyne, M. A. A.; Watson, R. T. Atomic Resonance Fluorescence and Mass Spectrometry for Measurements of the Rate Constants for Elementary Reactions: O 3PJ + NO 2 → NO + O2 and NO + O3 → NO 2 + O2. *J. Chem. Soc. Faraday Trans. 2 Mol. Chem. Phys.* 1974, *70*, 564–576.

(150) Atkinson, R.; Baulch, D. L.; Cox, R. A.; Crowley, J. N.; Hampson, R. F.; Hynes, R. G.; Jenkin, M. E.; Rossi, M. J.; Troe, J.; Center, P. R.; et al. Evaluated Kinetic and Photochemical Data for Atmospheric Chemistry: Volume I – Gas Phase Reactions of O. *J. Phys. Chem. Ref. Data* 2004, *I*, 1461–1738.

(151) No, I. R. I.; Tsang, W.; Herron, J. T. Chemical Kinetic Data Base for Propellant Combustion. 1991, *20*.

(152) Graham, R.A.; Johnston, H. S. The Photochemistry of NO3 and the Kinetics of the N2O5-O3 System. *J. Phys. Chem.* 1978, *82*.

(153) Ashmore, P.G.; Burnett, M. G. Concurrent Molecular and Free Radical Mechanisms in the Thermal Decomposition of Nitrogen Dioxide. *J. Chem. Soc. Faraday Trans. 2* 1962.

(154) Campbell, I. M.; Thrush, B. A. Behaviour of Carbon Dioxide and Nitrous Oxide in Active Nitrogen. *Trans. Faraday Soc.* 1966, *62*, 3366–3374.

(155) Nighan, W. L. Electron Rates Excited. 1970, *2*.

(156) Kossyi, I. A.; Kostinsky, A. Y.; Matveyev, A. A.; Silakov, V. P. Kinetic Scheme of the Non-Equilibrium Discharge in Nitrogen-Oxygen Mixtures. *Plasma Sources Sci. Technol.* 1992, *1*, 207–220.

(157) Beverly, R. E. Ion Aging Effects on the Dissociative-Attachment Instability in CO2 Lasers. *Opt. Quantum Electron.* 1982, *14*, 501–513.

(158) Whitaker, M.; Biondi, M.A.; Johnsen, R. Electron-Temperature Dependence of Dissociative Recomination of Electrons with N2^+. *Phys. Rev. A* 1981, *24*, 743–745.

(159) Gudmundsson, J. T.; Thorsteinsson, E. G. Oxygen Discharges Diluted with Argon: Dissociation Processes. *Plasma Sources Sci. Technol.* 2007, *16*, 399–412.

(160) Ionin, A. A.; Kochetov, I. V.; Napartovich, A. P.; Yuryshev, N. N. Physics and Engineering of Singlet

Delta Oxygen Production in Low-Temperature Plasma. *J. Phys. D. Appl. Phys.* 2007, *40*.

(161) Cenian, A.; Chernukho, A.; Borodin, V. Modeling of Plasma-Chemical Reactions in Gas Mixture of CO2 Lasers. II. Theoretical Model and Its Verification. *Contrib. to Plasma Phys.* 1995, *35*, 273–296.

(162) Beuthe, T. G.; Chang, J.-S. Related Content Chemical Kinetic Modelling of Non-Equilibrium Ar- CO 2 Thermal Plasmas. *Jpn. J. Appl. Phys.* 1997, *36*, 4997–5002.

(163) Eliasson, B.; Hirth, M.; Kogelschatz, U. Ozone Synthesis from Oxygen in Dielectric Barrier Discharges. *J. Phys. D. Appl. Phys.* 1987, *20*, 1421–1437.

(164) Mcfarland, M.; Dunkin, D. B.; Fehsenfeld, F. C.; Schmeltekopf, A. L.; Ferguson, E. E. Collisional Detachment Studies of NO-. *J. Chem. Phys.* 1972, *56*, 2358–2364.

(165) Adamovich, I. V.; MacHeret, S. O.; Rich, J. W.; Treanor, C. E. Vibrational Energy Transfer Rates Using a Forced Harmonic Oscillator Model. *J. Thermophys. Heat Transf.* 2008, *12*, 57–65.

(166) Esposito, F.; Armenise, I.; Capitelli, M. N-N2 State to State Vibrational-Relaxation and Dissociation Rates Based on Quasiclassical Calculations. *Chem. Phys.* 2006, *331*, 1–8.

(167) Esposito, F.; Armenise, I.; Capitta, G.; Capitelli, M. O-O2 State-to-State Vibrational Relaxation and Dissociation Rates Based on Quasiclassical Calculations. *Chem. Phys.* 2008, *351*, 91–98.

(168) Pinhão, N.; Moura, A.; Branco, J. B.; Neves, J. Influence of Gas Expansion on Process Parameters in Non-Thermal Plasma Plug-Flow Reactors: A Study Applied to Dry Reforming of Methane. *Int. J. Hydrogen Energy* 2016, *41*, 9245–9255.

LIST OF PUBLICATIONS

As first author

1. “Power Pulsing to maximize vibrational excitation efficiency in N_2 microwave plasma: A Combined Experimental and Computational Study” Van Alphen S., Vermeiren V., Butterworth T., van den Bekerom D.C.M., van Rooij G.J., Bogaerts A., J Phys Chem C 124, 1765 (2020). IF: 4.12

DOI: 10.1021/acs.jpcc.9b06053

2. “NO_x production in a rotating gliding arc plasma: potential avenue for sustainable nitrogen fixation” Van Alphen S., Jardali F., Creel J., Ahmadi Eshtehardi H., Axelsson M., Ingels R., Snyders R., Bogaerts A., Green Chem 23, 1748 (2021). IF: 10.18

DOI: 10.1039/D0GC03521A

3. “Sustainable gas conversion by gliding arc plasmas: a new modelling approach for reactor design improvement” Van Alphen S., Jardali F., Creel J., Trenchev G., Snyders R., Bogaerts A., Sustainable Energy & Fuels 5, 1786 (2021). IF: 6.04

DOI: 10.1039/D0SE01782E

4. “Effect of N_2 on CO_2-CH_4 conversion in a gliding arc plasmatron: Can this major component in industrial emissions improve the energy efficiency?” Van Alphen S., Slaets J., Ceulemans S., Aghaei M., Snyders R., Bogaerts A., J. CO2 Utiliz. 54 101767 (2021). IF: 7.07

DOI: 10.1016/j.jcou.2021.101767

5. “Effusion nozzle for energy-efficient NOx production in a rotating gliding arc plasma reactor” Van Alphen S., Ahmadi Eshtehardi H., O'Modhrain C., Bogaerts J., Van Poyer H., Creel J., Delplancke M-P., Snyders R., Bogaerts A., Chem Eng J 443, 136529 (2022). IF: 13.27

DOI: 10.1016/j.cej.2022.136529.

6. “Post-plasma quenching to improve conversion and energy efficiency in a CO_2 microwave plasma” Van Alphen S., Mercer E.R., van Deursen C.F.A.M., Righart T.W.H., Bongers W., Snyders R., Bogaerts A. van de Sanden M.C.M. , Peeters F.J.J., Fuels, 334 126734 (2023). IF: 6.609

7. “Modelling post-plasma quenching nozzles for improving the performance of CO_2 microwave plasmas” Van Alphen S., Hecimovic A., Kiefer C. K. , Fantz U., Snyders R., Bogaerts A. in press at Chem Eng J (2023). IF: 13.27

As Co-author

7. “CO_2 and CH_4 conversion in “real” gas mixtures in a gliding arc plasmatron: how do N2 and O2 affect the performance?” Slaets J., Aghaei M., Ceulemans S., Van Alphen S., Bogaerts A., Green Chem 22, 1366 (2020) IF: 10.18

DOI: 10.1039/C9GC03743H

8. “Spatially and temporally non-uniform plasmas: microdischarges from the perspective of molecules in a packed bed plasma reactor” van ‘t Veer K., Van Alphen S., Remy A., Gorbanev Y., De Geyter N., Snyders R., Reniers F., Bogaerts A., J Phys D Appl Phys 54, 174002 (2021). IF: 3.04

DOI: 10.1088/1361-6463/abe15b

CONFERENCE CONTRIBUTIONS

- Oral presentation at the International Symposium of Plasma Chemistry (ISPC) 2019 in Napels, Italy (June 2019), presenting “Gas temperature and vibrational temperature in a pulsed N_2 microwave plasma: a combined experimental and computational study to explore non-equilibrium conditions”

- Oral presentation at Chemistry Conference for Young Scientists (ChemCys) 2020 in Blankenberge, Belgium (February 2020), presenting “N_2 fixation in a rotating gliding arc reactor, a computational study”

- Oral presentation at the ERC – SCOPE online workshop (March 2021), presenting "NO_x in a rotating gliding arc plasma: potential avenue for sustainable N_2 fixation”

- Invited speaker at the Solvay workshop in Brussels, Belgium (November 2021), presenting “Plasma-based NO_x formation: potential avenue for sustainable N_2 fixation”

- Poster presentation at the Solvay workshop in Brussels, Belgium (November 2021), presenting “Effusion nozzle for energy-efficient NO_x production in a rotating gliding arc plasma reactor”

- Oral presentation at the 9th Central European Symposium for Plasma Chemistry (Cespc) 2022 in Vysoke Tatry, Slovakia (September 2022), presenting “Modelling study of CO_2 conversion in microwave plasmas using a quenching nozzle”

OTHER ACHIEVEMENTS

Thesis supervision

- Supervisor for the bachelor’s thesis of Sara Ceulemans at PLASMANT (2019)
- Supervisor for the master’s thesis of Joachim Slaets at PLASMANT (2019)
- Supervisor for the master’s thesis of Jens Bogaerts at PLASMANT (2021)
- Supervisor for the master’s thesis of Stein Maerivoet at PLASMANT (2022)

Teaching

- Teaching “multi-dimensional modelling” as part of the Plasma modelling master’s course (2020)

Organizing activities

- Organizing the workshop “Proefkot” to promote Science to children between 9 and 13 years old. (November 2019, October 2020 and Februari 2021)
- Part of organizing committee of “Kekulé lectures” in the University of Antwerp (2021)
- Part of organizing committee of “CRF-ChemCys”, an international conference for young scientists in Blankenberge (2022)